Experimental Tape Casting of Adjacently Graded Materials for Magnetic Refrigeration

Bulatova, Regina

Publication date:
2014

Document Version
Publisher's PDF, also known as Version of record

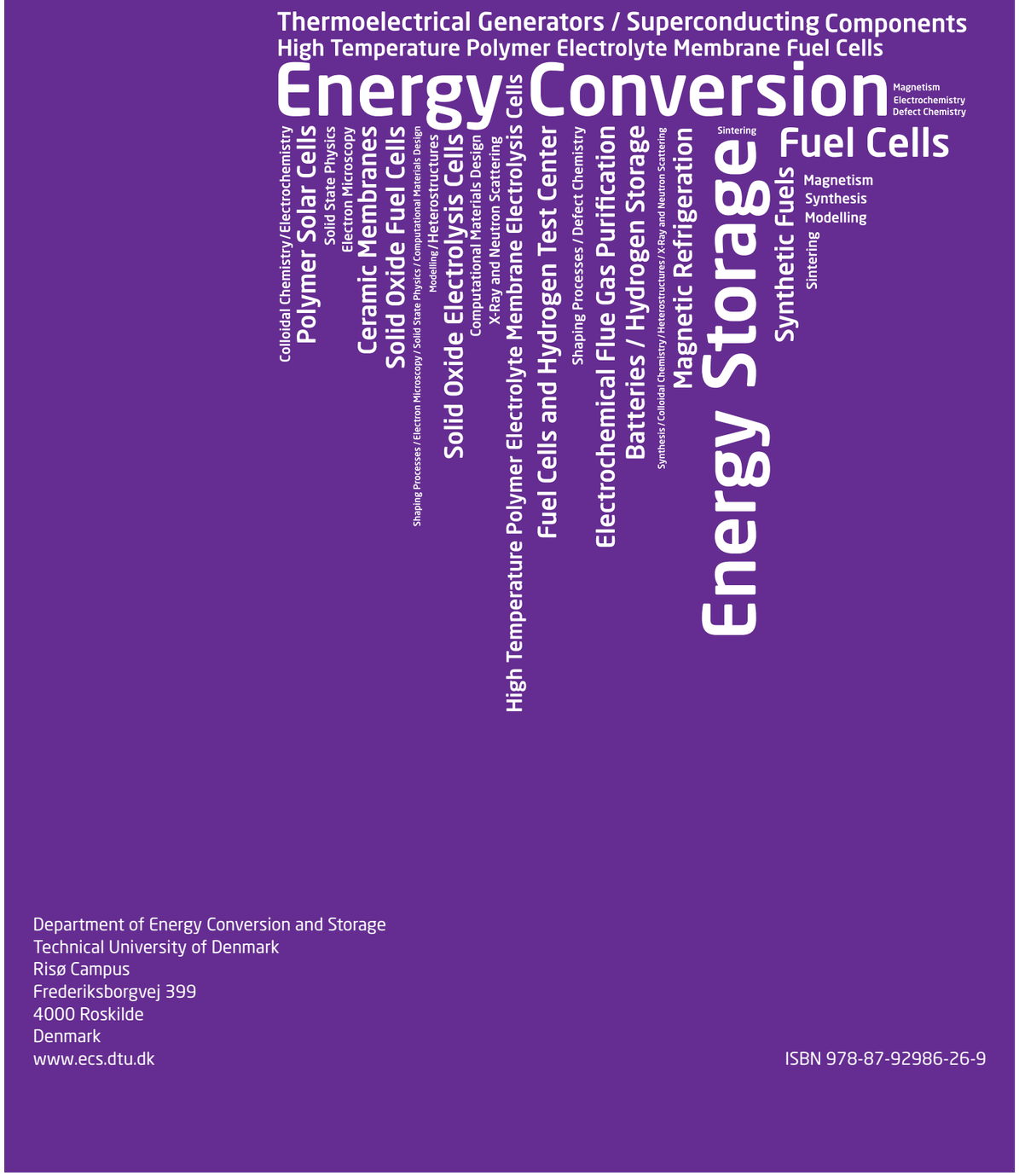

Department of Energy Conversion and Storage
Technical University of Denmark
Risø Campus
Frederiksborgvej 399
4000 Roskilde
Denmark
www.ecs.dtu.dk

ISBN 978-87-92986-26-9

Experimental Tape Casting of Adjacently Graded Materials for Magnetic Refrigeration

August 2014

Technical University of Denmark

DTU

Experimental Tape Casting of Adjacently Graded Materials for Magnetic Refrigeration

Regina Bulatova
Department of Energy Conversion and Storage

Ph.D. Thesis, August 2014

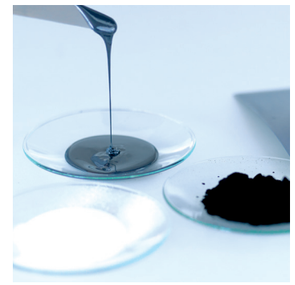

DTU Energy
Department of Energy Conversion and Storage

Experimental Tape Casting of Adjacently Graded Materials for Magnetic Refrigeration

PhD Thesis

Bulatova Regina

Department of Energy Conversion and Storage
Technical University of Denmark
August 2014

PhD thesis title:
Experimental Tape Casting of Adjacently Graded Materials for Magnetic Refrigeration

Author:
Regina Bulatova

Supervisor:
Senior Scientist Dr. Christian Robert Haffenden Bahl

Co-supervisors:
Development Engineer Dr. Kjeld Bøhm Andersen
Senior Scientist Dr. Michela Della Negra
Senior Scientist Dr. Andreas Kaiser

Assessment committee:
Prof. Andreas Roosen, University Erlangen-Nürnberg, Germany
Dr. Erling Ringgaard, Meggitt PLC, Denmark
Dr. Karsten Agersted, Technical University of Denmark, Denmark

Date of defense:
13 November 2014

Funding:
Scientific Research Councils on Technology and Production Sciences (FTP) (Contract No. 09-072888, OPTIMAC), which is part of the Danish Council for Independent Research (DFF)

Address:
Technical University of Denmark
Department of Energy Conversion and Storage
Frederiksborgvej 399,
P.O. Box 49, Building 779,
4000 Roskilde, Denmark,
Tel.: +45 4677 5800
info@ecs.dtu.dk

ISBN: 978-87-92986-26-9

Abstract

Functional graded materials are extensively applied in many innovative technologies, *e.g.* solid oxide fuel cells, solar cells, membranes, piezoactuators, capacitors, and thermoelectric systems. The synergy of advantageous combinations of composites with different composition and/or microstructure together with recently developed option for low cost manufacturing techniques progressively widens the diversity of functional materials design and the variety of their application range. Currently, application requirements in ceramic technology have advanced multilayered systems to a point where layered graded materials with well-controlled dimensional and mechanical characteristics can be successfully produced. This thesis presents a study of adjacently graded ceramic materials, achieved by a novel side-by-side tape casting technique.

Side-by-side tape casting produces continuous in-plane adjacently graded thin films. The motivation to create such adjacently segmented structures stemmed from a search of material and a materials design alternative to the expensive rare earth element gadolinium which is widely used as a magnetic regenerator in the emerging magnetic refrigeration technology.

Conventional tape casting involves the preparation of specially formulated slurry, which is cast by a blade to a thin flat tape, then dried into flexible so-called green solid tape and can be subsequently sintered into a hard ceramic material. The principal difference and, at the same time, a challenge of the side-by-side tape casting technique includes simultaneous adjacent co-flow of slurries, creating a uniform graded material with a well-defined interface, which is characterised by a high adhesion and no inter-diffusion between adjacent materials.

The PhD project focuses on the crucial challenges of the side-by-side tape casting technique: recognising critical parameters which affect the quality of a graded tape, shape and position of the interface area. Studied parameters can be divided into two categories: operational parameters and slurry formulation optimisation. The operational parameters encompass modification of the entire tape caster into a multi chamber unit, establishment of the optimal operating parameters such as casting gap, speed, and slurry level in the tape caster reservoir, and elucidation of the impact of chamber partition design on the quality of the final tape. The second research area focuses on optimisation of the slurry formulation suitable for adjacent co-flow, which includes a detailed study of the rheological behaviour of slurries, influence of slurry density, numerical analysis of the slurry flow beneath the doctor blade resulting in a greater control of material design desired to meet all requirements from the application side. Mechanical tests verified a high adhesion between co-cast materials, indicating that the formed adjacently graded tapes behave as a single material.

As the result of the tight collaboration between the present experimentally oriented project and a parallel project on numerical characterisation of tape casting, a new program for controlling the casting thickness was developed and practically applied. This new approach based on a continuous casting speed change, was compared with other approaches to control tape thickness and showed very promising results of decreasing the tape thickness gradient to 3%.

In addition to the development of side-by-side tape casting technique, a series of experiments were directed at investigating which of the available tape casting modes (*e.g.*, single-blade, double-blade, casting with use of pump system or the newly proposed speed change mode) forms a uniform green tape with precisely controlled tape thickness. The objective of performing these tests was to decide which tape caster design had to be used for the side-by-side tape casting.

Resume

Funktionelle graduerede materialer anvendes i vid udstrækning i mange innovative teknologier, såsom fastoxidbrændselsceller, solceller, membraner, piezo-aktuatorer, kapacitorer og termoelektriske systemer. Synergien af fordelagtige kombinationer af kompositmaterialer med forskellig sammensætning og/eller mikrostruktur sammen med valget af billige formningsteknikker udvider gradvist mangfoldigheden af materialedesignet som bliver anvendt og udvalget af deres anvendelighed. Som det er nu, har anvendelsesbehovet i keramiske teknologier avanceret multilags-systemer til det punkt hvor lagdelte graduerede materialer med velkontrollerede dimensionelle og mekaniske egenskaber nemt kan opnås. I denne afhandling præsenteres resultater fra tilstødende graduerede keramiske materialer, som var opnået ved hjælp af en ny side-om-side båndstøbnings-teknik.

Side-om-side båndstøbning er en forholdsvis ny støbeteknik som kan skabe kontinuerte, plane tilstødende graduerede tynde plader. Motivationen til at skabe sådanne tilstødende, segmenterede strukturer var en søgen efter alternative materialer og materialedesigns i stedet for den sjældne jordart gadolinium, som normalt anvendes til magnetiske regeneratorer i den voksende magnetisk køling teknologi.

Konventionel båndstøbning involverer special-fremstilling af en støbemasse, som bliver støbt ved hjælp af et rakelstål, til et tyndt, fladt bånd, hvorefter det bliver tørret og bliver til fleksible, såkaldte grønne, faste plader, som så efterfølgende kan sintres til et hårdt keramisk materiale. Den væsentligste udfordring ved side-om-side-båndstøbning indbefatter samtidig, strømning af støbemasser ved siden af hinanden, hvilket skaber et uniformt gradueret materiale med en veldefineret grænseflade som er kendetegnet ved en høj sammenklæbnings-evne og ingen diffusion imellem de tilstødende materialer.

Ph.d.-projektet fokuserer på de vigtige udfordringer ved side-om-side-båndstøbningsteknikken: Identificere kritiske parametre, der påvirker kvaliteten af graduerede bånd, form og position af grænsefladeområdet. De undersøgte parametre kan deles op i to områder: De operationelle parametre omfatter modificering af hele båndstøberen til en multi-kammer-enhed, fastsættelse af det optimale maskin-program, såsom støbespalte, hastighed og støbemasseniveauet i støbekarret og opklaring af konsekvenserne af støbekammerets opdelingsdesign på kvaliteten af det færdige bånd. Det andet forskningsområde har fokus på optimering af støbemassens udformning så den passer til støbning med tilstødende strømning. Dette indbefatter et detaljeret studie af støbemassens rheologiske opførsel, påvirkningen af støbemassens massefylde og numerisk analyse af støbemassens strømning under rakelstålet, hvilket resulterer i større kontrol med materialedesignet med ønsket om at imødekomme alle krav der måtte være til anvendelsesmulighederne. Mekaniske tests bekræfter en høj sammenklæbnings-evne mellem sammenstøbte materialer, hvilket indikerer at de skabte tilstødende graduerede bånd opfører sig som et enkelt materiale.

Som et resultat af det tætte samarbejde mellem dette eksperimentelt orienterede projekt og et projekt som er fokuseret på numerisk karakterisering af båndstøbning, er et nyt program som kontrollerer støbe-tykkelsen blevet udviklet og brugt i praksis. Denne nye tilgang baseret på en kontinuert ændring i støbehastigheden, blev sammenlignet med andre tilgange til kontrol af støbetykkelsen og viste et meget lovende resultat hvilket reducerede tykkelsesgradienten til 3%.

Udover udviklingen af SBS TC teknikken, blev en række eksperimenter hvis formål var at undersøge hvilke af de tilgængelige båndstøbnings-metoder (f.eks. enkelt-bladet, dobbelt-bladet, støbning med brug af et pumpesystem eller den nyligt foreslået hastighedsændrings-model) ville skabe et uniformt grønt bånd

med præcist kontrolleret båndtykkelse. Formålet med at udføre disse forsøg var at bestemme hvilket båndstøbningsdesign der skulle bruges til side-om-side båndstøbning.

Acknowledgment

Immensely grateful THANKS to Dr. Christian Robert Haffenden Bahl for the excellent engineering, practical and esthetical advices and guidance throughout my three years study, for his patience and critical view while correcting my reports and papers. Most importantly I would like to thank him for highly inspirational, helpful, enthusiastic supervision and for him always being ready to meet me with smile and smart jokes whenever I bothered him.

Many thanks to my co-supervisors Dr. Kjeld Bøhm Andersen, Dr. Michela Della Negra and Dr. Andreas Kaiser for a great support and for reminding me a practical side to things, guiding the project to a more complete end.

I'm also very grateful to Professor Nini Pryds for the financial support of this thesis research and a daily gratitude and encourangment. Many thanks to all people involved into OPTIMAC project for very valuable scientific advices and feedbacks on work. I would like to specifically acknowledge Dr. Masoud Jabbari and Professor Jesper Hattel, Dr. De Wei Ni, Dr. Tesfaye Tadesse Molla, Dr. Henrik Lund Frandsen for a fruitful discussions and nice collaboration that has been resulted to nice publications.

Specific gratitude to Karen Brodersen, Mads Gudik-Sørensen, Christophe Gadea, Dr. Jonas Gurauskis, Dr. Karl Tor Sune Thydén, Søren Christensen, Ebtisam Abdellahi for being always available to listen my ideas, add professional perspectives, mix all mentioned with a few minutes exchange of cheerful jokes and thanks a lot for always being ready to give me a hand for making some of my ideas to come true! It is so important and necessary input making to reach the success at the end of the day.

Thanks to the male group of Magnetic Cooling for accepting me as the only female member for all three years. It was always a great pleasure to have a fruitful meetings together, learn a lot of practical tips from you, celebrate any cake-appearance occasions, participate in DTU or DHL relay races and share a meal in lunch club a few times. I also extend my deepest gratitude to the whole group of Ceramic Engineering and Science and personally to Dr. Severine Ramousse for creating a nice friendly atmosphere in the group.

Personal support was undoubtedly provided with the excellent sense of humour and positive life position from my friends, among whom I would like to specifically mention Jean-Claude Nodzefon, David Marhauer-Nimb, Jesper Buch Jensen, Markus Hösel, NingYu Wu, Jihyun Lee, and Helge Grosch. The sickness leave with the broken arm, moving to another apartment, having not so pleasant experience with ex-tenants and the last month of thesis writing were still sunny, cheerful and very motivating thanks to you, guys! I hope I will have a life-long chance to thank you for making my days in this beautiful country to be as in real, warm and magic fairy tale. Especially thanks to my wizards for a very efficient help in proof reading, accelerating my office-home transportation, and providing me a hot meal of advices and laughs.

And the gratefullest thanks to my brilliant and internationally recognised the best for me parents, my mamochka Liudmila and papul'ka Raphael for being extremely supportive, patient, always positive and "no pasarán" motivative. Thanks to my sister Lena and to my 2 months niece Kristina for their shiny smiles. Thanks also to all my Russian friends, teachers, professors and ex-colleagues who never let me feeling like being abroad keeping me updated in all daily routine deals which happens in their family growing lives.

Thanks to Denmark for being a hygge home for these years and for a nice cultural, especially rich on art and architecture heritage, for unbelievably amazing sunset views in Risø, refreshing swimming in fjords, cycling skills, for smørrebrød and spandauer-delightfull mornings!

Contents

List of publications

1. R. Bulatova, K. B. Andersen, A. Kaiser, M. Della Negra, C. R. H. Bahl, Thickness Control and Interface Quality as Functions of Slurry Formulation and Casting Speed in Side-By-Side Tape Casting, *J. Eur. Ceram. Soc.*, vol. 34 (16), pp. 4285-4295, 2014.
2. R. Bulatova, K. B. Andersen, L. Theil Kuhn, C. R. H. Bahl, and N. Pryds, Functionally Graded Ceramics Fabricated with Side-By-Side Tape Casting for Use in Magnetic Refrigeration, *Int. J. Appl. Ceram. Technol.*, IJAC 12298.
3. R. Bulatova, M. Gudik-Sørensen, A. Kaiser, M. D. Negra, K. B. Andersen, C. R. H. Bahl, The Effect of Tape Caster Operational Parameters on the Quality of Adjacently Graded Materials –submitted to the *Journal of Materials and Design*.
4. C. R. H. Bahl, D. Velázquez, K. K. Nielsen, K. Engelbrecht, K. B. Andersen, R. Bulatova, and N. Pryds, High Performance Magnetocaloric Perovskites for Magnetic Refrigeration, *Appl. Phys. Lett*., vol. 100 (12), p. 121905, 2012.
5. M. Jabbari, R. Bulatova, J. H. Hattel, and C. R. H. Bahl, Quasi-Steady State Power Law Model for Flow of $(La_{0.85}Sr_{0.15})_{0.9}MnO_3$ Ceramic Slurry in Tape Casting, *Mater. Sci. Technol*., vol. 29 (9), pp. 1080–1087, 2013.
6. M. Jabbari, R. Bulatova, J. H. Hattel, and C. R. H. Bahl, An Evaluation of Interface Capturing Methods in a VOF based Model for Multiphase Flow of a Non-Newtonian Ceramic in Tape Casting, *Appl. Math. Model.*, vol. 38 (13), pp. 3222-3232, 2014.
7. Tesfaye Tadesse Molla, De Wei Ni, Regina Bulatova, Rasmus Bjørk, Christian Bahl, Nini Pryds, Henrik Lund Frandsen, Finite Element Modeling of Camber Evolution during Sintering of Bi-layer Structures, *J. Am. Ceram. Soc.*, vol. 97 (9), pp. 2965-2972, 2014.
8. M. Jabbari, R. Bulatova, J. H. Hattel, and C. R. H. Bahl, On the Modelling of Tape Casting: A Review of Current Methods and New Trends – submitted to the *Journal of American Ceramic Society*.
9. R. Bulatova, M. Jabbari, K. B. Andersen, C. R. H. Bahl The Variation of Interface Formation with Slurry Viscosity Change in Side-By-Side Tape Casting, 5th International Conference on Shaping of Advanced Ceramics, 2013.
10. M. Jabbari, R. Bulatova, J. Hattel, C. Bahl, Interface oscillation in the side-by-side (SBS) tape casting of functionally graded ceramics (FGCs), *Am. Phys. Soc. Bull.* (ISSN: 0003-0503), vol. 57 (17), pp. H7.00002, 2012.

List of nomenclatures and acronyms

AE LSM .....$La_{0.85}Sr_{0.15}MnO_3$ powder, supplied by American Elements
AMR .....active magnetic regeneration
BET .....Brunauer, Emmett and Teller method
CGO.....$Ce_{0.9}Gd_{0.1}O_2$
CSR test.....controlled shear rate test
CSS test .....controlled shear stress test
DB .....tape casting with use of a double blade set-up
DBP .....dibutyl phthalate
FGM .....functionally graded materials
HT LSM.....$La_{0.85}Sr_{0.15}MnO_3$ powder, supplied by Haldor Topsøe A/S
LCSM .....$La_{0.67}Ca_{0.33-x}Sr_xMn_{1.05}O_3$, $x \in [0.0375\text{-}0.0600]$,
LSM .....$La_{0.85}Sr_{0.15}MnO_3$
LVE .....linear viscoelastic range
MCE.....magnetocaloric effect
MEKET.....azeotropic mixture of methylethylketone and ethanol
MR .....magnetic refrigeration
PEG .....polyethylene glycol
PS .....tape casting with use of a pump system to continuously supply slurry into the tape caster reservoir
PSD.....particle size distribution
PVB.....polyvinyl butyral
PVP.....polyvinylpyrolidone
SB .....tape casting with use of a single blade set-up
SBS TC .....side-by-side tape casting
SC .....tape casting with use of a speed change mode to control tape thickness
SEM .....scanning electron microscope
XRD .....X-ray diffraction

1 Introduction

Regardless of climate, cooling and heating is a daily need all over the world in residential, industrial and public sectors. According to statistics, 34% of electricity is consumed by cooling appliances and 15% of the worldwide energy consumption involves the use of refrigerators [1]. Today almost all cooling systems use vapour compression refrigerators based on a compression and expansion cycle of the circulating refrigerant. A serious problem with vapour compression, however, is that the most commonly used refrigerants such as chloro-fluoro-carbons (CFCs) and hydro-chloro-fluoro-carbons (HCFCs) were recently banned in most countries due to their destructive effect on the ozone layer. Also, their alternative hydro-fluoro-carbons (HFCs) are greenhouse gases which have been proven to significantly contribute to global warming. Moreover, further development of conventional vapour-compression refrigeration is hindered by technological limitations because for the last 160 years since this technology was invented it has been already studied thoroughly and optimised a lot. In the midst of growing population, correlating to a high energy and resource consumption, and a simultaneous contemporary increase in environmental concern from modern society, the performance of conventional refrigeration is not competitive. This calls for alternative green solution of energy-efficient refrigeration technologies.

Over the last decades, the technology of room temperature magnetic refrigeration (*MR*) has been developed towards the level of becoming a potential substitute for the conventional compressor-based refrigeration and air conditioning [2]. Using a solid non-volatile magnetic material as a refrigerant and water, alcohol or air as the medium for heat transfer, magnetic refrigeration sufficiently counts as a sustainable emission-free technology. Without using a compressor as an auxiliary component, the working cycle of magnetic refrigerators is less noisy, operates at atmospheric pressure and low maintenance costs. Ultimately, the key competence of magnetic refrigeration is the great potential to be at least 15-20% more efficient compared to the performance of conventional refrigerators [3].

1.1 Magnetic refrigeration

1.1.1 The magnetocaloric effect

The principle of magnetic refrigeration relies on the magnetocaloric effect (MCE), *i.e.* the reversible temperature change of magnetocaloric materials as a response to the application of a magnetic field [4], [5]. The physics behind this effect is based on the interaction between the entropy, due to the disorder of atomic magnetic moments under applied magnetic field, and the entropy, due to the heat motions of the atoms in the crystal lattice.

A schematic illustration of the magnetocaloric effect is presented in Figure 1.1 In the absence of a magnetic field, the uncompensated spins of magnetic moments (represented as arrows) of the magnetocaloric material are disordered, and magnetic entropy is high. Application of a magnetic field tends to orient the spins thereby lowering magnetic entropy. The magnetic field affects only the magnetic entropy (S_M) of the magnetocaloric material, while the other two components of the material's entropy - the lattice entropy (S_L) and the electronic entropy (S_E) - are not directly affected by change in magnetic field. However, if the field application takes place adiabatically (*i.e.* the total entropy is preserved), the decrease in magnetic entropy is compensated by an increase in lattice entropy, *i.e.* an

increase in heat-induced motion followed by an increase in material temperature *T*. The reverse process takes place when the magnetic field is removed, resulting in an increase of magnetic entropy and a decrease in temperature of the adiabatic system. The described working cycle of magnetization/demagnetization of the magnetocaloric material is the principle behind the concept of magnetic refrigeration, analogous to compression/expansion cycle used in conventional refrigerators (Figure 1.1).

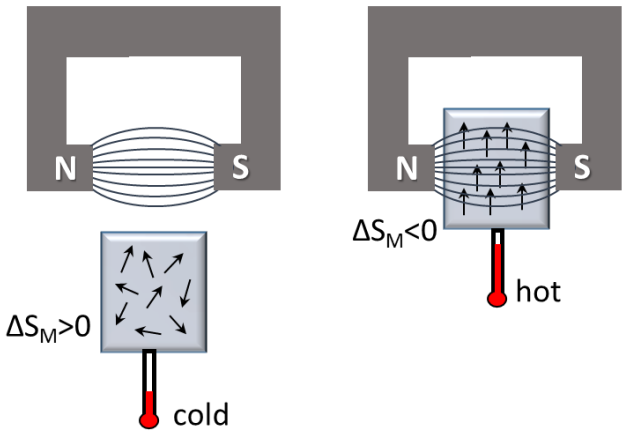

Figure 1.1. Simplified schematics of magnetocaloric effect. The applied magnetic field causes the alignment of spins in paramagnetic material, resulting in decrease in magnetic entropy and increase in material's temperature. Spins are schematically shown as arrows.

The qualitative correlation between the thermal and the magnetic constituents are generally presented in a temperature-entropy (*T-S)* diagram by two magnetic isofield curves under applied magnetic field (*H≠0*) and without magnetic field (*H=0*) (Figure 1.2). As described above, the magnetocaloric effect can be characterised by adiabatic temperature change ΔT_{ad} *(T, H)* upon applied magnetic field:

$$\Delta T_{ad} = -\mu_0 \int_0^H \frac{T}{c}\left(\frac{\partial M}{\partial T}\right)_H dH, \qquad 1.1$$

where μ_0 is vacuum permeability, H the final magnetic fields, T the temperature, c the specific heat capacity, M the magnetization [6]. Alternatively, the magnetocaloric effect can be described at constant temperature, whereby an applied magnetic field causes a change in magnetic entropy. This is known as the isothermal magnetic entropy change ΔS_M*(T, H)* given by:

$$\Delta S_M = \mu_0 \int_0^H \left(\frac{\partial M}{\partial T}\right)_H dH \qquad 1.2$$

From Eqs. 1.1 and 1.2 it is seen that magnetocaloric effect is dependent on the strength of the applied magnetic field. Furthermore, magnetocaloric effect is large when magnetisation changes rapidly with temperature (*i.e.* the ratio $\frac{\partial M}{\partial T}$ is high). This means that magnetocaloric effect is most pronounced in the vicinity of magnetic ordering temperature. For a magnetic transition such as from a ferro- to a paramagnetic state the characteristic transition temperature is called Curie temperature.

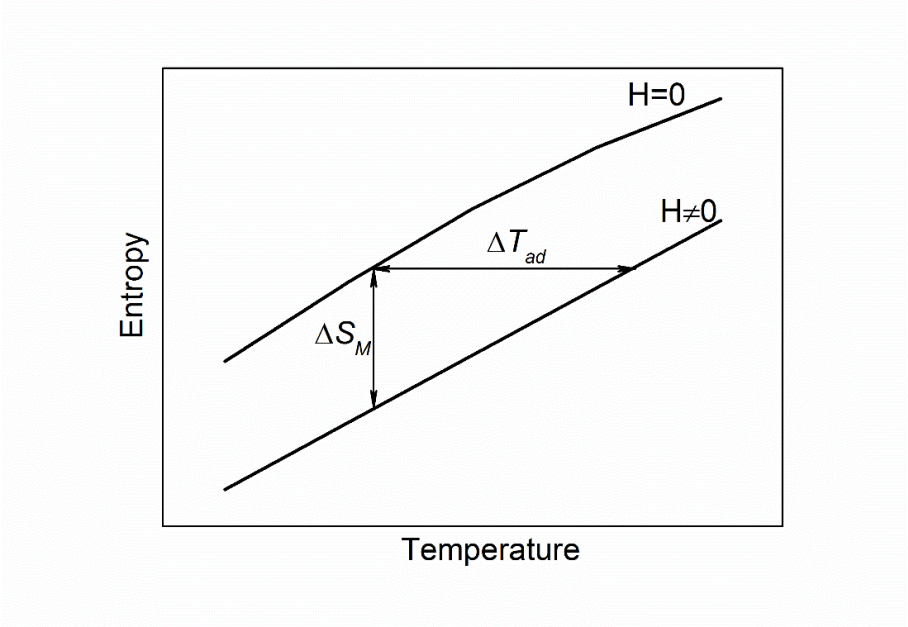

Figure 1.2. Thermodynamic temperature-entropy T-S schematic diagram for a paramagnetic-ferromagnetic material in zero (H=0) and non-zero (H≠0) magnetic fields. Arrows depict the change in the applied field under adiabatic conditions with a temperature change ΔT_{ad} (T, H) and under isothermal conditions with a change in magnetic entropy ΔS_M (T, H).

1.1.2 Active magnetic regenerators

In order to become a potential substitute for the conventional refrigeration, the working range of the magnetic refrigerators, *i.e.* the phase transition of the magnetocaloric material, must be around room temperature. Another challenge of MR is a desirable operating temperature range of tens of degrees termed as a temperature span. The temperature span created by MR needs to be enough to cool down the heat transfer fluid as minimum from room temperature to the desired temperature in the refrigerator. Normally this results in working range of 278 K - 298 K. The temperature span of the magnetocaloric materials itself is too small to satisfy the latter demand, therefore most magnetic refrigerators use regenerative heat exchangers, or more commonly called regenerators. A regenerator is a thermal exchanger, used both for storage and transfer of heat between the cold and hot ends of a device.

MR systems normally apply a so-called active magnetic regeneration (AMR) cycle, which was proposed and described in detail by Barclay and Steyert in 1982 [7]. In AMR, a large temperature gradient is attained by a magnetocaloric material, acting as a regenerator, and passing through it a heat transfer fluid. A series of repetitive magnetization/demagnetization cycles between the particular phases of the cooling process generates a temperature gradient significantly larger than the adiabatic temperature change of the magnetocaloric material used.

Besides the magnetocaloric material and the heat transfer fluid, a magnetic refrigerator consists of a permanent magnet or electromagnetic device to create a magnetic field and two external heat exchangers. The schematic structure of magnetic refrigerator with AMR and its principal working cycle are illustrated in Figure 1.3. For more illustrative explanation, the temperature at a certain spot in refrigerator will be given.

Figure 1.3a represents the initial steady-state condition of the magnetic cooling process with a temperature gradient from the left side, connected to a cold heat exchanger, to the right side, connected to the hot heat exchanger. The next operational steps are as follows (Figure 1.3):

b) adiabatic magnetisation takes place when AMR is exposed to a magnetic field, and the AMR is heated up to the temperature T_2 in the middle;

c) the fluid from the cold heat exchanger through the heated magnetocaloric material is transferred by piston or pump to the hot heat exchanger, wherein the temperature of the middle of regenerator in general decreases from T_2 to T_3. The heat (positive) received by the hot heat exchanger is emitted to the surrounding;

d) adiabatic demagnetisation leads to a decrease of the system's temperature at the middle to T_4 thereby cooling the fluid around the magnetocaloric material;

a') the fluid is displaced back from the hot external heat exchanger through the cooled magnetocaloric material to the cold heat exchanger, where the heat is absorbed from the surroundings. In steady state conditions with no hysteresis in magnetic properties of the magnetocaloric material, the temperature at the middle of the system returns to value T_1. The cycle then starts anew.

Thus, in a regenerative process the temperature span between cold and hot ends varies in a larger range from T_4 to T_1 when compared to the adiabatic temperature span of magnetocaloric material changing in a narrower range from T_1 to T_2.

In order to improve the performance of magnetic refrigeration, it is of crucial importance to find a competitive refrigerant material with a large magnetocaloric effect, a large temperature span and a tunable Curie temperature. As defined above the adiabatic temperature change and the isothermal magnetic entropy change are the two parameters providing information about the performance of magnetocaloric materials. However, along with the large magnetocaloric effect in a broad temperature range around room temperature, there are other characteristics which define the best candidate for refrigerant in MR: the structure of the refrigerant, its thermal properties, availability and price of the raw material, synthesis and shaping techniques suitability for up-scaling, chemical and mechanical stability of the material during storage and operational cycle, *etc.* [3]. For instance, the necessity to move heat transfer fluid through the regenerator implies that magnetocaloric material has to have either a porous structure [8] or is stacked into a bed with a parallel plates material design [9].

The first magnetocaloric material ever applied as a regenerator in a room temperature MR was gadolinium Gd in 1976 [10]. Since then several promising classes of materials have been proposed and tested in magnetic refrigerator prototypes, such as Gd and its alloys, perovskite and perovskite-like compounds, transition metal compounds as well as composite materials [3], [6]. The prime advantages of the perovskite materials in comparison to the benchmark material in MR Gd are no oxidation, easy shaping, high electrical resistance and much lower cost. Another very critical feature typical for perovskites is the close relationship between magnetism and electrical transport properties, *i.e.* doping level of perovskites (described in detail in Section 2.1). For instance, the Curie temperatures of $La_{0.67}Ca_{0.33}MnO_3$ and $La_{0.67}Sr_{0.33}MnO_3$ perovskites are about 260 K and 370 K, respectively, whereas the doped perovskite $La_{0.67}Ca_{0.26}Sr_{0.07}Mn_{1.05}O_3$ exhibits a high magnetocaloric effect at nearby transit temperature of 295 K [11]. Hence, the Curie temperature can be tuned by adjusting the doping level in perovskites.

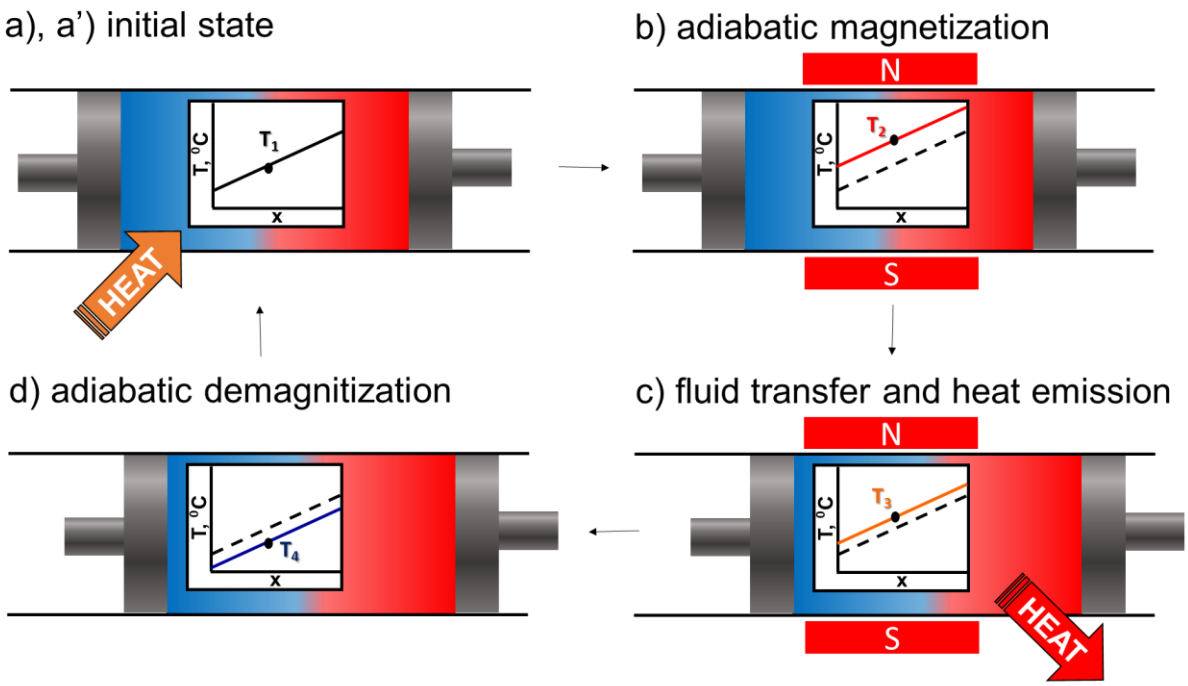

Figure 1.3. The schematic shows operational phases of a magnetic refrigeration cycle with an AMR: a) the AMR is in initial steady-state state; b) adiabatic magnetization of the system leads to increase in the temperature of the magnetocaloric material, which in turn leads to heating up of the whole system; c) the fluid is transferred towards the hot end of the system and the thermal energy is emitted to surrounding, reducing the temperature of the system; d) adiabatic demagnetization of the system causes further cooling of the system; a') the fluid is transferred toward to the cold end, where thermal energy is absorbed from the surrounding increasing the overall temperature of the whole AMR to the initial level. From here the cycle is repeated. The black line indicates the temperature profile along the AMR in the initial stage of the process as well as at the beginning of each cycle; the dotted and full lines depict the temperature profiles at the beginning and end of each phase, respectfully.

Instead of looking for a single material with a broad adiabatic temperature span, the desired temperature gradient can be achieved by combining a number of ceramic perovskites in the regenerator in the order of their growing Curie temperature values. For instance,, Bahl *et al.* showed that combining two perovskite materials adjacently in one plate, the temperature span reached 9.24 K (Paper IV) against a single material of 5.1 K [11].

1.2 Fabrication of ceramic thin films

First, the shape of the regenerator has to be determined. The design of magnetic refrigeration devices [12] (Figure 1.4), used by the magnetic refrigeration group in Risø campus of DTU, defines some geometrical requirements of the magnetocaloric materials to be used. Among all possible geometries [13], thin dense plates are desired due to the fact that these plates provide a low pressure drop and can transfer heat effectively. Plates with a thickness of about 300 µm are chosen for practical reasons of preparation, handling and stacking. The flatness of the plates is very important as it is desired to stack the plates as close as possible. A thickness variation of less than 5-10% of the average tape thickness is desirable in order to avoid maldistribution of the flow [14].

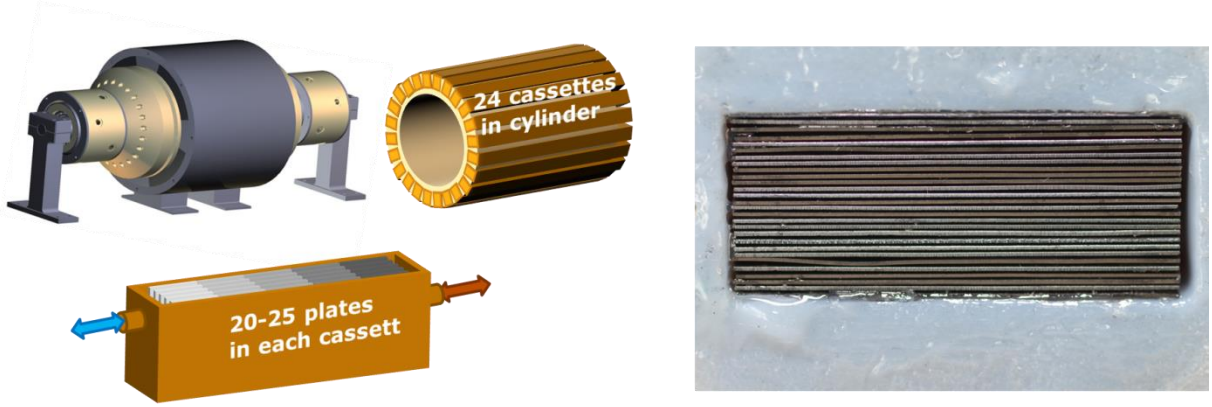

Figure 1.4. Schematic of magnetic refrigeration prototype and photo of stack of tapes, placed in cassettes. Adapted from [15].

The planar green ceramic geometries can be produced through various shaping techniques, *e.g.*: coating, printing, extrusion, dry pressing, roll forming, *etc*. Basically, these methods can be divided into three groups [16] depending on solvent content in the feedstock : (i) those requiring the use of slurries, slips or pastes are classified as liquid (wet) forming techniques (coating, printing, casting techniques), (ii) shaping of moulding masses which under high pressure become plastic is a basic for plastic forming techniques (injection moulding, extrusion, roll compaction); (iii) while those using merely powder as raw material belong to the dry forming techniques (calendaring, dry pressing). A deeper insight into technical details of all methods can be found in literature [16]–[18]. In order to review the advantages and disadvantages, suitability and efficiency of different shaping techniques, with which production of flat films is possible, a table (Table 1.1) has been compiled. In Thesis the focus is rather to give a brief overview of different techniques enabling fabrication of planar geometries with the final goal of finding the most suitable process.

The dry forming techniques are more suitable for the manufacture of exacting prototype shapes (dry pressing) and/or small series production (isostatic cold pressing) due to the high cost of used moulds. Among plastic forming techniques roll compaction is the one which allows producing required planar dense tapes in a large scale. The limitation of this method, however, is in formulation of a graded plate with well-pronounced inter-materials interface. The liquid forming techniques, however, were recently applied for fabrication of an extensive range of advanced materials (Table 1.1) [16], [19], [20]. This preference to wet techniques is based on their ability to formulate stable colloidal system for further shaping, uniform distribution of micro- or nano-scaled particles and their ease to take the shape of any mould. A distinct drawback of some of the described wet forming techniques (Table 1.1) (e.g., EPD) is their limitation to continuous automatically operated mass production. With focus on manufacturing dense films of about 300 µm in a large scale, tape casting is a preferred choice because of its suitability, relative simplicity and low implementation cost. Other advantages, significantly distinguishing tape casting from other processes, are potential to cast tapes with a wide variety of thickness, providing materials with dimensional stability, controlled microstructure, high surface quality, and wide range of possible densities. All of this drastically expends the variety of possible applications for cast tapes.

Table 1.1. Shaping techniques suitable for formation of planar ceramic circuits.

Shaping technique	***Film thickness***	***Processing speed***	***Viscosity***	***Advantages***	***Disadvantages***	***Ref.***
Liquid techniques						
Printing						
Rotary printing	0.2-1.5 µm	Ind. 30–80000 cm/min Lab. 100-1000 cm/min	0.01-0.1 Pas	High coating speeds, continuous operation, without the intermittent sweep and return of the printing squeegee;	Durable drying;	[21], [22]
Flatbed screen printing	1-50 µm	< 180 m/min	2-50 Pas	Allows to print on a variety of substrates, fine line resolution patterns;	Intermittent technique, limited by sheet size, during slow drying screen frames can eventually become warped and uneven;	[21], [23], [24], [25]
Soft lithography	0.03–100 µm	20 m/min	10-100 Pas	Fast prototyping and ability to deform the elastomeric stamp, not limited by optical diffraction and optical transparency	Limited by flexible organic molecules and materials (no inorganic particles), distortion and deformation associated with elastomeric materials, improve in the quality of the patterns and structures	[26], [27]
Coating techniques						
Slot-die coating	0.02-150 µm	0.3-800 m/min	0.001–1's Pas	High cross-directional uniformity, dense packing in green state, high production speed, positive coat weight control.	Limitation in solid content (<10 wt%), a small gap between die lip and substrate, sensitive to smallest sediments and air bubbles.	[21], [28]
Dip coating	0.1-200 µm	1-50cm/min	0.025-0.1 Pas	Light and heavy coating can be applied	Mostly polymer solutions, primers be needed	[29], [30]
Blade coating	100-1000 µm	5-150 cm/s	0.3-10 Pas	Minimal ink waste	The need to re-circulate the remaining coating fluid; ink behind the blade is exposed to environment which increase the risk of ink contamination	[31], [32]
Profile rod technique	0.25-3.5 µm	100-500 mm/s	<0.04 Pas	Minimal roughness, continuous process	Slurry behind the rod is exposed to environment	[33]
Electro-phoretic deposition (EPD)	1-20 µm	1-20 µm/min	<0.1 Pas	Uniform thickness without porosity, relatively high purity, applicability to wide range of materials, efficient utilization of the raw material	Need a conducting substrate, not continuous process	[34], [35]
Slip casting	150-850 µm	2-8 µm/s	0.5-1.5 Pas	Low material consumption	High dimensional tolerance, complex rheology, rough surface	[36]
Tape casting	1 – 3000 µm	5-100 cm/min	0.1-10 Pas	Large-scale production, variety of raw materials, various particle size distribution,	Drying is necessary	[37]

				high manufacturing capacity		
Plastic techniques						
Roll forming/roll compaction	100-3000 µm	5-10 cm/s	20-1000 Pas	Uniformity and consistency throughout the length, eliminate multiple stage operations, water-based technology, low and uniform shrinkage during sintering	Need a spray drier, surface quality is not high, tape cannot be laminated for multilayers, distortion with hemmed parts on the edges of post-cut green tapes	[38], [39], [17]
Dry techniques						
Calendaring/roll compaction	250-1000 µm	30-600 cm/min		High green density, fast production speed	Maintaining the roll surface quality, air trapped in the structure	[40]
Dry pressing	500-1000 µm	5-60 min per unit		Good reproducibility, limited drying, good dimensional accuracy	Density gradient possible, expensive moulding tools, expensive powder preparation, limitation in the part sizes	[18]
Spark Plasma Sintering (SPS)	10-500 mm, slices after cut: 0.1-500 mm	5-60 min per unit		High density, controlled structure, precise dimensions, high reproducibility	Limited size set, shape depends on the press form which is usually cylindrical	[41]

1.2.1 The processing principle of tape casting

The general schematic of tape casting (doctor blading, knife casting) processing steps is illustrated in Figure 1.5. In ceramic shaping process the first step consists of powder treatment with the aim to obtain a powder with the required phase content as well as particle size distribution and morphology. Further, the powder is stabilized with a dispersant, which preliminary diluted in solvent. The obtained suspension is milled and mixed to ensure homogenisation and destruction of agglomerates. After adding binder and plasticizers, the slurry is homogenised normally for one more day. The slurry is then sieved to eliminate possible agglomerates and de-aired in a vacuum chamber with the aim to remove air bubbles from the slurry volume. The stable homogenized slurry is then either poured manually or pumped into a fixed tape caster tank (reservoir) beneath which a band-type carrier (that be a steel belt or, as in our work, a politereftalat film with a commercial name Mylar coated with silicone adhesive coatings) is located. Tape casting is initiated when a moving carrier drags the ceramic slurry under the blade opening of the tank, which "doctors" or discharges a thin ceramic film behind. The cast tape, while still on the support carrier, dries in a ventilated drying chamber, after what it is removed from the carrier and then processed by punching, metallization, stacking and lamination if necessary. At this stage of the process, dried tape, also referred to as a green tape, is still flexible because it has a high percentage of organics in the form of dispersant, binder and plasticizers. Finally, during the burn-out and sintering processes the binder and any excess agents are burned out leaving a dense, strong, hard tape composed primarily of ceramics. A key factor for the achievement of a ceramic material with the required geometry and properties is a high control of each step in the process.

There are two types of tape casting working principles. First, batch process type of tape caster denominates traversed casting head with doctor blade over a stationary glass slab or another substrate. This type is rarely used in a lab-scale tape casting and never applied in industrial-scale production because of the limiting control and low precision of setting the casting operational parameters (*e.g.*, casting gap, casting velocity). The second, large-scale type of tape caster processes tapes when the casting head is fixed over the moving substrate. The slurry is placed in front of the fixed blade whereby the substrate moves relatively to the blade. Adjustable gap widths allow the deposition of wet layer thicknesses from low tens to hundreds of micrometers. The final wet layer thickness is roughly half of the gap high depending on the coating speed and drying kinetics/character.

The set of exact casting speed and casting gap depends upon the practical conditions as the length of the drying chamber and tape caster machine capacity, but most often chosen on a respect of the tape thickness and width needed, solvent system used, and morphology of used particles (*e.g.*, if alignment of elongated particles or pore formers needed in the resultant tape) of green tape required. Prof. R.E. Mistler in [17] defines 15 cm/s as a speed typical for continuous tape casting in standard practice and 50 cm/min as the one preferred for a batch cast.

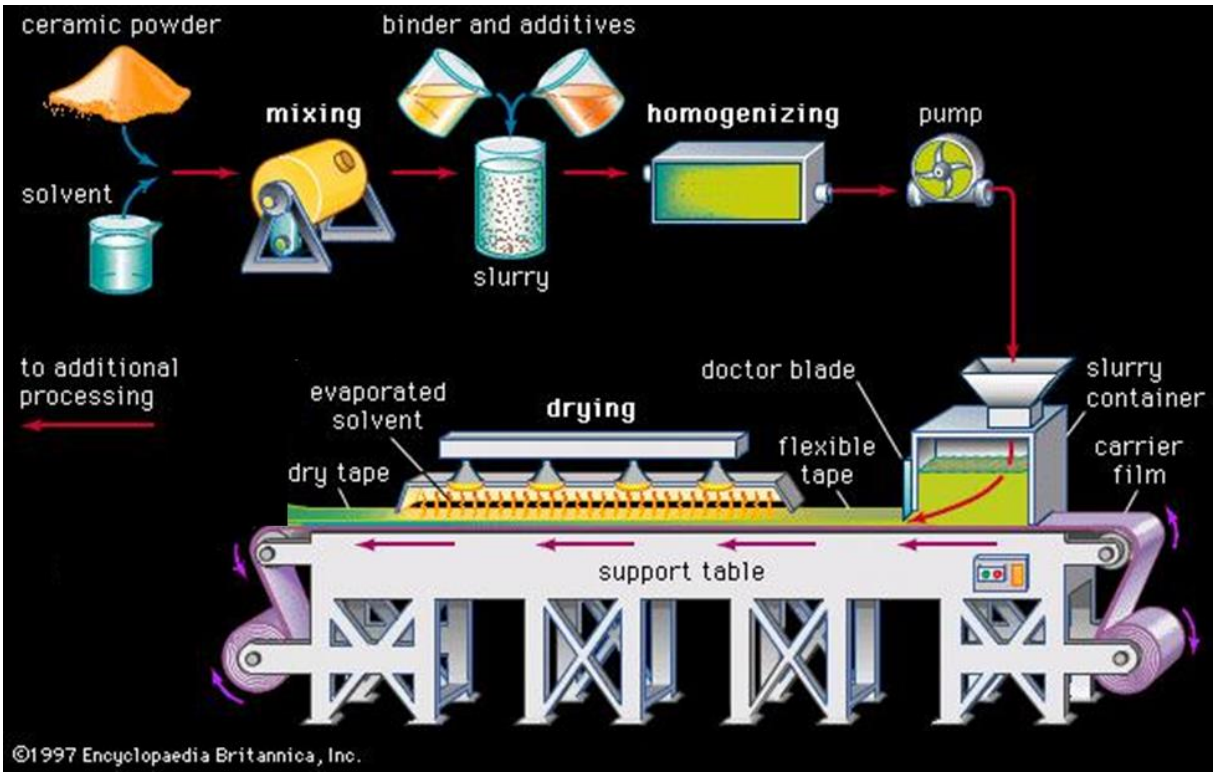

Figure 1.5. Standard steps in tape casting of ceramics, started from the preparation of dispersion and finishing with the peeling off a ceramic green tape from the carrier. Adapted from [42].

1.2.2 Tape casting development

Tape casting is a comparably young shaping technique, known since 1952 when Glen Howatt patented a new technique to produce multilayered dielectric ceramic for replacing a natural mica in a capacitor device [43]. However, the idea to combine ceramics and the electrodes into a bulk multilayered circuit with the target of achieving a larger capacitance in a smaller volume was implemented in the early forties and first described by Glen Howatt *et al.* in a paper from 1947 [44]. The shortage of materials during and immediately after World War II facilitated the development and use of dielectric ceramics produced by tape casting.

The next valuable improvement in tape casting development was the replacement of a stationary porous casting substrate with a moving nonabsorptive polymer carrier [45]. Since then continuous casting of long tapes became possible. Besides upscaling, the great value of this implementation was the ability to roll carrier film back for repetitive tape casting and easier formulation of multilayered packages. Later, in 1965 a lamination process of a green ceramic tapes was reported for the first time [46]. The lamination of green films became possible due to the ability of thermoplastic polymers, included in slurry, to soften and stick at relatively low temperatures and pressures. This discovery gave a tremendous impetus to the development of multilayered ceramic package (MLC) and multilayered ceramic capacitor (MLCC) industries. For instance, shortly after the lamination was first described, IBM produced a board with 33 layers and 100 flip chip bonded large scale integration (LSI) components to be applied in IBM's mainframe computers [47] and gave a start for further development of electronics multilayered boards with the overall goal to improve computer speed, performance and reduce size [48], [49], [50], [51].

The focus of works from the eighties and nineties was shifted more to the improvement of the recipe composition and broadening the variety of solid components to be cast. Meanwhile, a number of works from the last decades were devoted to the optimisation of the machinery design by means of receiving consistent uniform flow and homogenous tapes. Thus, the double doctor blade system with the goal to control the hydrostatic pressure behind the casting blade was implemented. Besides, Hagen Loest *et al.* suggested using a casting head with an inclined back wall in order to evenly distribute unyielded regions and eliminate vortices in casting reservoir [52].

Nowadays there are almost no restrictions on geometrical parameters of plates and also no limitations in machinery parameters. However, the most commonly used tapes are about 1-1500 µm thick, tens of millimetres in width and formed with speeds of 5 – 150 cm/min. The length of the cast tape could vary from tens of centimetres in a research oriented establishment to continuous tapes in a mass production scale, which includes also facilities for drying and pumping the slurries.

1.2.3 Application of tape casting

Development of tape casting opened new opportunities for the achievement in a diversity of applications and development of innovative products, which could not have been produced by any other technique. Applications include fabrication of thin and thick substrates typically from alumina or aluminium nitride used for the electronics industries [53], [54]; bi- or tri-layered components for solid oxide fuel cell (SOFC) and proton ceramic fuel cell (PCFC) [55], [56]; multilayered capacitors and actuators usually made from piezoelectric and other electro-ceramics [57]; laminated tapes containing indium tin oxide (ITO) with a good optical transparency and a high electrical conductivity for use in electroluminescent lamps [58], photovoltaic solar cells applying mullite tape cast substrates [59], metal matrix composites (MMC) being a major contributor in the advancement of the aircraft engine performance [60], etc.

Recently, the attention of many researchers has been directed to the fabrication and characterization of the new generation materials – the so-called functionally graded materials (FGM) [61]. The FGM is a class of graded materials with a gradual variation in structure and/or chemical composition over its volume and, as a consequence, with a gradual change in properties within the sample. By now, this class was limited by multilayered structures, fabricated mostly by tape casting and lamination processes. For instance, gradual intermix of tough, strong and thermally conductive β-SiAlON and hard α-SiAlON in one tape formed a graded bulk material with advantageous mechanical properties of both ceramic alloys based on silicon nitride and alumina [62]. Through the creation of FGMs it became possible to overcome a vexed problem in material science associated with a combination of metal and ceramics, in which thermal expansion coefficients are significantly different. Sabljic and Wilkinson fabricated a multilayered FGM, where series of layers of gradual slight different in ceramic/metal compositions minimise the stress between layers of pure metal and pure ceramic [63]. As an alternative to the lamination technique, the so-called “wet-on-wet” or “wet-on-dry” co-casting processes are proposed in literature. These two approaches are basically the same and include co-casting of one tape on top of another green tape, when the latter one already formed a dry skin on its surface or when it has completely dried.

So far, described FGMs had a layered design with layers produced by tape casting. However, for some applications not layered but planar gradual change of properties is required. For example, as described above, in

order to extend the temperature span of the MR device a graded material with varying T_C along the length is needed [64], [65].

1.2.4 Side-by-side tape casting

To form a planar graded ceramic material (Figure 1.6a), a novel tape casting technique called side-by-side tape casting (SBS TC) was recently proposed [66]. The principle of SBS TC, also referred to as adjacent co-casting, is based on simultaneous adjacent co-flow of compositionally distinct slurries from the same casting tank, which is divided into multiple chambers (Figure 1.6b). The resultant tape consists of parallel adjacent compositionally distinct "stripes" with inter-materials one-dimensional interfaces along the tape length. In general, the number and width of "stripes" is limited solely by the width of the conventional casting tank and the width of the tape casting chamber.

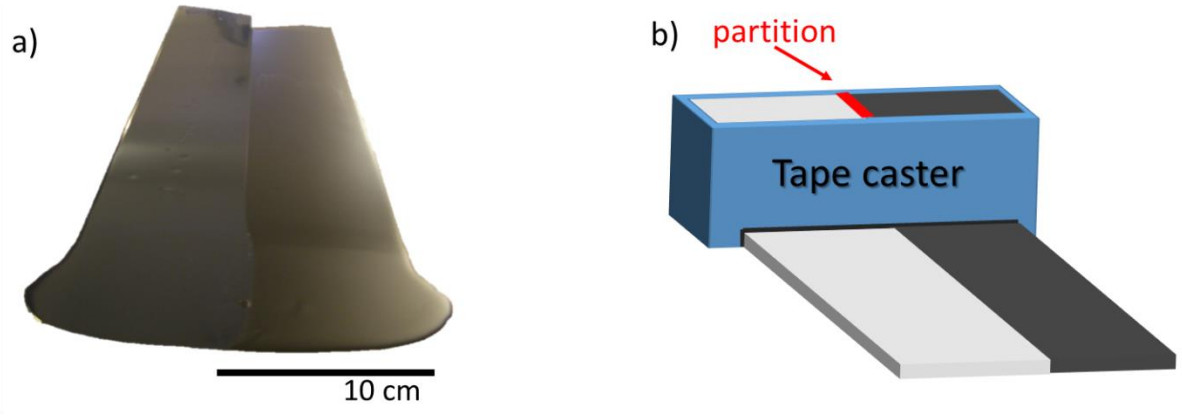

Figure 1.6. a) Photograph of side-by-side cast tape and b) schematic of casting tank employed for adjacent co-casting. The casting head is divided by a Teflon partition into two chambers to produce a tape with two compositions.

The fundamental difference between multilayered and planar graded design is the dimension of interfaces between structural units, *i.e.* layers and stripes respectively. The interface in multilayered geometries is two dimensional (planar), what favours formation of strong interface by macroscopic "ex-situ" bonding such as lamination. In planar graded structures, the interface is one-dimensional, resulting in weaker bonding compared to multilayer design. In order to improve adhesion between stripes, an "in-situ" formation of the graded materials, usually involving a liquid forming technique, had to be chosen.

Among processing challenges inherent for fabrication of both multilayered and SBS designs, thermal expansion mismatch and chemical stability are among the biggest, and both of these challenges potentially introduce residual stresses in the graded material. The mitigation of this problem, known from the multilayers fabrication experience, involves the usage of the same organics through the graded product. This in turn allows using the same burnout and sintering programs at the final stage of fabrication of the dense tape.

Outline of the thesis

This work was part of a larger project called "Optimised processing of multimaterial architectures for functional ceramics" (OPTIMAC) financed by Danish Council for Independent Research Technology and Production Sciences (FTP) which is part of The Danish Agency for Science, Technology and Innovation. The aim

was to expand knowledge on shaping and sintering of functionally graded multi-material architectures by investigating co-casting and co-extrusion processes both experimentally and numerically.

This thesis particularly focuses on experimental investigation and development of a novel shaping technique called side-by-side tape casting. The aim was to fulfil the missing knowledge on how to control the adjacent co-flow of ceramic slurries and determine what the main features defining the formation of uniform adjacently graded tape with a well-defined strong interface are.

The compounds which have been demonstrated in use as magnetocaloric materials are the series of doped perovskites $La_{0.67}Ca_{0.33-x}Sr_xMn_{1.05}O_3$ (LCSM), $x \in [0.0375\text{-}0.0600]$, which can exhibit a range of T_C by varying the ratio between Ca and Sr (Ca/Sr). This target composition was used for fabrication of a 5-striped graded tape, and studying the performance of pieces of pure magnetocaloric materials and pieces, containing interface. The above described adiabatic temperature changes and isothermal magnetic entropy changes were evaluated (Paper II, Paper IV). Since custom prepared LCSM perovskites are quite expensive, further study on fluid behaviour and tape formation was performed by co-casting a slurry with a pure strontium doped lanthanum manganite oxide $La_{0.85}Sr_{0.15}MnO_3$ (*LSM*) available in bulk amounts and a slurry, containing a mixture of LSM and gadolinium doped cerium oxide $Ce_{0.9}Gd_{0.1}O_2$ (*CGO*). LSM and CGO have been chosen as the main materials used in OPTIMAC taking into account their relevance for studied applications, sintering, thermal expansion, and availability. Moreover, they are widely applied as cathode or insulating layer in SOFC, as a solid constitute of the porous layer in gas purification applications and gas separation membrane. The LSM perovskite is characterised by high magnetotransport properties and is applied in memory and sensor applications [67], [68], [69]. The rich physics and chemistry present in LSM and CGO together with the innovative design of adjacently graded ceramics create a high potential for further extension of their application range.

Chapter 1 of this thesis starts with introduction of magnetic refrigeration and the regenerator theory, which is the direct application of developing adjacently graded tapes. The main challenges and requirements to the regenerator design are described. This chapter also serves as a comprehensive review of the shaping methods with extensive tabular listings of the methods' limitations and capabilities with the focus on fabricating planar geometries. The place of tape casting among other shaping processes is clearly defined, its processing steps, history of development and application range are briefly discussed. The side-by-side tape casting is introduced by describing its processing steps, and differences and similarities with a multilayered tape casting. Furthermore, all information is presented in a sequence of tape casting workflow steps.

Chapter 0 gives an introduction to the material system investigated in this work, namely, to the class of magnetic oxides called mixed-valence manganites. This chapter describes the general aspects of manganites, including their structural features and related physical properties. Further, necessity of powder calcination and main techniques directed on control of powder morphology are described.

Chapter 3 explains the choice of organic-based slurries for the novel side-by-side tape casting technique and describes the role of each slurry component. The main difference of side-by-side tape casting from the conventional tape casting technique is defined as necessity to use more viscous slurries. With the general goal to form steady slurries with fine dispersed particles, modification of the milling procedure is suggested. Rheology is assigned as the main tool for analysis of the fluid flow, thus, definition of main rheological terms and rheological experiments are given.

Chapter 4 is devoted to the setting and verification of tape casting parameters and numerical modelling of more trivial monolayer tape casting before starting the more complicated and unexplored in tape casting practice, adjacent co-flow. First, the main casting parameters usually determining the tape casting process, namely: casting gap, casting speed and slurry level in reservoir, was verified by casting LSM slurry into a single monolayer tape (Paper V). Varying the mentioned parameters one at the time, their influence on the tape thickness gradient was established and, based on that, the generalized analytical model was verified (Paper V) (Paper VI) (Paper X) (Paper VIII). In the next step of the investigation, the tape thickness consistency was systematically studied depending on tape casting mode (Paper III). The standard single-blade tape casting was compared to the tape casting with a double-blade, tape casting using a pump system for maintaining slurry column in a casting tank through the entire process, and a new method directed on control of the green tape thickness by balancing the casting speed and slurry level in reservoir.

Chapter 0 is dedicated to side-by-side tape casting of LSM and LSM_CGO slurries. It starts with selecting one of the described casting modes for further experiments to verify the effect of casting modes on the quality of the interface in adjacently graded tapes (Paper III). In order to form a thick graded tape with no compositional intermix in the interface area, the standard slurry recipe had to be adjusted (Paper I). Viscosity and rheological behaviour was tuned by changing the content of the binder system and the dispersant. After a working range of co-cast slurries viscosities was determined, the effect of casting speed change was investigated (Paper I) (Paper IX). The controlling features in the last two tests were a variation of the tape thickness and the shape of the interface between adjacently cast compositions in a green state. Adhesion between co-cast stripes was analysed by performing a tensile test on green adjacently graded tapes (Paper I). The next series of experiments were directed at revealing the impact of the design of a partition, dividing a conventional casting tank into compartments (Paper III). A subtle balance between partition shape beneath the doctor blade and casting speed was found to be a critical parameter defining if the graded tape could be formed or not.

In Chapter 6, the optimisation of de-binding and sintering programs of the graded tapes is given. This included modification of the sintering profile, an increase in sintering shrinkage by elucidation the issue of stacking LSM tapes to the sintered substrate. In addition, a brief study on shrinkage of individual LSM and LSM_CGO materials and tape containing interface was conducted (Paper VII). Finally, the complete study on target LCSM material, co-cast into a 5-striped graded tape, has been presented (Paper II) (Paper IV). Due to a high morphological similarity between co-cast compositions, the microstructural identification of the interface area was hindered. However, the constituent analysis based on magnetic measurements showed distinct differences between all five materials and their interfaces. High sensitivity of phase transition temperatures to the doping level in perovskites proved to be beneficial for characterisation of the diffusion in the interface area on post-sintered graded samples.

Chapter 7 proposes comb-like design as an alternative to a platelet design of the regenerator. For fabrication of this design, side-by-side tape casting was applied again. Due to revealed regularities in consequence of studying the effect of partition design, it was proven, that co-casting with a very narrow gap in the range of 100s microns is possible.

Chapter 8 gives the conclusion for the whole work described in Thesis and describes the future perspectives on the side-by-side tape casting technique optimisation and alternative applications.

As any new material or design, the quality of produced tapes had to be tested and verified in terms of its application needs. The magnetic refrigerator prototype, proposed by our group in the Energy Conversion Department (DTU), could not compete with other prototypes just by improving the design of the magnetic regenerator alone. There is continuous progressive work being done on investigation of new refrigerant materials, refrigerant systems, permanent magnets, and optimisation of refrigerator's working regime, all with a large support from numerical modelling. The main scope of this PhD project, as already mentioned, has been the identification and characterisation of the interface area using magnetic properties, while testing of graded regenerators in magnetic refrigeration prototype was performed by my colleagues; their results on tapes performance are thoroughly described in literature [70].

In addition to the main context of the PhD thesis, aiming to identify and describe the linkage between various slurry and processing features and quality of formulated adjacently graded tapes, other subjects were elaborated but less extensively. Finding the optimal method for measuring a density of green tapes, verifying the reproducible conditions for rheological measurements, studying of shrinkage during sintering, comparing side-by-side tape casting technique with an alternative way of producing graded materials using spark plasma sintering, just to name a few. Besides, a fundamental work on development of ethanol-based recipe have been completed and covered finding and optimizing the content of dispersant and binder system by providing rheological, sedimentation tests and green and post-sintered density characterizations. This study, however is planned to be combined with the study of effect of surface tension on quality of side-by-side graded tape and be published later.

2 Powder treatment and characterization

The purpose of this chapter is to show the relevance of employed materials as regenerators in MR, giving a general introduction to structural, electronic and magnetic properties of this class of perovskites. Without going into details, this chapter describes the basics of structural features of perovskites and originality of the magnetocaloric effect. Understanding of electronic structure and possible changes in unit cells will favour to control morphology of post-calcined powder. In the following sections some theoretical statements are applied on characterisation of the LSM powder, further used in current work for tape casting.

2.1 Structural properties of lanthanum manganites

Lanthanum manganites belong to a family of manganese oxides with the general formula $R_{1-x}A_xMnO_3$ ($x \in [0\text{-}1]$), where R is a rare earth cation (La^{3+}, Pr^{3+}, Nd^{3+},…) and A is an alkali- or alkaline-earth cation (Ca^{2+}, Sr^{2+}, Ba^{2+}, Na^{+}, K^{+},…). Thus, when the lanthanum is used as a rare earth cation, the two end members of this class of manganites are $LaMnO_3$ when x=0 and $AMnO_3$ when x=1. If part of La^{3+} ions are substituted with a bivalent alkali- or alkaline earth cation A^{2+} following hole doping mechanism, the corresponding number of manganese ions turns from a trivalent to a tetravalent state. In case of doping the $LaMnO_3$ with Sr^{2+} ions the resulting compound can be written as $La^{3+}_{0.85}Sr^{2+}_{0.15}(Mn^{3+}_{0.85}Mn^{4+}_{0.15})O^{2-}_{3}$. Due to the opportunity to replace part of the La^{3+} ions in the crystal structure of manganites, this class of materials is also referred to as mixed-valence manganites and doped manganites.

The doped manganites were first investigated by Jonker and Van Santen (1950), who found that among studied specimen $La_{1-x}A_xMnO_3$ (A=Ca, Sr, and Ba) the end members $LaMnO_3$ and $AMnO_3$ were antiferromagnetic and non-conductive, and for the intermediate values of x the corresponding samples were ferromagnetic and conductive [71]. They also found, that ferromagnetic interaction was strongest with x=2/3 and ferromagnetism is related to the sharp increase in electrical conductivity. A year later the relation between ferromagnetism and exchange coupling between magnetic ions in a different valence state was explained by a well-known double exchange model [72]. A few works contributed in establishment of the regions of ferro- and antiferromagnetism for $La_{1-x}Ca_xMnO_3$ and other rare earth perovskites [73], [74], [75]. After discovering magnetoresistance effect in 1954 [76], the new wave of interest in manganites was provoked just in the nineties after finding the giant magnetoresistance and colossal magnetoresistance in mixed-valence manganites [77]. Nowadays doped manganites are widely used as electrode materials in solid oxide fuel cells (SOFC), and a solid constitute of porous layer in gas purification application and gas separation membranes [78], [79]. Recently, it was shown [80] that the magnetic entropy change of $La_{0.67}A_{0.33}MnO_3$ (A=Ca, Sr, and Ba) is comparable with the benchmark material in MR Gd. The wealth of presented physical properties of manganites possibly because of the strong relation between lattices, orbital, magnetic and charge degrees of freedom is described below.

2.1.1 Structural properties

Lanthanum manganites belong to the group of perovskites named after a cubic structured mineral perovskite calcium titanium oxide ($CaTiO_3$) which is also referred to as ABO_3 structure (Figure 2.1a).

The BO_6 octahedra makes contact with neighbouring octahedras by vertices forming a three-dimensional network (Figure 2.1b) and A cations situate at the interstitial sites between the octahedras. in case of LSM the A-

site of the manganite is occupied by La^{3+} and the substituted cation Sr^{2+}, while the B-site is occupied partially by Mn^{3+} and partially Mn^{4+} ions.

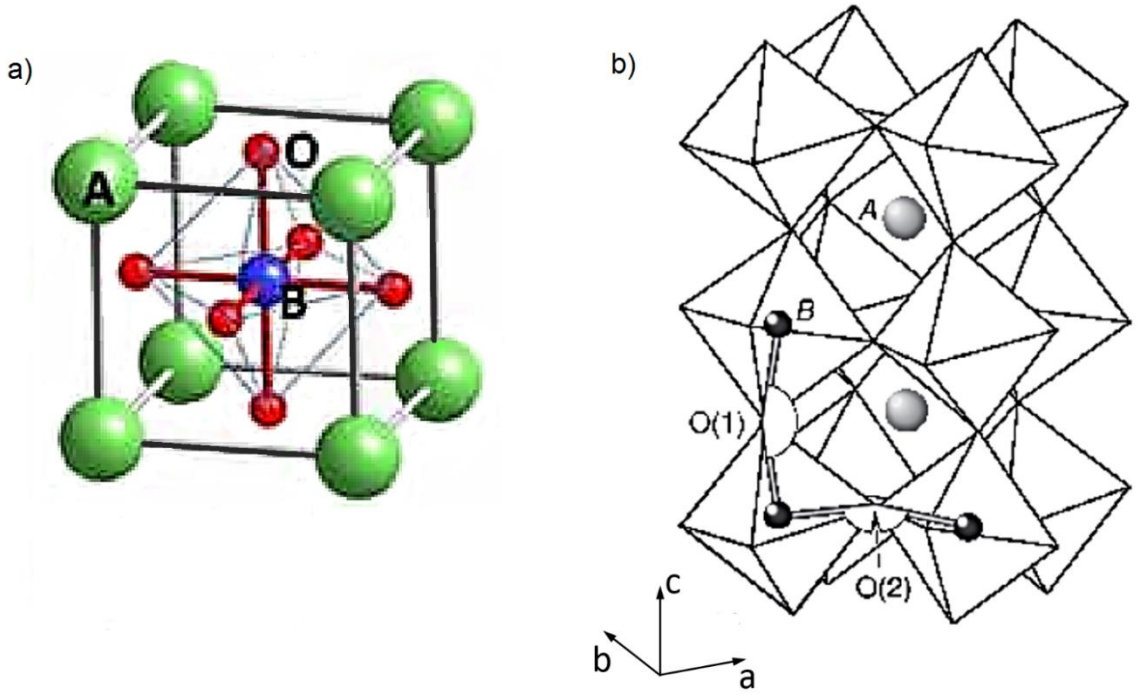

Figure 2.1. a) Unit cell structure of perovskite ABO_3 with the A cations in the corners, the B cations in the centre and the oxygen anions at the centre of the faces of the cubic structure; b) the BO_6 octahedra forms a three-dimensional structure by connecting at the vertices, the A ions are between the octahedras at the interstitial sites. Here the octahedras are tilted (angle of the bond B-O-B is not equal to 180°), what is termed as a $GdFeO_3$–type of orthorombically distorted perovskites.

2.1.2 Ionic size distribution

Usually perovskite unit cells do not have a cubic structure as mismatch between sizes of A-site cations and B-site cations leads to distortion resulting in the orthorhombic lattice (Figure 2.1b). The stability of the perovskites is defined by the tolerance factor t^* also called a Goldschmidt factor in honour of the scientist who proposed this criteria [81]:

$$t^* = \frac{r_A + r_O}{\sqrt{2}(r_B + r_O)}, \qquad 2.1$$

where r_A and r_B are the mean radii of the ions occupying the A-sites and the B-sites, respectively, and $r_O$is the ionic radius of oxygen.

The tolerance factor is a measure of the degree of distortion of a perovskite from the ideal cube. For the ideal cubic perovskites $t^* = 1$, which is possible when the radius of A-site cation equals the radius of oxygen (0.140 nm), and the radius of the B-site cation matches the size of the interstitial sites formed by the oxygen and equal to $(\sqrt{2} - 1)r_O = 0.058$ nm. If t^* differs from unity, the cations are displaced from their ideal cubic positions in order to minimise the free energy by forming a distorted perovskite structure. For example, the BO_6

octahedra tilt about the b and c axes is associated with the orthorhombic structure, while the octahedra tilt about each axis leads to formation of the rhombohedral structure. It was established that stable perovskites are obtained if the tolerance factor is in range $t^* \in [0.89; 1.02]$ [82].

The tolerance factor for the studied doped manganite LSM was calculated taking into account that in distorted perovskite structures the coordination number for A cations differs from the ideal twelve-fold coordination number of cubic structure (Table 2.1). The mean radius for the A-site (r_A) is calculated as a sum of 0.85*$r_{La^{3+}}$ and 0.15*$r_{Sr^{2+}}$; the radius for the B-site was given as a sum of 0.85*$r_{Mn^{3+}}$ and 0.15*$r_{Mn^{4+}}$ in order to balance the substitution of trivalent La^{3+} with a divalent Sr^{2+}ions:

$$t^* = \frac{0.85 * 0.1216 + 0.15 * 0.1310 + 0.140}{\sqrt{2}(0.85 * 0.0645 + 0.15 * 0.0530 + 0.140)} = 0.92, \qquad 2.2$$

The calculated tolerance factor for LSM $t^* = 0.92$ lies in the mentioned range classifying LSM as a stable structure. However, the criterion of ideal cubic structure ($t^* = 1$) is not satisfied here, identifying that the LSM cell is distorted.

Table 2.1. Ionic radii in $La_{0.85}Sr_{0.15}MnO_3$ perovskite [83].

A-site	B-site	O-site
La^{3+} 0.1216 nm	Mn^{4+} 0.0530 nm	O^{2-} 0.140 nm
Sr^{2+} 0.1310 nm	Mn^{3+} 0.0645 nm	
9-fold coordination	6-fold coordination	8-fold coordination

2.1.3 Jahn Teller effect

Apart from the distortion caused by size mismatch between the A-site and B-site cations, another typicality of transition metals effect is the Jahn-Teller (**JT**) distortion. In current work the understanding of JT effect is important due to the presence of the transition metal manganese in LSM structure and due to the final application in magnetic cooling being very sensitive to any magnetic or electronic transformation happening in LSM.

The JT effect in manganese occurs due to doubly degenerate ground levels in d^9, d^7 low spin and d^4 (Mn^{3+}) high spin states typical for octahedrally coordinated transition metals. Electronic configuration in valence orbitals for trivalent Mn^{3+} and tetravalent Mn^{4+} are $3d^4$ and $3d^3$, respectively. All five d-orbitals are split by the octahedral crystal field, built by six oxygen anions, into three-fold degenerate low-energy t_{2g} orbitals (d_{xy}, d_{yz}, and d_{zx}) and two high-energy e_g orbitals ($d_{x^2-y^2}$, d_{z^2}). The reason for splitting in energy is the difference of Coulomb repulsion between orbitals. According to the Hund rule the lowest energy (stable state) is achieved when electrons occupy degenerate orbitals (orbitals with the same energy) before pairing in the same orbital. Thus, the electron configuration for Mn^{3+} and Mn^{4+} is as given in Figure 2.2 [84].

The tetragonal elongation of the octahedron surrounding of Mn^{3+} cations is balanced by splitting electrons between t_{2g} and e_g orbitals (Figure 2.2). The saving in energy from lowering the d_{yz} and d_{zx} levels is exactly balanced by the rising of the d_{xy} level. In that case it is energetically favourable to distort the octahedron environment of manganese anions along the tetragon because the spent elastic energy in that case is balanced by a resultant electronic energy savings, arising due to the JT splitting (Figure 2.2).

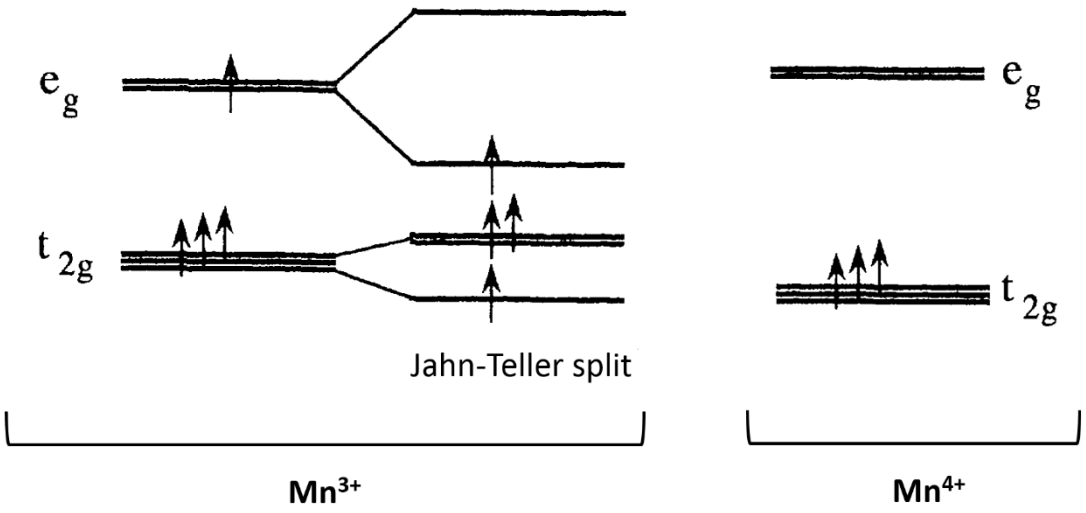

Figure 2.2. Electronic structure of Mn^{3+} and Mn^{4+} in octahedral coordination. For Mn^{3+} the electron structure is shown before and after Jahn-Teller distortion. Adapted from [84].

The t_{2g} orbitals have their lobes oriented between the lobes of oxygen p orbitals (Figure 2.3a), hence three t_{2g} electrons of Mn^{3+} and Mn^{4+} form a localised spin 3/2. For e_g orbitals the lobes of Mn^{3+} overlap strongly with a lobes of p orbital of the neighbouring oxygen creating a σ* band (Figure 2.3b) [85].

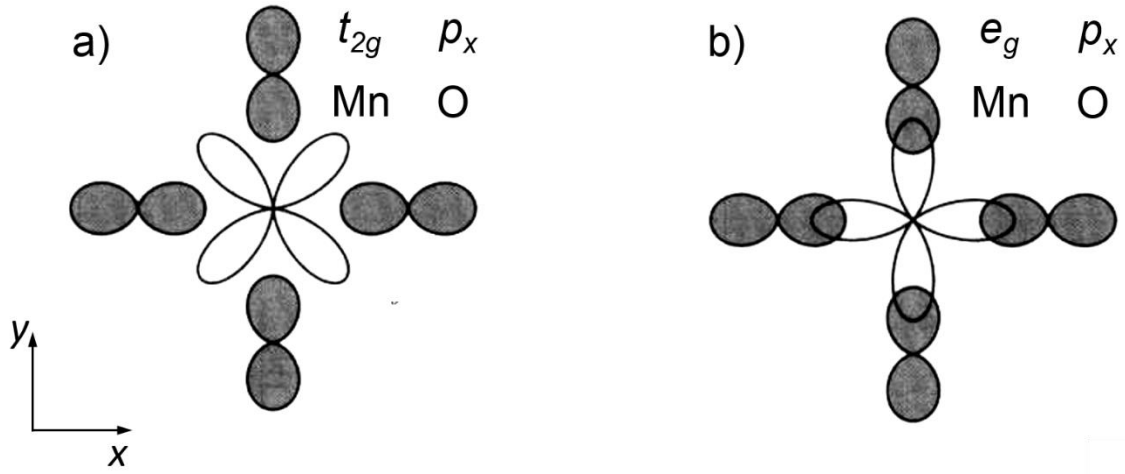

Figure 2.3. Illustration of orbitals interaction between a) Mn t_{2g} and b) Mn e_g orbitals (white lobes) with a p orbital of neighbouring oxygen anion (grey lobes). Adapted from [85].

2.1.4 Double exchange mechanism as the origin of perovskites' magnetic properties

The end-member of the series of manganites the $LaMnO_3$ is an antiferromagnetic insulator, where the magnetism is assigned by a typical for an oxides superexchange through the oxygen. $LaMnO_3$ possess Mn^{3+} (the JT ion), and characterised by an A-type antiferromagnetic ordering. When trivalent La^{3+} cations are partially substituted by a divalent Sr^{2+} as in LSM, the JT effect is balanced (vanished) and the system becomes ferromagnetic, meaning that the σ* electrons can travel from the Mn^{3+} cation to the Mn^{4+} cation.

The exchange coupling associated with the electron transfer from the Mn^{3+} cation to the Mn^{4+} cation through the σ* bond (Figure 2.3b) with the oxygen, is known as a double exchange. The e_g electron from the Mn^{3+} ion can hop to the vacant orbital of the neighbouring ion Mn^{4+} when the first Hund's rule is satisfied. According to it, for a given electron configuration the maximum multiplicity, or the maximum spin angular momentum, is favourable for the system to reach the minimum energy. Hence, the electron will hop to the neighbouring Mn^{4+} ion just when it will be aligned to other three electrons in t_{2g} level of Mn^{4+} (Figure 2.4 a). The antiparallel direction of the received e_g electron (Figure 2.4b) comparing to the electrons direction in Mn^{4+} ion violates the Hund's rule, meaning that it is energetically unfavourable.

As the electron transfer requires aligning of electrons (magnetic moments) of the neighbouring ions, the double exchange mechanism sufficiently influences the magnetic and conducting properties of the mixed-valence manganites. Ferromagnetic alignment in neighbouring ions requires a high arrangement of electrons in the donating and receiving ions in the whole structure. Therefore, magnetic properties of doped manganites change as a function of Mn^{4+} ions. For example, $La_{1-x}A_xMnO_3$ with x=0 was shown [86] to be antiferromagnetic. As *x* grows the amount of tetravalent manganese ions in the system increases leading to an increase in the ferromagnetic moment of the manganite. However, this tendency has a maximum at x=0.33, after which further doping would cause a direct overlap between the manganese t_{2g} known as antiferromagnetic coupling [87]. The latter is the result of the absence of the spin-down electrons in the system. At x=0.5 and further, the antiferromagnetic coupling becomes dominant.

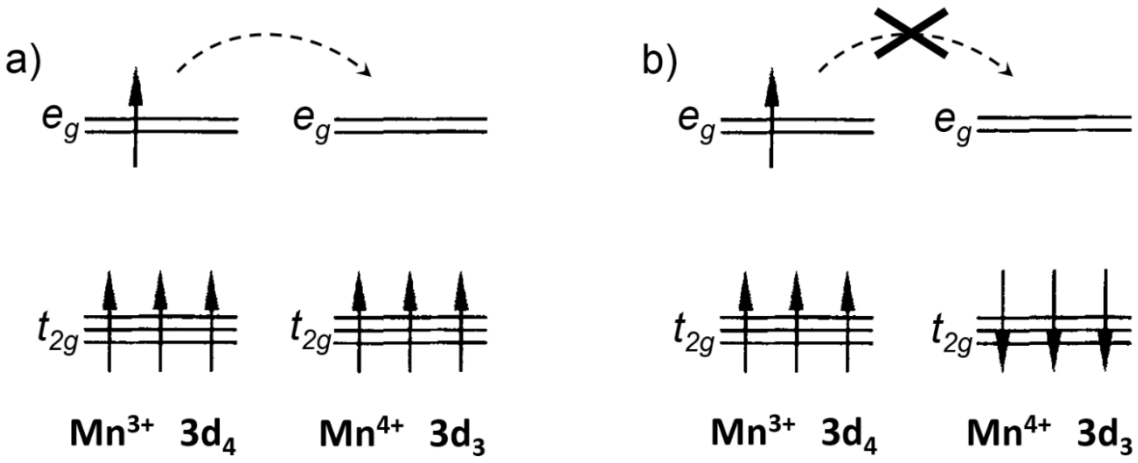

Figure 2.4. Double exchange mechanism raises ferromagnetic coupling between the Mn^{3+} cations to the Mn^{4+} cations. The hopping of the e_g electron is possible if a) neighbouring ions are ferromagnetically aligned, and not if b) neighbouring ions are antiferromagnetically aligned.

2.2 Powder calcination

Normally the purchased or synthesized powder does not have morphology and properties required for the final product. However, powder's surface area, density, degree of hydration are just to name a few parameters, which strongly affect the subsequent processing steps and determines properties of the final material. Aiming to better control and modify if needed powder's morphology and surface chemistry, one of the following methods are normally used: powder washing and drying, hydration of powder surface, chemical surface treatment, calcination, etc. [37]. Calcination, which is a heating treatment at temperatures below

melting point of material, is applied whenever surface oxidation, diffusion or reaction between mixed materials is needed. In our laboratory calcination is mostly used in order to increase a crystallite size and/or provoke particles agglomeration.

Detailed background on the phase transition and lattice analysis of LSM under heating can be found elsewhere and goes beyond the scope of present study. The purpose of X-ray diffraction analysis and others morphology and particles size descriptive methodics in current work serve more for a routine qualitative analysis of powder before being used for further processing.

2.2.1 Experimental methods

The morphology of the powders was investigated on scanning electron microscope TM3000 (Hitachi TM3000, Hitachi High-Technologies Europe GmbH, Germany) at 15kV. For measuring the particle size distribution (PSD) powders were dispersed in ethanol. The average particle sizes (d_{50}) of as-received and calcined powders were obtained by laser scattering (LS 13320, Beckman Coulter Inc., USA). The specific surface area values were determined by Brunauer, Emmett and Teller method (BET) (SA3100, Beckman Coulter Inc., USA).

The average crystallite sizes and constituent phases were determined by high temperature X-ray diffraction (XRD) analysis using the Cu-k_α radiation with 2θ=20-90° (Bruker D8 diffractometer, Bruker AXS, Germany). The data were recorded "*in-situ*" at temperatures given in Figure 2.5. Scherrer's equation was used to calculate the average crystallite size (D), adopting an average of the four most intense XRD peaks, as follows:

$$D = \frac{\kappa\lambda}{\beta \cos\theta'}, \qquad 2.3$$

where κ is the coefficient equal to 0.94; λ the wavelength of the X-ray (λ (Cu-k_α)=0.154 nm), β the full width at half maximum of the X-ray reflection, θ the diffraction angle.

Powder $La_{0.85}Sr_{0.15}MnO_3$ (LSM, Haldor Topsoe A/S, Denmark) was characterised as received, and after calcination at 800 °C, 1000 °C and 1200 °C. All three samples were calcined with a heating rate of 100 °C/h and a dwell time of 2 h. Before analysis, particles were milled for 10 min to break the big blocks/agglomerates of powder formed during the calcination.

2.2.2 Effect of calcination regimes on powders morphology and size distribution

First, phase identification is necessary. As it was described above, 15% strontium doped lanthanum manganese oxide (LSM15) has a distorted perovskite-type structure with formulae $La_{0,85}Sr_{0,15}Mn(III)_{0,71}Mn(IV)_{0,29}O_{3,07}$ [88], [89]. As the X-ray pattern for exactly the same structure have not been found in the JCPDS database, powders diffraction patterns were compared with orthorhombic $La_{0,88}Sr_{0,12}MnO_3$ (0-053-0057) and rhombohedral $La_{0,8}Sr_{0,2}MnO_3$ (0-053-0058).

The evolution of the crystalline phase of LSM with a heating up to 1150 °C is illustrated in Figure 2.5. The crystal structure transformation observed at around 900 °C is normally ascribed to the transition between distorted cubic symmetry to rhombohedral structure of LSM perovskite. Another phenomena, occurred due to cation vacancies and non-stoichiometry in oxide in $La_{0,85}Sr_{0,15}MnO_{3+\delta}$ structure is oxidation. Gaudon *et al.* [90] reported that during cooling LSM undergoes oxidation from 1000 °C to 700 °C, reduction from 700 °C to 200 °C and second oxidation from 200 °C to room temperature. The appearance of the secondary phases is normally attributed to oxidation of Mn cations on the surface. A decomposition of manganite phases observed around

850 °C - 900 °C is possible due to immiscibility region between perovskite, lanthanum manganite and strontium manganite phases at elevated temperatures [91].

Table 2.2. shows the micrographs and values of specific surface area and particles/crystallite sizes for four analysed LSM powders. For uncalcined LSM and LSM calcined at 800 °C the measurement of particles size from SEM images was hindered because samples had a sponge porous structure rather than a shape of distinctive particles. The PSD measurement though shows the clear tendency of increasing the average particle size and an equivalent decrease of surface area with increase in calcination temperature, as seen from BET analysis. This is in a good agreement with the results (D), estimated from XRD line broadening. The characteristic peaks of LSM (Figure 2.5.) show stronger and sharper profiles what indicates continuous crystallization and gradual grain growth with increase in calcination temperature. The sharp decrease of the surface area at temperatures around 900-1000 °C is most likely associated with an agglomeration of fine LSM particles formed during the powder synthesis into coarse lumps.

This complete analysis of particles physical characteristics is of crucial importance and has to be a part of a regular procedure at processing laboratories. The practical issue with which we have experienced in our laboratory was the change of powder supplier from Haldor Topsøe A/S (LSM HT) to American Elements (LSM AE).

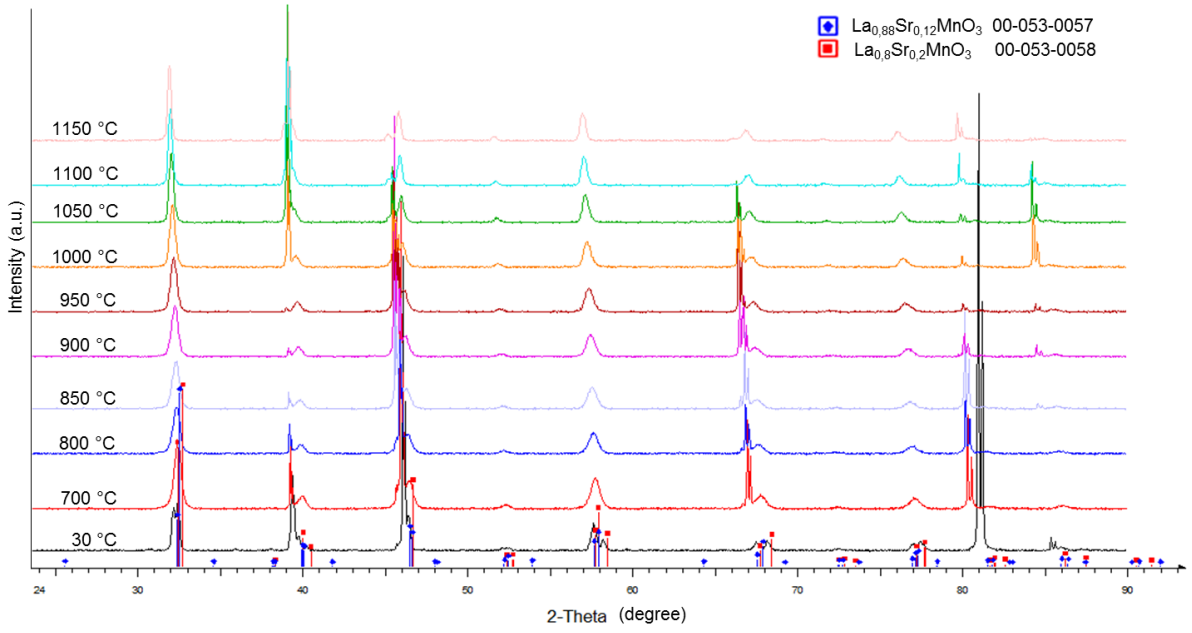

Figure 2.5. High temperature XRD patterns of $La_{0.85}Sr_{0.15}MnO_3$.

The SEM pictures of LSM HT (Table 2.2) and LSM AE (Table 2.3), calcined at 1000 °C and 1200 °C were characterised with the identical particles sizes. However, sintering shrinkage of the tape, produced with use of LSM HT (calcination temperature T_{calc} was 1000 °C) was significantly higher compared to the tape of LSM AE (T_{calc}=1000 °C) with a very minor shrinkage during sintering. The morphology and crystallite size of LSM AE remained identical for uncalcined and calcined LSM AE powder, because the raw material was synthesized by solid state reaction at 1200°C and therefore it had been subjected to temperature higher than the calcination temperature (Table 2.4).

Table 2.2. SEM micrographs and results of particles size, calculated from the SEM images (d_{SEM}), average particle size d_{50}, average crystallite size (D), and specific surface area (S_{BET}) of uncalcined and calcined $La_{0.85}Sr_{0.15}MnO_3$, purchased from Haldor Topsøe A/S.

	uncalcined	**800 °C**	**1000 °C**	**1200 °C**
SEM	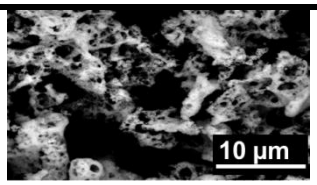	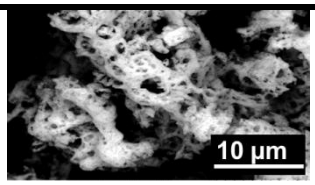	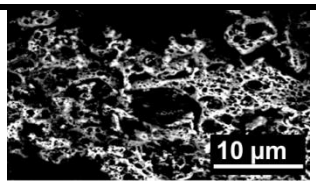	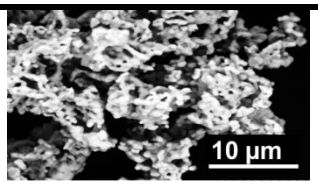
d_{SEM}, µm	-	-	1.8(3)	1.6(8)
d_{50}, µm	2.00(5)	2.37(1)	3.18(4)	3.40(1)
D, nm	17.69	20.51	71.34	92.20
S_{BET}, m^2/g	23.35(3)	22.09(2)	2.65(2)	1.63(3)

Table 2.3. SEM micrographs and results of particles size, calculated from the SEM images (d_{SEM}), average particle size d_{50}, average crystallite size (D), and specific surface area (S_{BET}) of uncalcined and calcined $La_{0.85}Sr_{0.15}MnO_3$, purchased from American Elements.

	uncalcined	**800 °C**	**1000 °C**	**1200 °C**
SEM	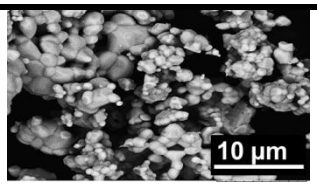	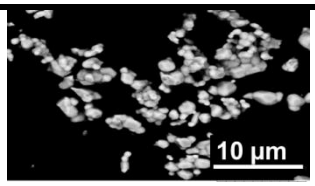	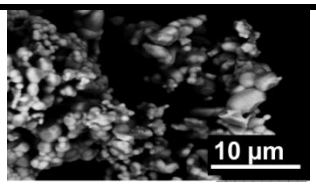	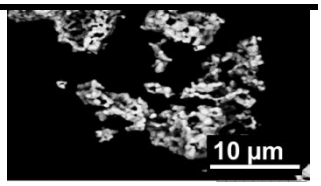
d_{SEM}, µm	1.9(5)	1.9(1)	2.0(3)	2.1(7)
d_{50}, µm	8.67(2)	11.80(1)	12.42(4)	14.82(2)
D, nm	94.3(7)	96.3(2)	95.8(8)	93.6(3)
S_{BET}, m^2/g	3.82(9)	3.76(4)	3.77(8)	4.80(5)

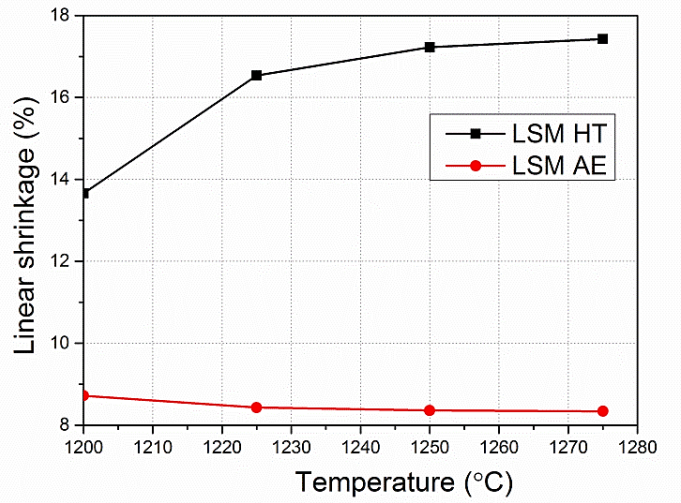

Figure 2.6. The linear sintering shrinkage of tapes, produced with use of LSM HT and LSM AE powders.

Table 2.4. Details of production method and characteristics of uncalcined LSM HT and LSM AE

	Production method	**Synthesis heating treatment**	**S_{BET}, m^2/g**	**d_{50}, µm**
LSM HT	Glycine-nitrate combustion synthesis	700 °C	23.35(3)	2.00(5)
LSM AE	Mature solid state reaction	1200 °C	3.82(9)	8.67(2)

Based on present study one conclude, that heating of the LSM15 powder has influence both on crystal structure and particle size of the sample. For identification if the synthesis method affects the magnetic properties of the LSM powder, the performance of uncalcined and calcined LSM HT (T_{calc}=1200 °C), and calcined LSM AE (T_{calc}=1200 °C) were compared (Figure 2.7) in a low magnetic field of H=1 Oe (10 mT). The uncalcined LSM HT has a broad magnetic transition with the $Tc \approx 270 \pm 5K$. The calcined LSM HT and LSM AE powders present a sharper magnetic transition which is assumed to be caused by the increased crystallinity proven by the data from the XRD analysis. However, the LSM HT (T_{calc}=1200 °C) exhibits transition temperature around desired room temperature at $Tc \approx 300 \pm 2K$, while the transition temperature of LSM AE is lower $Tc \approx 236 \pm 3K$. Despite the fact, that the magnetisation of LSM AE is significantly higher than the magnetization of LSM HT, the latter powder was chosen for the tape casting experiments presented in the Thesis. Further in the text LSM HT will be referred as LSM powder.

After the choice of powder supplier, the calcination temperature for LSM powder has to be determined. The general preference in liquid processing techniques is use of particles with a low surface area. The smaller the surface area, the lower the amount of dispersant is required for sufficient powder stabilisation. In turn, the lower the polymer content, the fewer pores and stresses will be accumulated during the organics burn out stage. Another advantage of using micrometer particles compared to finer submicron- and nano-sized powders is that the latter ones pack in very dense structures, which causes an increase in capillary forces on drying stage and provokes stress and crack nucleation [92]. In the same work [92] professor Rosen defines that the particles

which are easy to cast into uniform tape are typically in size of 1-5 µm or characterised by a surface area of 2-5 m^2/g. Therefore, for further processing LSM powder calcined at 1000 °C was chosen.

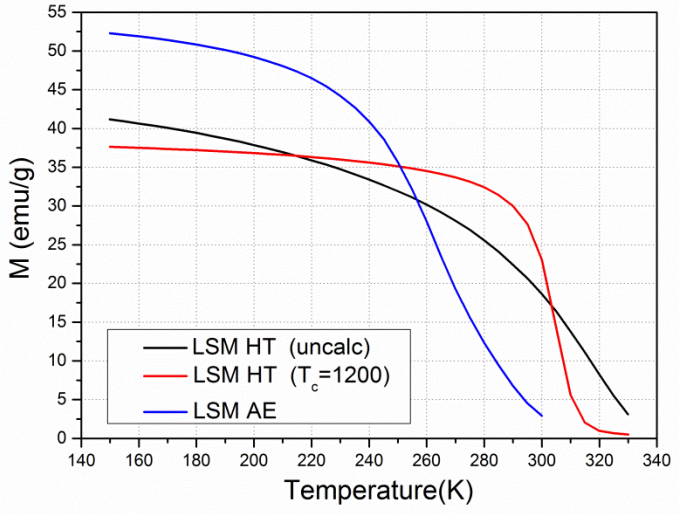

Figure 2.7. Temperature dependence of magnetization for uncalcined and calcined (T_{calc}=1200 °C) LSM HT and uncalcined LSM_AE in H=1000 G.

3 Slurry formulation

The main ingredient in slurry composition, as it was said above, is a powder. This is the only fraction which formulates the final product, and, obviously, determines the properties of a shaped material. Since tape casting is a liquid forming technique, solvent is needed to create a media and carry powder under the casting blade, dissolve and assure a homogeneous distribution of all other slurries components. Solvent also features a resultant mixture with the fluid characteristics, such as viscosity, side flow, *etc*. In order to keep powders separated and homogeneously distributed in the volume of the solvent, particles surface should be modified by either having a double electrostatic layer or covering surface with a dispersant (dispersing agent, deflocculant). Next slurry component, binder, forms the only continuous phase in a green tape, which supplies a matrix for holding all constituents together, retains the formulated shape of material, featuring it with flexibility, plasticity, strength, and possibility to be laminated. Finally, other additives like plasticizers or sintering agents are usually added into any casting system just upon necessity to improve either mechanical parameters of green tape (flexibility, plasticity, *etc.*) or mechanical and physical parameters of sintered tape (density, microstructure) and a heating kinetics. The specific role of each component in slurries, used in current work, will be explained further.

With the goal to reduce any intrinsic stresses at the interface of the graded tape it is reasonable to use of the same organic systems in adjacently co-cast slurries. The application of the same solvent and organic ingredients assure identical drying shrinkage rates and identical burning-out kinetics in neighbouring materials.

*Table 3.1. Formulation of MEKET-based slurry. * Polymers supplier and exact molecular weights are excluded due to confidentiality.*

Component	Function	Producer
LSM or LSM/CGO or LCSM	Ceramic powder	Haldor Topsøe A/S, Denmark Rhodia, France CerpoTech AS, Norway
Azeotropic mixture of methylethylketone and ethanol (MEKET) (2:1 wt.%)	Solvent	Alfa Aesar GmbH&Co KG, Germany CCS Healthcare AB, Sweden
Polyvinylpyrolidone (PVP)	Dispersant	-*
Polyvinyl butyral (PVB)	Binder	-
Dibutyl phthalate (DBP)	Plasticizer	-
Polyethylene glycol (PEG)	Plasticizer	-
Additol	Release and wetting additive	-

The type and amount of each component has undoubtedly a profound influence on quality of the final tape. The obtained slurry is a multiphase system and therefore it is extremely complicated and sensitive to variations. Fortunately, tape casting as a shaping process has matured in recent decades from being a trial and search-based science to a well-developed engineer discipline, where finding the best organic system is no longer the main focus. Therefore, instead of building up a new organic system, it was decide to apply one of well-studied MEKET-based slurry composition [37], [93] (Table 3.1) and concentrate on developing of SBS TC

technique instead. The role and the choice of every component in the composition will be given in the following chapters though.

Before a real processing, the validation and analytical control of slurry composition for a certain shaping technique is qualitatively determined by rheological characteristics of slurry. A short but comprehensive outlook of a variety of rheological flow behaviours, rheological models with their usage in analytical and numerical modeling, main rheological characteristics and potential to be used in tape casting for the efficient fabrication of adjacently graded tape are also presented below.

3.1 Choice of solvent and organic additives

3.1.1 Solvent

The main criterion for solvent choice was mentioned to enable dissolving all organic additives and uniformly distribute them in a mixture. In tape casting both organic (non-aqueous) and water solvents can be applied. Although water is valued as a promising solvent because of availability and especially a health and environmental aspects, and also due to possibility to easily adjust a pH of media [94], slow drying of aqueous-based slurries leads to initiation of pin-holes and bubble on tape surface, foam formation, and hydration of ceramic powder issues. Besides, the selection of organic ingredients is harder as the variety of organics soluble in water is restricted to a very few systems. Moreover, high surface tension of water implies the use of extra additives as wetting agents to promote the adhesion with a carrier support. Typical for water based slurries (i) slow drying and (ii) absence of the shear thinning behaviour, *i.e.* increase of viscosity when stresses are released after a blading procedure, are two extremely unfavourable factors for successful adjacent co-casting of a graded tape with a sharp interface. Furthermore, as a requirement from the application needs there is a desire to tape cast self-supporting thick dense tapes, suggesting the use of highly viscous slurries [37], [95], which is difficult to achieve using water-based slurry.

Meanwhile, adjacent co-casting of slurries into a dense comparably thick tape is possible when using an organic solvent. The organic-based solvents are so widely applied in tape casting recipes that they are normally referred as a solvent or solvent-based casting. Normally, applied in tape casting organic solvents such as alcohols, ketones or hydrocarbons are less environmentally friendly comparing to water, nevertheless, we choose to work with organic-based slurries to take advantage of the flexibility in choosing powders and organics for slurry formulation. Additionally, organic solvents have a low boiling point, low heat of vaporization, and high vapour pressure, and all of that facilitates shortening the drying time. Azeotropic mixture MEKET was chosen as it was shown to form a stable slurries [96] with enhanced wetting behaviour [97]. MEKET is widely used in tape casting as medium polar solvents like the azeotropic mixture are compatible with many commonly applied dispersants and binders. The azeotrope has to be applied as pure methylethylketone evaporates too fast forming skin and lumps at the tape surface and blocking further evaporation; while addition of the ethanol delays formation of the solvent-depleted regions, thus allowing entire drying to take place more uniformly and quickly [37].

3.1.2 Dispersant

After calcination, described in Section 2.2.2., powders normally have a particles size distribution from hundreds of nanometers to tens of microns. When they are placed in liquid, ceramic particles of mentioned size

are usually exposed to colloid forces rather than gravity forces. Due to a large surface area of comminuted particles, they are exposed to clump together forming either a soft (low energy) agglomerates due to inteparticles Van der Waals forces and can be broken by simple stirring, or strong agglomerates requiring very energetic methods to disperse particles.

The presence of agglomerates of any nature is undesired because soft agglomerates, for instance, can trap an air which will lead to non-uniform drying and ends in highly localized porosity in tape. In addition, presence of flocculated particles in slurries leads to slurry inhomogeneity and defective packing with a lower green density as a result. In order to keep the stable slurry and control the morphology of cast tape, powder should be stabilized.

3.1.2.1 Powder stabilization

There are three distinctive methods to stabilize colloidal system to avoid agglomeration: electrostatic, steric and a combination of the first two so–called electrosteric method (Figure 3.1).

Electrostatic stabilization (Figure 3.1a) is caused by creation of electrical charge on particles surface happening mostly in water and caused by [34]: surface group ionisation (driven by the pH of the dispersed media), differential solubility of ions, or isomorphous replacement lattice substitution. The ions of which the solid particles are composed, hydrogen and hydroxyl ions or ions capable to form insoluble salts with the solid's surface, create electrical double layer. First layer (Stern layer) comprises ions adsorbed directly at the surface of the particle as being attracted by the oppositely charged surface of the particles, and a second diffusive layer composes of counter-ions. When a colloidal particle moves in the dispersion medium, a layer of the surrounding liquid remains attached to the particle. The boundary of this layer is called slipping plane (shear plane). The value of the electric potential at the slipping plane is called Zeta potential (ζ). Zeta potential reflects the variation in surface potential for a specific material in a polar medium and the adsorption of ions into the inner part of the double layer. The pH where the particle surface carries no net electrical charge, *i.e.* where ζ=0 is termed the isoelectric point (pl). Hence, in order to generate a stable system, ζ has to have a large value by module, therefore, the pH of a working media has to be sufficiently away from pl. This type of stabilization is normally used for dispersing nano- or submicron-size particles and normally applied in water-based systems [95].

Below pictured test shows the result of test oriented on study of ionization of LSM particles in ethanol as part of the MEKET azyotrope. For that experiment 10 wt.% of LSM was diluted in ethanol. Ethanol was tested to not conduct electricity because it does not ionize to a sufficient extent (not shown here). Addition of an electrolyte cause to a slight conductivity but that is normally not enough for the electrostatic stabilization of the micron-sized particles. The zeta potential measured on LSM in ethanol is also very low (Figure 3.2), what demands for searching for the dispersant which could stabilize LSM with a steric mechanism.

Steric stabilization (Figure 3.1b) is the alternative which hinders the close contact between particles by adsorbing organic molecules, usually short polymeric chains, on the surface of powders. The adsorption have to be strong enough to avoid desorption during the next processing steps. Besides, formed polymeric shell should be of a certain thickness and density to surmount the Van der Waals forces between particles. The steric stabilisation is often applied for covering micrometer sized powder in ceramic processing techniques as it also helps to regulate rheology of used suspensions.

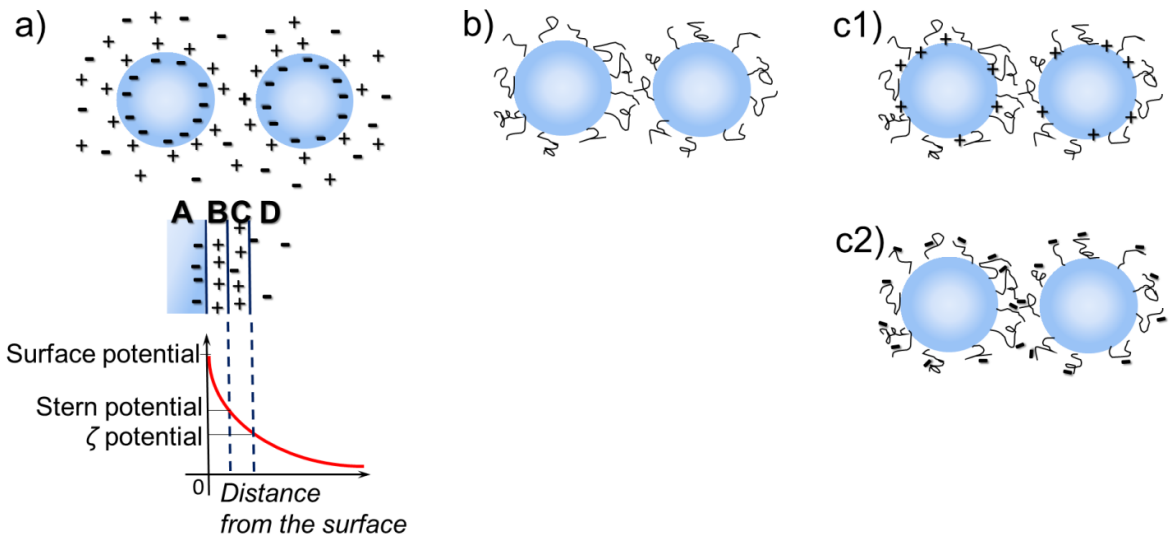

Figure 3.1. Schematic of colloidal stabilization methods: a) electrostatic stabilization and an illustration of the double layer and potential drop across the double layer where (A) is a surface charge, (B) Stern layer, (C) slipping plane, and (D) diffuse layers of counterions; b) steric stabilization; c) electrosteric stabilization, which can be realized by (c1) charges and nonionic hydrophilic polymer or (c2) polyelectrolytes.

The third method is electrosteric stabilisation, which can be realised by (i) a combination of charges and nonionic hydrophilic polymers (Figure 3.1c1) or (ii) by adsorbing polyelectrolytes on the particles surface (Figure 3.1c2). The use of polyelectrolytes is very common in tape casting practice [54].

In the current work the steric stabilization by polar non-ionic polymer PVP (M_w=10000 g/mol) was chosen, since PVP was shown [93], [98] to form a stable slurry with non-agglomerated particles and improved packing of green tapes.

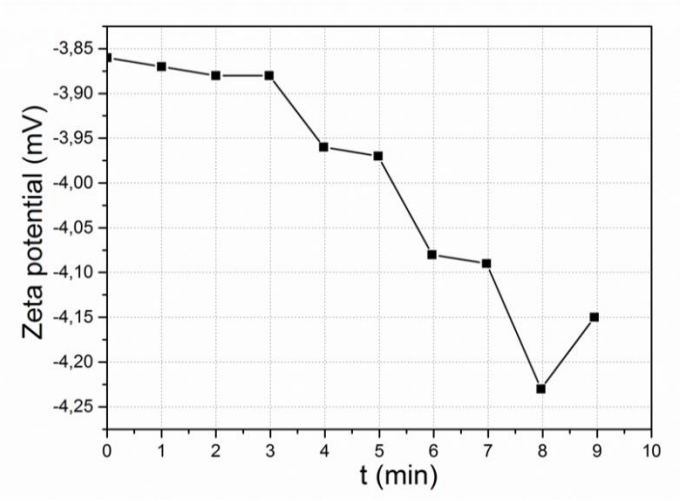

Figure 3.2. Zeta potential of 10 wt.% dispersion of LSM in ethanol.

3.1.3 Binder and plastisizers

The binder provides strength to the green tape after the solvent is evaporated by bridging ceramic particles into continuous material. The majority of binders used in organic-based slurries fall into two groups: polyvinyls (vinyl) and polyacrylates (acrylic) with the main difference in burnout kinetics in different atmospheres. In current work, cohesion between stabilized particles was ensured with a PVB binder. PVB is often used in solvent tape casting recipes because of excellent green tape functional characteristics, which it provides [99], [100].

Surface morphology, wetting behaviour and adhesion of tapes while using PVB was improved with additive Aditol. To soften the strong but stiff and brittle binder in the drying stage, and also modify flexibility, strength and viscosity of slurry, PEG and DBP were added [101]. These plasticizers break the close alignment and bond in the binder net, sufficiently increasing the flexibility and workability of the tape.

3.1.4 Ingredients interaction

Aside from purposeful functions of each component in the system, the side interaction between ingredients is possible due to complexity and multiphase nature of slurries [37]. Here, the effect of possible unintended interactions between organic molecules will be briefly described with the aim to easily distinguish and prevent them in currently used slurry.

a) Binder-Dispersant interaction

Normally, molecular weight of binder is higher comparing to this value for the dispersant. It can happen that insufficient cover of particles' surface by a dispersant will induce the binder to behave as a dispersant too. Despite, binder can replace dispersant from the particles surface [102], therefore, the order of ingredients addition is very important. In these cases, competitive adsorption can cause flocculation of particles or formation of polymeric micro globules which cause disarranging of the slurry's homogeneity, or reduction of the amount of binder networking the particles which weaken the strength of the tape. The clear evident of unintended binder behaviour is reduction of the slurry viscosity with increase in binder content, which is not the case for slurries used in current work (Section 5.3).

b) Binder-Plasticizer interaction

This interaction is normally desirable but requires at least 12 h for plasticizer to modify the binder polymer in order to increase tape's flexibility.

c) Dispersant-Plasticizer interaction

Normally these two ingredients don't interact. However, sometimes non-adsorbed dispersant chains can act as a plasticizer [37].

3.2 Requirement for formulation of slurry used in SBS TC

Unlike traditional tape casting recipes, which intended to cast thin films usually below 200 µm [95], [100], [103], [104], magnetic refrigeration requires use of thicker tapes of about 300 µm. From the casting experience it is well known that the thicker tapes are to be obtained the more viscous slurries are to be used . Increase in casting viscosity can be also beneficial for adjacent co-casting because most viscous slurries are less prone to a side flow contributing to formation of distinctive intermaterial interface without mutual diffusion.

Hence, traditional solvent-based slurry recipe [37], [93] had to be adapted to a novel SBS TC technique. For the first experiments the amount of solvent in standard solvent recipes was reduced and the amount of a binder system content increased (Figure 3.3.a). The details on compilation of the slurry formulation and its influence on quality of adjacently graded tape is widely described in Section 5.3, Paper I and Paper IX.

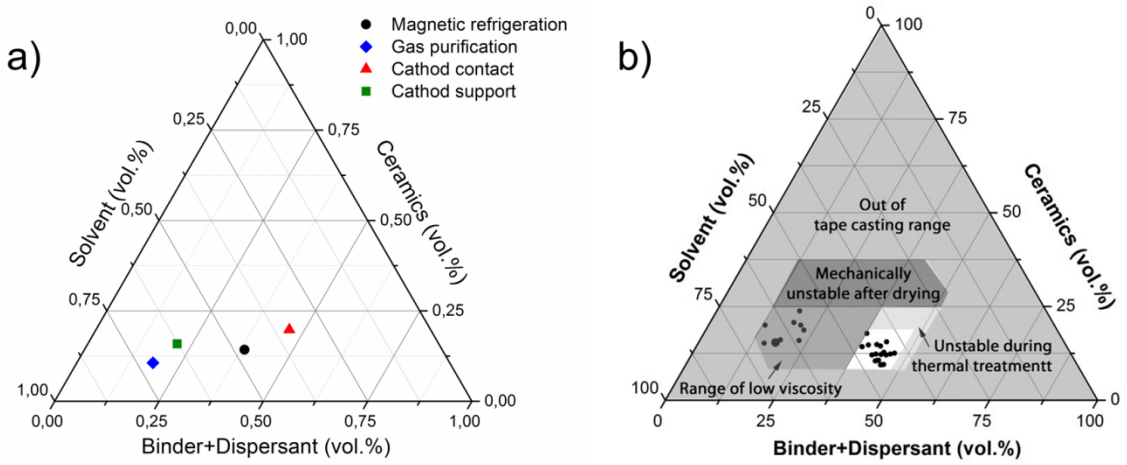

Figure 3.3. a) Compositional triangle of tape casting formulations used in various applications and b) compositions of the present work (dots in white area in the plot) compared to the recipes found in literature (dots in grey area in the plot).

Systematic change in the binder system's and the solvent's mass loading lead to a consistent volumetric change of the total slurry volume, making the components volume percentage look inconsistent. Thus, the components of the slurries (Table 3.2.) are given both in volumetric percentage for easier comparison with standard slurry formulations (Figure 3.3b) and in volumetric ratios of binder system and solvent to constant ceramics load, BS/C and S/C, consequently.

The literature based slurry compositions (Figure 3.3b) contain about 55-75 vol.% of solvent and 15-25 vol.% of polymeric part including binder system (binder PVB, plasticizers DBP and PEG and wetting additive Additol) and dispersant PVP. The binder system content varies from 13 to 24 vol.%. Apparent viscosity of these slurries with comparable molecular weight polymers was below 1000 mPas at 10 s^{-1} shear rate.

The weight of powder in all prepared slurries was fixed to be a 100 g. The weight ratio of LSM/CGO powders in LSM_CGO slurry was fixed at 8.9:1.1. The weight of dispersant in LSM and LSM_CGO slurries was set at 1.72 g (1.2 g/cm^3) and 1.98 g, correspondingly. Since mass of solvent and binder system were changed alternatively, the total weight and, hence, the total volume of slurries was changed from experiment to experiment. Hence, the relative and not absolute value for solvent and binder system contents were defined as relative ratio of binder system volume to constant in slurry ceramics volume BS/C ratio and volume of solvent MEKET with respect to the ceramics volume S/C:

$$BS/C = \frac{summary\ volume\ of\ all\ components\ in\ binder\ system}{volume\ of\ ceramics} = \left[\frac{ml}{ml}\right] = [-] \qquad 3.1$$

$$S/C = \frac{volume\ of\ solvent}{volume\ of\ ceramics} = \left[\frac{ml}{ml}\right] = [-] \qquad 3.2$$

The optimal slurries formulations for SBS TC were determined based on the flexibility and surface quality of the obtained green tapes and the absence of cracks and deformations after the sintering process (Figure 3.3b). The increase in binder content together with an increase in viscosity was aimed to improve adhesion between adjacently co-cast materials, but exceeding the binder system content over 47 vol.% was shown to form tapes with a very fragile post-sintered structure. Based on these results, feasible binder solution content was established as 35.5-43.5 vol.%, or 2.01-3.62 with respect to the ceramics volume (BS/C ratio). Another approach to increase slurry viscosity included reduction of the solvent content. Experiments showed, that using MEKET in concentrations below 40 vol.% leads to formation of cracks during the drying stage, which were provoked by accumulated stress due to constrained volume shrinkage.. Hence, the optimum solvent content was found to vary as 40-48 vol.%, which corresponds to relative amounts, S/C of 2.50-3.61. Significant decrease in the amount of solvent as the only homogenizer in slurry formulation identified the need for dividing the milling process into 3 steps, as it is described in Section 3.3.1.

Table 3.2. Content of LSM and LSM_CGO slurries used in current work.

	Solvent vol.%	Binder syst. vol.%	S/C $Vol_{solv.}/Vol_{ceram}$	BS/C $Vol_{bind.syst.}/Vol_{ceram}$
LSM	42.9	41.2	2.3	2.8
LSM_CGO_1	43.9	42.5	3.6	3.4
LSM_CGO_2	43.4	42.4	3.6	3.4
LSM_CGO_3	42.8	43.7	3.5	3.6
LSM_CGO_4	41.7	44.5	3.4	3.6
LSM_CGO_5	40.6	45.3	3.2	3.6
LSM_CGO_6	40.6	41.8	2.9	2.6
LSM_CGO_7	41.1	41.6	2.6	2.6
LSM_CGO_8	40.5	40.7	2.1	2.5

3.3 Preliminary slurry preparation processes for tape casting

A complete de-agglomeration of the calcined powder is of a major importance, because further no high shear will be applied during the process which would be able to destroy agglomerates. In turn, presence of any agglomerates or inhomogeneities in casting slurry provoke non-uniform green packing and are usually the source of crack nucleation during drying and sintering stages. In order to disperse particles evenly, high energy techniques like wet ball milling are applied. Along with breaking soft and hard agglomerates, milling distributes uniformly organics on the powders surface, and creates stable slurry.

3.3.1 Milling

The ball milling is the most commonly used procedure before casting. In order to eliminate the potential for competitive adsorption, mentioned above, the slurry is normally mixed in two steps. First, the powder(s), dispersant and solvent are mixed with a milling media in a jar. A dispersion milling procedure can vary from 4-72

h. After the powder is broken into individual particles, which are evenly covered with the dispersant, the second step including addition of binder and plasticizers comes. The slurry is then homogenized for the next 12-24 h at a very low speed, which is an effective way to remove the air from the slurry content and form a homogeneous binder net.

The grinding kinetics for LSM (η=4200 mPas), LSM_CGO_1 (η=2700 mPas) and LSM_CGO_3 (η=38000 mPas) (Table 3.2), appeared to be not-dependent on viscosity and the fine structures of 2 µm and 2.5 µm were achieved. First, 85 wt.% LSM powder used was suspended in MEKET with 80 wt.% dispersed PVP dispersant and ball milled for 40 h (220 rpm) (the weight percentage is specified out of the total component's mass used). CGO, if any, and the last 15 wt.% of the LSM with the rest of 20 wt.% PVP, was then added to the suspension; and the slurry was milled for further 30 h (220 rpm). After adding the binder system (binder PVB, plasticizers DBP, PEG, and Additol) preliminary dissolved in MEKET to the obtained suspension, the slurry was milled for another 20 h (85 rpm). This program was also applied for preparation of LCSM slurries.

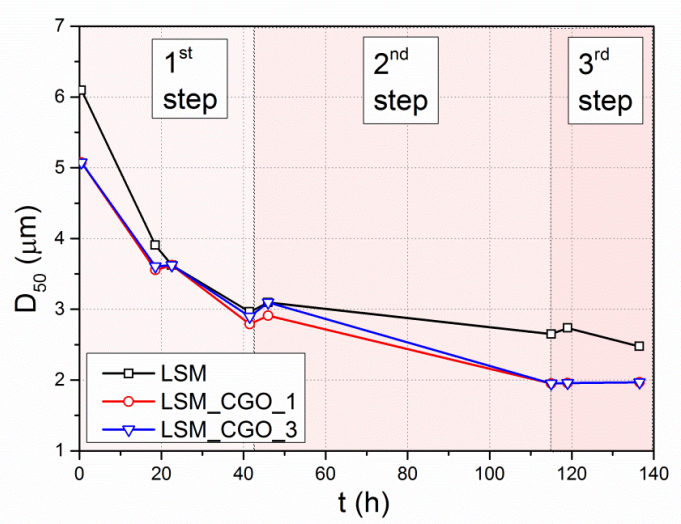

Figure 3.4. Effect of ball milling time on average size of LSM and LSM_CGO particles in LSM, LSM_CGO_1 and LSM_CGO_3 slurries (Table 3.2). The 1st step of ball milling included milling of 85 wt% of PVP dispersant dissolved in solvent and 80 wt% of the ceramic powder. The rest 15 wt% of PVP dispersant and 20 wt% of the ceramic powder were added on the 2nd step. The binder system dissolved in solvent was added to the mixture at the 3rd step.

3.3.2 Filtration

After slurry is homogenized, the next step is to filter out unwanted inhomogeneties such as residual not destroyed agglomerates, undissolved binder, debris from the milling media or from container. For that, nylon tulle with mesh size of 100 µm was clamped between a bottleneck and a bottle lid with a hole in it. The slurry was squeezed through the tulle to another bottle. The size of meshes is defined by the size of the defects that need to be removed, the thickness of the tape to be formed and the time allocated to the filtration process.

3.3.3 De-air

During milling and filtration steps the air bubbles can easily be entrained into the volume of slurries. Presence of air bubbles in slurry cause defects in green tape such as "pinholes" ("giraffe dots"), what is very

typical for thick tape fabricated from high viscous slurries, or “crow foot” defects, which is crack radially propagated from the pinholes. Sometimes air bubbles become trapped under the doctor blade during tape casting, which cause the formation of streaks. Being a region of thickness variations, streaks are visually detected as thin lines at the tape surface parallel to the casting direction, and tapes with such kind of defects are not applicable for further casting processes.

The most common technique for removing air from the slurry before casting is vacuum de-airing accompanied by a gentle stirring or agitation. Too high vacuum or de-airing for a long time will tend to remove a large volume of solvent along with the air bubbles. For small volumes of slurries (two liters or less), the time for complete air removal is generally five to eight minutes.

Depending on slurry formulation, prepared volume and slurry pre-treatment, bubbling action can be detected visually. In that case, completion of bubbling defines completion of de-airing process. In current work slurries were de-aired at 100 mbar vacuum and visual detection of bubbling action was complicated due to high viscosity of slurry and a narrow bottleneck. For detecting how much time it is required to remove air bubbles, how fast solvent evaporates at given pressure and how viscosity changes with de-airing, the mass control and viscosity were measured as functions of evaporation time.

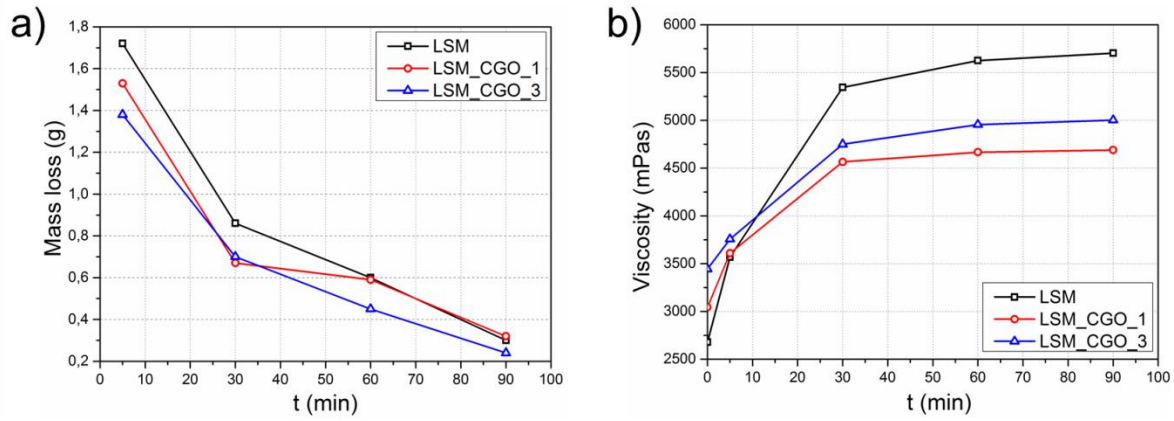

Figure 3.5. a) Mass loss and b) viscosity change of LSM, LSM_CGO_1, LSM_CGO_3 (Table 3.2) slurries as a function of duration of de-airing process hold in vacuum at 100 mbar pressure.

Figure 3.5a illustrates that during the first 30 min through the surface of 28.3 cm^2, 2-2.5 g of solvent evaporates, therefore, viscosity also changes drastically (Figure 3.5b). The initial stage is when together with entrapped air a lot of solvent evaporates from the slurry surface. The solvent’s mass loss is gradually decreases to the point where most of air is removed, solvent from the top layers of slurry has already evaporated, forming dried film on slurry surface and blocking evaporation, and diffusion of solvent through the slurry volume to the surface takes much more time.

The slurry viscosity should be also taken into consideration for determining the de-airing time. LSM_CGO_1 (composition in Table 3.2) of lower viscosity contains more solvent, thereby, making air removal easier and faster. Solvents are more difficult to remove from the more viscous slurries as LSM_CGO_3 (composition in Table 3.2), and they also require more time for agitation and complete de-airing.

To achieve consistent results during de-air processing, the same volume of slurries were prepared, and they were all kept at 100 mbar vacuum for 5 minutes.

3.4 Slurry characterization

When the slurry is ready to be cast, a number of characterization analyses are advised to be provided to control slurries uniformity, stability and suitability to tape casting. Among standard quality control tests are: viscosity, density (specific gravity), and particles size distribution.

Particles size distribution must not be changed if the same batch of material is used and slurry preparation is identical. However, slurry viscosity and density are very sensitive to any minor changes in slurry, therefore, they have to be measured for each prepared slurry.

Slurry density is normally measured using pycnometer. A fixed volume container is filled with slurry and weighted; a capillary tube is used to accurately determine the volume of suspension. The same method was applied in current work and the impact of slurry density on SBS TC will be explained further in Section 5.3 and it is described in details in Paper I and Paper IX.

Viscosity is a key rheological property of the slurry, however, the scope of rheology in tape casting manufacturing also encompasses the study of a liquid flow and a solid-liquid interaction. Identification of the most sufficient dispersion agent and binder system for the specific powder, determination of the optimum amount of polymeric additives for composing a stable slurry, elicitation of inhomogeneties in slurry, representation the response of slurry flow behaviour on applied stresses are just to name a few characteristics which rheology suffice to estimate. A short introduction into rheology and the main rheological tests will be described in the following section since rheology is widely employed in the present study.

3.4.1 Rheology

This section aims to describe the methodology developed for study the rheological behaviour of casting slurries around which the further experimental tape casting work will be reported in this Thesis. In the following paragraphs, the terminology describing the slurries rheological behaviour will be given.

Table 3.3. Overview on different kind of rheological behaviour representing different materials.

Liquids		Solids	
Viscous	**Viscoelastic**		**Elastic**
(ideal-) viscous	viscoelastic liquids	viscoelastic solids	(ideal-) elastic
flow behaviour	flow behaviour	deformation behaviour	deformation behaviour
The deformation is fully dispersed by flowing under the application of very small stresses	The deformation is partially recovered after the removal of the applied stress and partially dissipated by flowing		The deformation is fully recovered after the removal of the applied stress
De<<1	De≈1		De>>1
Newton's flow	Maxwell's law	Kelvin/Voigt's law	Hooke's law
water, oils	slurries, glues	pastes, gels	stones, steels
←← rotational tests →→			
←← ←← oscillatory tests →→ →→			

Rheology is the science of deformation and flow under externally exerted forces. All kinds of materials, which can be described rheologically, are viewed as being in between two extremes: flow of ideally viscous fluid and deformation of ideally elastic solid (Table 3.3). The category of any material depends from the ratio of the

time, required for the material to adjust to applied stresses or deformations (relaxation time) and time of the experiment. This parameter is called a Deborah number:

$$De = \frac{t_c}{t_p} \qquad 3.3$$

where De is the Deborah number, t_c the stress relaxation time, t_p the time scale of experiment. Therefore, all existing materials at certain external conditions (temperature, pressure) can be attributed into the viscous, viscoelastic or elastic categories depending on their response on the exerted deformation (Table 3.3.). Slurries used in tape casting are characterised by the viscoelastic behaviour.

3.4.1.1 Definition of terms

Viscosity (apparent viscosity, shear viscosity, dynamic viscosity) is one of the basic parameter in rheology, presenting simply a resistance of material to flow. The parallel-plate model is usually used to ease the definition of fundamental rheological terms (Figure 3.6.) [105]. The upper plate with the shear area *A* is set in motion by the shear force *F* and the resulting velocity v is measured. The lower plate is stationary (v=0). Between two plates there is the distance h, where the tested fluid is sheared. It is assumed that the following shear conditions are maintained: (i) the sample shows adhesion to both plates without any wall-slip effects, (ii) the tested flow is laminar, *i.e.* flow can be imagined in the form of parallel layers as opposed to vortices typical for the turbulent flow. Similar system of shearing between two plates is identical to the shearing occurring during rheological measurements, where rheometer support and moving measuring spindle form two parallel plate system. The two parallel plates system resembles the tape casting system, when slurry is sheared in the gap between the set motion carrier and parallel to it stationary blade.

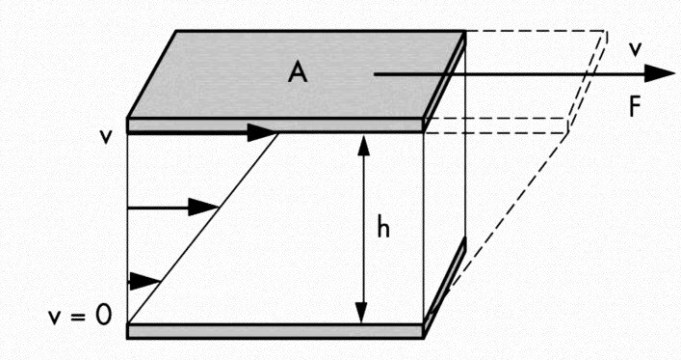

Figure 3.6. The two-plates model for shear experiments to illustrate the fluid velocity distribution in the shear gap. Adapted from [105].

A force *F* (Figure 3.6) applied tangentially to an area *A,* being the interface between the upper plate and the liquid underneath, gives rise to a shear stress in the liquid layer:

$$\tau = \frac{F}{A} = \left[\frac{N}{m^2}\right] = [Pa] \qquad 3.4$$

The shear stress τ causes the liquid to flow in a special pattern. The maximum flow speed v_{max} is found at the upper boundary. The speed drops across the gap size h down to $v_{min} = 0$ at the lower boundary contacting the stationary plate. Laminar flow means that infinitesimally thin liquid layers slide on top of each

other. The shear rate $\dot{\gamma}$ is the gradient of velocity dv between two neighbouring flowing layers determined for the infinity small thickness $d\mathrm{h}$ of a single flowing layer and in its general form is mathematically defined by a differential:

$$\dot{\gamma} = \frac{dv}{d\mathrm{h}} = \left[\frac{m/s}{m}\right] = [s^{-1}] \qquad 3.5$$

The dot above the $\dot{\gamma}$ indicates that shear rate is the time-derivative of the strain caused by the shear stress.

For ideally viscous fluids analysed at a constant temperature, the value of the ratio of shear stress τ and corresponding shear rate $\dot{\gamma}$ is a material constant defined as dynamic viscosity η or usually called in literature just as a viscosity (diverse from the kinematic viscosity):

$$\eta = \frac{\tau}{\dot{\gamma}} = \left[\frac{Pa}{s^{-1}}\right] = [Pas] \qquad 3.6$$

The correlation between shear stress and shear rate determining the flow behaviour of liquid is graphically displayed in the diagram called flow curve [106] (Figure 3.7a). For described above ideally viscous liquid, also called a Newtonian liquid, the flow curve is linear, and viscosity is determined as a tangent of the angle to abscissa. Another diagram, corresponding to the flow diagram and commonly used for liquid characterization is dependence of viscosity from the shear rate. This diagram is referred as a viscosity curve (Figure 3.7b).

3.4.1.2 Rheological models and properties

Many liquids in practice deviate from the Newtonian flow and are no longer described by Eq. 3.6. Apparent viscosity of such non-Newtonian liquids is dependent on applied shear rate (Figure 3.7). If viscosity decreases with the shear rate, the rheological behaviour of such fluid is called pseudoplasticity or shear thinning. If viscosity increases with the shear rate, the rheological behaviour is referred as a dilatant or shear thickening. Both pseudoplastic and dilatant fluids can be characterised with a yield point (yield stress) τ_y, *i.e.* stress which has to be applied for slurry to start flowing. The presence of yield point is attributed to the initial super-structure of liquid due to a chemical-physical network of interactive forces, which requires employment of a certain stress to break this structure and cause material's flow or deformation. However, it is worth to mention, that the yield point is not the material constant since its value depends on the measuring method and on the analysis method used. The dilatant liquid will not be described here as it is the characteristic behaviour, for instance, for high solid concentrated systems which are not typical for tape casting slurries.

Presence in casting slurries of large polymeric molecules and/or anisotropic particles violates the linear dependence of shear stress from shear rate, which is distinctive for Newtonian flow. At rest, both anisotropic particles and long polymer molecules with looping molecular chains maintain irregular internal order causing sizable internal resistance against flow, *i.e.* high viscosity [106]. Under casting shear anisotropic particles orient toward a casting direction, chain-type polymeric molecules stretch, soft sphere-shaped particles deform being smaller in diameter but longer, soft agglomerates or lumps if any break-up, and all of that accelerates slurry flow, *i.e.* reduces the slurry viscosity. The decrease of viscosity with increase in shear rate was mentioned to correspond to the pseudoplastic liquids.

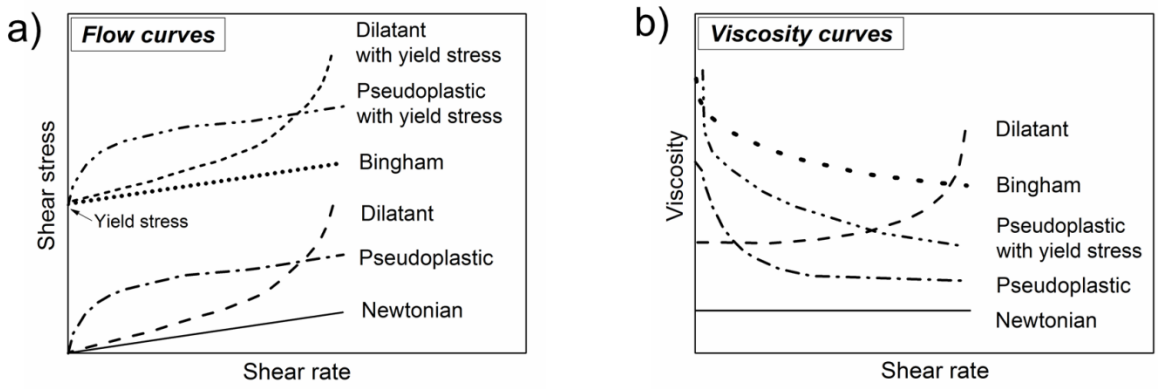

Figure 3.7. Schematic of various types of common flow behaviour presented on flow and viscosity diagrams.

Pseudoplasticity, ascribed to casting slurries due to employing long chain polymeric molecules and presence of anisotropic particles, is significantly beneficial and required for tape casting processing. At rest the viscosity of pseudoplastic slurry is high, which avoids the ceramic particles settling and preserves a homogeneous distribution of the slurry constituents in cast tape by reducing their mobility. The decrease of slurry viscosity when it passes below the casting blade enables a steady flow in shear area. After stresses are released, which is identical to moving the slurry from the blade region to free area in a drying chamber, viscosity again arises confining the uncontrollable side flow. Whereby the formed shape of the tape is retained as it was formed in the shearing region. Therefore, pseudoplasticity facilitates the maintenance and precise control of the tape shape during the casting process.

However, the same pseudoplastic behaviour challenges the control of flow field through the casting blade gap: the actual shear rate and, thereby, viscosity continuously change while holding in the tank, being sheared, and being released to the free area [37]. This subject will be considered further in Section 5.3.

In order to compare shear thinning and viscosity of different casting slurries, a number of various constitutive flow models were developed [106], [107] and the most often used are presented in Table 3.4. The flow is usually governed by the mass conservation equations, momentum and energy equations in regards of incompressible liquids and laminar flow [108], [109]. The general tendency is that most of models are solved under steady-state conditions assuming constant slurry column in reservoir for the entire casting process duration.

Table 3.4. List of rheological models and their references in articles describing flow behaviour of solvent-based slurries.

Rheological model	References
Ostwald-de-Waele model (power law)	[93], [110], [104], [111], [112], [113], [114], [115]
Bingham plastic model	[115], [116], [117], [118]
Herschel-Bulkley model	[114], [119], [120], [121]
Casson model	[122]

Ostwald-de-Waele model is probably the most widely encountered rheological model describing behaviour of non-Newtonian slurry in tape casting:

$$\tau = k\dot{\gamma}^{n} \qquad 3.7$$

then the apparent viscosity of power law slurry will be described as:

$$\eta = k\dot{\gamma}^{n-1} \qquad 3.8$$

where k is the consistency index, and n is the shear thinning constant (power law index). For shear pseudoplastic behaviour $d\eta/d\dot{\gamma} < 0$, *i.e.* the value of shear thinning constant n should be smaller than unity. Moreover, departure of shear thinning value from unity indicates how much given slurry is different from Newtonian fluid with $n = 1$. Thus, polymer melts or solutions are characterised by power law with index in the range 0.3-0.7 depending upon polymer's molecular weight or concentration. The fluids with even lower shear thinning index 0.1-0.5 are accounted for the presence of fine particles in suspensions like bentonite-in-water, kaoline-in-water, etc. [123]. In practice, for identifying the power law parameters, flow curves are plotted in log-log coordinates. Tok *et al.* [104] and Liu *et al.* [114] used power law constitutive model in analytical modelling to describe the influence of flow behaviour beneath the doctor blade on thickness of resultant green tape.

Slurries containing long polymeric chains exposed to interlinkage or bonded particles require a certain applied stress τ_y to initiate the flow [16]. These materials can be described by a Bingham model:

$$\tau = \tau_y + \eta_p\dot{\gamma} \qquad 3.9$$

or, in terms of apparent viscosity:

$$\eta = \left({}^{\tau_y}/_{\dot{\gamma}}\right) + \eta_p \qquad 3.10$$

where η_p is the viscosity limit at high shear rates also called constant plastic viscosity. Bingham model was applied by Joshi *et al.* [115] in analytical model for identification of slurries rheology impact on the thickness of the final tape. In another work, Bingham model was used for description the flow under the doctor blade and determination of the critical velocity v_c, with which carrier had to move to exceed the yielding stress [116].

A more general constitutive equation taking into account a yield point is the Herschel-Bulkley model:

$$\tau = \tau_y + k\dot{\gamma}^{n} \qquad 3.11$$

Unlike the Bingham model, Herschel-Bulkley equation provides non-linear shear stress-shear rate dependence and represents an Ostwald-de-Waele fluids but with a yield point.

Another model, describing non-Newtonian fluid system with weakly bonded particles, is Casson constitutive equation:

$$\sqrt{\tau} = \sqrt{\tau_y} + \sqrt{\eta\dot{\gamma}} \qquad 3.12$$

The assumption behind the Casson model is that suspension consists of chain-like polymeric units which control viscosity [16]. The change in applied stresses cause change in elongation of the bounded polymeric system varying viscosity with the shear rates. A generalized form for the Casson model is:

$$\eta_a^m = \eta_\infty^m + \left({}^{\tau_y}/_{\dot{\gamma}}\right)^m \qquad 3.13$$

where η_∞ is the viscosity limit when the chain-like structure is broken at a very high applied shear rates, and m is the constant indication the deviation from linearity. From the literature survey it is clearly seen that Casson model usually describes the rheological behaviour of water-based slurries [124], [125], [126].

3.4.1.3 Rotation test

The performance of rotational tests to investigate non-Newonian flow behaviour is usually divided into two categories: tests with controlled shear rate (CSR tests) and tests with controlled shear stress (CSS tests). In CSR tests the rotational speed or shear rate is preset and controlled by a rheometer [105]. This method is usually selected if the fluid shows no yield-point and if viscosity should be measured at a certain shear rate. This is the case if certain process conditions have to be simulated as it will be described in the Section 5.5. When accomplishing CSS tests, the torque or shear stress is preset and controlled by rheometer [105]. This method is applied to determine a yield point of fluids. Usually flow curves time-dependent effects are measured by CSR tests.

3.4.1.4 Time-dependent rheology: thixotropy

The rheological behaviour has to independent of pre-shearing history and shearing time. In order to eliminate the pre-shearing history and create a reproductive rheological measurements slurry is normally sheared for about 60-120 s at a very low shear rate with subsequent rheological measurements.

The time dependent behaviour, also known as a thixotropy, is a fluid characteristic usually caused by flocculated structure of slurry network and, in opposite to the pre-shearing history, it cannot be eliminated. Thixotropy is defined as misalignment between flow curve corresponding to the decrease of the viscosity at applied shear rate – “up-curve”- and measured instantaneously flow curve corresponding to a gradual recovery of the viscosity when the shear stress is removed – “down-curve”.

There are two main ways to estimate the thixotropic behaviour of fluids. First method includes sweeping the shear rate in a loop. The indication of thixotropic behaviour is when viscosity curves do not coincide when the shear rate is increased and decreased. Alternatively, another method includes instantaneous stepwise change of applied shear rate from the low values to high and again to the low shear rate values. Reproducibility of slurry viscosity for the first and third step at decreased shear rates defines non-thixotropic slurry behaviour, while the mismatch between viscosities at low shear rates attest slurry’s thixotropic behaviour. The second method also represents so-called structure-recovery test and will be in details presented in Section 5.5.

3.4.1.5 Oscillatory tests: the study of viscoelastic behaviour.

Running the oscillatory test means that upper plate of rheometer is no longer turning continuously like in rotational test, but it deflects with a sinusoidal time-function for the small angle φ in clock- and anticlock-wise directions. Oscillation is often performed at very low applied stresses and strains, normally significantly below the yield point of a sample. The tested fluid placed in between rheometer plates is thus forced in a similar sinusoidal function resulting in resisting stresses in the sample [106]. The response strain γ is measured as a function of the time. The shift of the strain response to the applied stress is termed as a delay time δ (phase shift angle, loss angle) between the preset and the resulting curve (Figure 3.8). The loss angle is specified in degrees (°) or, more rarely, in rad [105].

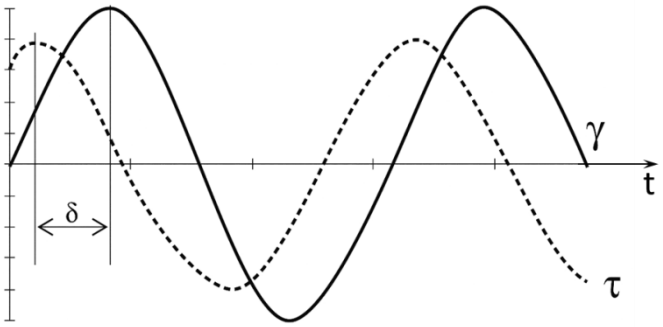

Figure 3.8. The schematic of strain (γ) response to an oscillating stress (τ) applied to a material over time t. Adapted from [105].

Depending on kind of the test, the measuring parameters of sinusoidal oscillatory shearing are complex modulus (G^*), elastic (or storage) modulus (G') and viscous (or loss) modulus (G"), phase angle (δ) and tangent of the phase angle (tan δ). The physics of the complex modulus is clear when the Hooke's law is applied:

$$G^* = \tan\frac{G'}{G''} = \tan\delta = \frac{\tau(t)}{\gamma(t)} = \frac{[Pa]}{[1]} = [Pa] \qquad 3.14$$

Phase angle together with complex modulus define a viscoelastic map differentiating elastic solids and viscous liquids (left to right) and high to low rigidity or viscosity (top to bottom) (Figure 3.9).

Viscoelastic behaviour of all materials consists both viscous and elastic portions, which sum can be illustrated by a vector diagram with G' on the x-axis and G'' on the y-axis (Figure 3.10).

$$|G^*| = \sqrt{(G')^2 + (G'')^2} \qquad 3.15$$

where the storage modulus G' measures the deformation energy stored by the sample during shearing. The lost modulus G'' measures the deformation energy used by sample during sharing and it is spent during the process of changing the material structure, *i.e.* when the sample is flowing [105]. The length of the vector G^*, being the sum of the vectors G' and G'', characterizes complete viscoelastic behaviour which is composed of elastic and viscous portions.

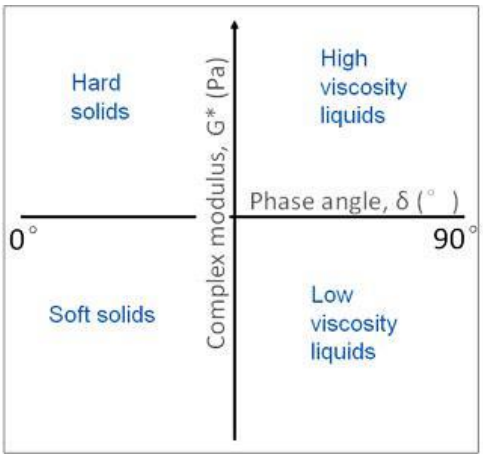

Figure 3.9. Viscoelastic map describes the viscoelastic nature of materials by defining the phase angle and complex modulus. Adapted from [127].

Alternatively to the complex modulus G^* a complex viscosity η^* can be determined:

$$\eta^* = \frac{G^*}{i\omega} = \frac{\tau_0}{\gamma_0 \omega} \qquad 3.16$$

which describes the total resistance of fluid to a dynamic shear. The complex viscosity again contains the storage viscosity η' – the elastic component, and the storage viscosity η'' - the viscous component.

Oscillatory shear testing is a term generalizing techniques that can be applied to characterize and quaintly describe the presence, rigidity and integrity of materials internal structure. The most common techniques applied for fluids are amplitude and frequency sweep tests.

The amplitude sweep (strain sweep) is oscillatory test performed at different strain amplitudes, while keeping frequency and measuring temperature constant. This test provides information about the soft-solid rigidity and yield stress of any kind of suspensions. At low amplitude values, in the so-called linear viscoelastic (LVE) range, both G'- and G''-curves display constant plateau values identifying that the fluid structure is preserved. As the strain increases, the incrementing applied stress leads to the disruption inside fluid structure. This yield process is visualised in amplitude sweep test by decrease in elasticity and rigidity.

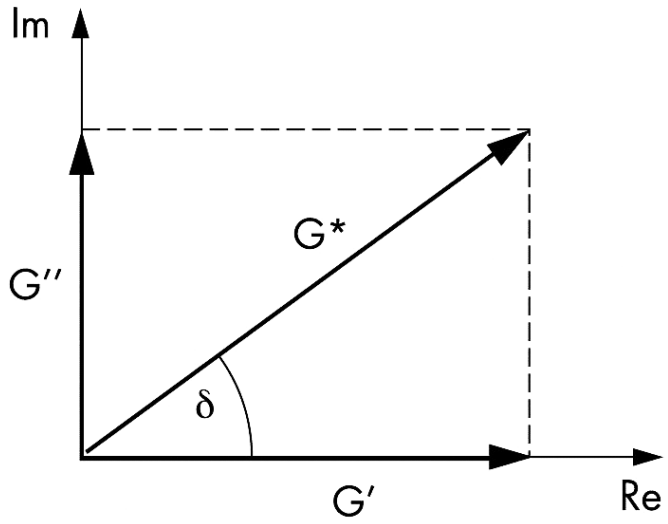

Figure 3.10. Vector diagram showing the storage modulus G', loss modulus G'' and the resulting vector of complex modulus G^*. Adapted from [105]

The viscoelastic character of fluids, applied in current work will be analysed on the example of LSM_CGO_2 (Table 3.2) slurry (Figure 3.11). Here, the slurry was analysed with a strain sweep experiment with the amplitude from 0.001% to 500% at 1 Hz frequency. The rheometer was equipped with a solvent trap to prevent evaporation of solvent during measurement and ensure consistent measurement conditions. This sample as well as all slurries used further for SBS TC exhibits a liquid character. Even higher viscous slurries with entangled polymeric molecules show this behaviour. At rest, however, slurries are usually not stable, which cause necessity to mix slurries continuously before pouring them into tape caster tank. However, for SBS TC such behaviour is also beneficial because of the ability of these fluids for self-levelling (Section 5.5.), which unifies the surface of fluidly deformable tape when slurry just passed the blade gap.

Often strain amplitude test is performed for determination at which strain values the frequency sweep test has to be done. The permissible maximum strain (deformation) for applied slurries is around 10%, so further the frequency sweep test was performed at strain 0.5%.

Frequency sweep (dynamic oscillation) is oscillatory test performed at variable frequencies, while keeping the strain and temperature at a constant value [105]. This test is used to characterize time-dependent deformation behaviour as the frequency is the inverse value of time. Thus, short-term behaviour is simulated by a rapid motion, *i.e.* at high frequencies, and the long-term behaviour by slow motion, *i.e.* at low frequencies.

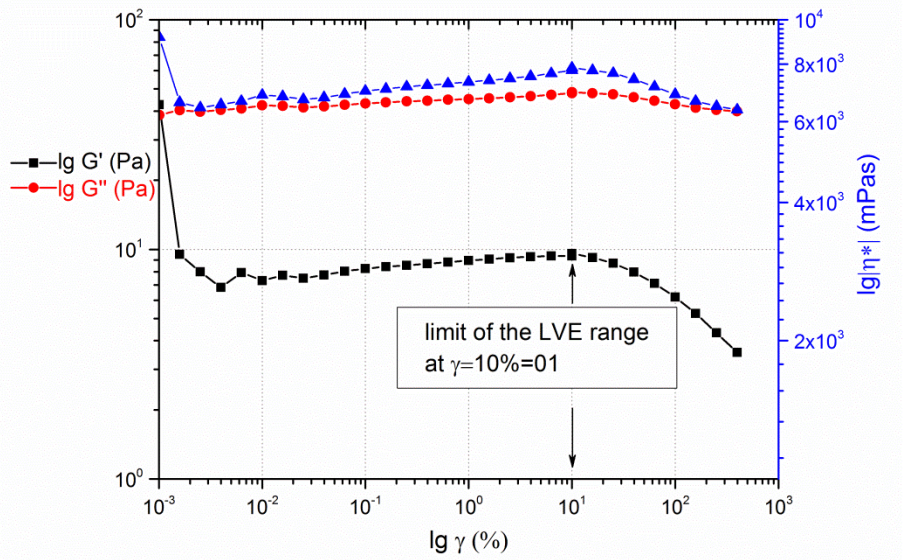

Figure 3.11. Strain amplitude sweep test of viscoelastic LSM_CGO_2 (Table 3.2) slurry at applied frequency of 1 Hz.

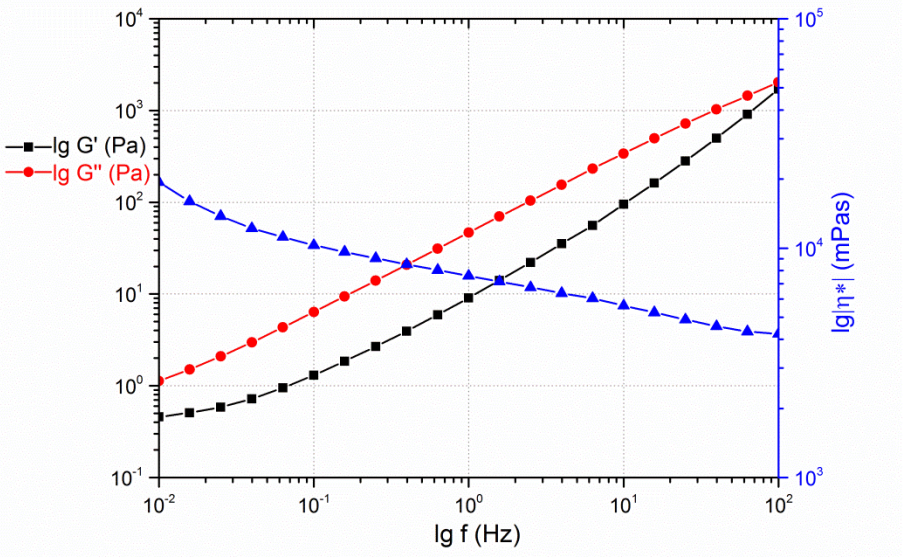

Figure 3.12. Frequency sweep test of viscoelastic LSM_CGO_2 (Table 3.2) slurry at applied strain of 0.5%.

Figure 3.12. shows the trend of storage and loss modulus together with complex viscosity obtained for slurry LSM_CGO_2 (Table 3.2) at frequency sweep test. Although the viscous component G'' of slurry dominates over the elastic component G', at high frequencies both curves are crossed. That means that in a long-term period slurry is unstable and requires a continuous mixing in order to prevent sedimentation or other inhomogeneities. Continuous rising of complex viscosity value with decrease in frequency identifies slurry as a viscoelastic with a well cross-linked structure [105].

4 Monolayer tape

Conventionally, there are a number of governing characteristics, which are measured along the ceramics manufacturing process in order to identify defects in the earliest stage and/or control the reproducibility of running experiments. Among the most important parameters to control in tape casting are thickness uniformity and flatness of the cast tapes. These parameters determine geometrical stability of tapes and homogeneity of the tape parts properties. As the main goal of the tape casting technique is production of thin functional films of a certain thickness with a high morphological reproducibility and shape stability, green tape thickness is one of the first features characterizing the quality of the green tape.

4.1 Thickness control

Tape thickness is a very complicated parameter and, at the same time, the one which requires a precise control regardless of the application and design of the tape. Some straight forward factors, which directly affect the tape thickness and whose effects are verifiable by calculations, are gap size, drying shrinkage and shrinkage happening during de-binding and sintering. The decrease in tape thickness caused by drying shrinkage is proportional to the amount of solvent in the slurry; while the amount of organics in the system and particles compaction (grain growth) processes determine the tape thickness decrease during de-binding and sintering stages.

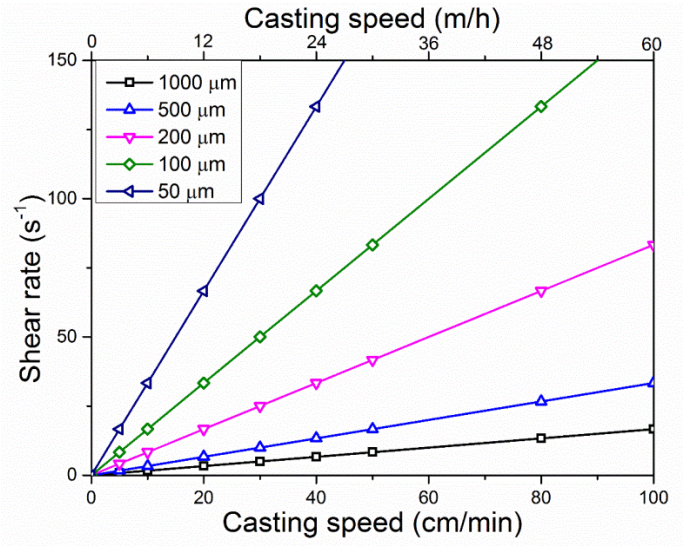

Figure 4.1. The correlation between casting speed and casting gap with a shear rate. The shear rate values were calculated as a ratio of the casting speed to the gap.

Indirect factors, however, affect the tape formation already at the shearing stage, when the slurry passes the doctor blade region. At the current stage of tape casting development three indirect factors are distinguished [37], namely: slurry viscosity, slurry level in reservoir (hydrostatic pressure behind the casting blade), and casting speed. The exact role and degree of influence of each of these factors on tape thickness formation is never clear from the experiment. The character of influence of each parameter is rather individual for each slurry and features an intricate function of the blade gap. For instance, the complicated correlation between casting speed and gap value results in a varying shear rate applied to the slurry flow during the tape

casting process (Figure 4.1). As most of the casting slurries are characterised by a shear thinning behaviour, viscosity as a function of changing shear rate also changes, yielding to the significant changes in the tape thickness.

A number of analytical and numerical models have been developed to study the correlation between mentioned parameters and tape thickness (Table 4.1.). The general concept of these works is based on description of the slurry behaviour with one of the constitutive flow model (Table 3.4.) and derivation of the equation for the thickness calculation through the analytical or numerical description of the flow.

Among a very few existent formulas governed the value of tape thickness [104], [114], [128], [129], there are two equations which are highly applicable on practice. Chou *et al.* [128] derived the equation 4.1, where they used a Newtonian flow behaviour and assumed the flow in a blade gap region
to be linear combination of pressure and drag flow. On one hand, the use of Newtonian flow model is simplified and seldom applied as for the casting fluids more complex non-Newtonian behaviour is typical. On another hand, due to use of well-defined processing parameters this formula is often used by experimenter for a rough estimation of which casting parameters have to be imposed for achieving a certain tape thickness:

$$\delta = \frac{\alpha\beta}{2}\frac{\rho}{\rho'}h\left[1+\frac{h^2\Delta P}{6\eta u L}\right] \qquad 4.1.$$

where δ is the dried tape thickness, α the correction factor for side flow, β the correction factor for weight loss during drying, ρ the fluid density, ρ' the density of the formed tape, h the casting gap, ΔP the hydrostatic pressure exerted by slurry head, η the slurry viscosity, u the casting speed,L the length of the doctor blade. Using a similar approach of completely developed flow at the exit of the casting channel, Tok *et al.* [104] derived equation for calculation tape thickness using the Ostwald de Waele power law constitutive model (Eq. 3.7):

$$\delta = \frac{\alpha\beta}{2}\frac{\rho}{\rho'}\left[\frac{1}{2}h+\frac{2(h/2)^{1/n+2}(\Delta P)^{1/n}}{L(1/n+2)k^{1/n}u}\right] \qquad 4.2.$$

where k is the consistency index, and n is the shear thinning constant (power law index).

Currently, one of the most challenging points of tape casting flow simulation is the necessity to develop a material model suitable for each specific ceramic slurry. In the current work a number of detailed experimental investigations were performed with the purpose to extract material parameters and build a numerical model. In this respect, tape casting conditions were first verified on a simple model of casting a monolayer tape before starting the work on more complicated SBS graded design of tape.

Table 4.1. List of analytical and numerical models for the flow field beyond the casting blade.

Analytical models	Numerical models
Chou *et al*., 1987 [128]	d'Halewyu *et al.*, 1990 [130]
Pitchumani *et al*., 1995 [131]	Loest *et al*., 1994 [52]
Huang *et al*., 1997 [132]	Gaskell *et al*., 1997 [133]
Tok *et al.*, 2000 [104]	Wonisch *et al*., 2011 [134]
Joshi *et al*., 2002 [115]	
Zhang *et al*., 2002 [116]	
Terrones *et al*., 2005 [135]	
Kim *et al*., 2006 [129]	

The single-blade tape caster set-up was chosen as it is the most common batch configuration of the tape caster often applied in lab scale experiments, in trial research tests and when developing a new recipes or setting up a tape casting parameters. Along with being the simplest doctor blade arrangement, the single blade configuration has not been modified for elimination of any accompanying tape casting phenomena or processes as, for instance, a double blade configuration was created to reduce the effect of the gradual pressure flow. Therefore, the single blade design preserves all the physics behind the tape casting process and is beneficial for the detailed analysis and understanding the role of each parameter in a new developing system.

This work is aimed at filing the lack of numerical and analytical solutions, where most of the currently used models are solved under steady-state conditions (Table 4.1.), investigating the tape thickness change as a function of casting speed and not considering the free surface of the slurry in the blade exit region.

The details of this work, presenting a quasi-steady state description of the casting velocity and continuously changing pressure field behind the casting blade in combination with a power law model for the fluid flow, are published in Paper V and Paper VIII.

4.1.1 Analysis

Before exploring the flow rate and modelling the tape thickness, the velocity field equation has to be developed. In regards to fluid mechanics, the slurry flow beneath the doctor blade can be described as a superposition of two velocity profiles [92]. One of the factors generating slurry velocity profile is the moving belt, which drags the slurry from the reservoir and, hence, creates a shear rate profile in a parallel channel between the stationary blade and the carrier belt. This type of flow is called Couette or drag-driven flow and its profile is given in Figure 4.2a [128]. Another velocity profile is governed by the hydrostatic pressure of the slurry column behind the casting blade with stationary boundary conditions both at the carrier and a blade surfaces. Such flow is denominated as a Poiseuille or pressure-driven flow (Figure 4.2b) [128]. In reality, velocity profile (Figure 4.2c) is affected by both drag- and pressure-driven flows and also the geometry of the doctor blade and the casting head [136].

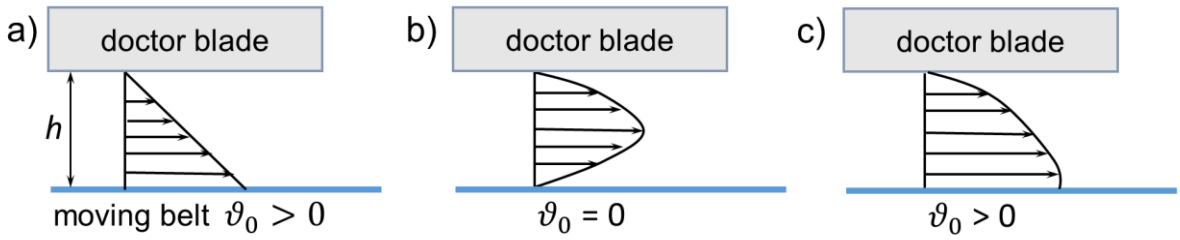

Figure 4.2. Velocity profiles for a) plane Couette flow, b) pressure flow in a parallel channel and c) a superposition of both at carrier velocity $\vartheta_0 \neq 0$.

For obtaining the high quality tapes, it is important that the resulting shear rate profile beyond the doctor blade, retained constant during the whole casting period. To achieve this in laboratory scale tape casting, a double-blade set-up usually used as it ensures a constant hydrostatic pressure in between casting and rear doctor blades. However, in the chosen single-blade set-up, continuously changing value of the hydrostatic pressure significantly affects the tape thickness consistency.

The schematic of the single-blade design, used in the current work, is presented in Figure 4.3. The thickness of the green tape δ was studied by changing the casting gap h, the velocity of the moving carrier v_0 and the height of the slurry column in tape casting reservoir H_0. The geometrical parameters of the casting head are specified by the width of the doctor blade W, the depth of the reservoir d, the inclined length of the reservoir l, and the angle of the reservoir's back wall θ.

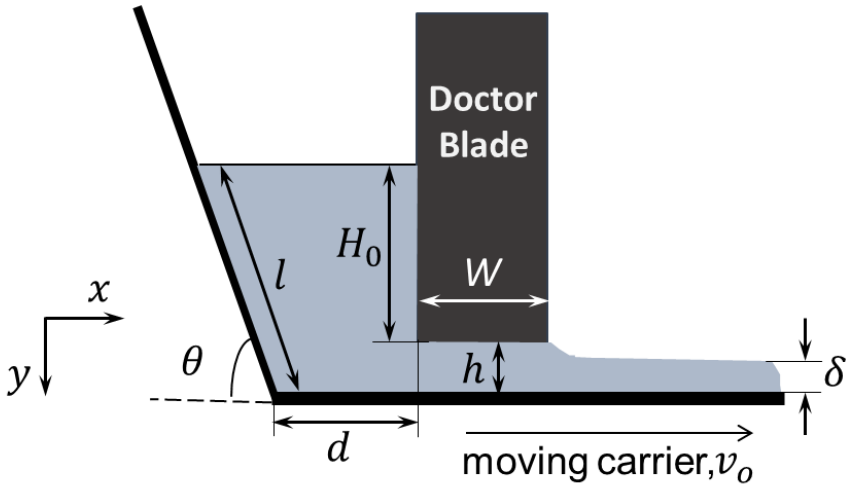

Figure 4.3. Schematic geometry of the casting head and main tape casting parameters.

The pressure gradient inside the channel is determined by the hydrostatic pressure of slurry column behind the doctor blade [116]:

$$\frac{dp}{dx} = -A_0 = -\frac{\rho g H_0}{W} \qquad 4.3.$$

where ρ is the density of the slurry, and g is the acceleration due to gravity.

Assuming an infinitely wide and long plate comparing with tape thickness and taking into consideration the momentum conservation in x direction under steady state conditions, one receive the following equation [104], [116]:

$$\frac{d\tau}{dy} = \frac{dp}{dx} \qquad 4.4.$$

From equations 4.3. and 4.4. the shear stress τ is determined as:

$$\tau = -A_0 y + A_1 \qquad 4.5.$$

where A_1 is an integration constant.

For fluid described by Oswald de Waele power law behaviour (Eq. 3.7.) the shear stress can be given as following:

$$\tau = k\left(\frac{\partial v}{\partial y}\right)^n \qquad 4.6.$$

where it has been considered that the only velocity defining the applied shear stress is the velocity v in the x direction.

Combining equations 4.5. and 4.6. and integrating along the casting gap h, we receive:

$$\int_0^h (-A_0 y + A_1)\, dy = \int_0^h k \left(\frac{\partial v}{\partial y}\right)^n dy \qquad 4.7.$$

and taking into account that k and n are constants for the certain slurry used, we get

$$v = \left(-\frac{A_0}{k}\right)^{1/n} \cdot \frac{y^{\frac{1}{n}+1}}{\frac{1}{n}+1} + \left(\frac{A_1}{k}\right)^{\frac{1}{n}} \cdot y + A_2 \qquad (0 < y < h) \qquad 4.8.$$

where A_2 is another integration constant.

The boundary conditions for equation 4.8. in the casting gap region are:

$$\begin{cases} v(0) = 0 \\ v(h) = v_0 \end{cases} \qquad 4.9.$$

Implementing these boundary conditions 4.9. into equation 4.8. we obtain:

$$\begin{cases} 0 = \frac{\psi}{\chi} A_1^{\chi} + A_2 \\ u_0 = \frac{\psi}{\chi}(-A_0 h + A_1)^{\chi} + A_2 \end{cases} \qquad 4.10.$$

where

$$\chi = \frac{1}{n} + 1 \qquad 4.11.$$

and

$$\psi = -\frac{1}{A_0 k^{\,1/n}} \qquad 4.12.$$

The equations 4.10. can be re-written to

$$\begin{cases} A_2 = -\frac{\psi}{\chi} A_1^{\chi} \\ v_0 = \frac{\psi}{\chi}\left[(-A_0 h + A_1)^{\chi} + A_1^{\chi}\right] \end{cases} \qquad 4.13.$$

The integration constant A_1 can be determined by using the Newton-Raphson method. For that, the following equation has to be solved numerically:

$$F(A_1) = \frac{\psi}{\chi}\left[(-A_0 h + A_1)^{\chi} + A_1^{\chi}\right] - v_0 = 0 \qquad 4.14.$$

after that, the integration constant A_2 can be found from the upper equation in the system 4.13.

By applying mass conservation, the wet thickness of the tape δ_w can be determined by integrating u over the gap height h and dividing by the tape velocity:

$$\delta_w = \frac{1}{v_0}\int_0^h v \mathrm{d}y = \frac{-\left[(-A_0 h + A_1)^{\chi+1} - A_1^{\chi+1}\right]}{v_0 A_0 \psi \chi(\chi+1)} + A_2 h \qquad 4.15.$$

Now, the modification of standard steady state model [104], [116], [128], [129], [131] is needed in order to make it dependent on the gradually decreasing slurry level in the casting reservoir, *i.e.* to develop a quasi-steady state model. To achieve that, the continuity equation is applied with assumptions that the slurry used is incompressible, *i.e.* the volume of the slurry which drops down in reservoir is equal to the volume of the slurry which is discharged on the moving carrier out from the blade region to the free space. Supposing that for the short period Δt, the height of the slurry decreases from the initial level H_0 to the level H_1, then the changed volume which is discharged to the free space will be equal to:

$$\Delta S_1 = \left[d + \frac{1}{2} l \cos\theta \left(1 + \frac{H_1 + h}{H_0 + h}\right)\right](H_0 - H_1) \qquad 4.16.$$

This area is discharged from the doctor blade region with the constant here casting velocity of v_0 on the distance of $v_0 \times \Delta t$, hence, this slurry volume is equal to $v_0 \times \Delta t \times \delta_1$. The next step will include the decrease of slurry volume in reservoir from the level H_1 on the new area in the free space ΔS_2, found from the equation 4.16., and so forth.

There are few assumptions in this model. First, in the tape casting when the slurry is discharging from the doctor blade region, it flows also in a transverse directions (here, in the z direction) which is so-called as a side flow. However, since the cast tape is very wide in the z direction compared to its thickness, the side flow is relatively small and rather negligible.

Due to luck of the tool for measuring wet thickness of the cast tape, experimental verification of the model is possible by evaluation the tape thickness just after drying stage. After drying the tape thickness is reduced due to solvent loss. Both side flow and evaporation are taken into account by Chou *et al.* [128] (Eq. 4.1) in the following equation:

$$\delta = \frac{\alpha\beta\rho}{\rho'} \cdot \delta_w \qquad 4.17.$$

4.1.2 Experimental procedure

For verification of the proposed quasi-steady state model, LSM slurry with the composition (Table 3.2) and the subsequent steps of slurry preparation described in Section 0, was used. The mean particles size and slurry density were 2.73 µm and 3.52 g/cm^3, respectively. Experiments were carried out using a single-blade of 6.4 mm width (W) and a casting head with d=8.8 cm and θ=45°.

The doctor blade gap was set using an etalon measuring paddle and a micrometer gauge on a tape caster head with an accuracy of 0.01 mm. The thickness of the tapes was metered every 10 cm along the tape length after tapes dried for five days in a drying chamber ventilated by the airflow.

Table 4.2. Set-up of experimental parameters.

Parameter	Case 1	Case 2	Case 3
v_0, mm/s	3.67 10 14.67	3.67	3.67
h, mm	1	0.25 0.4 1	0.4
H_0, mm	1.2	10.6	3.1 6.6 20.8

The tape thickness δ was studied as a function of the casting velocity u, doctor blade height h and the slurry level in reservoir H_0. As the influence of one variable was studied, the other variables were kept constant (Table 4.2). The first set of the experiments *Case 1* included tape casting of a series tapes with a three various casting velocities v_0, but the same amount of LSM slurry and the same casting gap. In the second set of

experiments *Case 2* the casting gap h varied, while slurry load and casting velocity were remained. Then, in the *Case 3* tapes were cast with a constant casting gap and velocity and varied slurry load in reservoir H_0. The interplay between casting speed, gap and slurry level in reservoir was directed on clear understanding of the correlation between drag- and pressure-driven forces and a casting parameters on the side flow amount.

The thickness values of the green tapes were collected about 2 cm from the edges of the tapes on both sides every 10 cm along the length using a circle flat dual point digital micrometer of 15 mm diameter.

4.1.3 Results and discussion

The rheological behaviour of the LSM slurry agrees well with the Ostwald de Waele power law (Figure 4.4.) with the correlation between the shear stress and the shear rate as follows:

$$\tau = 3.31 \cdot (\partial u/\partial y)^{0.90} \qquad 4.18.$$

where the consistency index k is equal to 3.31 and the shear thinning constant n which is the amount of deviation from a Newtonian fluid is equal to 0.90 quite close to the unit typical for the Newtonian flow.

The side flow constant α was calculated comparing the doctor blade width and the found values lay in the interval 0.8<α<0.9. The drying weight loss parameter β was obtained by the additional experiment when the tape was cast manually on a laser profilometer support. Wet thickness was measured immediately after the casting and further compared with the thickness of the dried tape. As a result, the obtained β fell within the range between 0.58 and 0.64.

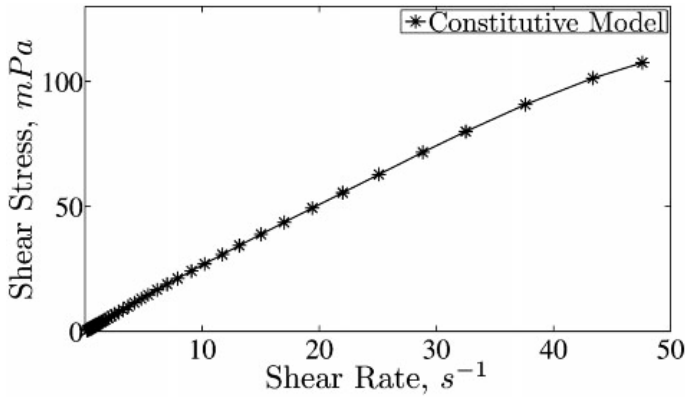

Figure 4.4. Rheological behaviour of an actual LSM slurry and the Ostwald de Waele power law simulation.

4.1.3.1 Effect of the casting velocity

Figure 4.5a shows the tape thickness obtained experimentally as the function of casting velocity, compared to the numerically obtained data from the steady state and quasi-steady state models. The thickness can be seen to decrease hyperbolically with increasing casting velocity, which is also evident from equation 4.15. In previous works [111], [128], [131] it was shown that the influence of the pressure flow decrease when tape casting is enhanced by increasing velocity of the carrier support, *i.e.* when the drag flow increases.

Figure 4.5b illustrates velocity profiles of slurry flow below the doctor blade for three different casting velocities. For higher carrier velocities, the profile approaches a linear distribution which corresponds to the pure drag-driven flow and absence of any pressure-driven flow. When the casting velocity decreases, the role of the pressure becomes significant and starts to perturb the linear Couette flow, in this specific case causing a

maximum velocity at around 0.25 mm above the moving carrier. This flow is characterised as a combination of the Couette and Poiseuille flows and describes the dependence of the velocity profile, and, hence, the thickness of the cast tape, on the slurry level in the reservoir. This tendency of increased influence of the pressure-driven flow as the casting process slows down was also proved by analytical flow models developed by Kim *et al.* [129].

Required for tape casting shear thinning behaviour of fluid also explains the tendency of tape thickness reduction when the casting process accelerates. Increase in the casting velocity applies higher shear rates to slurries flow, the slurry viscosity subsequently decreases which means that there is less resistance for slurry to flow aside and form a thinner tape. The side flow and the corresponding slurry flow behaviour is described in Section 5.5.

The results shown in Figure 4.5a demonstrate that the quasi-steady state model is in better agreement with experimental data compared to the steady state models proposed in literature [128], [129]. This is because the developed quasi-steady state model considers continuous decrease of the slurry level in reservoir typical for a real tape casting process. It should be noted, that the variation of the slurry load in the reservoir will lead to the change in A_0 and, consequently, change in A_1 and A_2, which can be calculated numerically.

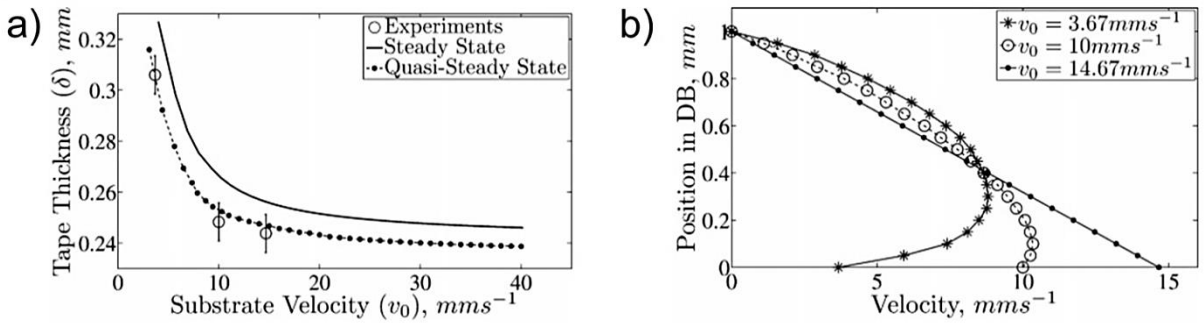

Figure 4.5. a) Effect of the casting velocity on tape thickness and b) average velocity profiles of slurry sheared under the doctor blade with different carrier velocities.

4.1.3.2 Effect of the casting gap

The expected tendency of increase in the tape thickness with a higher doctor blade gap is shown in Figure 4.6. However, the slopes of the curves differ significantly. The thickness of tapes cast at high casting speeds are proportional to the gaps used, but at low casting speeds the thickness of the tapes cast with a higher gap of 1 mm is significantly larger comparing with the thickness of tape cast with a lower gap of 0.4 mm. As it was mentioned earlier, at high casting speeds the flow is formed solely by a drag-driven flow with a linear behaviour of slurry velocity along the gap height, while at low casting speeds the flow is defined both by drag- and continuously changing pressure-driven flow. Using a high doctor blade gap means that more material is passed through the blade region and it is easier for pressure behind the blade to push more slurry out of the reservoir, in most cases exceeding the gap height. At low casting gaps, this post-doctor blade exceess is proportionally smaller and hampered for high viscous slurries.

In the experiments focused on analysis of the blade gap effect, the proposed quasi-steady state model also shows a better agreement with experimental data comparing to the steady state model. The higher deviation between data was observed at larger blade gaps, which can result from the fact that for all casting

gaps the side flow was assumed to be constant (Eq. 4.17.). However, the side flow effect, as it will be shown in Section 5.5., is affected by the gap value.

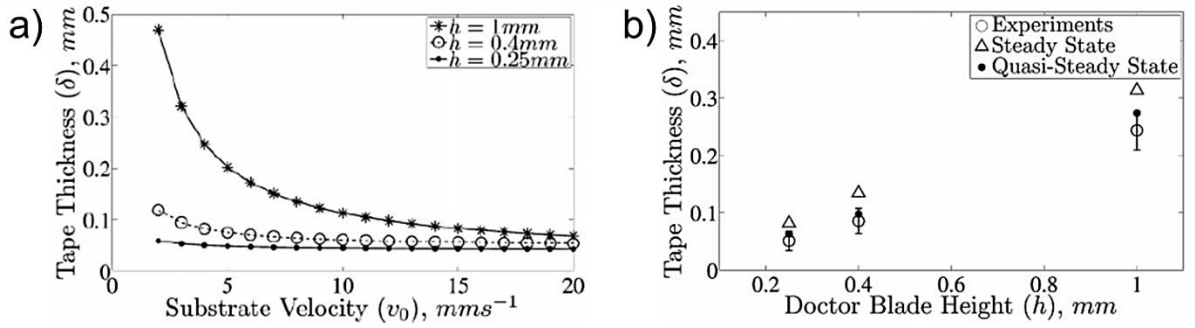

Figure 4.6. a) Effect of the casting gap on tape thickness and b) comparison of proposed quasi-steady state model with steady state model and experimental results of tape cast with a velocity of 3.67 mm/s.

4.1.3.3 Effect of the slurry load

In the experiments described above, the data were given at initial slurry load H_0, which corresponds to the slurry level in the reservoir at the beginning of the casting process. In this study, since the slurry load in reservoir is the main studied parameter, the data from the steady state model will be presented at initial slurry load H_0 as well as at some average slurry fill in reservoir H_m, which supposed to correspond to the fill of reservoir in the middle of the casting process. The value H_m is the average between the initial slurry height in reservoir H_0 and the level of reservoir equal to the gap height, *i.e.* the last point where the fluid is experienced the hydrostatic pressure in reservoir. It is assumed that the decrease in the slurry level in the reservoir is linear as a function of time, which is different from the real parabolic trend (will be discussed in details in Section 4.2).

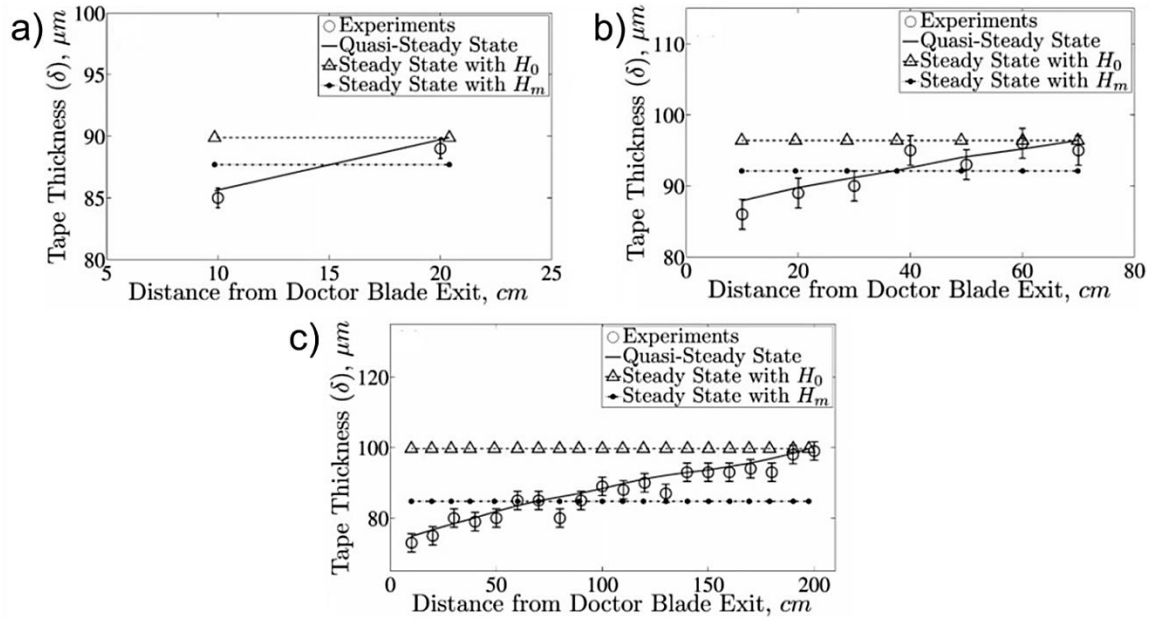

Figure 4.7. Comparison of results of quasi-steady state modelling and steady state modelling at H_0 and H_m with experimental tape casting, performed with a slurry load a) $H_0 = 3.1\,mm$, b) $H_0 = 6.6\,mm$, and c) $H_0 = 20.8\,mm$.

With an increase in the slurry load, the length of the tape and grows (Figure 4.7). This trend is expected as the higher the slurry load is, the larger the volume of slurry to be cast in the process will be.

There is a general tendency of decrease in the tape thickness from the beginning to the end of the process (from the right side of the plot to the left side of the plot corresponding to the end of the process) for the presented slurry loads of 3.1 mm, 6.6 mm, and 20.8 mm (Figure 4.7). This is because the slurry flow is driven by the sum of drag- and pressure- driven flows at the beginning of the casting process, while the effect of the pressure continuously decreases during the process, thus, decreasing the volume of slurry passing the blade region per time unit. Moreover, the higher the level of the slurry load, the thicker the tapes are obtained. This effect is also accounted for the higher hydrostatic pressure behind the casting blade when more slurry is filled into reservoir (Eq. 4.3). The trend of gradual decrease of the tape thickness during the casting process cannot be detected by the steady state model neither for slurry height H_0 nor for slurry height H_m. The quasi-steady state model, in turn, repeats data from the experiment with a very high accuracy. The minor differences between the experiments and the proposed model can be attributed to neglecting the influence of the side flow in the model, which will be studied in details in Section 5.5).

In order to understand the effect of the slurry height in the reservoir on the tape thickness clearly, the velocity profile below the doctor blade was analysed in detail for one of the test in the *Case 3* (Table 4.2.): $H_0 = 20.8\,mm$, $h = 0.4\,mm$ and $v_0 = 3.67\,mm/s$. As can be seen from Figure 4.8a, the decrease in the hydrostatic pressure behind the casting blade caused by decrease of the slurry load in the reservoir cause a change in the velocity profile and the area under the corresponding curves. Earlier, Kim *et al.* showed [129] that the area formed by velocity curves behind the doctor blade is proportional to the "velocity profile area" out of the blade (Figure 4.8b). Therefore, the decrease of hydrostatic pressure behind the blade is shown [129] to decrease the resultant thickness of the tape.

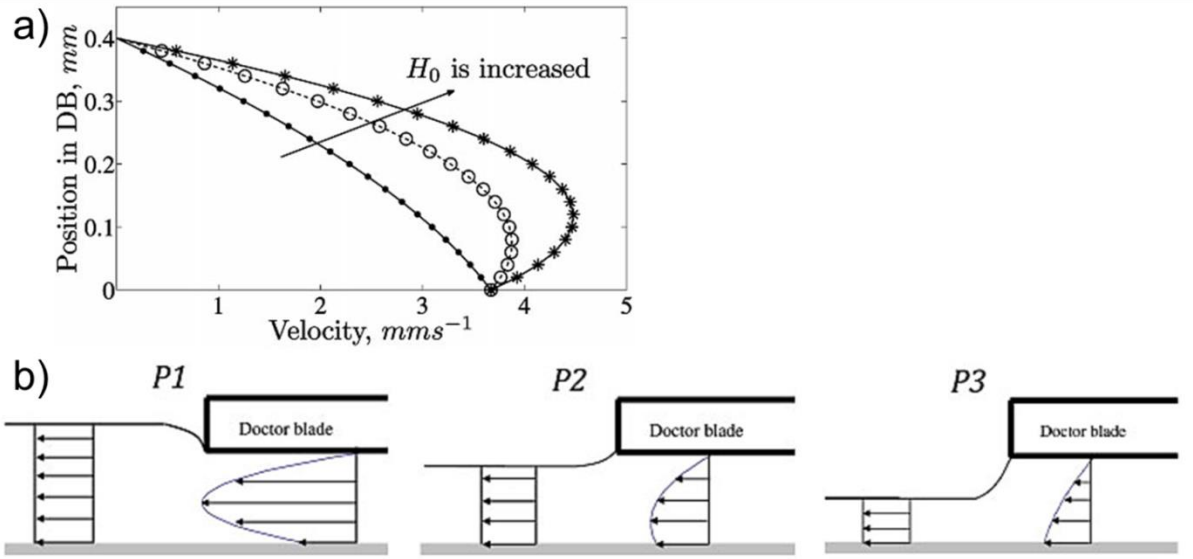

Figure 4.8. a) Effect of variation in slurry load on velocity profile below the doctor blade region and b) schematic illustration of effect of the increasing pressure behind the casting blade on tape thickness (P1>P2>P3) [129].

4.1.4 Conclusion

The influence of the main tape casting parameters, namely, casting speed, doctor blade gap and the slurry load in the reservoir, on the tape thickness consistency were studied both experimentally and numerically. The proposed quasi-steady state model describes the flow behaviour of non-Newtonian fluids and, unlike steady state models, includes the decrease of the slurry level in the reservoir. A good agreement has been found between experiment and a quasi-steady state model.

The cumulative character of the constant drag-driven flow (Couette flow) and continuously decreasing along the casting process pressure-driven flow (Poiseuille flow) was shown to determine the thickness of the produced tape. It has been found that the tape thickness decreases with increase in the casting velocity as the Poiseuille flow is not dominant as for the case with a low casting velocity. The influence of the pressure-driven flow increases with the casting gap, because the high blade gap let a larger amount of slurry a time to pass by the blade region. Thick tapes formed due to larger casting gap tend to have inherent big variations in tape thicknesses as the process progresses; thin tapes cast with a small gap, in turn, are very sensitive to the exact adjustment of the gap over the entire tape width. Moreover, by increasing the slurry load in the reservoir, differences in thickness at the beginning and end of the tape arises. This is due to increased influence of the pressure-driven flow, which changes the velocity profile behind the doctor blade.

Although the presented quasi-steady state model has minor inaccuracies due to the assumption of the same side flow used for different experiments, it describes the experimental results more precise than steady state models found in literature. Despite the fact, that the LSM slurry, used in this experiment, has a slight difference from the Newtonian fluid ($n = 0.90$), the model contains all parameters that influence the process and it has flexibility to describe behaviour of non-Newtonian power law fluids.

4.2 Thickness control modes. Manufacturing strategies.

The developed quasi-steady state model investigates flow behaviour using a single-blade configuration, which is applied on a regular basis in a batch-scale tape casting. However, the aforementioned study elucidated and proved that the main reason of tape thickness inhomogeneity is the compilation of the slurry flow formed by (i) intentionally fixed steady motion of the carrier, which drags the slurry from reservoir, and (ii) gradually decreasing pressure behind the casting blade, which by pushing the slurry from reservoir under gravity forces also participates in slurry flow formation. The continuous decrease of slurry pressure in the casting reservoir results in thinning of the tape throughout the casting process. This processing issue is well known in literature [111], [115] and a number of engineering solutions and casting modes have been proposed in order to achieve constant tape thickness. Some of those methods, however, were not accustomed in tape casting practice because of the complexity of the required tape casting set-ups or demands to slurries, which are to be used. For instance, the installation of a free-riding roller in the drying chamber [137] with the purpose to redistribute mass of fluidly deformable tape in order to achieve flat homogenous tape surface was not widely applied because of the accompanying risk of changing the microstructure of the film.

The strategy of the most applicable solutions relies on a complete elimination or partial balancing of impact of the hydrostatic pressure during the flow formation and not in a post-casting processes like in [137]. The typical lab-scale solution is to use a double-blade configuration. The rear blade creates an extra pool, which is assumed to control the hydrostatic pressure drop behind the casting blade more accurately. Runk and

Andrejco (1975) were the first to study the influence of the differences between gap variation on the thickness of the formed tape [138]. They found that tape with the smallest thickness tolerance was obtained when both blades were mounted at exactly the same height.

The industrial finding for a pressure control differs from the lab-scale solution mainly because of the higher volume of slurry used. It solves the problem by keeping the same level of slurry in a single blade casting head by continuously pumping slurry into the reservoir. The reason of irrelevance of this method in lab-scale tape casting is accounted for a large loss of slurry required for adjustment of pumping and casting speeds as well as outage of slurry in a pumping supplying units like tubes.

Another novel casting mode for keeping tape thickness constant was created as a result of the work mentioned in Section 4.1. (Paper V and Paper VIII). This novel method also includes modification of the flow rather than correcting the tape thickness after tape casting completed. The concept of this method relies on applying two revealed regularities: (i) at the beginning of the casting process, the tape is usually thicker because of the cumulative effect of shear-driven and pressure-driven flow (Section 4.1.3.3); (ii) tape thinning with increase in casting speed (Section 4.1.3.1). Thus, the novel method proposed here implies compensating of the hydrostatic pressure decrease by a gradual decrease in a casting speed.

In order to distinguish which of the described tape casting modes is preferable to form tape of even thickness and, consequently, which one is to be chosen for future application in an advanced SBS TC, all four modes were compared in a series of experiments. The thickness of green tape, cast on a single blade set-up (SB) was taken as a reference and correlated with results of thickness when tape was cast using the double-blade setup (DB), continuously supplying slurry into reservoir by a pump system (PS), and by applying a new developed speed change (SC) program. Hence, this study focuses on finding the most adequate casting conditions and a process workflow to guide the experimenters in choosing the casting mode satisfying application needs. The details of this analysis are presented in Paper III.

4.2.1 Experimental procedure

The experiments were performed using LSM and LSM_CGO_4 (Table 3.2) slurries to ensure that obtained regularities are applicable to slurries of various composition of similar viscosity though. The slurries were prepared according to processing steps described in Section 0.

The apparent viscosity η measurements were conducted with pre-shearing and reversing increase of shear rate up to 50 s^{-1} using a cone-plate system (angle 1°) at 21 °C (MCR 301, Anton Paar GmbH, Austria). A solvent trap was used to minimise the evaporation of the organic solvent during the rheological measurements.

Single-blade tape casting (SB) was taken as a referring test. The precise description of the casting head set is described in details in Section 4.1.2.

In double-blade tape casting (DB) the distance between blades were 20 mm, and the width and design of casting blades were identical to one, used in SB tape casting. According to data found in literature [116], [136], the gap of rear doctor blade was chosen to be at 1.2 mm height, and the front casting gap was fixed at 1 mm height.

The single blade casting unit, which was identical to those used in the SB series of experiments, was applied in tape casting with use of a pump system (PS). Hence, the casting gap was also adjusted on height of 1 mm. the differential pump system and plastic tubes with internal diameter of 18 mm were set to pump slurry from polyethylene bottles.

For the speed change (SC) mode, invented during this PhD project, setting the sequence and value of casting speeds were required. This was accomplished, first, by re-calculation of the mass conservation and trend of LSM tape thinning with an increase in casting speed (data from Section 4.1.3.1.). Based on preliminary re-calculated program of speed change provided from the modelling work, the regularity of changing casting speed and values of casting speeds were corrected after a number of preliminary experiments. After testing, the speed change program (Figure 4.9) was successfully exported to the process control machine and implemented for tape casting with further thickness analysis.

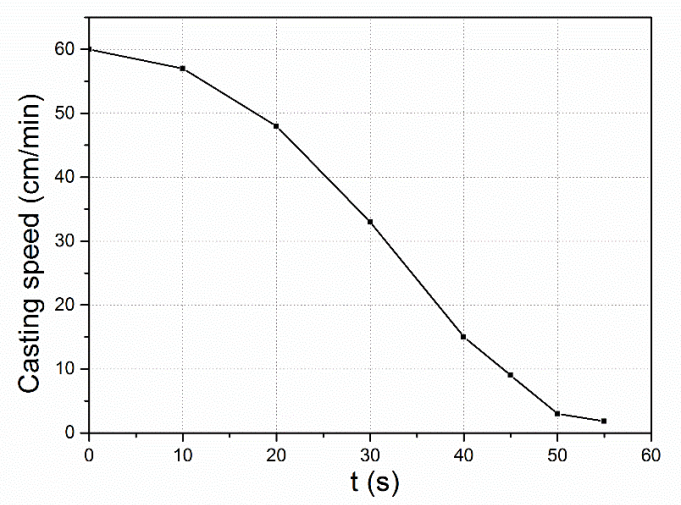

Figure 4.9. Casting program exported to the tape caster machine for improving the constancy of the dried tape thickness by continuous change of the casting speed.

SB, DB and PS tape casting experiments were accomplished with a casting speed of 30 cm/min. The initial slurry load in the reservoir H_0 was about 25±3 mm. The thickness values of the green tapes were measured about 2 cm from the edges of the tape on both sides of the tapes, every 10 cm along the length using a 15 mm diameter circle flat dual point digital micrometer.

The ideal way to control and monitor the slurry level in the reservoir is usually accomplished by using a sensor (ultrasonic, photonic, air or capacitance), whereas the ideal way to justify the impact of the shear process on tape formation would be to measure the thickness of the wet tape right after the blade region by using, for example, a γ-ray back-scatter apparatus. Due to lack of this equipment in our laboratory, however, the slurry level in reservoir was governed by the mark in the tank and instead of controlling a wet thickness, dry thickness was analysed with the assumption that drying process was uniform along the tape length. In order to ensure that the flow starts with the move of the Mylar carrier, the casting gap was occluded by a Duct adhesive tape. This guarantees the high accuracy of experimental tape casting in regards of modelling simulations by preventing instantaneous run of slurry through the gap before driving forces are applied.

4.2.2 Results and discussion

Figure 4.10 shows that both LSM and LSM_CGO_4 slurries are characterised with a shear thinning behaviour with extremely low yield stresses (inset in Figure 4.10), which is required for tape casting. Therefore, the flow behaviour of the slurries can be described by the Ostwald-de Waele power law equation 3.7. Due to thixotropy, viscosity curves for both LSM and LSM_CGO_4 slurries showed individual hysteresis loops. The

rheological behaviour and power law constitutive equation fit were chosen to be described by the reverse viscosity curves as they characterize the re-built viscosity. Fitting the experimental data of Figure 4.10 to power law constitutive equation 3.7, relatively high values of the correlation coefficient R^2 were obtained (Table 4.3) which demonstrates a good compatibility of slurry fluid behaviour with the Ostwald de Waele model. The corresponding consistency indexes k and shear thinning constants n for LSM and LSM_CGO slurries are given in Table 4.3.

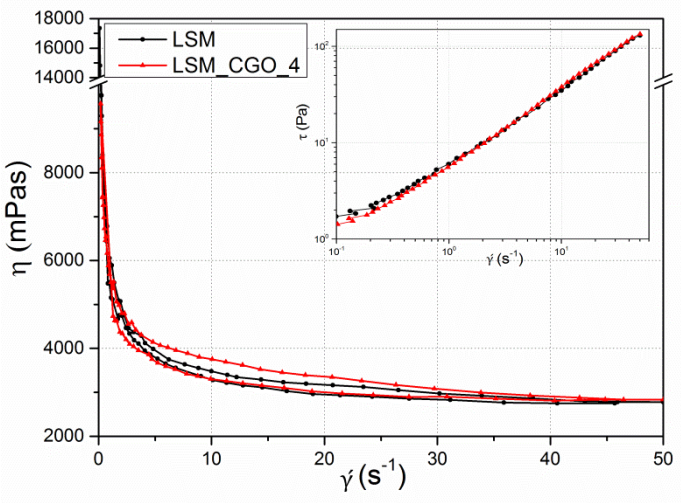

Figure 4.10. Viscosity curves and flow curves (in the inset) of LSM and LSM_CGO_4 slurries.

Table 4.3. Ostwald-de Waele power law model's fitting parameters and a correlation coefficient R^2.

	k	n	R^2
LSM	6.63(2)	0.73(6)	0.994
LSM_CGO_4	6.19(4)	0.77(7)	0.996

Rheological behaviour of LSM and LSM_CGO_4 slurries were described by a power law equation in order to estimate the theoretical tape thickness (Eq. 4.2) [104], which would be formed if the casting flow was formed by a superposition of pressure- and drag-driven forces or when flow is generated by a pure drag-driven flow.

Figure 4.11. depicts thicknesses of LSM and LSM_CGO_4 slurries, produced by four different casting modes. Position of curves at zero distance from the doctor blade exit corresponds to ends of tapes formulated last, *i.e.* when there was almost no slurry in reservoir. Another end of the curves, further referred as the beginning of the tape, was formulated at the beginning of the process, *i.e.* when the casting reservoir was filled by slurry.

Both LSM and LSM_CGO_4 slurries show the similar tendencies for all the tested casting modes. However, the thicknesses of the dried tapes produced by SB and SC modes are slightly different for the LSM and LSM_CGO_4 slurries (Figure 4.11). Among feasible reasons for this distinction in dried thicknesses can be either difference in shear rate profiles or difference in drying kinetics of the LSM and LSM_CGO_4 slurries during the SB and SC tape casting, which leads to various packing in green tapes. Another reason for the differences in tape

thickness between the LSM and LSM_CGO_4 slurries can be their minor mismatches in viscosity curves which might affect the shear rate profile and a side flow, resulting in different dried thickness.

Tapes are also shown to have a slightly different length because of a minor uncertainty in the initial slurry load in the reservoir. Since there was no an automatic control of slurry filling at the reservoir, the slurry load was controlled manually, the difference in resultant length of slurry was predictable and permissible. In order to ensure that the thicknesses of the tapes are comparable to having the same slurry level in tape caster, the curves correlated to tape thickness were aligned by the zero position, *i.e.* when the reservoir was definitely empty in all the tested casting modes.

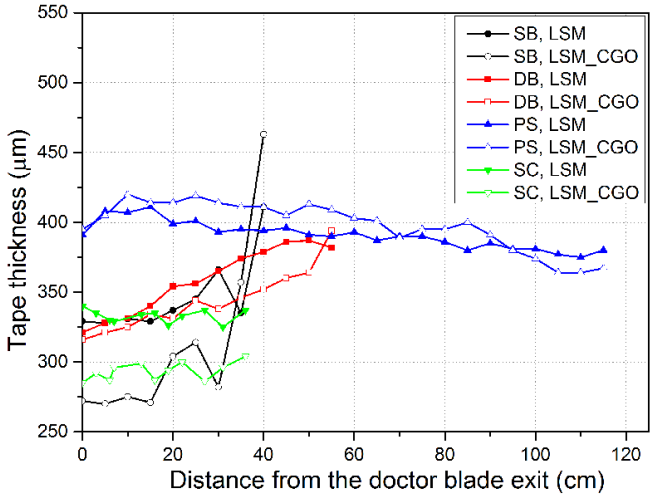

Figure 4.11. Thickness deviation of tapes cast using the single-blade (SB), double-blade (DB), single blade and pump system (PS), single-blade and a program of casting speed change (SC). The estimated error in tape thickness measurement is 15 µm.

The ideal condition providing the most uniform thickness across the entire tape length is when the actual slurry flow rate is equal to the carrier flow rate, *i.e.* when the flow is determined just by the first term in equation 4.2. or when the actual slurry flow is constant for the whole duration of the casting process, *i.e.* when the flow speed is determined by the superposition of both terms in equation 4.2. which is constant during the whole casting process.

The second concept is realized in industrial application by continuously pumping slurry into the tank. The limitation of this method is that the viscosity of slurries has to be low enough to prevent clogging and ensure homogeneous flow in tubes supplying slurry to the reservoir. Slight thickness changes of 7 and 9 % for the LSM and LSM_CGO_4 slurries, respectively, were a result of adjusting the casting parameters and pumping speeds. Depending on the chosen slurry level in reservoir, which is analogue to the hydrostatic pressure, the wet thickness might be even higher than the casting gap. In that case the slurry experiences so-called “welling” [37] also mentioned in literature and adapted here as a “swelling” phenomenon [136]. Swelling occurs when the hydrostatic pressure pushes a large volume of slurry under the doctor blade so that the slurry exceeds the gap level. Swelling is normally determined by the height of the casting gap, polymer content in the slurry, slurry viscosity and casting speed. An indirect method of measuring swelling is by comparing the thickness of tape obtained by a PS method and the stable part of a tape obtained by SB method. For instance, for LSM slurry cast

with 30 cm/min speed and maintaining a slurry level in reservoir at 22 mm, the swelling extent is found to be 70-80 µm (Figure 4.11). The direct method of measuring the swelling level is measuring the slurry trace on the side of the blade facing the drying area. The LSM slurry rise was 140-150 µm, which is higher than the values obtained from the analysis of the thickness curves in Figure 4.11.

An alternative method to minimise the influence of the hydrostatic pressure and maintain the same slurry level behind the casting blade is the DB approach. Tape thickness formed by DB tape casting was on average 10% smoother comparing to the SB method. Nevertheless, the 20 % thickness gradient across the whole tape length was presumably because the gap under the rear blade was too high to keep constant the hydrostatic pressure in relief reservoir. Moreover, inconsistence in tape thickness can be also caused by swelling as it was proven [136] to be typical for DB tape casting with a large (over 1mm) casting gap. Despite careful adjustment of gaps values, the final tape thickness showed a smoothly decrease toward the end of the tape, both in the LSM and LSM_CGO_4 tapes. However, further optimisation on the adjustment of the gaps in the double blade setup was discontinued due to presence of a vortex flow in the relief reservoir, which was proved numerically [134] and experimentally [139]. Later, Roosen *et al.* [136] found that vortex originates from the velocity gradient: between two blades the shearing velocities are much lower than velocities under blades. The vortex flow affects the rheological behaviour of the slurry, making a shearing flow during casting uncontrollable which is undesirable for the processing technique.

In the newly implemented technique SC, tape thickness was prescribed by a change in the casting speed u due to decrease in the hydrostatic pressure ΔP in the casting head. As a result, the thickness tolerance stayed within 5%, identifying the SC approach as the most appropriate tool for processing with high precision thickness control. Achieved thickness values of LSM and LSM_CGO_4 tapes are in concert with the thickness values of tape, produced by SB tape casting, exactly as the framework of the speed change program was settled and optimised. Moreover, the SC approach was shown to form the smoothest dried tapes compared to other casting modes. However, the SC method should be used bearing in mind that if the casting slurry is unstable or if it contains elongated particles, the speed fluxions during casting process is undesired as it drastically affects the applied shear rates and the resulting microstructure of the tape.

Based on the conducted studies, the novel casting mode of continuous speed change showed to form the most smooth tape surface, but from the casting experience we can expect that use of SC mode in systems containing poreformer and/or elongated powder will originate significant instabilities in morphology and/or porosity along the green tape. The SB approach was seen to be preferential for a small-scale co-casting as the thickness tolerance is within 10 % if the first 10 mm are not taken into account and the slurry flow is better described and analysed in literature compared to the DB mode, where the velocity gradient within the casting unit was proven to generate uncontrolled slurry vortices. PS mode would be beneficial for study an adjacent tape casting in large scale but this is out of the scope of the current study.

4.2.3 Conclusion

The newly established mode of tape casting was shown to ensure formation of smooth green tapes with a high consistency of tape thickness. Determination of the casting program is individual for each slurry formulation; but it is easy to build the program if the kinetics of the slurry reduction with a casting time is known. The proposed method of changing the casting speed has shown the best results among other casting modes with regard to the tape thickness constancy exhibiting a thickness tolerance of less than 5%.

The high accuracy and constancy of LSM and LSM_CGO_4 tapes formed by pumping the slurry into the tape casting reservoir had a limitation of how viscous slurry can be pumped without creating clogs and providing a uniform fluid flow inside the polyethylene tubes used in pumping system. This method, however, is highly recommended if a large slurry volume is to be cast so that the high losses during slurry supply will be reasonable.

The double blade configuration of the tape caster showed that it was necessary to adjust the blade gaps at first in order to guarantee a steady slurry level behind the casting blade. The work on adjustment of the gap height discontinued because of another drawback of DB mode associated with inhomogeneous flow inside the casting unit [134], which results in formation of vortex flow. Nevertheless, this method has seen an increasing attention for the fabrication of small lab-scale devices in recent works [140]–[142].

Tape casting with a single blade tank design appeared to have a high tape thickness increase at the beginning of the process due to high pressure resulting in high swelling at the beginning of the casting process. However, after casting about 10 mm with the speed of 30 cm/min the rise is decreasing and the tolerance of the dried thickness become no more than 10% until the end of the casting process.

5 Side-by-side tape casting

The newly proposed shaping technique SBS TC achieves parallel joining of dissimilar materials into functional adjacently graded tapes. The fact that the adjacent co-casting method itself was independently proposed by two scientific groups, working on magnetic refrigeration [66] and on improvement of a laser gain element [143], indicates a high potential of SBS TC for gaining a broad commercial acceptance and development. Although the range of application scenarios for adjacently graded materials continuously grows and become of concern as a structure beneficial for thermoelectric generator [144], detailed analysis of processing parameters influencing the quality of cast tape till needs to be carried out.

The current work is aimed to identify and systematically explore the slurry properties and operational parameters affecting the quality of the interface between co-cast materials. A twofold approach has been adopted as the basis for recognising the controlling parameters:

- One of the approaches focuses on “operational parameters” that covers the practical issues of co-casting feasibility such as dividing a conventional tape caster into a multichamber one with sufficient isolation, finding optimum settings for the tape caster unit (like single- or double-blade design), establishment of applicable correlation between casting speed and gap and tape thickness consistency.
- The second approach is “slurry focused” and consists of analysis of the quality of the graded tape in respect to the slurry composition, its density and flow behaviour.

These two approaches were applied in sequential and iterative order, unravelling the complex co-flow process and providing a comprehensive view on the SBS TC issues, which will be discussed further.

The output parameters characterizing the quality of the produced tapes are tape thickness consistency and the shape of the interface. Results on tape thickness consistency are presented by comparison of absolute thickness values and thickness gradient. The shape of the interface at the confluence area have one of the following profiles (Figure 5.1a): steep vertical, arc shape, angled to the surface of the substrate, or the boundary can be blurred due to mixing and interdiffusion between adjacently co-flowed slurries. The third case is so-called overlapping, which is covering or extending one of the SBS co-cast materials over another due to the overflow of slurries in the interface area. In order to measure the extent of overlap between adjacently co-cast materials, the position of the interface viewed from the top side of the tape was compared with the interface position, viewed from the Mylar bottom side of the tape (Figure 5.1b). From the tape profile view (z-y plane), the interface looked like either a steep line, giving an extent of overlap equal to zero, or like an angled line. In the last case the extent of overlap was measured in mm as the distance between interfaces seen from either side and some line, parallel to the side edge of the tape.

First, the conceptual idea of co-casting and necessary modification of a conventional casting tank is described. Then the casting modes are considered again but in terms of formulation of a stable flow and straight interface along the tape length. With the casting mode chosen to facilitate the most clear recognition of phenomena happening with a flow field during co-casting, the effect of slurry density and viscosity as well as casting speed are briefly described in Thesis. More details on this subject can be found in Paper I. Adhesion assessment was required to define if adjacently graded tape behaves as a single material or as a combination of weakly joined individual tapes. Hence, as the next step, mechanical tests were performed on green tapes with and without interface, characterizing the adhesion forces between the co-cast materials. After establishment of

slurry parameters and casting speed, the design of the partition dividing the casting tank into chambers is investigated (Paper III). The side flow is shown to be a critical parameter determining the dimensional stability of cast tapes, and shape and strength of the interface and its effect is summarised at the end of this Chapter under Section 5.4.

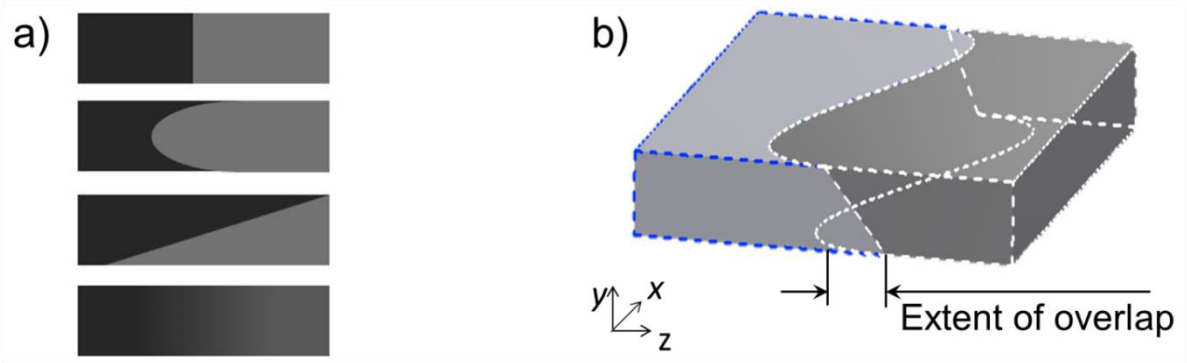

Figure 5.1. a) Schematic of possible shapes of interfaces formed between adjacently co-cast materials in SBS TC and b) determination of extent of overlap between SBS co-cast tapes. The scale of the tape doesn't match to the real size of green tape, and proportions between tape width and length are exaggerated. The sketch aims to show how the interface position change along the tape and definition of the extent of overlap.

5.1 Design of the tape caster

SBS TC includes simultaneous co-shearing of a number of slurries next to each other, forming a thin tape. To accomplish that, a conventional tape casting tank has to be divided into chambers. The width and the amount of chambers depends on the application needs (Figure 5.2a). In the current work, partitions were cut off from the Teflon plate 1.95 mm wide (Figure 5.2b). The material for the partition is free of choice as long as it is chemically inert to the chemicals used in slurry and the surface tension between the partition and slurry such that it does not affect the flow next to the tape caster walls and the partition. Kupp *et al.*, for instance, used a steel partition to divide the casting tank into chambers [145].

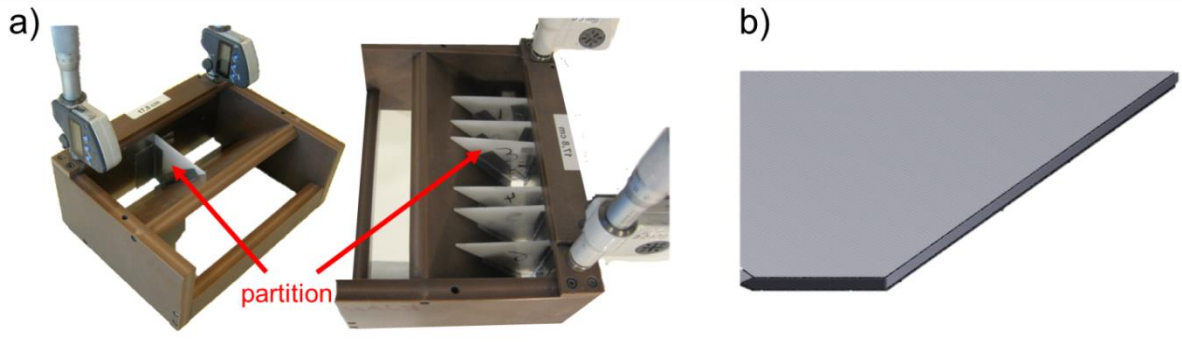

Figure 5.2. a) Photography of casting tanks for SBS TC with seven and two chambers and b) schematic of Teflon partition designed to divide casting tank into chambers.

The shape of the partition has to precisely repeat the shape of the casting reservoir. Before tape casting, the required number of partitions were fixed in the casting tank by use of Duct tape. The Duct tape was also intended to prevent the interleakage of slurries between adjacent chambers.

It was found that a tapered front edge of the partition was required since a blunt flat partition was shown to leave traces on dried green tape and led to an undesired inhomogeneity at the interface area (Figure 5.3). These traces on the tape surface were a consequence of the significant distance between the two slurries created by a blunt partition, which co-casting viscous slurries had to overflow just by flowing sideways. To overcome this challenge either less viscous slurries could be used but that would affect the shape of the interface between co-cast materials and final thickness. Another solution was sharpening the partition at the front edge in order to create a smooth merge for co-casting slurries (Figure 5.2b and Figure 5.3). The use of the sharpened partition opened a chance to co-cast slurries with a wide variety of viscosity values including highly viscous ones.

In order to guarantee simultaneous shearing of adjoining slurries, the gap between doctor blade and the carrier was closed with Duct tape in such a way that it prevented a drain of slurry before the carrier substrate started moving. At the start-up of the process, the carrier pulls slurries out of the casting tank with Duct tape moving with a front flow of co-casted materials. This optimisation was implemented as an engineering solution while casting of a monolayer tape (Chapter 0) in order to adapt experimental conditions to the numerical modelling.

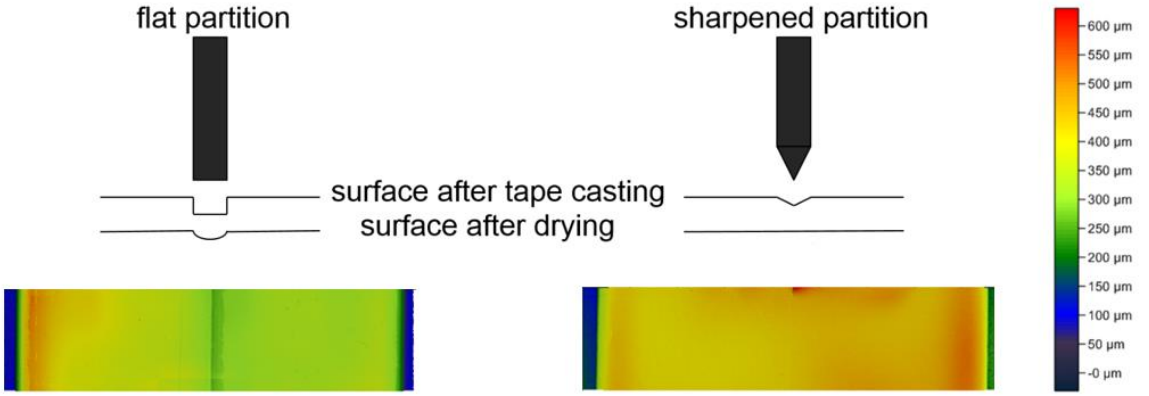

Figure 5.3. Schematic representation of surfaces of green graded tapes after co-casting using a non- sharpened and sharpened partition and below the pictures of surface topography of green tape samples, which were analysed by means of laser profilometry. The short slit on the sample, cast with the tapered partition, was made by knife in order to later identify the interface region on a completely smooth graded tape. The length of each piece of tape was 20 mm, and the width was 80 mm.

5.2 Evaluation of tape casting modes in side-by-side tape casting

Section 4.2. described a variety of optimal casting modes, their challenges and advantages in a matter of formulating green tapes with a low thickness gradient. In this section the significance of casting modes in terms of the interface shape and the extent of overlap will be investigated. For that, the same LSM and LSM_CGO_4 slurries were co-cast adjacently with a speed of 30 cm/min for SB, DB, and PS casting modes.

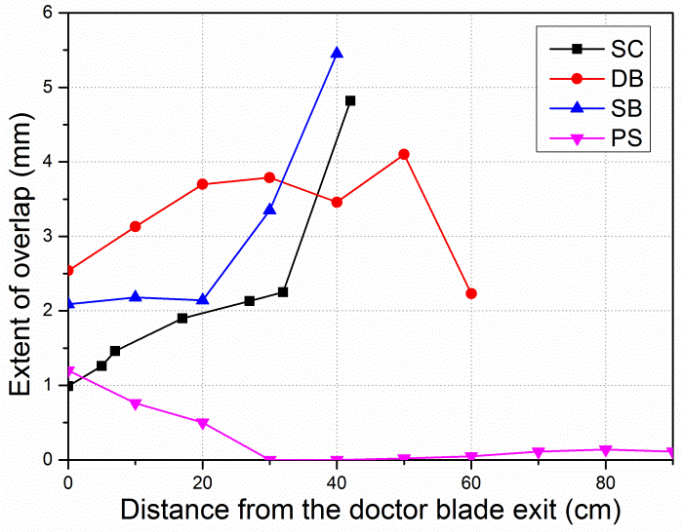

Figure 5.4. Extent of overlap in a green tape, formed between co-cast LSM and LSM_CGO_4 slurries in single blade (SB), double-blade (DB), speed change (SC), and with use of a pump system (PS) modes.

Figure 5.4. shows that the steepest interface was formed in tape casting where slurry was supplied to the casting tank by pump system. Minor fluctuations in the extent of the overlap are attributed to continuous manual adjustment of the pumping speed to casting speed. An absence of an overlap (1st model in Figure 5.1a) identifies PS casting mode as the mode, which guarantees a steady slurry flow and formation of a uniform green tape with a steep interface.

The decreasing overlap observed as the casting proceeds, typical for tapes obtained by SB and SC modes is presumably associated with fluid irregularities at the beginning of the tape casting process. A large overlap at the beginning of the graded tapes can be induced by a high pressure in the initial stage of the process and the resultant swelling, which does testify the unstable flow. The fact, that SC and SB modes have similar overlapping profiles indicates that the casting speed probably does not affect the extent of overlap. A detailed study of the casting speed on interface shape, however, is described further in Section 5.3.

The large overlap between slurries, co-cast by a DB system, can be attributed to the vortex and the continuous viscosity change described in [134]. Because of uncontrolled flow in the spare reservoir and beneath the blades, this method will not be considered for future analysis.

For further adjacent co-casting experiments, the single-blade casting head was chosen. The SB mode is beneficial for lab-scale research of co-casting, as it simplifies the modelling of main parameters on flow formation, and saves a considerable amount of slurry and time for individual castings. But the main reason to use a single blade system instead of a stable flow in pump system approach is to investigate the effect of superposition of pressure- and drag-driven flows on formation of interface in SBS TC.

5.3 The effect of slurry properties and casting speed on quality of graded tape

The general advantage of all liquid forming techniques is that they offer a high level of control over the fluid mechanics in the process, which makes it an ideal tool for fabricating tapes of various chemical composition and microstructure. A number of researches have been carried out using that correlation and

establishing a pattern between tape thickness constancy, alignment of particles along the casting direction and drying shrinkage coefficient as a dependence of slurry parameters like density and viscosity [146]–[150].

Because the fluid field inside the casting unit showed to define the dimensional characteristics of the final green tape (Section 4.1), it was decided to start the study on the SBS TC was decided to start by distinguishing the slurry viscosity and density values suitable for co-casting. From tape casting experience known, that for fabrication of thick tapes, viscous slurries (above 2000 mPas at a casting shear rate) have to be used. The variation of slurry viscosity is usually achieved by varying the solid load, solvent or/and binder content. In the current work, it was decided to keep the solid load constant as the ceramics to dispersant ratio was already optimised and the already defined concentration of ceramics had been shown to have the highest possible value [93], [98], [151]. The most straight-forward method to increase viscosity leaving the same solid loading includes increasing the polymer content. However, the range of binder concentration has to be minimal because during the next step, pyrolysis, a high concentration of organics should be burned off, which in extreme cases can give undesirable high porosity in the final tape. Hence, the slurry viscosity was varied by changing the solvent and binder concentrations.

For systematic analysis, composition of one of the co-cast slurry LSM decided to preserve over all set of viscosity experiments, while viscosity of the adjacently cast LSM_CGO slurry was gradually changing. The composition of LSM slurry was tailored such that no surface defects were observed. The viscosity of the LSM_CGO slurry was varied by changing the content of solvent MEKET and binder system as described above (Table 3.2). Along with interface control, tape thickness was also verified as a function of slurry viscosity. After the optimum slurry composition was chosen, the effects of casting speed on tape thickness gradient and interface shape were investigated.

This study addresses the experimental approach of SBS TC with the aim to understand the character and weight of slurry viscosity variation and casting velocity on the quality of adjacently graded tape. The full examination of the rheological behaviour of the slurries and casting velocity on thickness consistency and interface quality are described in Paper I and Paper IX.

5.3.1 Experimental procedure

Table 5.1. shows the LSM and LSM_CGO slurries compositions used for the co-casting. Slurries were prepared according to milling conditions, filtering and de-air as it was described in Section 3.3. Measurements of apparent viscosity (η) were conducted on pre-sheared and recovered (50 s^{-1} for 20 s, 0 s^{-1} for 10 s) slurries with reversing increase of shear rate $\dot{\gamma}$ up to 50 s^{-1} using a parallel-plate sensor system (Haake RheoStress 600, Thermo Electron GmbH, Germany). A solvent trap filled by ethanol was designed to prevent evaporation of organic solvent during rheological measurements. The densities of slurries were measured using a pycnometer as described in Section 3.4.

The casting head used in the experiment was divided into two chambers and had single blade geometry. The partition front side was sharpened and the gap under the casting blade was occluded by Duct tape (Section 5.1.). The casting gap was set to 1000 µm, and the slurry load in the reservoir was 22±2 mm. After pouring into adjacent chambers, slurries were kept in there for 30 s to reset stress history and then simultaneously cast with a velocity of 20 cm/min.

An analogous procedure was used for the set of experiments where the influence of casting speed on quality of graded tape was studied. LSM and LSM_CGO_4 slurries were co-cast onto a graded tape at a speed between 10 cm/min and 40 cm/min.

Table 5.1. Dependence of slurry's viscosity on the content of MEKET solvent and binder system. Because of experimental uncertainty, viscosity values were rounded to the nearest 100.

	Solvent vol.%	Binder syst. vol.%	S/C $Vol_{solv.}/Vol_{ceram}$	BS/C $Vol_{bind.syst./}Vol_{ceram}$	Viscosity η mPas ($\dot{\gamma}$=3.3 s^{-1})	Density ρ g/cm^3
LSM	42.99	41.24	2.98	2.86	4200	3.52
LSM_CGO_1	43.98	42.47	3.61	3.48	2700	3.64
LSM_CGO_2	43.44	42.45	3.57	3.45	3200	3.68
LSM_CGO_3	42.84	43.73	3.54	3.62	3800	3.86
LSM_CGO_4	41.78	44.53	3.39	3.62	4300	3.82
LSM_CGO_5	40.69	45.37	3.24	3.62	4500	3.78
LSM_CGO_6	40.65	41.83	2.93	2.68	6000	3.35
LSM_CGO_7	41.02	41.69	2.63	2.68	6700	3.39
LSM_CGO_8	40.50	40.74	2.01	2.50	9400	3.34

The produced tapes were dried for one day in a drying chamber and subsequently for 2 days in ambient atmosphere. The thickness values of green tapes were measured like in previous experiments by a digital micrometer with 15 mm diameter flat circle plates. The interface behaviour was characterised by the extent of overlap (Figure 5.1b). Cross sections of green tapes containing interface were examined with a scanning electron microscope (SEM) (Inspect, 50 nm at 30 kV, FEI Company, Kyoto, Japan) with energy dispersive X-ray spectroscopy (EDX, Oxford Instruments, Abingdon, United Kingdom). For reproductive comparison of interface shapes, samples for SEM and EDX were punched 10 cm from the end of each tape. Since polishing of green samples is impossible, the tapes were frozen in liquid nitrogen and then broken apart in order to have a smooth surface. The samples were retained between two plastic plates and covered by nanocarbon.

5.3.2 Results and discussion

The LSM and LSM_CGO slurries formulations used in the current study were selected from slurries (Figure 3.3a), which have been found to form green tapes without any surface defects. The variation of solvent and binder system in that range, however, did not affect the slurry density to a wide extent (3.60 ± 0.26 g/cm^3) (Table 5.1). That is because the density of slurries is mainly determined by the load of the heaviest fraction, *i.e.* by the load of ceramics in the studied system. However, in the current work, the mass of ceramics was kept constant, which gives only minor variations in slurry density, complicating further study of the impact of slurry density on the interface formation in SBS TC.

Nevertheless, the effect of slurry density was studied numerically by applying experimentally determined parameters (rheological parameters and densities of LSM and LSM_CGO slurries, dimensions of casting head) in the model described in Section 4.1. The tested range of slurries densities was wider than in the current experimental work, and amounted to 2-4 g/cm^3 [152]. Results of co-flow simulations found no influence

of the slurries' density on the interface shape and position. Hence, the role of slurries density was neglected in the current study.

Unlike slurry density, slurry viscosity was undoubtedly dependent on content of solvent and binder system in slurries. As expected, the viscosity of highly viscous slurries was more sensitive to changes in the binder system or solvent content compared to the viscosity of less viscous slurries. Thus a slight increase in solvent concentration in a very viscous slurry would decrease the slurry viscosity drastically. The fact that the increase of binder system content increased slurry viscosity, proved the conjectured hypothesis (Section 3.1.3.) that the binder interacted as an adhesive agent without replacing dispersant from the powder surface [37], [113]. Thus the dispersant is acting as intended and is not accumulated between polymeric chains of the binder, which could deteriorate the mechanical properties.

Shear thinning, required for tape casting, was typical for all prepared slurries (Figure 5.5a). Here, data of a few slurries are presented (Figure 5.5) (Table 5.2) assuming that the rheological behaviour of the rest of the used slurries (Table 5.1) are similar. By fitting the rheological parameters of the slurries to the Herschel-Bulkley model (Eq. 3.9.) (Table 5.2) and plotting flow curves in a logarithmic scale (Figure 5.5b), the yield point of the used slurries was evaluated. Taking into account that at the beginning of the casting process the estimated (Eq. 4.3) hydrostatic pressure behind the casting blade is about 700 Pa, yield stresses below 10 Pa (Table 5.2) are assumed to be negligible. Hence, the developed numerical model (Section 4.1) (Paper V and Paper VIII) with incorporated power law rheological behaviour of slurries is suitable for further analysis.

The slurry LSM_CGO_8 will not be considered further because of extremely high viscosity and low shear thinning capabilities (Figure 5.5a), which are undesired for the tape casting process. The influence of viscosities on quality of the produced tape was decided to study deeper on the following five slurries: two slurries with a similar rheological behaviour LSM and LSM_CGO_4, two the least viscous slurries LSM_CGO_1 and LSM_CGO_2 and the most viscous slurry LSM_CGO_6. LSM slurry was co-cast with all four LSM_CGO slurries in sequence.

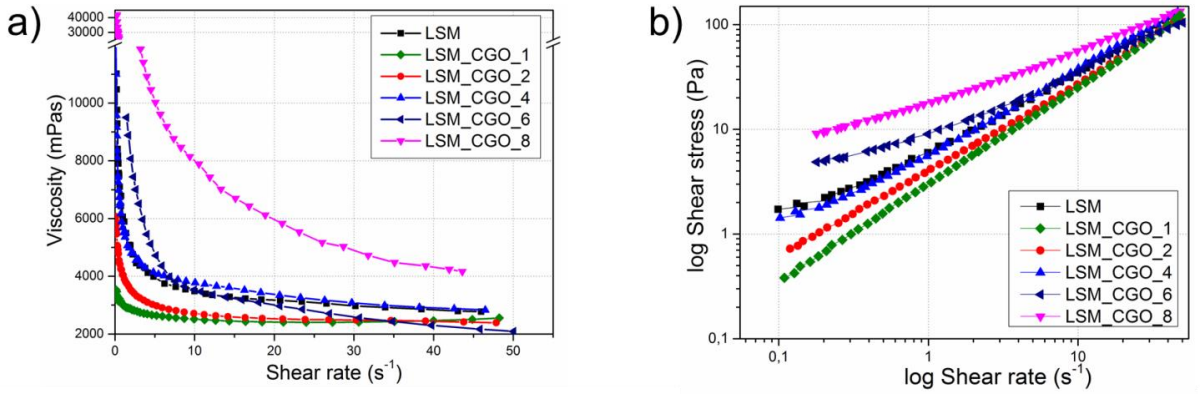

Figure 5.5. a) Viscosity curves and b) flow curves of the studied slurries.

The flow field beneath the blade was shown to be the main cause of particles orientation and the degree of shrinkage [134], [146]. Hence, before starting a close investigation of slurry viscosity as a factor determining the shape of the interface, a clear definition of the fluid field of used slurries inside the casting unit during the whole tape casting process has to be determined.

Table 5.2. Rheological behaviour of cast slurries.

	k	n	Yield point τ_y Pa	R^2
LSM	4.7(7)	0.85(6)	1.0(8)	0.999
LSM_CGO_1	2.0(2)	1.00(3)	0.8(2)	1.00
LSM_CGO_2	3.0(8)	0.93(2)	0.7(6)	0.999
LSM_CGO_4	5.8(2)	0.81(2)	1.0(4)	0.999
LSM_CGO_6	6.2(9)	0.71(2)	4.8(3)	0.999
LSM_CGO_8	13.4(2)	0.58(8)	6.2(7)	0.999

It is very common, both in laboratory and industrial practice, to characterize slurries referring just to one viscosity value, measured on rheometer and given (i) either at a certain shear rate or (ii) viscosity value taken from the viscosity curve at a certain cast shear rate. This certain cast shear rate is determined as a ratio between the casting velocity and the casting gap [100], [126]. For instance, in current work, the cast shear rate is 3.3 s^{-1} as tapes are cast with a gap of 1000 µm at casting speed of 20 cm/min. But the above mentioned formula only gives a rough estimation of casting shear rate, because it anticipates continuous nature of dragging forces and neglects descending pressure drop. The real flow profile during tape casting is more complicated; shear thinning character of slurries, complicated system of slurries surface tension, and wetting behaviour are just a few forces imparting the flow of the slurries. In order to minimise the uncertainties and determine the actual viscosity profile during SBS TC, the quasi-steady state model (Section 4.1) (Paper V) combined with a power law model and slurry height dependent flow has been applied.

Figure 5.6a displays that the shear rate profile is very sensitive to the slurry load in reservoir. The higher the slurry level behind the blade, the higher the deviation in shear rate profile and, hence, the higher the viscosity across the casting gap is. Thus, it is of a crucial matter to keep the slurry level equal in adjacent chambers in SBS TC and always start casting experiments with the same initial slurry volume in reservoir in order to have reproducible experiments of high accuracy.

As long as slurries were loaded up to the same level in the casting chamber, the flow field appeared to be independent on rheology of cast slurries (Figure 5.6b). The influence of hydrostatic pressure drop was found by shifting the roughly calculated share rate value of 3.3 s^{-1} to a wider range of shear rates. The carried modeling determined the region of shear rates, acting during the whole casting process and for slurries applied in this work belonging to the interval of 0.6 s^{-1} to 5 s^{-1} (Figure 5.6c). That fact allows describing slurries' flow behaviour by referring to one value of viscosity.

All four LSM_CGO slurries described above were adjacently co-cast with LSM slurry, and the four produced SBS graded tapes were dried under the same conditions. Figure 5.7. depicts that the thickness of green tape is a function of slurry viscosity and not the slurry density, as it was also shown above. The leap at the beginning of each curve is associated with the sharp launch of tape casting process with high hydrostatic pressure in the slurry column. Another observed tendency is that more viscous slurries form thicker tapes with a higher gradient of tape thickness along the casting direction. For example, the LSM_CGO_6, LSM_CGO_4 and LSM_CGO_2 slurries have the thickness deviations on last cast 20cm of the tapes of 20.17%, 9.67% and 3.24%, respectively. This is caused by a higher resistance of viscous slurries to side flow, while less viscous slurries tend

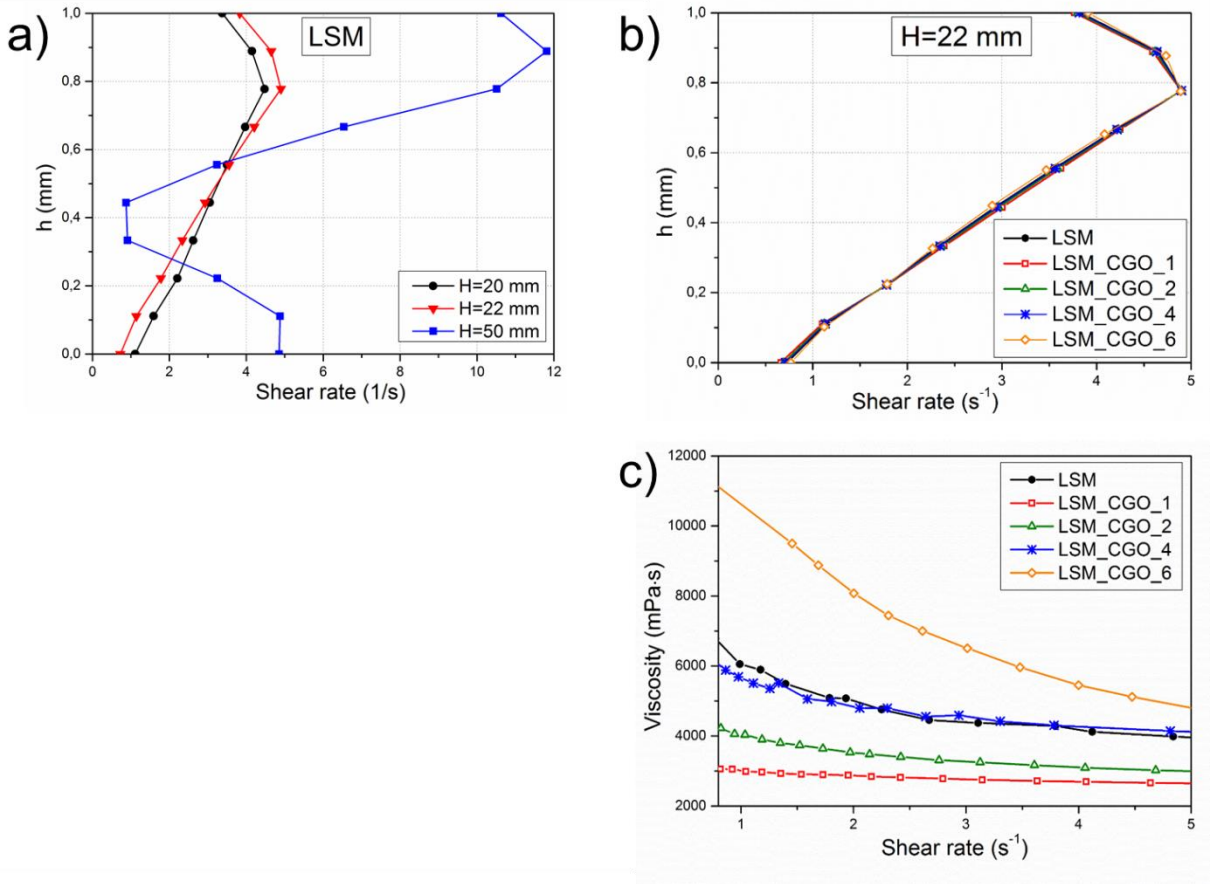

Figure 5.6. Shear rate profile across the casting blade a) for LSM at different slurry load in reservoir, b) for various slurries at slurry load H=22mm; c) corresponding interval of slurries viscosity curves at re-calculated working shear rates acting underneath the doctor blade during the casting process.

to easier flow aside, redistributing the slurry volume and reducing the tape thickness. Higher thickness gradient typical for more viscous slurries is assumed to originate from the swelling phenomena. Higher content of binder in more viscous slurries supposed to adsorb better on the front side of the blade restricting the uniform controlled slurry flow. This phenomenon causes the draw of slurry not directly from the initially determined side, but after slurry being protruded over the casting blade. The gradual decrease of tape thickness inherent for slurries of all tested viscosities is caused by the superposition of steady drag-driven flow and decaying pressure-driven flow explained above (Section 4.1.). The effect of hydrostatic pressure diminishes continuously with process duration as the volume of slurry in the reservoir continuously decreases and the rate of change in the hydrostatic pressure is reduced. As a consequence, the green thickness values of tapes, cast from slurries with different viscosity values, converge with decreasing slurry amount in reservoir.

Furthermore, the impact of casting velocity on the thickness of green tape is presented (Figure 5.8). Since the detailed study on speed-tape thickness correlation was already presented in detail in Section 4.1.3.1., the relation will be only considered here in order to highlight the main reasons of tape thinning and applying these reasons while study the SBS cast tapes. The differences in thickness of the LSM and LSM_CGO_4 sides at the same speeds was presumably due to different solvent content, which evaporated in the drying process. The

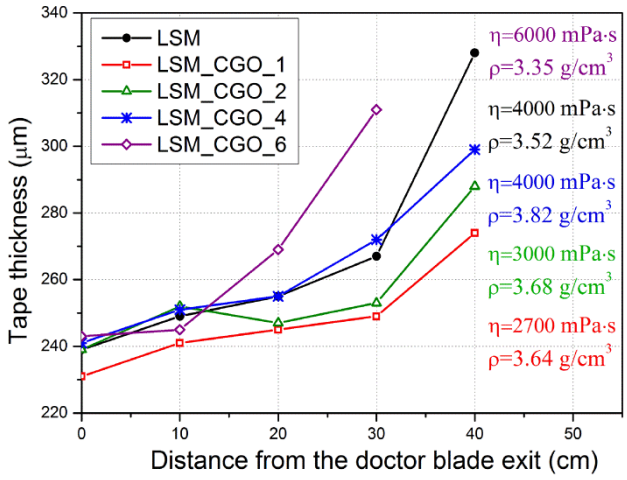

Figure 5.7. Tape thickness gradient along the green tape length. Viscosity values are given at a shear rate $\dot{\gamma}$ =3.3 s^{-1} (corresponds to the casting speed of 20 cm/min); density values are referred to the slurry density values given in Table 5.1. The estimated error is 15 μm.

drying ratio, estimated from equation 4.2, approximated to 30-40% for the LSM side and 35-50% for the LSM_CGO_4 side. As having a different binder system load in adjacent materials, a minor systematic additive error is possible during thickness measurement due to different softness of materials. This uncertainty disappears after the de-binding step, forming a dense solid material with equal thicknesses on both sides of the graded tape. The obvious tendency of thickness smoothing after first 10 mm cast, proves the fact that tapes are mostly formed by a drag-driven flow, defining the steady flow during the most of tape casting process.

Another aspect of casting velocity impact is the difference in shearing or, equivalently, casting time. Fast tape casting reduces the time when slurry is sheared, hence, limiting the time when slurry is capable of undergoing pressure-driven flow. On the other hand, slow cast slurries experience pressure and viscosity effects for a longer time. As a consequence, at low casting speeds the actual slurry volume flow below the blade is higher than the volume flow with a speed equal to the carrier speed. Due to capillary forces, thick slurries experience swelling after crossing the blade gap zone, causing thickening of dried tape cast with a slow speed. The same tendency of decrease of the swelling height with increase in casting speed was declared in [136]. Casting velocity also affects the drying kinetics. Tapes, which cast fast are dragged for longer distances in a drying chamber being “fluidly deformable”. As it was shown by Prof. Roosen [136] the velocity profile changes with the distance from the front edge of casting blade. However, more experiments on this subject will be described further in Section 5.5.

The most illustrative and precise way to show the character of interface dependence is to compare the interface shape with the energy dispersive X-ray (EDX) mapping as adjacent materials are often barely distinguishable on SEM pictures. Samples were punched from the graded tapes 10 cm away from the end of the tape, corresponding to the end of the process, thus guaranteeing the same pressure in the reservoir during the casting process. No diffusion or intermix between adjacently co-cast materials was found (Figure 5.9.).

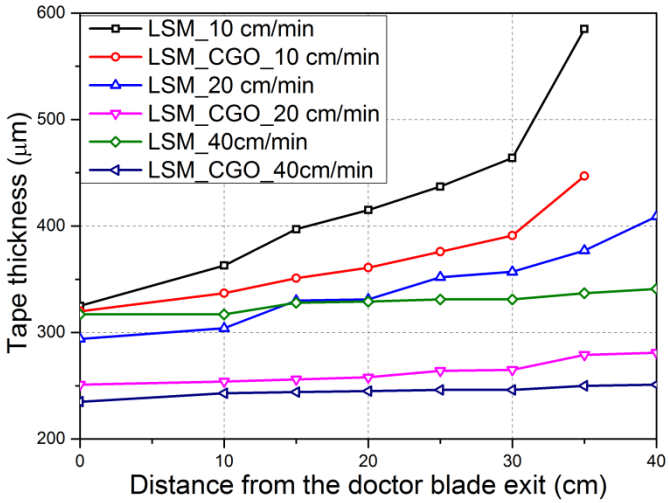

Figure 5.8. The effect of casting speed on green tape thickness measured along both edges on LSM and LSM_CGO_4 sides. The estimated error is 15 µm.

It was decided to investigate the effects of slurry viscosity and casting speed in a parallel study in order to make tendencies more clear. The increase in casting speed from 10 to 40 cm/min for our particular slurry formulations resulted in a decrease of overlap from 1.2 mm to none at all (Figure 5.9a). This behaviour can be explained by the duration of the slurry co-shearing process and side flow. Thus, slurries which were co-cast fast have a very short time beneath the blade to flow aside and barely merge to form the interface; in the drying zone dried slurries are not capable of moving anymore. In turn, slurries, cast at lower speeds, have more time in a low viscosity state, leading to formation of wider contact area between adjacent materials. For casting speeds of 20 cm/min and 30 cm/min, the increased role of surface tension between adjacent slurries is evident by a sudden change in the straight line interface shape to the arced shape (second scheme of interface shape in Figure 5.1a). The correlation between slurry surface tension and interface shape formation is a subject planned to be studied in our future work.

Figure 5.9b depicts that the impact of slurry viscosity on the extent of overlap between co-cast materials is significantly larger compared to casting speed. More viscous slurries are restricted to flow aside, and due to less content of solvent they dry fast. Due to more content of solvent low viscous slurries are fluidly deformable after passing the blade region. That explains their capability to flow aside and spread over more viscous adjacent material. Hence, low viscous slurries intend to form a wide overlapping region or overflow over the more viscous co-cast slurry (Figure 5.9b). The absence of intermixing between slurries in the interface region can be explained by apparently high enough capillary hydrostatic forces of co-sheared slurries.

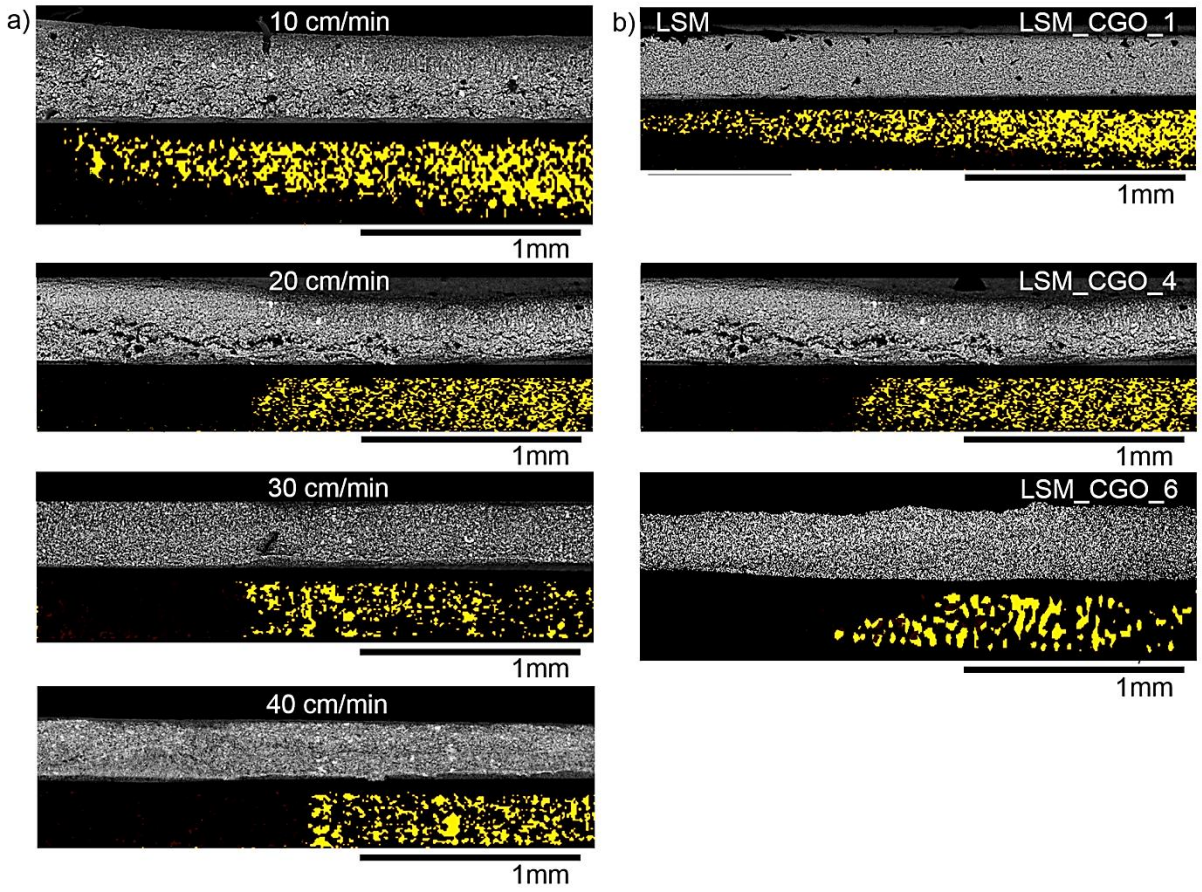

Figure 5.9. SEM pictures and corresponding EDX image below visualizing the interface area of SBS co-cast a) LSM and LSM_CGO_4 materials at various casting speeds, given on SEM pictures; b) LSM and LSM_CGO slurries of different formulations at casting speed 20 cm/min. CGO phase is marked with a yellow colour here.

5.3.3 Conclusion

LSM and LSM_CGO co-cast slurries were proven to have a negligibly low yield point, thus, the developed quasi-steady state model with a power law fluid model is relevant for co-flow numerical description. Most importantly, this model verified that slurry velocity profile across the casting blade depends significantly on slurry load in the reservoir irrespectively of the slurry viscosity.

Highly viscous slurries were shown to form thicker tapes with high thickness gradients compared to casting of less viscous slurries. Thickness constancy, however, is likely to be improved by casting slurries with a speed of 30 cm/min and above.

Adjacent co-casting of slurries of certain viscosity with various speeds is shown to change the shape of the interface in a narrower range. The line of contact can be either settled into a long line tilted to the substrate surface when tape casting slowly (in case of SBS co-cast LSM and LSM_CGO_4 at 10 cm/min), or be rounded toward the drying surface of the green tape and toward the carrier film (20 cm/min), or be steep, almost perpendicular to the substrate (40 cm/min). In the experiment with varying LSM_CGO viscosity, the dominant factor of forming the shape of green tape is the side flow, so it affects the extent of overlap but not the interface shape.

5.4 Adhesion between co-cast materials

The discrete interfaces are often weaker than the surrounding continuous material and also act as stress concentrators, a dangerous combination that can lead to structural failure. The current challenge for manufacturing FGMs is to develop a shaping process that can easily control the evolution of the gradient architecture within a structure in order to optimise structural performance. SBS TC, on one hand, has an advantage forming the interface during the liquid forming technique, so the stresses can be relaxed while the slurry is fluidly deformable. On the other hand, the one-dimensional interface between co-cast materials does not guarantee as good adhesion as the two-dimensional interface in multilayered structures. Thus, the series of tests on adhesion between adjacently cast materials was aimed to identify if obtained graded tapes behave as a single or unified material.

The adhesion between co-cast LSM and LSM_CGO slurries in graded green tapes was tested mechanically. For measurement of fracture tensile stress (strain-stress resistivity) of the green tapes and evaluation of the interface quality, green samples of 100x10 mm were cut with the interface in the middle of the long side. These pieces were fixed in an Instron tensile machine (the cell load was 5 N, 5900 Testing System, Instron, MA). To secure getting relevant data, at least four tests for each specimen were collected. The data obtained from the specimens which failed nearby the fitting clips were excluded from evaluation. The tensile test was also performed on individual samples of LSM and LSM_CGO, which were punched from the graded sample but far from edges and interfaces to ensure homogeneity and purity of analysed specimens.

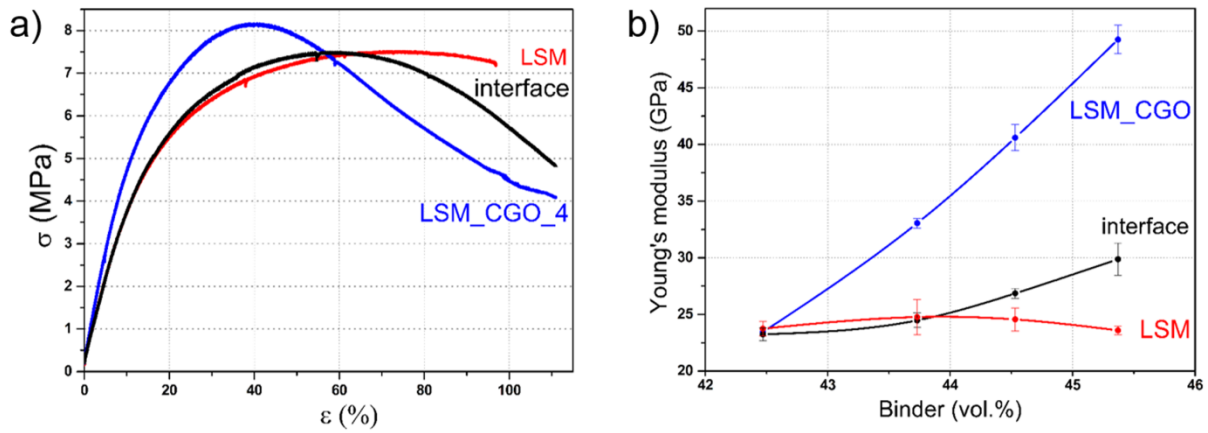

Figure 5.10. a) The stress-strain relations of green tapes of pure LSM, pure LSM_CGO_4 strips, and interface area; b) Young's modulus change with binder content in the LSM_CGO material side and interface, the content of LSM side is constant.

The green strengths of pure LSM and LSM_CGO materials, as well as a graded tape, are shown to be high because of the high content of polymers, and, particularly, binder system content (Figure 5.10a). Using the same polymer loading in adjacent materials the plasticity of both tapes is very similar despite the content of particles with different surface area, which according to Yoon and Lee [153] is supposed to have a dominant influence on the tensile strength of the green tapes.

Considering the LSM_CGO slurry, it can be seen that slightly higher binder content generates higher green tape elasticity (Figure 5.10b). This can be attributed to increasing adhesion strength and uniform

distribution of the binder, as it is the only continuous phase in the green tape. The same tendency of increasing green tape elasticity was observed for the adjacently graded tape, as the pure LSM stripe composition remains constant from sample to sample (Figure 5.10b). All the specimens of the graded tapes always broke on the pure LSM material side, characterised by a lower green strength. Therefore, adherence between the adjacently co-cast materials was proven to be strong enough to keep the interface area intact while applying the tensile stress. By carrying out the tensile test on green samples, it was proven that it is possible to shape a side-by-side graded material with a good adhesion in a one-dimensional interface (Paper I).

In addition to proving a high adhesion between stripes, high strength performance of SBS tapes guarantees an easy removal of green samples from the Mylar substrate without deforming the green sample.

5.5 Partition design

Apart from determination of quality of materials by specifying fluid properties in liquid forming techniques, optimisation of operational parameters is also to some extent required for successful production of a target material. A partition as a distinctive operational unit in SBS TC has already showed the importance of its design for improving the quality of green tape surface (Section 5.1.). Moreover, partition shape was different in work on magnetic refrigeration [66] and on improvement of a laser gain element [143]. In Kupp's *et al.* study [145], the partition separated the casting tank and covered the whole gap below the doctor blade. In works, directed on co-casting for magnetic refrigeration application, as well as in study described above, partition covered just the reservoir space. Hence, co-flowed slurries in the latter example were flowing together below the casting blade.

Another aspect of dividing the casting tank into segments, which was found in literature, is the aim to improve alignment of elongated particles into the casting direction [154]. This is caused by a torque, generated next to the tank walls, which was proven to affect the rotation of the particles even more than an increase in casting speed [155], [156]. In a comparison of a set of tapered blades installed 5 mm apart from each other at the exit of the tank and an array of sharpened pins 0.7 mm from each other, the latter ones shown to exhibit a higher degree of particle orientation in a cast tape [154].

As can be seen, the new idea of separating a standard casting tank into compartments is used for as different purposes as joining dissimilar materials into functional graded tape and forming the high-ordered thin films. Nevertheless, information on partition shape influence on slurry flow is still needed. Current work is aimed to define and systematically explore which features of tapes it is possible to control, changing the design of the partition and casting speed as one of the settings of operational characteristics. From previous experience, the presence of the division between slurries in the casting region below the blade was assumed to be of high importance. Hence, tests were built by using a continuous change of the division below the blade by changing the length of the partition located in the casting gap. This chapter contains information extracted from Paper III.

5.5.1 Experimental procedure

All tests were carried out using the same LSM and LSM_CGO_4 slurries with the same formulation and pre-casting rheological parameters as ones used in our previous tests (Section 5.3.). The single blade tape casting unit has been applied. Experiments were conducted with different length of partition tongue at various casting speeds. The series of experiments were set as follows. First three experiments included co-casting of

LSM and LSM_CGO_4 slurries with the whole partition length and 10 cm/min, 15 cm/min and 30 cm/min casting speeds, consequently. Afterwards, the partition tongue was shortened by a quarter, the front edge was sharpened, and co-casting continued with a 0.75 fraction of partition with 20 cm/min and 30 cm/min alternately, *etc*. The shearing surface of blade was cleaned after each time and the sub-reservoirs were emptied in order to create reproducible conditions for each test.

Measurements of apparent viscosity (MCR 301, Anton Paar GmbH, Austria) were analogous to the ones described in Section 4.2. Viscosity curves are given in Figure 4.10. A special four step experiment was designed on the rheometer aiming to reproduce the tape casting process. The test was performed using a spindle of 25 mm diameter and with holes on top (Figure 5.11) in order to improvise the drying process giving solvent opportunity to evaporate.

The green tape thicknesses were measured both on the LSM and LSM_CGO_4 sides of the tape, about 2 cm from either edge of the tapes in order to avoid possible edge defects. Measurements were performed using a flat dual point digital micrometer of 15 mm in diameter every 10 cm along the tape length. Precise collection of thickness data was necessary in order to track the general tendency of tape thickness regularities along the length. Besides, the extent of overlap was measured using an optical microscope by comparing position of interface, seen from the top and the Mylar sides of green tape. The side flow was studied on a laser profilometer CyberScan Vantage CT300 (Cyber Technologies GmbH, Germany).

Figure 5.11. Photos of spindle PPR25/23 from the Anton Paar spindle set used for the imitation of the drying process, happening after tape casting process.

5.5.2 Results and discussion

Each dot in Figure 5.12a corresponds to a SBS TC experiment, carried out at casting speeds in a range from 10 cm/min to 50 cm/min, and at certain lengths of the partition tongue (Figure 5.12b). The partition tongue here is the part of the Teflon partition situated beneath the blade. Here, the partition tongue is the length of the Teflon partition beneath the casting blade (Figure 5.12b), with a height identical to the casting gap of 1 mm, the width is equal to width of the whole partition, 1.95 mm; the maximum length of used partition matches the width of the casting blade of 6.5 mm and is referred to here as the whole (fraction of one) of the partition (Figure 5.12b). The partition width of about 2 mm was required as it was complicated to set a thinner partition precisely in the middle of the tank. Besides, it is also challenging to fasten a thinner partition tight to the tank walls, causing leaking of slurries in between adjacent reservoirs at the seams. Use of thick partitions

would hinder the merging of co-flowing slurries and would limit the use of highly viscous slurries with confined side flow.

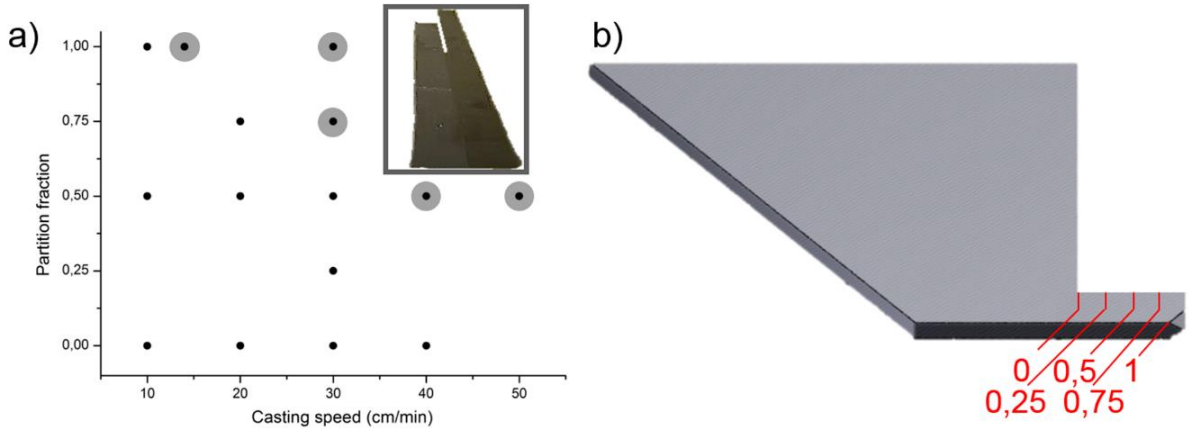

Figure 5.12. a) Experiments identifying the effect of the partition design and casting velocity; marked grey dotes denote co-casting tests where splitting between co-cast materials was observed (shown in the inset); b) Side view of Teflon partition design; red lines show the way of cutting the partition length for experiment on identifying the effect of partition design on adjacent fluids flow. Given numbers imply the fraction of partition tongue which was used in the experiment.

The grey dots in Figure 5.12a represent tests, where co-cast slurries did not merge and a gap in the interface area was formed (inset in Figure 5.12a). The ability of adjacently cast slurries to merge in the confluence area and form an interface was shown to improve as the casting speed was reduced and the partition tongue shortened.

To quantify the influence of flow behaviour on the formation of the graded tape, the tape casting process was reproduced on a rheometer according to the shear rates applied to slurries during each step of the real casting process. Essentially, tape casting is considered as a consequence of shearing processes: first, we pour slurries into reservoir applying a certain shear rate assumed to be about 5 s-1, later we keep slurries in the reservoir for 10-15 s in order to remove any effects of sampling on the rheological history of the slurries Afterwards the casting process starts where shear rates can be approximately re-calculated as casting speed divided on the height of the gap under the blade. The last step is drying, which is assumed to be a step where no shear stresses are applied, ignoring the shrinkage stress and possible edge effects. During this multistep program, the viscosity of LSM and LSM_CGO_4 slurries were measured as a response to the applied shear rates. Unlike the previous conclusion (Section 5.3) (Paper I) that the real working shear rate is much wider than the one re-calculated from the casting speed and casting gap, the slurries used in this work was show (Figure 5.6c) to have a steady viscosity in the whole range of the applied shear rates. Thus, to simplify rheological test, a single shear rate value was chosen as representation of the casting process.

Figure 5.13a illustrates changes in the rheological behaviour of the LSM and LSM_CGO_4 slurries during the test imitating tape casting at 10 cm/min casting speed. Tracking the flow field in the tape caster unit, three clear regions of characteristic viscosity changes are identified: (i) after pouring slurries into the tape caster reservoir and allowing the slurry to rest, the molecules of the binder in the highly viscous slurries start to form a

polymeric matrix increasing the viscosity of the slurries; (ii) under an applied shear rate, polymeric chains elongate causing uniform viscous flow of slurries under the casting blade; (iii) when slurries flow in a free space, reciprocal action of the polymeric matrix formation and the drying process increase the viscosities of the slurries. Hence, the changes in the system are caused by both shear thinning behaviour of casting slurries and the drying process.

The thixotropic behaviour (Section 3.4.1.), characteristic for both LSM and LSM_CGO_4 slurries, requires approximately 7 s to 10 s to completely recover the initial structure and retrieve initial viscosity. During that time the slurry is assumed to be fluidly deformable. The fluidly deformable state is a state of cast tapes at the initial stage of the drying process when the dried film is still not formed at the tape surface and its edges are capable of shifting under the weight of the tape.

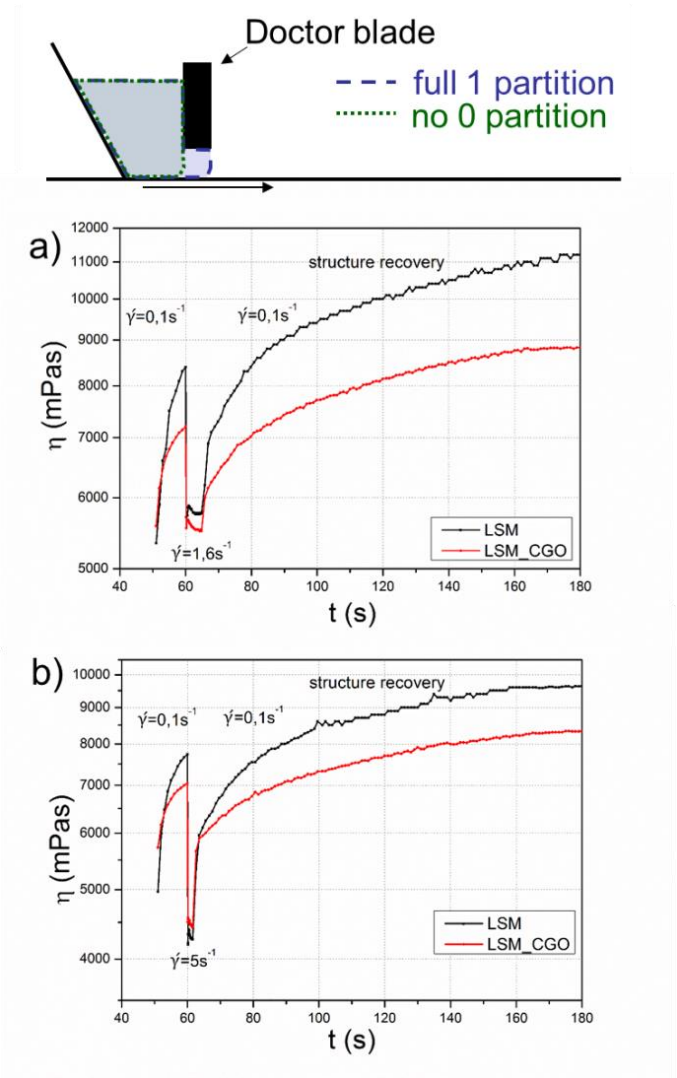

Figure 5.13. Structure recover test for LSM and LSM_CGO slurries co-cast at a) 10 cm/min and b) 30 cm/min casting speed.

Decrease in viscosity, typical for casting slurries while passing the blade region, allows the slurry to flow aside under the influence of gravity, surface tension forces and levelling without revealing stresses in surfaces.

Thus, complete absence or a short partition tongue below the blade improves merging of co-flowing slurries and formation of a uniform interfaces. When the partition tongue divides the co-flowing slurries all the way under the blade, the slurries are free to flow aside just after passing the blade region. Casting with a speed of 10 cm/min, the fluidly deformable state of slurries lasts for at least 7 s to 10 s. That time was proven (Figure 5.12a) to be enough for slurries to merge and form a well-defined interface.

However, when the slurries are cast faster, the duration when slurries are fluidly deformable drastically shortens (Figure 5.13b). Thus, the faster the casting speed, the lower is the possibility for co-casting slurries to merge when the whole partition tongue is used (horizontal tendency in Figure 5.12a). For instance, in the current work the relatively small change in casting speed from 10 cm/min to 14 cm/min results in splitting between co-cast materials.

Another noteworthy result is the shortening of the shearing time with an increase of the casting speed. For example, when the partition tongue divides the casting gap at a fraction of 0.75 of the blade width, the time, during which the slurry has a low viscosity at the casting speed of 10 cm/min is 6 s (Figure 5.13a) and less than 3 s for a casting speed of 30 cm/min (Figure 5.13b). Thus, the time for adjacent flowing slurries to merge in the partition free area beneath the blade is 1.5 s and less than 0.75 s for 10 cm/min and 30 cm/min casting speeds, respectively. The results show (Figure 5.12a) that 1.5 s in a low viscosity state is enough for adjacent slurries to join in the confluence area of 1.95 mm (the width of the partition), while 0.75 s is too short time for slurries to flow aside and form the interface.

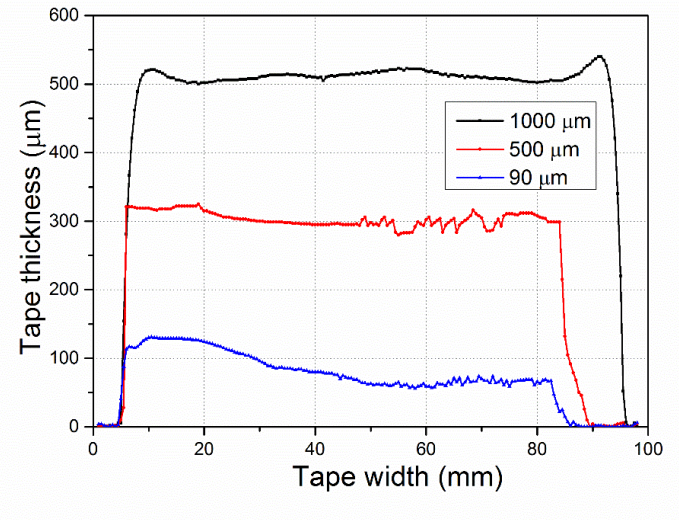

Figure 5.14. Cross-section profile of the LSM slurries made on a laser profilometer showing the side flow effect.

Normally, gravity is ignored in tape thickness studies as it is assumed that its effect is negligible for tape dimensional consistency, but in SBS TC an accurate determination and tuning of all parameters, which influence the forming of the confluence interface area, is of great importance. The study of the impact of gravity was built on the well-known fact that the tape thickness decreases when the casting speed is increased (Paper I). Thus, the tape thickness of the same slurry was shown to be halved when the casting velocity was increased from 10 cm/min to 40 cm/min (Paper I). In order to estimate the role of gravity forces on the side flow effect (the correction factor for side flow α in Eq.4.2.), three 80 mm wide tapes were cast manually on a laser profilometer substrate covered with a Mylar film. The speed was about 80 cm/min and casting gaps of 1000 µm, 500 µm, and

90 µm were chosen. LSM slurry was used for all three experiments. The laser profilometer was used in order to measure the tape thickness gradient in-situ. Results showed (Figure 5.14) that the side flow of tapes cast with a 1000 µm gap, which was supposed to represent tape casting with slow casting speeds, exceeded 10 mm (α=0.89), while for the tape cast with 500 µm (α=0.96) and 90 µm (α=1) gaps, which were supposed to refer to faster casting, these numbers were 3.5 and 0 mm, consequently. In the experiment with a casting speed change, proportional change in tape thicknesses would lead to the proportional changes in side flow. When the partition creates a 1.95 mm wide confluence area to be filled by co-cast slurries from both sides, the side flow plays a crucial role. However the side flow is of practical value as long as slurries are able to flow, *i.e.* being at low viscous state.

5.5.3 Conclusion

In this work, the influence of partition geometry on the quality of graded tape was studied. It was shown that the likelihood of obtaining a uniform adjacently graded tape decreases with increasing length of the partition tongue beneath the casting blade and with increasing the casting speed. Moreover, unlike the regular practice in shaping techniques, where rheological study of processing slurries and their numerical description are limited by providing viscosity and flow curves, a new approach of describing and measuring slurries fluid behaviour was proposed. The most distinct difference between the proposed approach and conventional rheological examination of pre-casting slurries is the consideration of rheological test as a representation of the dynamic sequence of the tape casting processes. Nevertheless, the application of standard rheological programs with pre-shear and increasing shear rate is required in order to analyse and be able to compare shear thinning behaviour of casting slurries.

6 De-binding and sintering

Once the tape was cast, it was left to dry in the drying chamber for two to three days. The drying process is very complicated and includes not just solvent evaporation, which reduces the tape thickness, but mass re-distribution under gravity and shrinkage of the organic system, leading to densification of the green tape. Cracks or surface defects like pine-holes [157], [158] can be developed as a result of the pressure gradient caused by capillary tension on the drying tape. The mechanism and main challenges of the drying process are profoundly described elsewhere [149], [159] and is not a subject of research and optimisation in this work. Later, the desired shape of green ceramics is obtained by punching the sample with hardened steel knifes of a certain shape template [37] or cutting of the required green shape with a precise computer controlled laser [160].

Due to relatively high amount of organics present in cast tapes (Figure 3.3b), their burn-out is very critical for obtaining uniform defect-free tapes. Among wicking, supercritical fluid extraction and other de-binding techniques, thermal de-binding is utilized the most. Thermal de-binding includes a number of simultaneous processes like decomposition of organic species, chemical interaction between organic components, mass transport of reactants including volatile species, change in the distribution of condensed polymers within the pores formed, just to name a few. In order to minimise and/or avoid defect formation during de-binding, the balance between the time for organic removal and defect propagation time is essential. The mechanism of de-binding depends on the molecular weight of the polymers used, the interaction between the particles and the organics, the heating rate, *etc*.

The processing step, following the de-binding which is required for tape densification, is called sintering. To achieve a dense hard ceramic material, high temperatures and sometimes pressure are applied. The mechanism of sintering is described in details by German [161], where he presented the main steps in the sintering process (Table 6.1).

Table 6.1. Stages of sintering. Adapted from [161].

Stage	Process	Surface Area Loss	Densification	Coarsening
Adhesion	Contact formation	Minimal unless compacted at high pressures	None	None
Initial	Neck growth	Significant, up to 50% loss	Small at first	Minimal
Intermidiate	Pore rounding and elongation	Near total loss of open porosity	Significant	Increase in grain size and pore size
Final	Pore closure, final densification	Negligible further loss	Slow and relatively minimal	Extensive grain and pore growth

It can be assumed, that for high mechanical and thermal resistance to stresses, the tapes with small and homogeneous pore sizes and high sintering densities, few and small residual porosities are desired. The possibility to achieve a controlled grain growth, which happens at the last stage of sintering (Table 6.1), requires a slowed grain growth and simultaneous increase in the densification rate. Hence, some of the most crucial parameters to control are: powder composition, particle size and particles size distribution, density of green tapes, amount and size of green tapes, heating rate, sintering temperature, sintering time, and sometimes using a sintering atmosphere different from the ambient air (pressure, gas atmosphere).

Thus, after the brief introduction of de-binding and sintering processes, given above, this Chapter aims to optimise the de-binding and sintering profiles for obtaining high quality post-sintered graded tapes. The techniques applied here, such as thermogravimetric analysis and differential scanning calorimetry of the green tapes provided the valuable information about the heating path which should be followed for tape densification. Further, densification kinetics of pieces of LSM, LSM_CGO_4 and a piece containing the interface SBS_LSM_CGO was compared using an optical dilatometer TOMMI. The observed issue of LSM tapes being stuck to the repton plate after sintering required an extra study in order to find a solution fast. After optimisation of all the processing steps starting from the powder treatment and slurry preparation and ending with simultaneous co-casting and sintering step optimisation, five slurries containing a target for magnetic refrigeration LCSM material have been processed and the quality of their interface has been analysed. The details on some of the studies and challenges presented in this chapter, can be found in Paper II and Paper VII.

6.1 Optimisation of the de-binding program

The amount of binder in the system was shown to affect the mechanical features of the green tapes strongly (Section 5.4.), as well as the functional properties of the final post-sintered films. However, complete removal of all organics from the system is needed to ensure a defect-free structure and maximum densification. Incomplete organic burn-out causes poor mechanical strength, low density, and poor thermal, electrical, or magnetic performances.

A number of studies were conducted in order to optimise de-binding programs of similar organic system [100], [162]. However, due to a slight modification of slurries recipes, resulting in fabrication of thick dense materials, it was decided to optimise a heating program by studying organic burn-out steps obtained in current work. This work includes a study of temperatures, when the burn-out of organics occurs as well as it considers the effect of the heating speed on the quality of tapes.

Thermal analysis was used to monitor the burn-out process in real-time. This analysis encompassed control of enthalpy change, studied by differential scanning calorimetry (DSC), and control of weight loss, studied by thermogravimetric analysis (TGA). Since organic burn-out is assumed to occur at temperatures far below sintering temperatures, DTA and TGA were performed up to 700 °C (Netzsch STA 409CD, Netzsch GmbH, Germany). For that, an LSM_CGO_4 green tape was chosen. After three days of drying, a small piece of green tape about 0.32mm x 9.5mm x 10.2 mm was cut off. The study of the effect of heating speed was conducted with heating rates of 300 °C/h, 60 °C/h, and 30 °C/h.

Figure 6.1a depicts TGA curves of LSM_CGO_4 at various heating rates. For the same temperatures, the weight loss was higher at lower heating rates. Also, the faster the heating was applied the higher the decomposition temperature became.

In addition, examination of the enthalpy of the transition reaction was performed (Figure 6.1b). The sharp and high peak, observed when the sample was heated to 300 °C/h, is representative of a fast and drastic change in system energy. Such sharp and large energy transfers are unfavourable during burn-out process as they can cause large stresses in the system and further nucleation of cracks and other defects. Hence, slow heating rates are preferable.

TGA analysis performed with a heating rate of 30 °C/h, reveals a two-step weight loss of about 3% starting at about 50 °C and completed at 150 °C, presumably corresponding to evaporation of MEKET residues, the degradation of DBP and PEG. During heating at 150 °C-370 °C the second weight loss has occurs, which

corresponds to the degradation of PVB and PVP. In order to relieve stresses, a dwell time was added at temperatures corresponding to decomposition temperatures. Thus, the heating program was defined as shown in Figure 6.2. The heating rate up to 400 °C was 15 °C/h; the dwell temperatures were set at 100 °C, 200 °C and 400 °C. The subsequent heating rate of 30 °C/h up to the sintering temperature of 1300 °C; finally, the cooling rate was set to 60 °C. This sintering profile was applied for all co-cast green tapes in this work.

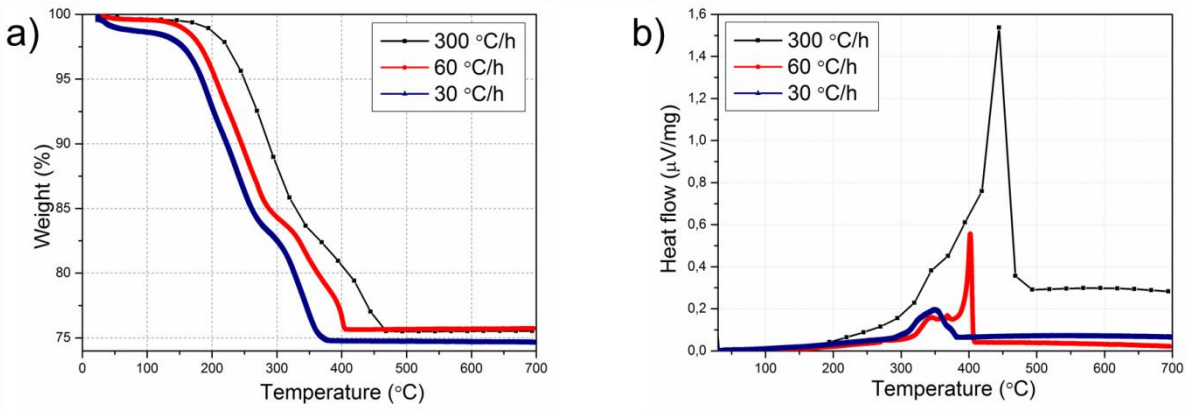

Figure 6.1. a) TGA and b) DSC thermograms of LSM_CGO_4 tape at heated rates of 300 °C/h, 60 °C/h, and 30 °C/h.

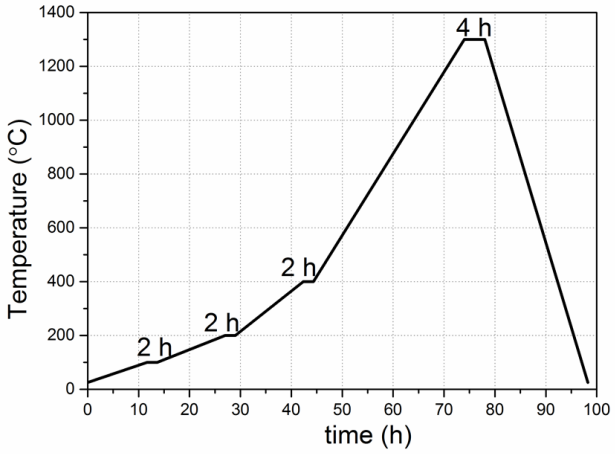

Function	Rate	Set point
Ramp	15 °C/h	100 °C
Hold	2 h	100 °C
Ramp	15 °C/h	200 °C
Hold	2 h	200 °C
Ramp	15 °C/h	400 °C
Hold	2 h	400 °C
Ramp	30 °C/h	1300 °C
Hold	4 h	1300 °C
Ramp	60 °C/h	25 °C

Figure 6.2. Sintering profile used for de-binding and sintering of LSM and LSM_CGO tapes.

6.2 Sintering of adjacently graded tapes

For understanding the sintering kinetics of adjacently graded tapes as well as further possible optimisation of the sintering profile aiming to obtain defect-free sintered graded materials, a detailed analysis of densification kinetics was performed. For this experiment graded tapes obtained by co-casting of LSM and LSM_CGO_4 slurries were chosen. In order to correlate shrinkage behaviour of the graded tapes, it was compared with the shrinkage of pure LSM and LSM_CGO_4 materials. Experimental analysis was carried out in a scanning electron microscope, a gas displacement density analyser and with the use of optical dilatometry.

6.2.1 Experimental procedure

Commercially available $La_{0.85}Sr_{0.15}MnO_3$ (LSM, calcined at 1200°C; d_{50}: 3.4 µm) and $Ce_{0.9}Gd_{0.1}O_2$ (CGO, uncalcined; d_{50}: 0.27 µm) were used as starting materials. The LSM and LSM_CGO_4 slurries were co-cast as it was described above (Section 5.3.). The mass-median-diameters (d_{50}) of particles in pre-casted slurries were 2.01 µm and 6.43 µm for the LSM and LSM_CGO_4 slurries, correspondingly.

The thickness of the dried green tape was measured along the length of the graded tape, both on LSM and LSM_CGO_4 sides, and were about 400 µm. Rectangular samples of 1x10 cm size with rounded corners were punched out for the free-sintering test, carried out in a chamber furnace. The only difference between the sintering program presented in Section 6.1 (Figure 6.2) and the sintering program applied here was a sintering temperature of 1300 °C. Three samples were cut from the LSM, LSM_CGO_4 parts of the green tape and one sample SBS_LSM_CGO containing an interface area in the middle of the 10 cm side. Obtained tapes were rolled and pressed so to form three "bulky" samples of LSM, LSM_CGO_4 and SBS_LSM_CGO to perform test in the optical dilatometer (TOMMI, Fraunhofer ISC, Germany) (Figure 6.3.). By this method, the shape development during de-binding and sintering is followed *in-situ* by gathering a sequence of images of the samples´ shadows projected by a source of visible light onto a high definition camera [163]. To observe the bending effect of graded SBS_LSM_CGO tapes a 1x10 cm piece was also placed in the chamber of the optical dilatometer with a wire indicating the interface area. The same de-binding and sintering program (Figure 6.2) was performed in the optical dilatometer. Linear dimensional changes were delivered by the instrument as the ratio l/l_0, where l is the instant dimension, and l_0 is the current dimension of the sample. Here, the term dimension is referring both to the height and width of the projected sample.

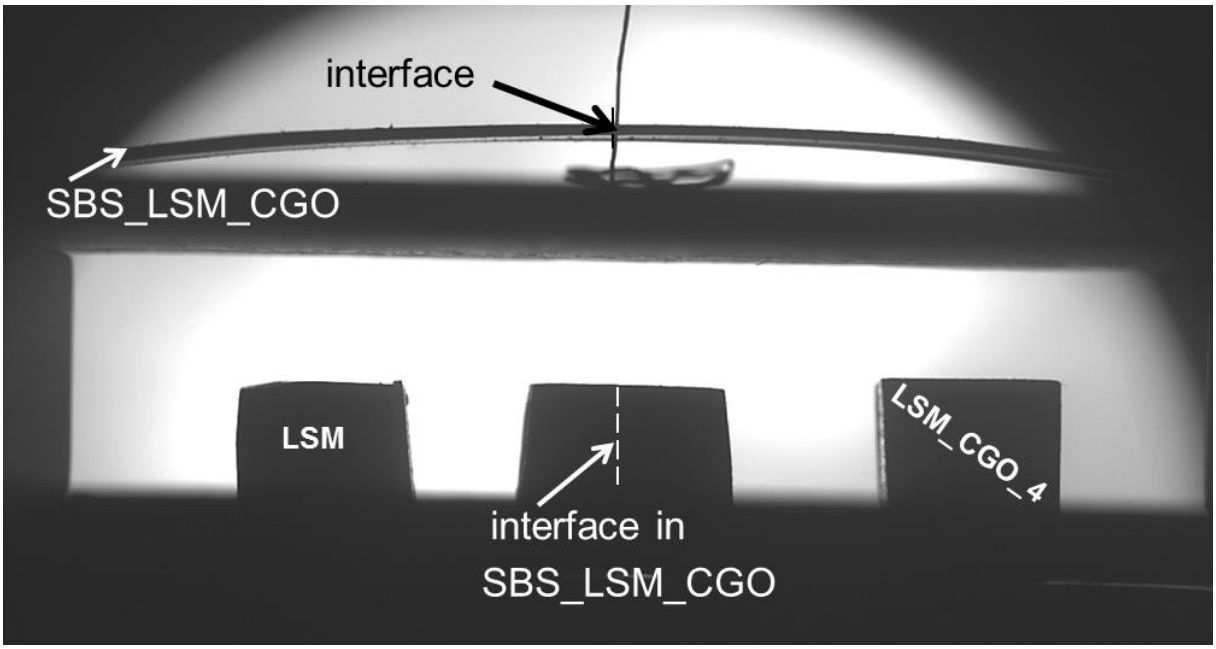

Figure 6.3. Photos of LSM, LSM_CGO_4 and graded SBS_LSM_CGO, which were rolled and pressed to obtain "bulky" materials, and SBS_LSM_CGO tape in profile in the optical dilatometer chamber at 200 °C.

The microstructure of tapes cross-sections were studied in a scanning electron microscope (SEM, Hitachi TM3000, Japan). The relative density was calculated based on SEM images by post-image processing using ImageJ software. In order to reduce errors, density values were re-calculated from 5 different positions chosen randomly for each sample. Densities of green, de-bindered and sintered tapes were also measured in a gas displacement density analyser (AccuPyc II 1340, Micromeretics Instrumental Corporation, GA).

6.2.2 Results and discussion

Figure 6.4. shows that cracks were formed during the heating experiment in the optical dilatometer. In order to elucidate the origin of these cracks, densification behaviour of pure LSM, LSM_CGO_4 and the graded sample SBS_LSM_CGO had to be compared. Figure 6.5 shows the variation of shrinkage in temperature range of 600 °C to 1300 °C, heated with 30 °C/h; the shrinkage during de-binding was subtracted. The strain curves for all three samples has a similar trend, however, the shrinkage behaviour of LSM_CGO_4 is slower compared to an LSM pellet (Figure 6.5a). The strain curve of the graded SBS_LSM_CGO tape is between the strain curves of pure LSM and LSM_CGO_4 pellet. Moreover, the temperature at which LSM_CGO_4 starts shrinking is about 60 °C lower comparing to LSM and SBS_LSM_CGO pellets. This tendency is even more obvious from the strain rate curves (Figure 6.5b). The shrinkage of LSM_CGO_4 starts at about 700 °C and achieves highest shrinkage at 1000 °C. The shrinkage rate of graded SBS_LSM_CGO starts slower together with the shrinkage of the LSM pellet at about 840 °C, but at temperatures higher than 900 °C it has a higher strain rate and achieves maximum shrinkage at about 1000 °C. The highest shrinkage of the LSM pellet is achieved at approximately 1010 °C. De Wei *et al.* [164] showed, that densification behaviour is sensitive to the shaping technique. Hence, there is a chance of minor uncertainties in strain and strain rate curves, which is attributed to stresses presumably occurring during the pressing of cast tapes into pellets.

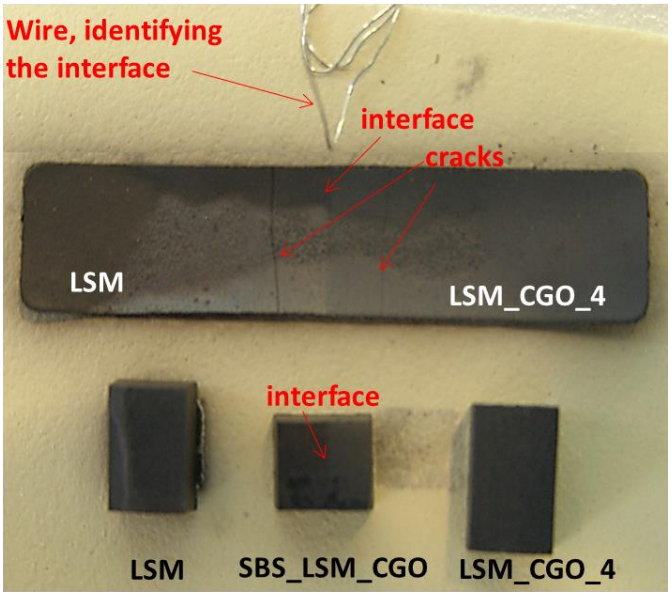

Figure 6.4. Photo of "bulky" LSM, LSM_CGO_4, and graded SBS_LSM_CGO samples, and SBS_LSM_CGO tape after sintering in the optical dilatometer.

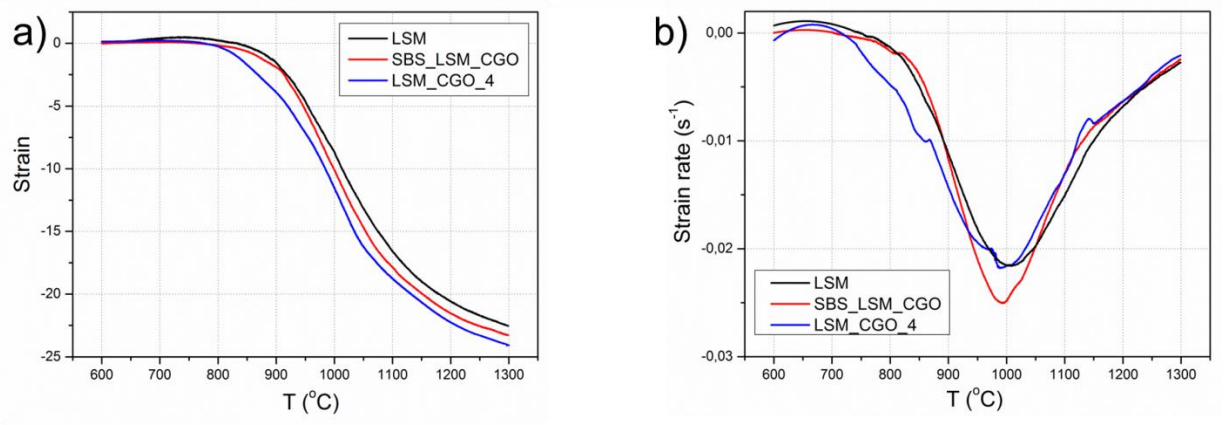

Figure 6.5. a) Strain upon sintering temperature and b) corresponding sintering strain rate for LSM, LSM_CGO_4 and graded SBS_LSM_CGO "bulky" samples, carried out in optical dilatometer.

The usage of the optical dilatometer TOMMI allows non-contact *in-situ* following of the sample densification process during firing with the possibility to register both swelling and shrinkage in a certain range of sizes and with a high enough resolution [165], [166]. Resolution of the optical dilatometer is usually enough to analyse shrinkage of cast tapes with a typical high content of organics, which burns off during the de-binding process. In order to calculate the tapes shrinkage, the shrinkage was assumed to be isotropic. The relative density was calculated based on the shrinkage strain measured on TOMMI:

$$\rho(T) = \rho_0 exp^{-3\varepsilon} \qquad 6.1.$$

where ρ_0 is the relative density of the green sample, and ε the linear strain. The green densities (the density of samples after de-binding) of the LSM and LSM_CGO_4 are given in the Table 6.3. Density evaluation during sintering was also examined based on SEM images (Figure 6.7) by a post-image processing technique (Table 6.2.) and it was measured in a gas displacement density analyser (Table 6.3).

Figure 6.6. depicts the variation of relative densities for all three pellets LSM, LSM_CGO_4 and SBS_LSM_CGO at a heating rate of 30 °C/h in the temperature range of 600 °C to 1300 °C. As in previous analyses of densification rate, this test also detects that densification of the LSM_CGO_4 pellet starts to densify earlier at around 800 °C. Densification of the LSM and SBS_LSM_CGO pellets starts 100 °C later at around 900 °C. The relative density for all three pellets is later increased continuously without forming a typical plateau at the final stage of sintering. The latter identifies that a further decrease in porosity is possible, hence, for future works on SBS TC it was decided to achieve by increasing a sintering time from 4 to 6 h.

Significant differences in the values of sintering densities during the firing was observed for the LSM and LSM_CGO_4 pellets compared to the densities of the SBS_LSM_CGO pellet. The same tendency is observed from the measurement of sintered densities by the post-image processing technique (Table 6.2) and gas displacement density analysis (Table 6.3.). Despite the increased porosity in the area next to the interface (about 2 mm to both sides of interface), what supposed to testify that the interface region is the weakest part of the sintered graded material, cracks if any were usually observed about 1.5-2 cm far from the interface line.

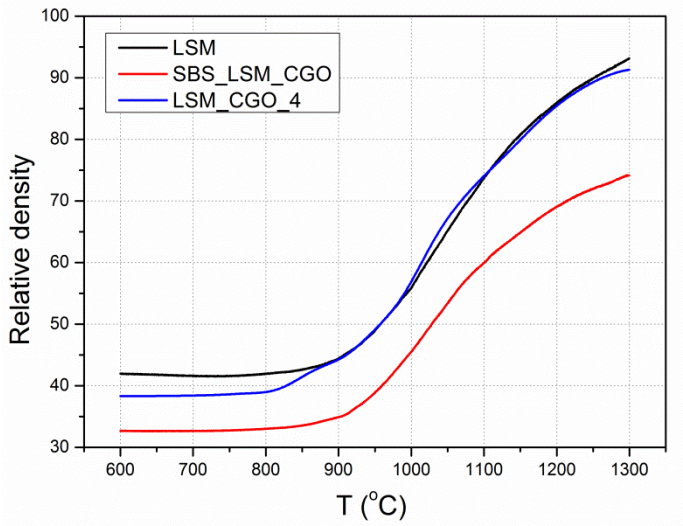

Figure 6.6. Relative density evolutions of LSM, LSM_CG_4 and SBS_LSM_CGO "bulky" laminated samples as a function of temperature during free sintering in optical dilatometer.

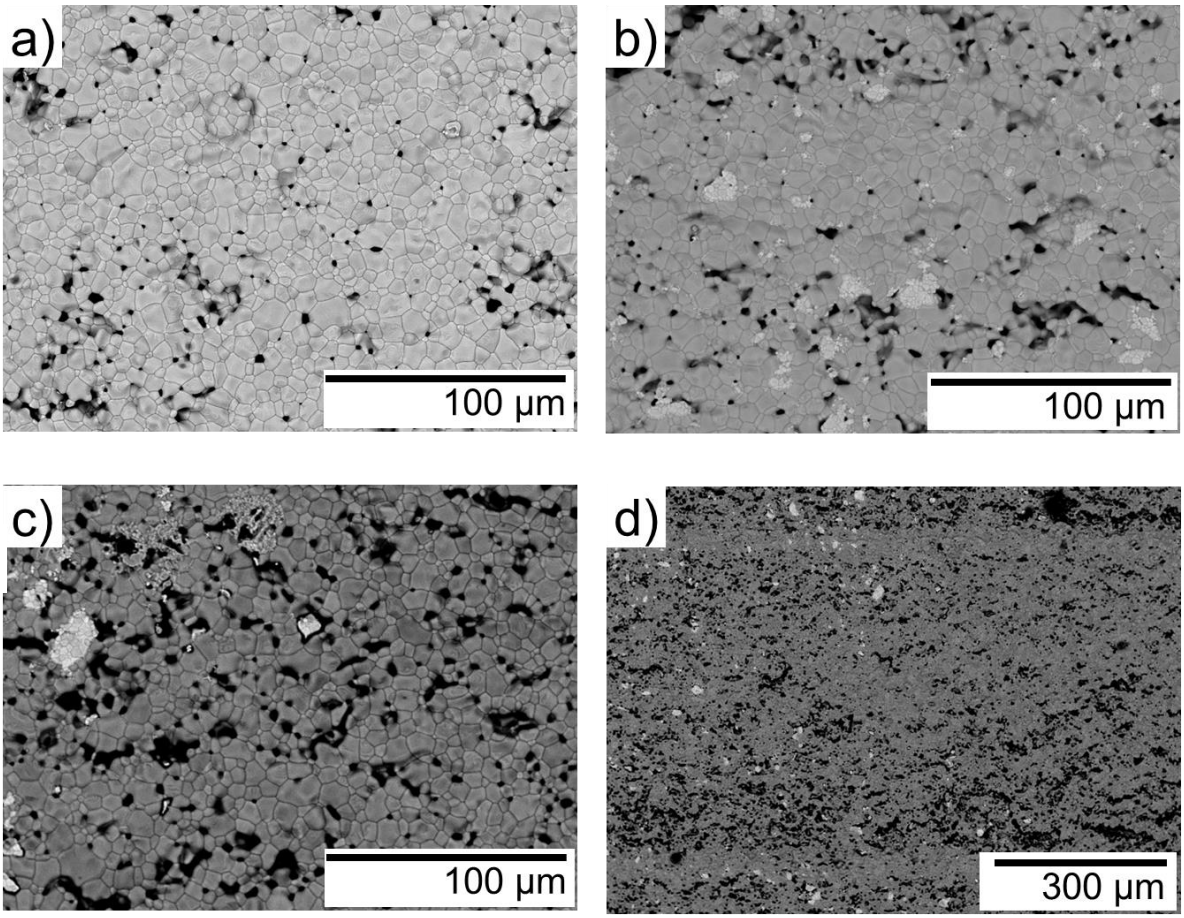

Figure 6.7. SEM images of cross sections for the sintered in optical dilatometer a) LSM, b) LSM_CGO_4, and c), d) SBS_LSM_CGO tapes.

Table 6.2. Density values (%), estimated from SEM images using ImageJ software.

	LSM	LSM_CGO_4	SBS_LSM_CGO
Green tape	45.58(5)	40.99(3)	-
De-bindered	50.73(4)	44.47(4)	-
Post-sintered	93.10(2)	91.45(5)	84.16(7)

Table 6.3. Density values (g/cm^3), measured by gas displacement density analyser.

	LSM	LSM_CGO_4	SBS_LSM_CGO
Green tape	3.606(1)	3.310(4)	3.633(3)
De-bindered	6.446(2)	6.462(4)	6.231(2)
Post-sintered	6.764(3)	7.075(2)	6.54(2)

Meanwhile, it was noticed that cracks were observed when thin films are cast on the repton plates, to which they were stick. Literature survey showed that a repton plates coated with ZrO_2, which at elevated temperatures reacts with strontium present in both LSM and LSM_CGO_4 and, furthermore, Mn ions dissolves into ZrO_2 [167]–[170]. LSM and LSM_CGO slurries were believed to penetrate into the pores of the repton plate in the de-binding stage, where tapes are partially melted due to the presence of binders. In order to eliminate this issue of sticking the sample to the repton plate, which presumably affects the degree of densification and further contributes to cracking, other sintering substrates were tested. Thus, graded tapes were sintered on LSM powder, paper, Al_2O_3 sintering plate and on a repton plate. Among these sintering substrates, paper was chosen for further sintering experiments. The criteria of choosing a sintering substrate were chemical inertness between tapes and substrates, absence of cracks and curvatures of sintered tapes, and smooth surfaces. Sintering on paper showed the best result in terms of unity of the sample, however, the

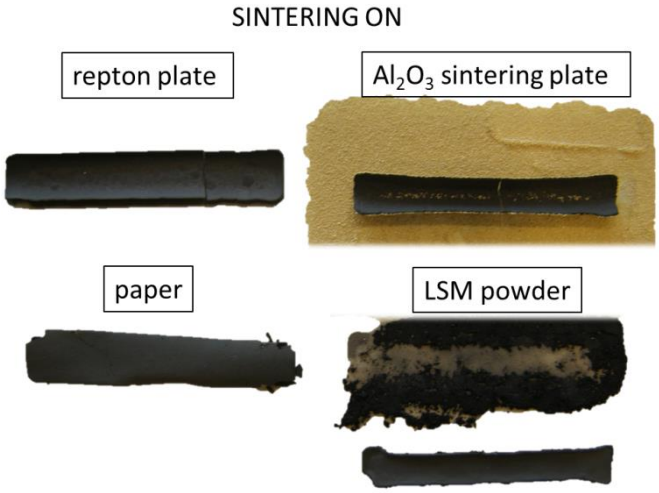

Figure 6.8. Photos of tapes sintered at repton plate, Al_2O_3 sintering plate, a piece of paper and LSM powder.

material was shown to be very fragile. In order to After sintering on paper, which is burned during the de-binding stage, defect-free tapes were obtained (Figure 6.8.).

The detailed study on distortions and camber developments during sintering is described both numerically and experimentally in Paper VII.

6.2.3 Conclusion

Compared sintering of pellets, obtained by pressing of cast tapes, densification of LSM and SBS_LSM_CGO starts at 900 °C, what is on 100 °C higher than densification start of LSM_CGO_4 pellet. All three pellets achieve their highest shrinkage rate at approximately 1000 °C. However, the relative density of the graded SBS_LSM_CGO pellet was shown to be lower during the whole sintering process, which is also proven by a porous microstructure observed next to the interface of the post-sintered tape. However, that does not make the interface area the weakest part of the graded tape as post-sintered cracks were always observed relatively far from the interface. The cracks were believed to originate in areas, which stick to the repton plate restraining sintering shrinkage. In order to suppress this issue, sintering of LSM and LSM_CGO contained thin plates was conducted on a paper.

6.3 Characterisation of the interface after sintering

When the main principles of SBS TC processing have been investigated and the whole shaping procedure from powder treatment to sintering as well as operational characteristics and slurries properties were consistently modified, the optimised patterns were applied for a lab-scale formation of a target magnetocaloric material. Five compositions of the magnetocaloric perovskite $La_{0.67}Ca_{0.33-x}Sr_xMn_{1.05}O_3$ (LCSM) with various $x \in [0.0375\text{-}0.0600]$ and, hence, exhibiting various T_C (Paper IV), were chosen to be co-cast into an adjacently graded magnetocaloric material. Since LCSM powder has a surface area different from LSM and CGO powders, new adjustments of five LCSM slurries recipes were required to obtain a final viscosity of about 4000 mPas. The details on tailoring slurries viscosities, adjacent co-casting and sintering can be found in Paper II. The goal of the current section is to verify the above stated principles for fabricating a distinctive steep interface between SBS cast materials and to demonstrate different approaches for its characterisation.

6.3.1 Experimental procedure

Spherical particles of a series of commercially available manganites with five different compositions $La_{0.66}Ca_{0.33-x}Sr_xMnO_3$ in the range of $x \in [0.0375\text{-}0.0600]$ (LCSM) (CerpoTech AS, Heimdal, Norway) were prepared by spray pyrolysis; subsequent calcination at 1000°C for 2 h was applied to remove the absorbed water from the powders and to increase the phase purity and get a coarser structure. The five LCSM powders were named from LCSM1 to LCSM5 according to the increasing Curie temperature (T_C) (Table 6.4) as the T_C is very sensitive to the composition of doped perovskites (Paper IV). The Curie temperature was measured as the point of maximum heat capacity in a zero applied magnetic field. This was measured on a custom built Differential Scanning Calorimeter (DSC) [172], and the results are shown in Figure 6.9. Due to the chemical similarity of the powders the exact composition of each powder is not known exactly. However, the correlation between the Curie temperature and the intended composition is consistent with that given in [173].

Table 6.4. Characteristics of the calcined LCSM powders.

	T_C, [K]	PSD (d_{50}), [µm]	BET [m^2/g]
LCSM1	272	1.43	7.53
LCSM2	277	2.04	10.85
LCSM3	281	2.08	7.97
LCSM4	284	1.63	15.04
LCSM5	288	1.74	10.86

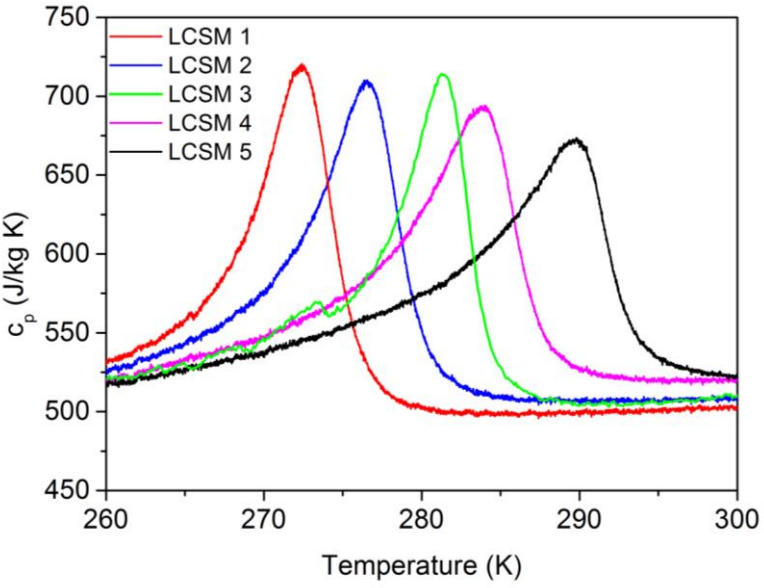

Figure 6.9. DSC data of the five LSCM powders at zero applied field after calcination at 1000°C.

The specific surface area of the powder was measured using the Brunauer, Emmett and Teller method (BET) (SA3100, Beckman Coulter Inc., Miami, FL) (Table 6.4). The slurry preparation was according to the earlier described procedure (Section 3.3.). The optimised composition of LCSM slurries (Paper II) were co-cast adjacently with a casting speed of 20 cm/min, gap of 1000 µm and no partition tongue beneath the casting blade, resulting in the formation of uniform defect-free green tape (Figure 6.10.). Further, samples of 100 mm length were punched from the green tape for further burn-out and sintering. Sintering conditions and heating profile are with respect to optimisation described in Section 6.1.

The magnetic properties were analysed using a Vibrating Sample Magnetometer (VSM) (Model 7407, Lake Shore Cryotronics Inc., Westerville, OH). Magnetisation as a function of the magnetic field and temperature was measured in fields up to 1.2 T. The magnetic entropy change ΔS_M (T,H) was calculated from magnetization curves employing the thermodynamic Maxwell relation:

$$\Delta S_M(T,H) = \int_0^H \left(\frac{\partial M}{\partial T}\right) dH \qquad 6.2.$$

Figure 6.10. Adjacently graded LCSM green tape. The width of the graded ceramic tape is 17.8 cm, and the length is 110 cm.

The interface regions of green and sintered graded tapes were investigated structurally by scanning electron microscopy. For a distinct identification of the interface region and analysing the degree of cross interface diffusion, the isothermal entropy change was measured by a vibrating sample magnetometer since the magnetic transition temperature (Curie temperature) is very sensitive to the dopant level in ceramics.

6.3.2 Results and discussion

As a result of a number of optimisation studies of LCSM slurries recipes and subsequent sintering, uniform defects-free adjacently graded tapes have been produced. Cross section between LCSM1 and LCSM2 for both green and sintered tapes was studied by SEM. In the case of the green tape, different particle and pore

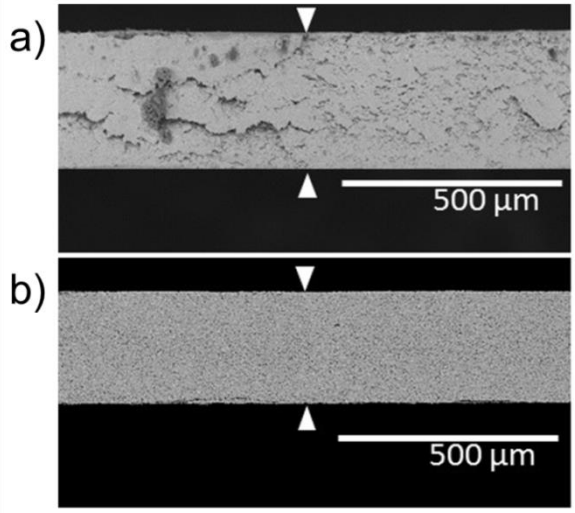

Figure 6.11. SEM microstructure of interface between LCSM1 and LCSM2 stripes in a) green and b) sintered states. The arrows indicate the interface between co-cast LCSM1 and LCSM2.

sizes of the adjacent materials indicate the position of the interface (Figure 6.11a). Unlike the green tape, the interface area in the sintered tape was difficult to find due to a uniform grain size and pore distribution along the whole graded tape (Figure 6.11b). This image confirms that the recipes of all the slurries were adjusted well enough, such that there is a perfect match in the shrinkage and strain development between neighbouring materials. Due to the very similar chemical compositions of the five LCSM materials used in this work, energy-dispersive X-ray spectroscopy (EDS), which would normally be used for the elemental analysis of chemical differences, was not able to resolve the interface.

Due to the high sensitivity to the exact composition of the materials magnetic properties of the different LCSM materials are used here to differentiate adjacently cast materials and distinguish the interface area. Figure 6.12 shows the isothermal entropy change ΔS_M of sintered tapes of the five materials LCSM1 through LCSM5 in an applied field of 1.2 T. These samples were cast and sintered individually in order to prevent any risk of contamination between co-cast materials. The entropy changes shown in Figure 6.12. can be seen to be relatively evenly spaced, with the peak height decreasing as the temperature increases. The peaks are found at values a few degrees higher than the specific heat peaks shown in Figure 6.9., which is presumably due to distributions of the dopants in the samples [174].

The ΔS_M peaks of individual materials (Figure 6.12) appeared to be very broad and located only a few degrees apart, the resulting ΔS_M curves from the samples cut from the interface region showed just one broad peak. In order to better characterise the interface region between two co-cast materials, samples were taken from a tape using two other compositions of LCSM from a similar batch. The temperature spacing between the ΔS_M peaks of these two adjacently cast LCSM materials was approximately 20 K, so that the two peaks are easily recognisable. Figure 6.13 shows the ΔS_M data recorded from the interface region in a field of 0.25 T. The low field strength was used in order to make the peaks narrower and thus easier to distinguish. The sample used for the measurements was broken from an area of the sintered tape containing the interface, with about

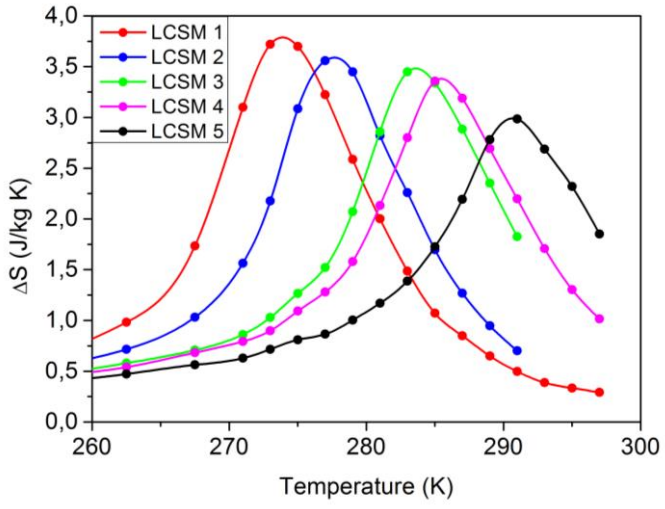

Figure 6.12. Temperature dependence of magnetic entropy change for LCSM stripes of sintered graded tape in the field of 1.2 T.

1 mm of material on either side of the interface. Since it was difficult to break the samples accurately to get the position of interface right in the middle, there was a difference in the height of the two peaks due to a difference in the amounts of the two materials on either sides. The red curve in Figure 6.13 represents a superposition of data recorded from individual samples of the two materials taken far from the interface region. It was found that using a ratio of 3.35 between the high and low transition temperature datasets reproduced the heights of the measured interface data best. It is observed that the peaks in the data recorded from the interface piece are spaced slightly closer together than the data from the individual pieces. This be due to some inter-diffusion of Ca and Sr between the two materials at the interface, causing the difference in the Ca/Sr ratio to even out. The profile of the peak in the ΔS_M data is determined by the local Ca/Sr ratios in the measured sample.

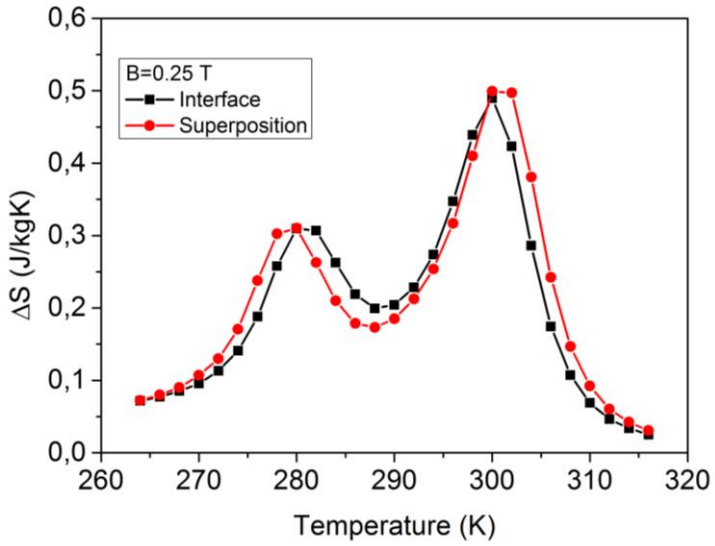

Figure 6.13. Temperature dependence of magnetic entropy change for sintered sample, containing interface between two LCSM stripes, and for the superposition of the data from the individual materials in an applied magnetic field of 0.25 T.

The cation diffusion constant for similar materials at 1275 K is in the order of 10^{-17} m^2/s [174]. Over a sintering time of four hours, this will only give rise to diffusion on the length scale of 10 μm. However, even a small overlapping of these thin tapes will result in a relatively large interface area. Thus diffusion and grain growth of mixed grains during the sintering process well explain the small shifting of the peaks in Figure 6.13.

6.3.3 Conclusion

Elaborated principles of SBS TC, studied on LSM and LSM_CGO slurries, are shown to be applicable for successful co-casting of other perovskite powders $La_{0.66}Ca_{0.33-x}Sr_xMnO_3$, $x \in [0.0375\text{-}0.0600]$. Uniform green tapes with a well distinguished in green state steep interfaces were obtained.

In order to distinguish the interface region, the magnetic properties of a graded plate were quantified. Curie temperature values, being very sensitive to dopant concentrations, showed a very good correlation of data measured empirically from the interface piece and re-calculated as a superposition of entropy change of

the individual materials. However, at elevated sintering temperatures only minor diffusion between co-cast materials was found, which proves that quite well defined interfaces between the materials can be maintained.

Tapes of adjacently side-by-side casted $La_{0.67}Ca_{0.33-x}Sr_xMn_{1.05}O_3$ materials have been produced in a quantity of 3 kg. These tapes are currently in use in a large scale magnetic refrigeration prototype.

7 Fabrication of alternative regenerator geometry

As it was described in Section 1.1., the performance of magnetic refrigeration is determined not only by the design and strength of the magnet and the magnetic properties of the materials, but the geometry of the regenerator is also of crucial importance. The greatest challenge of the mostly used regenerator design, which are packed spheres/particles and the parallel plate geometries, which were described earlier, is the precise spacing required between the plates/particles for the flow of heat transfer liquid. A well-packed material have been proven to yield the largest temperature spans and cooling powers [174]. However, these systems provide a large pressure drop resulting in a significant increase in losses. The requirements to the optimal geometry is a dense structure with highly ordered channels, for facilitating the movement of the heat transfer liquid, with an estimated diameter of 97 µm-129 µm [175]. This thesis proposes a new shaping process, based on the knowledge and experience obtained from the SBS TC technique. Furthermore, the main principles of producing a dense bulk material with highly ordered channels, which display equivalent performance to the packed-particles regenerator, but exhibit a lower pressure drop resulting in less losses.

The phenomenon observed earlier, when slurries were co-cast at high speeds and with the use of a long partition tongue, left a gap in the confluence area. This is a drawback for fabrication of uniform adjacently graded materials (Section 5.5). However, this drawback opens up for a possibility to create a comb-like structure by using a new co-casting technique. The engineering approach for fabrication of a highly ordered dense regenerator was a combination of: (i) a dense flat monolayer and (ii) a striped layer of the same material with a gap between the stripes of about 100 µm as well as a thickness of about 100 µm. If laminating a number of striped-flat-striped layers on top of each other (Figure 7.1a), the comb-like structure with highly-ordered open channels of 100 µm x 100 µm (Figure 7.1b) can be obtained.

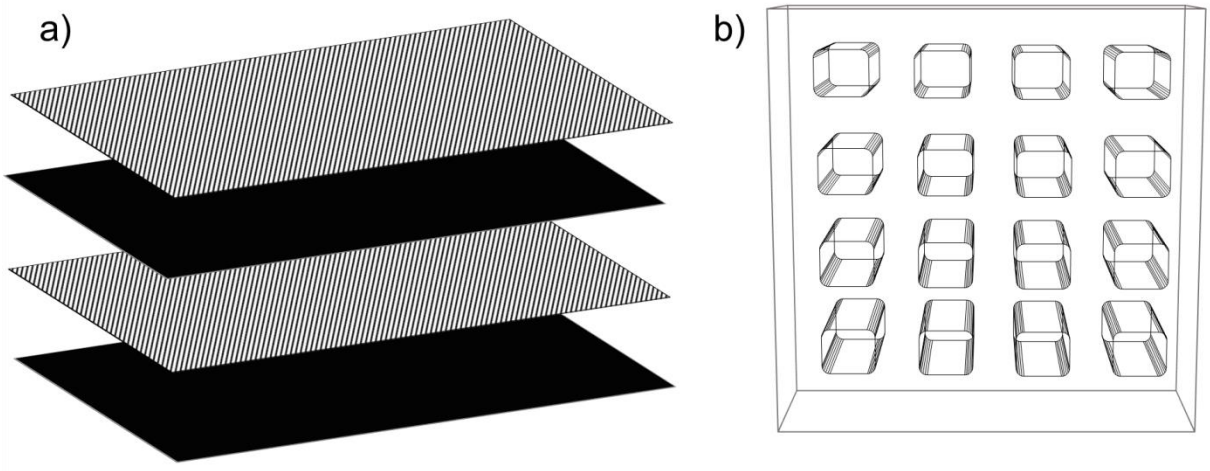

Figure 7.1. a) Schematic of stripped layer (stripped plate) produced by SBS TC at high casting speed and long partition length and uniform flat layer (black plate); b) the comb-like structure formed after lamination of stripped and flat layers.

For the current experiment, the LSM slurry was cast with a gap of 250 µm and a casting speed of 70 cm/min, forming a uniform flat monolayer. The thickness of the resultant flat green layer was 120±10 µm. In order to yield a striped layer, the LSM slurry was cast with the same casting gap of 250 µm and a speed of 70 cm/min, but in this case there were obstacles of 1 mm wide in front of the casting blade. Thus, the LSM slurry flow was separated by the obstacles after passing the casting blade region. As it was shown in Section 5.5., after passing the blade region, the slurry exhibits fluid deformable properties, *i.e.* free flow is hindered by a sharply increasing viscosity and simultaneous drying process. The last two phenomena were beneficial for forming a striped layer with the gap between the stripes of about 200 µm to 300 µm. High reproducibility of the LSM stripes' width and thicknesses was shown, by thickness measurements performed at different places along the striped tape, which implies formation of a uniform green tape with a high consistency in tape thickness.

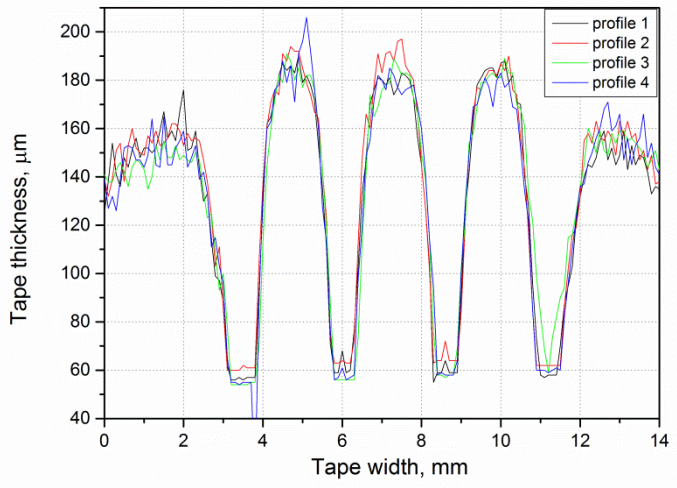

Figure 7.2. A number of profiles of stripped layer recorded at different places along the cast tape. The profile was measured by laser profilometer.

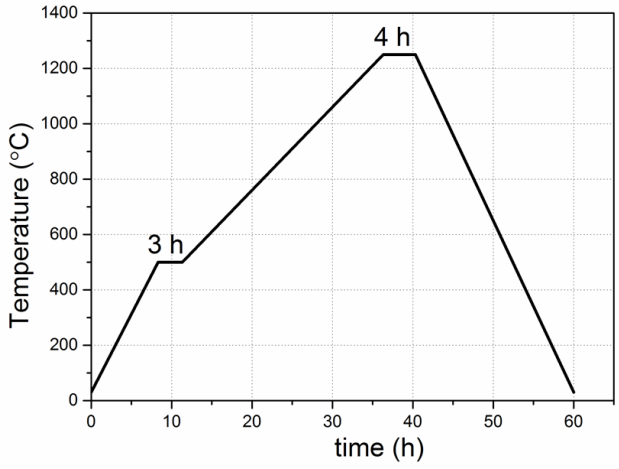

Function	Rate	Set point
Ramp	60 °C/h	500 °C
Hold	3 h	500 °C
Ramp	30 °C/h	1250 °C
Hold	4 h	1250 °C
Ramp	60 °C/h	25 °C

Figure 7.3. Sintering profile used for de-binding and sintering of LSM comb-like structure.

In order to obtain the required comb-like structure, flat and striped materials were first laminated at 80 °C. When the thickness of the laminated stacks exceeded 3 mm, they were hot pressed at 80 °C (30 s, 10 N) (Fortune Presses, Fortune, USA). For the sintering process, a very fast heating program was used in order to prevent filling the open channels by melting polymers (Figure 7.3). During the heating, the stack was inclined at about 30° to the chamber surface in order to minimise the effect of gravity on possible deformations.

The microstructure of the green and sintered comb-like geometry was studied in an optical microscope. Unfavourable coalescence of a number of striped layers, were observed already in the green state (Figure 7.4a), which was caused by inhomogeneous stress development in the lamination process. One of the suggested solutions aims to prevent coalescence, which includes closing the open channels by paraffin. Paraffin in this case, will support the shape of open channels during mild hot pressing and de-binding without leaving any residues. Another suggestion for eliminating the issue of coalescence is optimisation of the program used in the hot press machine. Despite issues with the green sample, the comb-like structure was shown to maintain the shape of the material and open channels (Figure 7.4b). Hence, if the challenge of collapsing striped layers can be solved, the comb-like geometry is expected to be a very promising alternative to existing regenerator structures.

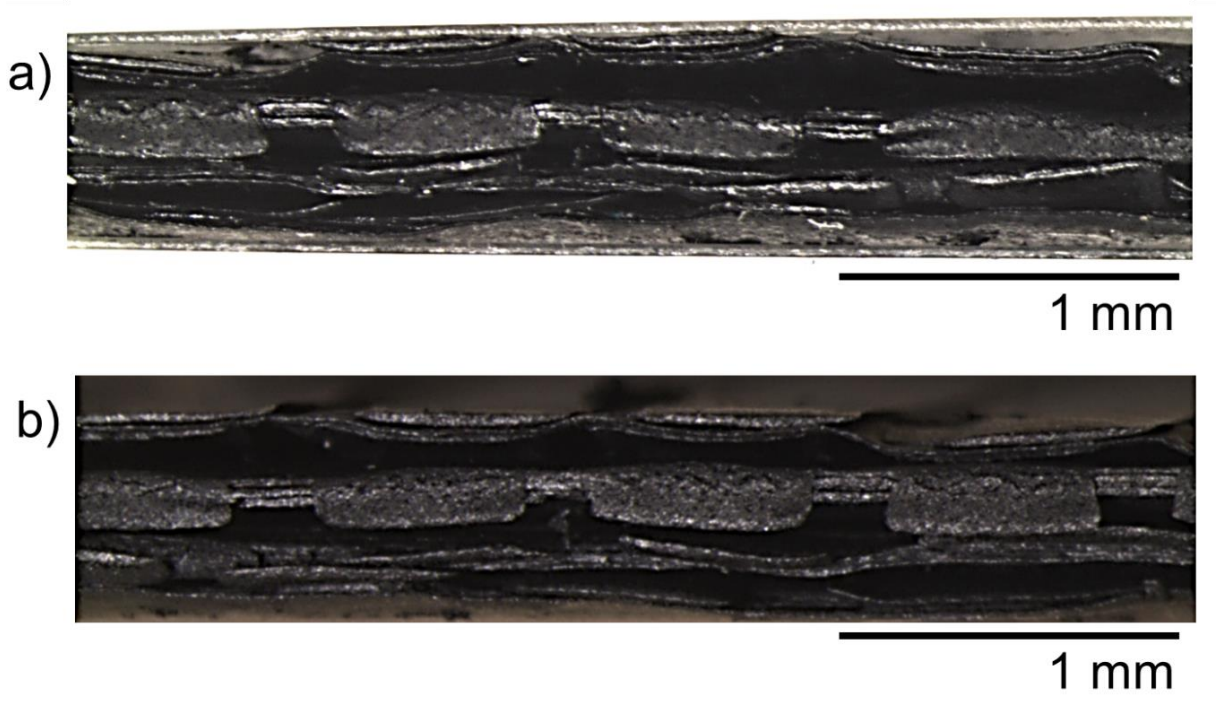

Figure 7.4. Microstructure of LSM comb-like geometry in a) green and b) sintered state.

8 Conclusion and Outlook

This PhD thesis describes the main challenges and identifies qualitative characteristics of the newly proposed design of adjacently graded thin tape and side-by-side tape casting as the main shaping technology used for its production. One of the fundamental parts was the recognition of the relevance and limitation of side-by-side tape casting, and tape casting in general, among other shaping techniques, what was aimed to expand and clarify the choice of an experimenter. Side-by-side tape casting was shown to be not just a new processing tool but rather an important contribution towards the creation of new designs for materials with promising features, with a possibility for up-scaling and applying a wide range of functional materials.

In collaboration with DTU MEK a novel quasi-steady state model has been developed, which together with distinguishing the role of the main casting parameters was the first to take into consideration a continuously decreasing slurry level in the tape caster reservoir. Creation of such a model was meaningful for the elaboration of further tape casting experiments with precisely-defined dimensional characteristics of cast tapes. Moreover, the developed quasi-steady state model based on experimental data established the kinetics program with which the pressure behind the casting blade reduces. Combining this program together with the tendency of tape thickness decrease with increase in casting speed, the new method to control the tape thickness during the casting process was developed. As the result of tape casting with use of proposed speed change mode, tapes with the highest thickness consistency have been obtained.

Contrary to the majority of existing reports it was shown that a single blade co-casting is sufficient to produce tapes with a high precision thickness control if a certain parameters are tailored. Thus, decrease of the casting gap, increase in the casting speed and reduction of slurry level in reservoir was shown to produce tapes with uniform tape consistency. Comparison of casting modes with use of a single blade, double blade, casting while supplying the slurry by a pump system and proposed method of continued processing speed change was aimed to be beneficial for most of fluid forming techniques in general. Looking for a casting mode which would guarantee a stable flow during co-casting, tape casting with the single blade was identified to be the most reliable for fabrication of lab-scale graded tapes.

In the scope of co-casting, the modification of the tape casting tank was described and the optimal slurry composition window was determined. Slurries with viscosities of 3000-6000 mPas at casting shear rates were shown to have good results. The control loss arises with increase in slurry viscosity since the shearing is not constant under the blade. The tape casting of low-viscous slurries on such segmented structures has been shown to be very complex and rather unsuccessful leading to poor interface qualities. One of the key requirements, which guarantee the possibility for slurries to be co-cast and form defect-free tapes, is the necessity to co-cast slurries with the same organic system and identical solid and organics load. The main finding was that slurry viscosity and the difference between viscosities of co-cast slurries define the extent of overlap, wherein casting speed is rather capable to determine the extent of overlap on a micro-scale and define the shape of the interface. Mechanical test verified that adhesion between co-cast materials is strong enough to hold the load of 5 N and to be broken far from the interface area. The partition length under the blade together with the casting speed was shown to be critical parameters influencing if co-cast slurries form an interface in confluence area or produce a two separated stripes of materials with splitting in between. Optimisation of de-binding and sintering programs was shown to gain crack-free post-sintered tapes.

Side-by-side tape casting reached the level what opens a wide horizon of various applicable technologies for new materials fabricated by co-casting. Thus, an alternative way to create a comb-like structure with the use of side-by-side tape casting technique has been proposed in current work. Side-by-side tape casting is already researched for the production of thermoelectric generators [144] and believed to promptly expand the application range among other emerging technologies.

The future development of side-by-side tape casting should be addressed to study of slurries surface tension as the impact factor on the interface quality; co-casting materials with various chemical composition, particle size and morphology. Besides, new interesting concepts like lamination of adjacently graded tapes are revealed and have to be studied in order to extent the design of promising functional graded materials.

9 Bibliography

[1] "National Research Council, Commercial Buildings Energy Consumption Survey Letter Report," Washington, DC, 2010.

[2] K. A. Gschneidner and V. K. Pecharsky, "Thirty years of near room temperature magnetic cooling: Where we are today and future prospects," *Int. J. Refrig.*, vol. 31, no. 6, pp. 945–961, 2008.

[3] B. F. Yu, Q. Gao, B. Zhang, X. Z. Meng, and Z. Chen, "Review on research of room temperature magnetic refrigeration," *Int. J. Refrig.*, vol. 26, no. 6, pp. 622–636, 2003.

[4] A. M. Tishin and Y. I. Spichkin, *The Magnetocaloric Effect and its Applications*. CRC Press, 2003, p. 476.

[5] V. K. Pecharsky and K. A. Gschneidner Jr, "Magnetocaloric effect and magnetic refrigeration," *J. Magn. Magn. Mater.*, vol. 200, no. 1, pp. 44–56, 1999.

[6] K. A. GschneidnerJr, V. K. Pecharsky, and A. O. Tsokol, "Recent developments in magnetocaloric materials," *Reports Prog. Phys.*, vol. 68, no. 6, pp. 1479–1539, 2005.

[7] J. A. Barclay and W. A. Steyert, "Active magnetic regenerator," US4332135 A, 01-Jun-1982.

[8] T. Okamura, K. Yamada, N. Hirano, and S. Nagaya, "Performance of a room-temperature rotary magnetic refrigerator," *Int. J. Refrig.*, vol. 29, no. 8, pp. 1327–1331, 2006.

[9] S. L. Russek and C. B. Zimm, "Potential for cost effective magnetocaloric air conditioning systems," *Int. J. Refrig.*, vol. 29, no. 8, pp. 1366–1373, 2006.

[10] G. V. Brown, "Magnetic heat pumping near room temperature," *J. Appl. Phys.*, vol. 47, no. 8, p. 3673, 1976.

[11] K. Engelbrecht, C. R. H. Bahl, and K. K. Nielsen, "Experimental results for a magnetic refrigerator using three different types of magnetocaloric material regenerators," *Int. J. Refrig.*, vol. 34, no. 4, pp. 1132–1140, 2011.

[12] C. R. H. Bahl, T. F. Petersen, N. Pryds, and A. Smith, "A versatile magnetic refrigeration test device.," *Rev. Sci. Instrum.*, vol. 79, no. 9, p. 093906, 2008.

[13] A. Smith, C. R. H. Bahl, R. Bjørk, K. Engelbrecht, K. K. Nielsen, and N. Pryds, "Materials Challenges for High Performance Magnetocaloric Refrigeration Devices," *Adv. Energy Mater.*, vol. 2, no. 11, pp. 1288–1318, 2012.

[14] K. K. Nielsen, C. R. H. Bahl, and K. Engelbrecht, "The effect of flow maldistribution in heterogeneous parallel-plate active magnetic regenerators," *J. Phys. D. Appl. Phys.*, vol. 46, no. 10, p. 105002, 2013.

[15] M. Kirchgässner, "Sådan køler DTU-forskere med magneter," *Ingeniøren*, Apr-2012.

[16] J. S. Reed, *Principles of ceramics processing*, 2nd ed. A Wiley-Interscience Publication, 1995.

[17] R. A. Terpstra, *Ceramic processing*. Chapman & Hall, 1995.

[18] M. Grant Norton, *Ceramic Materials*. New York, NY: Springer New York, 2007.

[19] H.W. Stetson, "Method of making multilayer circuits," US3189978 A, 22-Jun-1965.

[20] K. Lindqvist and E. Lid, "Preparation of Alumina Membranes Casting and Dip Coating by Tape," vol. 2219, no. 96, 1997.

[21] A. A. Tracton, *Coatings Technology: Fundamentals, Testing, and Processing Techniques*. CRC Press, 2007.

[22] R. R. Søndergaard, M. Hösel, and F. C. Krebs, "Roll-to-Roll fabrication of large area functional organic materials," *J. Polym. Sci. Part B Polym. Phys.*, vol. 51, no. 1, pp. 16–34, 2013.

[23] E. H. Jewell, T. C. Claypole, and D. T. Gethin, "Viscosity control in the screen printing of ceramic transfers," *Surf. Coatings Int. Part B Coatings Trans.*, vol. 86, no. 2, pp. 155–163, 2003.

[24] E. Messerschmitt, "Der Siebdruck mit Thermoplastischen (Hot-Melt-)Farben aus Glas und Keramik. left bracket Screen Pressure with Thermoplastic (Hot-Melt-) Glass and Ceramic Paints right bracket" *Sprechsaal*, vol. 118, no. 8, pp. 660 – 663, 1985.

[25] J. De Vicente, *Rheology*. InTech, 2012.
[26] Y. Xia, "Soft lithography," *Annu. Rev. Mater. Sci.*, vol. 28, pp. 153 – 184, 1998.
[27] M. R. Mackley, "The high shear rheology of lithographic emulsions," *Surf. Coatings Int. Part B Coatings Int.*, vol. 83, no. 5, pp. 234 – 239, 2000.
[28] N. J. Arsten, P. J. P. Buskens, and M. Rooijmans, "Slot Die Coating Process," 20120058260, 2012.
[29] Y. Takahashi, S. Okada, R. Bel Hadj Tahar, K. Nakano, T. Ban, and Y. Ohya, "Dip-coating of ITO films," *J. Non. Cryst. Solids*, vol. 218, pp. 129–134, 1997.
[30] P. Yimsiri and M. R. Mackley, "Spin and dip coating of light-emitting polymer solutions: Matching experiment with modelling," *Chem. Eng. Sci.*, vol. 61, no. 11, pp. 3496–3505, 2006.
[31] T. M. Sullivan and S. Middleman, "Film thickness in blade coating of viscous and viscoelastic liquids," *J. Nonnewton. Fluid Mech.*, vol. 21, no. 1, pp. 13–38, 1986.
[32] E.-C. Chen, P.-T. Tsai, B.-J. Chang, C.-M. Wang, H.-F. Meng, J.-Y. Tsai, Y.-F. Chang, Z.-K. Chen, C.-H. Li, Y.-H. Hsu, C.-Y. Chen, H.-W. Lin, H.-W. Zan, and S.-F. Horng, "Multilayer rapid-drying blade coating for organic solar cells by low boiling point solvents," *Jpn. J. Appl. Phys.*, vol. 53, no. 6, p. 062301, 2014.
[33] N. Straue, S. Prado, S. Polster, and A. Roosen, "Profile Rod Technique: Continuous Manufacture of Submicrometer-Thick Ceramic Green Tapes and Coatings Demonstrated for Nanoparticulate Zinc Oxide Powders," *J. Am. Ceram. Soc.*, vol. 94, no. 6, pp. 1698–1705, 2011.
[34] L. Besra and M. Liu, "A review on fundamentals and applications of electrophoretic deposition (EPD)," *Prog. Mater. Sci.*, vol. 52, no. 1, pp. 1–61, 2007.
[35] F. Bozza and N. Bonanos, "Fabrication of supported Ca-doped lanthanum niobate electrolyte layer and NiO containing anode functional layer by electrophoretic deposition," *Solid State Ionics*, vol. 213, pp. 98–102, 2012.
[36] N. Miura, "Oxygen semipermeability of mixed-conductive oxide thick-film prepared by slip casting," *Solid State Ionics*, vol. 79, pp. 195–200, 1995.
[37] R. E. Mistler and E. R. Twiname, *Tape Casting: Theory and Practice*. Wiley-American Ceramic Society, 2000.
[38] G. T. Halmos, *Roll Forming Handbook*. Press, CRC, 2005.
[39] A. Lakota, W. E. Lock, J. A. Schultes, and J. C. Thomas, "Precision glass roll forming process and apparatus," US20120304695 A1, 09-Apr-2012.
[40] T. Hyatt, "Electronics - Tape Casting, Roll Compaction," *Am. Ceram. Soc. Bull.*, vol. 74, no. 10, pp. 56 – 59, 1995.
[41] R. K. Suárez, T. K. M. Suárez, A. Fernández, J.L. Menéndez, R. Torrecillas, H. U. Kessel, J. Hennicke, "Challenges and Opportunities for Spark Plasma Sintering: A Key Technology for a New Generation of Materials," in *Sintering Applications*, B. Ertug, Ed. InTech, 2013.
[42] http://www.britannica.com/EBchecked/media/262/Steps-in-doctor-blading-atape-casting-process-employed-in.
[43] G. N. Howatt, "Method of producing high dielectric high insulation ceramic plates," US2582993 A, 22-Jan-1952.
[44] G. N. Howatt, R. G. Breckenridge, and J. M. Brownlow, "Fabrication Of Thin Ceramic Sheets For Capacitors," *J. Am. Ceram. Soc.*, vol. 30, no. 8, pp. 237–242, 1947.
[45] P. J. J. Lawrence, "Manufacture of ceramics," US2966719 A, 03-Jan-1961.
[46] W. J. Gyurk, "Methods for manufacturing multilayered monolithic ceramic bodies," US3192086 A, 29-Jun-1965.
[47] Schwartz, "Laminated ceramics," *Seventeenth Electron. Components Conf.*, pp. 17–26, 1967.
[48] C. W. Ho, D. A. Chance, C. H. Bajorek, and R. E. Acosta, "The Thin-Film Module as a High-Performance Semiconductor Package," *IBM J. Res. Dev.*, vol. 26, no. 3, pp. 286–296, 1982.

[49] B. Schwartz, “Microelectronics packaging II,” *Am. Ceram. Soc. Bull.*, vol. 63, no. 4, pp. 577–581, 1984.
[50] R. R. Tummala, “Ceramic and Glass-Ceramic Packaging in the 1990s,” *J. Am. Ceram. Soc.*, vol. 74, no. 5, pp. 895–908, 1991.
[51] K. Niwa, “Recent progress in multilayer ceramic substrates,” *Multilayer Electron. Ceram. devices*, vol. 97, pp. 171 – 182, 1999.
[52] H. Loest, R. Lipp, and E. Mitsoulis, “Numerical flow simulation of viscoplastic slurries and design criteria for a tape casting unit,” *J. Am. Ceram. Soc.*, vol. 77, no. 1, pp. 254 – 262, 1994.
[53] T. Chartier, E. Streicher, and P. Boch, “Preparation and characterization of tape cast aluminum nitride substrates,” *J. Eur. Ceram. Soc.*, vol. 9, no. 3, pp. 231–242, 1992.
[54] M. Descamps, G. Moreau, M. Mascart, and B. Thierry, “Processing of aluminium nitride powder by the tape-casting process,” *J. Eur. Ceram. Soc.*, vol. 13, no. 3, pp. 221–228, 1994.
[55] A. S. Thorel, “Tape Casting Ceramics for high temperature Fuel Cell applications,” in *Ceramic Materials*, W. Wunderlich, Ed. 2010, pp. 49–69.
[56] R. Costa, J. Hafsaoui, A. P. Almeida de Oliveira, A. Grosjean, M. Caruel, A. Chesnaud, and A. Thorel, “Tape casting of proton conducting ceramic material,” *J. Appl. Electrochem.*, vol. 39, no. 4, pp. 485–495, 2008.
[57] H. Jantunen, T. Hu, A. Uusimäki, and S. Leppävuori, “Tape casting of ferroelectric, dielectric, piezoelectric and ferromagnetic materials,” *J. Eur. Ceram. Soc.*, vol. 24, no. 6, pp. 1077–1081, 2004.
[58] N. Straue, M. Rauscher, M. Dressler, and A. Roosen, “Tape Casting of ITO Green Tapes for Flexible Electroluminescent Lamps,” *J. Am. Ceram. Soc.*, vol. 95, no. 2, pp. 684–689, 2012.
[59] C. Fiori and G. De Portu, “Tape Casting: A Technique For Preparing And Studying New Materials,” *Br. Ceram. Proc.*, no. 38, pp. 213 – 225, 1986.
[60] P.-M. Geffroy, T. Chartier, and J.-F. Silvain, “Innovative Approach to Metal Matrix Composites Film by Tape Casting Process,” *Adv. Eng. Mater.*, vol. 9, no. 7, pp. 547–553, 2007.
[61] B. Kieback, A. Neubrand, and H. Riedel, “Processing techniques for functionally graded materials,” *Mater. Sci. Eng. A*, vol. 362, no. 1, pp. 81–106, 2003.
[62] N. C. Acikbas, E. Suvaci, and H. Mandal, “Fabrication of Functionally Graded SiAlON Ceramics by Tape Casting,” *J. Am. Ceram. Soc.*, vol. 89, no. 10, pp. 3255–3257, 2006.
[63] D. B. Sabljic and D. S. Wilkinson, “Fabrication of Ni-NiO composites by tape casting,” *Ind. Heat.*, vol. 63, no. 9, pp. 85 – 87, 1996.
[64] A. Rowe and A. Tura, “Experimental investigation of a three-material layered active magnetic regenerator,” *Int. J. Refrig.*, vol. 29, no. 8, pp. 1286–1293, 2006.
[65] D. S. Arnold, A. Tura, and A. Rowe, “Experimental analysis of a two-material active magnetic regenerator,” *Int. J. Refrig.*, vol. 34, no. 1, pp. 178–191, 2011.
[66] A. R. Dinesen, S. Linderoth, N. Pryds, and A. Smith, “A magnetic regenerator, a method of making a magnetic regenerator, a method of making an active magnetic refrigerator and an active magnetic refrigerator,” PCT/EP2005/013654, 20-Jul-2006.
[67] A. Thorel, “Ceramic Materials,” W. Wunderlich, 2010.
[68] A. Basile and S. Nunes, *Advanced Membrane Science and Technology for Sustainable Energy and Environmental Applications*. Elsevier, 2011.
[69] Z. Peng and M. Liu, “Preparation of Dense Platinum-Yttria Stabilized Zirconia and Yttria Stabilized Zirconia Films on Porous $La_{0.9}Sr_{0.1}MnO_3$ (LSM) Substrates,” *J. Am. Ceram. Soc.*, vol. 84, no. 2, pp. 283–88, 2004.
[70] K. Engelbrecht, R. Bjørk, D. Eriksen, A. Smith, N. Pryds, and C. R. H. Bahl, “Design Concepts for a Continuously Rotating Active Magnetic Regenerator,” *4th Int. Conf. IIR Magn. Refrig. Room Temp.*, pp. 351 – 358, 2010.

[71] J. H. Van Santen and G. H. Jonker, “Electrical conductivity of ferromagnetic compounds of manganese with perovskite structure,” *Physica*, vol. 16, no. 7–8, pp. 599–600, 1950.
[72] Zener, “Interaction between the d shells in the transition metals,” *Phys. Rev.*, vol. 81, pp. 440 – 444, 1951.
[73] E. O. Wollan and W. C. Koehler, “Neutron Diffraction Study of the Magnetic Properties of the Series of Perovskite-Type Compounds $La_{1-x}Ca_xMnO_3$,” *Phys. Rev.*, vol. 100, no. 2, pp. 545–563, 1955.
[74] W. C. Koehler and E. O. Wollan, “Neutron-diffraction study of the magnetic properties of perovskite-like compounds LaBO3,” *J. Phys. Chem. Solids*, vol. 2, no. 2, pp. 100–106, 1957.
[75] W. Koehler, E. Wollan, and M. Wilkinson, “Neutron Diffraction Study of the Magnetic Properties of Rare-Earth-Iron Perovskites,” *Phys. Rev.*, vol. 118, no. 1, pp. 58–70, 1960.
[76] J. Volger, “Further experimental investigations on some ferromagnetic oxidic compounds of manganese with perovskite structure,” *Physica*, vol. 20, no. 1–6, pp. 49–66, 1954.
[77] S. Jin, T. H. Tiefel, M. McCormack, R. A. Fastnacht, R. Ramesh, and L. H. Chen, “Thousandfold change in resistivity in magnetoresistive la-ca-mn-o films.,” *Science*, vol. 264, no. 5157, pp. 413–5, 1994.
[78] W. Vielstich, A. Lamm, and H. A. Gasteiger, *Handbook of Fuel Cells: Fundamentals, Technology, and Applications, Bind 4,Del 2*. 2003.
[79] D. D. L. Chung, *Functional Materials: Electrical, Dielectric, Electromagnetic, Optical and Magnetic Applications,*World Scientific Publishing Company, 2010.
[80] D. T. Morelli, A. M. Mance, J. V. Mantese, and A. L. Micheli, “Magnetocaloric properties of doped lanthanum manganite films,” *J. Appl. Phys.*, vol. 79, no. 1, p. 373, 1996.
[81] V. M. Goldschmidt, “Die Gesetze der Krystallochemie,” *Naturwissenschaften*, vol. 14, no. 21, pp. 477–485, 1926.
[82] G. H. Jonker and J. H. Van Santen, “Ferromagnetic compounds of manganese with perovskite structure,” *Physica*, vol. 16, no. 3, pp. 337–349, 1950.
[83] R. D. Shannon, “Revised effective ionic radii and systematic studies of interatomic distances in halides and chalcogenides,” *Acta Crystallogr. Sect. A*, vol. 32, no. 5, pp. 751–767, 1976.
[84] J. Coey, M. Viret, L. Ranno, and K. Ounadjela, “Electron Localization in Mixed-Valence Manganites,” *Phys. Rev. Lett.*, vol. 75, no. 21, pp. 3910–3913, 1995.
[85] S. Blundell, *Magnetism in condensed matter*. Oxford University Press, 2003.
[86] J. Coey, “Mixed-valence manganites,” *Adv. Phys.*, vol. 48, no. 2, pp. 167 – 293, 1999.
[87] J. B. Goodenough, “Theory of the Role of Covalence in the Perovskite-Type Manganites [La, M(II)]MnO_3,” *Phys. Rev.*, vol. 100, no. 2, pp. 564–573, 1955.
[88] E. Krogh Andersen, I. G. Krogh Andersen, P. Norby, and J. C. Hanson, “Kinetics of Oxidation of Fuel Cell Cathode Materials Lanthanum Strontium Manganates(III)(IV) at Actual Working Conditions:In SituPowder Diffraction Studies,” *J. Solid State Chem.*, vol. 141, no. 1, pp. 235–240, 1998.
[89] I. G. K. Andersen, E. K. Andersen, P. Norby, and E. Skou, “Determination of Stoichiometry in Lanthanum Strontium Manganates(III)(IV) by Wet Chemical Methods,” *J. Solid State Chem.*, vol. 113, no. 2, pp. 320–326, 1994.
[90] M. Gaudon, C. Laberty-Robert, F. Ansart, P. Stevens, and A. Rousset, “Preparation and characterization of $La_{1-x}Sr_xMnO_{3+\delta}$ ($0 \leqslant x \leqslant 0.6$) powder by sol–gel processing,” *Solid State Sci.*, vol. 4, no. 1, pp. 125–133, 2002.
[91] A. A. Rabelo, M. C. de Macedo, D. M. de A. Melo, C. A. Paskocimas, A. E. Martinelli, and R. M. do Nascimento, “Synthesis and characterization of $La_{1-x}Sr_xMnO_{3\pm\delta}$ powders obtained by the polymeric precursor route,” *Mater. Res.*, vol. 14, no. 1, pp. 91–96, 2011.
[92] A. Roosen, “Tape casting,” in *Ceramics Science and Technology*, R. Riedel and I.-W. Chen, Eds. Weinheim, Germany: Wiley-VCH Verlag GmbH & Co. KGaA, 2011, pp. 39–62.

[93] H. Raeder, C. Simon, T. Chartier, and H. L. Toftegaard, “Tape casting of zirconia for ion conducting membranes: A study of dispersants,” *J. Eur. Ceram. Soc.*, vol. 13, no. 6, pp. 485–491, 1994.
[94] D. Hotza and P. Greil, “Review: aqueous tape casting of ceramic powders,” *Mater. Sci. Eng. A*, vol. 202, no. 1–2, pp. 206–217, 1995.
[95] S. Guillemet-Fritschc, “The thickness of $BaTiO_3$ tape castings as function of the slip system,” *J. Ceram. Process. Res.*, vol. 13, no. 2, pp. 101 – 104, 2012.
[96] C. Wang, H. Ji, and J. Wang, “Effects of solvent system on tape casting of the $BaSrTiO_3$-MgO-based dielectric ceramics containing B_2O_3,” *J. Mater. Sci.*, vol. 47, no. 5, pp. 2486–2491, 2011.
[97] Z. Jingxian, J. Dongliang, L. Weisensel, and P. Greil, “Binary solvent mixture for tape casting of TiO_2 sheets,” *J. Eur. Ceram. Soc.*, vol. 24, no. 1, pp. 147–155, 2004.
[98] P. H. Larsen and K. Brodersen, “Improved method for the manufacture of reversible solid oxide cells,” CA2611362, 02-Oct-2012.
[99] F. Li, C. Wang, and K. Hu, “Optimization of non-aqueous nickel slips for manufacture of MCFC electrodes by tape casting method,” *Mater. Res. Bull.*, vol. 37, no. 12, pp. 1907–1921, 2002.
[100] J.-K. Song, W.-S. Um, H.-S. Lee, M.-S. Kang, K.-W. Chung, and J.-H. Park, “Effect of polymer molecular weight variations on PZT slip for tape casting,” *J. Eur. Ceram. Soc.*, vol. 20, no. 6, pp. 685–688, 2000.
[101] A. Ceylan, E. Suvaci, and H. Mandal, “Role of organic additives on non-aqueous tape casting of SiAlON ceramics,” *J. Eur. Ceram. Soc.*, vol. 31, no. 1–2, pp. 167–173, 2011.
[102] I. Rachas, T. . Tadros, and P. Taylor, “The displacement of adsorbed polymer from silica surfaces by the addition of a nonionic surfactant,” *Colloids Surfaces A Physicochem. Eng. Asp.*, vol. 161, no. 2, pp. 307–319, 2000.
[103] S. L. Natividad, V. R. Marotto, L. S. Walker, D. Pham, W. Pinc, and E. L. Corral, “Tape Casting Thin, Continuous, Homogenous, and Flexible Tapes of ZrB2,” *J. Am. Ceram. Soc.*, vol. 94, no. 9, pp. 2749–2753, 2011.
[104] A. I. Y. Tok, F. Y. C. Boey, and Y. C. Lam, “Non-Newtonian fluid flow model for ceramic tape casting,” *Mater. Sci. Eng. A*, vol. 280, no. 2, pp. 282–288, 2000.
[105] T. G. Mezger, *The Rheology Handbook: For Users of Rotational and Oscillatory Rheometers*, 3rd revise. Hanover, Germany: Vincentz Network GmbH & Co KG, 2006.
[106] G. Schramm, *A Practical Approach to Rheology and Rheometry*. Karlsruhe: Gebrueder HAAKE GmbH, 1994.
[107] A. K. Kordon, R. Pitchumani, A. N. Beris, V. M. Karbhari, and P. S. Dhurjati, “A rheological model for particulate ceramic slurries at low temperatures,” *Scr. Metall. Mater.*, vol. 29, no. 8, pp. 1095–1099, 1993.
[108] R. Byron-Bird, “Rheology And Flow Of Viscoplastic Materials,” *Rev. Chem. Eng.*, vol. 1, no. 1, pp. 1 – 70, 1983.
[109] R. B. Bird, “Transport phenomena,” *Appl. Mech. Rev.*, vol. 55, no. 1, p. R1, 2002.
[110] A. Mukherjee, B. Maiti, A. Das Sharma, R. N. Basu, and H. S. Maiti, “Correlation between slurry rheology, green density and sintered density of tape cast yttria stabilised zirconia,” *Ceram. Int.*, vol. 27, no. 7, pp. 731–739, 2001.
[111] A. I. Y. Tok, F. Y. C. Boey, and M. K. A. Khor, “Tape Casting of High Dielectric Ceramic Substrates for Microelectronics Packaging,” vol. 8, no. August, pp. 469–472, 1999.
[112] M. D. Snel, J. van Hoolst, a.-M. de Wilde, M. Mertens, F. Snijkers, and J. Luyten, “Influence of tape cast parameters on texture formation in alumina by templated grain growth,” *J. Eur. Ceram. Soc.*, vol. 29, no. 13, pp. 2757–2763, 2009.
[113] N. Li, Z. Wen, Y. Liu, X. Xu, J. Lin, and Z. Gu, “Preparation of Na-beta”-alumina film by tape casting process,” *J. Eur. Ceram. Soc.*, vol. 29, no. 14, pp. 3031–3037, 2009.

[114] S. L. Liu, Q. Shen, G. Q. Luo, M. J. Li, and L. M. Zhang, "Calculation of Tape Thickness for Ceramic Tape Casting," *Key Eng. Mater.*, vol. 512–515, pp. 328–333, 2012.
[115] S. C. Joshi, Y. . Lam, F. Y. . Boey, and A. I. . Tok, "Power law fluids and Bingham plastics flow models for ceramic tape casting," *J. Mater. Process. Technol.*, vol. 120, no. 1–3, pp. 215–225, 2002.
[116] G. Zhang, Y. Wang, and J. Ma, "Bingham plastic fluid flow model for ceramic tape casting," *Mater. Sci. Eng. A*, vol. 337, no. 1–2, pp. 274–280, 2002.
[117] M. Jabbari and J. Hattel, "Bingham plastic fluid flow model in tape casting of ceramics using two doctor blades – analytical approach," *Mater. Sci. Technol.*, vol. 30, no. 3, pp. 283–288, 2014.
[118] J. Li, "Preparation of Non-Aqueous Mg Green Tapes by Tape Casting," *Synth. React. Inorg. Met. NANO-METAL Chem.*, vol. 42, no. 5, pp. 758 – 763, 2012.
[119] D. Gardini, M. Deluca, M. Nagliati, and C. Galassi, "Flow properties of PLZTN aqueous suspensions for tape casting," *Ceram. Int.*, vol. 36, no. 5, pp. 1687–1696, 2010.
[120] J. Yang, "Preparation of $Y_3Fe_{4.85}O_{12}$ ferrite substrates by non aqueous tape casting," *Rengong Jingti Xuebao/Journal Synth. Cryst.*, vol. 41, no. 3, pp. 753 – 758, 2012.
[121] N. Chantaramee, S. Tanaka, Z. Kato, N. Uchida, and K. Uematsu, "Characterization of particles packing in alumina green tape," *J. Eur. Ceram. Soc.*, vol. 29, no. 5, pp. 943–948, 2009.
[122] K. Kumari, "Dispersion and rheological studies of Y-PSZ tape casting slurry," *Bull. Mater. Sci.*, vol. 28, no. 2, pp. 103 – 108, 2005.
[123] H. A. Barnes, J. F. Hutton, and K. Walters, *An introduction to rheology*, vol. 31, no. 4. Amsterdam: Elsevier, 1989, p. 199.
[124] B. Bitterlich, C. Lutz, and A. Roosen, "Rheological characterization of water-based slurries for the tape casting process," *Ceram. Int.*, vol. 28, no. 6, pp. 675–683, 2002.
[125] C. A. Gutiérrez and R. Moreno, "Influence of slip preparation and casting conditions on aqueous tape casting of Al_2O_3," *Mater. Res. Bull.*, vol. 36, no. 11, pp. 2059–2072, 2001.
[126] J. Gurauskis, C. Baudín, and a. J. Sánchez-Herencia, "Tape casting of Y-TZP with low binder content," *Ceram. Int.*, vol. 33, no. 6, pp. 1099–1103, 2007.
[127] "Rheology & Viscosity Testing & Profiling Techniques & Methods." Available at: http://www.rheologyschool.com/testing/testing-examples.
[128] Y. T. Chou, Y. T. Ko, and M. F. Yan, "Fluid Flow Model for Ceramic Tape Casting," *J. Am. Ceram. Soc.*, vol. 70, no. 10, pp. C–280–C–282, 1987.
[129] H. J. Kim, M. J. M. Krane, K. P. Trumble, and K. J. Bowman, "Analytical Fluid Flow Models for Tape Casting," *J. Am. Ceram. Soc.*, vol. 2775, no. 21321, p. 060623005134007, 2006.
[130] S. d'Halewyu, "Numerical simulation of the cast film process," *Polym. Eng. Sci.*, vol. 30, no. 6, pp. 335 – 340, 1990.
[131] R. Pitchumani and V. M. Karbhari, "Generalized Fluid Flow Model for Ceramic Tape Casting," *J. Am. Ceram. Soc.*, vol. 78, no. 9, pp. 2497–2503, 1995.
[132] X. Y. Huang, C. Y. Liu, and H. Q. Gong, "A Viscoplastic Flow Modeling of Ceramic Tape Casting," *Mater. Manuf. Process.*, vol. 12, no. 5, pp. 935–943, 1997.
[133] P. Gaskell, "The effect of reservoir geometry on the flow within ceramic tape casters," *J. Eur. Ceram. Soc.*, vol. 17, no. 10, pp. 1185 – 1192, 1997.
[134] A. Wonisch, P. Polfer, T. Kraft, A. Dellert, A. Heunisch, and A. Roosen, "A Comprehensive Simulation Scheme for Tape Casting: From Flow Behavior to Anisotropy Development," *J. Am. Ceram. Soc.*, vol. 94, no. 7, pp. 2053–2060, 2011.
[135] G. Terrones, P. A. Smith, T. R. Armstrong, and T. J. Soltesz, "Application of the Carreau Model to Tape-Casting Fluid Mechanics," *J. Am. Ceram. Soc.*, vol. 80, no. 12, pp. 3151–3156, 2005.

[136] M. Svec, M. Schmidt, T. Betz, A. Roosen, F. Koppe, and H. Münstedt, "The influence of different blade geometries on the local flow behavior of ceramic slurries in the tape casting unit," *Ceram. Forum Int.*, vol. 79, no. 5, pp. E39–E43, 2002.
[137] S. Hurwitt, "Method for controlling the thickness of ceramic tape," US3991149 A, 1976.
[138] R. Runk, "Precision tape casting machine for fabricating thin ceramic tapes," *Am. Ceram. Soc. Bull.*, vol. 54, no. 2, pp. 199 – 200, 1975.
[139] M. Schmidt, H. Münstedt, M. Svec, A. Roosen, T. Betz, and F. Koppe, "Local Flow Behavior of Ceramic Slurries in Tape Casting, as Investigated by Laser-Doppler Velocimetry," *J. Am. Ceram. Soc.*, vol. 85, no. 2, pp. 314–320, 2004.
[140] C. . Gutiérrez and R. Moreno, "Tape casting of non-aqueous silicon nitride slips," *J. Eur. Ceram. Soc.*, vol. 20, no. 10, pp. 1527–1537, 2000.
[141] K. V. Arunkumar, R. N. Panicker, K. G. Vasanthakumari, M. Satheesh, N. Raghu, and N. V. Unnikrishnan, "Dispersion and Rheological Characterization of TiO_2 Tape Casting Slurry," *Int. J. Appl. Ceram. Technol.*, vol. 7, no. 6, pp. 902–908, 2010.
[142] S. Nayak, B. P. Singh, L. Besra, T. K. Chongdar, N. M. Gokhale, and S. Bhattacharjee, "Aqueous Tape Casting Using Organic Binder: A Case Study with YSZ," *J. Am. Ceram. Soc.*, vol. 94, no. 11, pp. 3742–3747, 2011.
[143] "Method for manufacture of transparent ceramics," US3974249 A, 21-Sep-2010.
[144] N. Van Nong, N. Pryds, C. R. H. Bahl, A. Smith, and S. Linderoth, "Structure useful for producing a thermoelectric generator, thermoelectric generator comprising same and method for producing same," US2012126626A1, 26-Sep-2012.
[145] E. R. Kupp, G. L. Messing, J. M. Anderson, V. Gopalan, J. Q. Dumm, C. Kraisinger, N. Ter-Gabrielyan, L. D. Merkle, M. Dubinskii, V. K. Simonaitis-Castillo, and G. J. Quarles, "Co-casting and optical characteristics of transparent segmented composite Er:YAG laser ceramics," *J. Mater. Res.*, vol. 25, no. 03, pp. 476–483, 2011.
[146] H. Watanabe, T. Kimura, and T. Yamaguchi, "Particle Orientation During Tape Casting in the Fabrication of Grain-Oriented Bismuth Titanate," *J. Am. Ceram. Soc.*, vol. 72, no. 2, pp. 289–293, 1989.
[147] a. Sanson, P. Pinasco, and E. Roncari, "Influence of pore formers on slurry composition and microstructure of tape cast supporting anodes for SOFCs," *J. Eur. Ceram. Soc.*, vol. 28, no. 6, pp. 1221–1226, 2008.
[148] M. P. Albano and L. B. Garrido, "Influence of the slip composition on the properties of tape-cast alumina substrates," *Ceram. Int.*, vol. 31, no. 1, pp. 57–66, 2005.
[149] J. A. Lewis, K. A. Blackman, A. L. Ogden, J. A. Payne, and L. F. Francis, "Rheological Property and Stress Development during Drying of Tape-Cast Ceramic Layers," *J. Am. Ceram. Soc.*, vol. 79, no. 12, pp. 3225–3234, 1996.
[150] P. M. Raj and W. R. Cannon, "Anisotropic Shrinkage in Tape-Cast Alumina: Role of Processing Parameters and Particle Shape," *J. Am. Ceram. Soc.*, vol. 82, no. 10, pp. 2619–2625, 2004.
[151] J. E. Schroeder and H. U. Anderson, "Multilayer ceramic oxide solid electrolyte for fuel cells and electrolysis cells and method for fabrication thereof," 4957673, 1990.
[152] M. Jabbari, J. Spangenberg, and J. H. Hattel, "Interface Behavior in Functionally Graded Ceramics for the Magnetic Refrigeration: Numerical Modeling," *Appl. Mech. Mater.*, vol. 325–326, pp. 1362–1367, 2013.
[153] D.-H. Yoon and B. I. Lee, "Processing of barium titanate tapes with different binders for MLCC applications—Part II: Comparison of the properties," *J. Eur. Ceram. Soc.*, vol. 24, no. 5, pp. 753–761, 2004.
[154] D.-S. Park and C.-W. Kim, "A modification of tape casting for aligning the whiskers," *J. Mater. Sci.*, vol. 34, no. 23, pp. 5827–5832, 1999.

[155] H. Yang, P. Zhang, Q. Wu, H. Ge, and M. Pan, “Effect of monovalent metal substitution on the magnetocaloric effect of perovskite manganites $Pr_{0.5}Sr_{0.3}M_{0.2}MnO_3$ (M=Na, Li, K and Ag),” *J. Magn. Magn. Mater.*, vol. 324, no. 22, pp. 3727–3730, 2012.
[156] M. Wu and G. L. Messing, “Fabrication of Oriented SiC-Whisker-Reinforced Mullite Matrix Composites by Tape Casting,” *J. Am. Ceram. Soc.*, vol. 77, no. 10, pp. 2586–2592, 1994.
[157] T. Soltesz, “A rheological process control diagram for tape casting,” *Adv. Dielectr. Ceram. Mater.*, vol. 88, pp. 391 – 402, 1998.
[158] A. S. Nesaraj, “Tape casting of alternate electrolyte components for solid oxide fuel cells,” *Indian J. Eng. Mater. Sci.*, vol. 13, no. 4, pp. 347 – 356, 2006.
[159] G. W. Scherer, “Theory of Drying,” *J. Am. Ceram. Soc.*, vol. 73, no. 1, pp. 3–14, 1990.
[160] S. Schwarzer and A. Roosen, “Tape casting of piezo ceramic/polymer composites,” *J. Eur. Ceram. Soc.*, vol. 19, no. 6–7, pp. 1007–1010, 1999.
[161] R. M. German, *Wiley: Sintering Theory and Practice* -. Wiley-Interscience, 1996, p. 568.
[162] L. A. Salam, R. D. Matthews, and H. Robertson, “Pyrolysis of polyvinyl butyral (PVB) binder in thermoelectric green tapes,” *J. Eur. Ceram. Soc.*, vol. 20, no. 9, pp. 1375–1383, 2000.
[163] J. Baber, A. Klimera, and F. Raether, “In situ measurement of dimensional changes and temperature fields during sintering with a novel thermooptical measuring device,” *J. Eur. Ceram. Soc.*, vol. 27, no. 2–3, pp. 701–705, 2007.
[164] D. W. Ni, C. G. Schmidt, F. Teocoli, A. Kaiser, K. B. Andersen, S. Ramousse, and V. Esposito, “Densification and grain growth during sintering of porous $Ce_{0.9}Gd_{0.1}O_{1.95}$ tape cast layers: A comprehensive study on heuristic methods,” *J. Eur. Ceram. Soc.*, vol. 33, no. 13–14, pp. 2529–2537, 2013.
[165] F. G. Raether, “Current State of In Situ Measuring Methods for the Control of Firing Processes,” *J. Am. Ceram. Soc.*, vol. 92, pp. S146–S152, 2009.
[166] F. Raether and P. Schulze Horn, “Investigation of sintering mechanisms of alumina using kinetic field and master sintering diagrams,” *J. Eur. Ceram. Soc.*, vol. 29, no. 11, pp. 2225–2234, 2009.
[167] T. Noguchi, T. Ōkubo, and O. Yonemochi, “Reactions in the System ZrO_2 -SrO,” *J. Am. Ceram. Soc.*, vol. 52, no. 4, pp. 178–181, 1969.
[168] H. Yokokawa, “Thermodynamic Analysis of Reaction Profiles Between $LaMO_3$ (M=Ni,Co,Mn) and ZrO_2,” *J. Electrochem. Soc.*, vol. 138, no. 9, p. 2719, 1991.
[169] G. Stochniol, E. Syskakis, and A. Naoumidis, “Chemical Compatibility between Strontium-Doped Lanthanum Manganite and Yttria-Stabilized Zirconia,” *J. Am. Ceram. Soc.*, vol. 78, no. 4, pp. 929–932, 1995.
[170] S. Ping Jiang, J.-P. Zhang, and K. Föger, “Chemical interactions between 3 mol% yttria-zirconia and Sr-doped lanthanum manganite,” *J. Eur. Ceram. Soc.*, vol. 23, no. 11, pp. 1865–1873, 2003.
[171] S. Jeppesen, S. Linderoth, N. Pryds, L. T. Kuhn, and J. B. Jensen, “Indirect measurement of the magnetocaloric effect using a novel differential scanning calorimeter with magnetic field.,” *Rev. Sci. Instrum.*, vol. 79, no. 8, p. 083901, 2008.
[172] A. R. Dinesen, PhD manuscript “Magnetocaloric and magnetoresistive properties of $La_{0.67}Ca_{0.33-x}Sr_xMnO_3$”, ISBN 87-550-3224-9, 2004.
[173] C. R. H. Bahl, R. Bjørk, A. Smith, and K. K. Nielsen, “Properties of magnetocaloric materials with a distribution of Curie temperatures,” *J. Magn. Magn. Mater.*, vol. 324, no. 4, pp. 564–568, 2012.
[174] K. K. Nielsen, “Modeling of Active Magnetic Regenerators for Magnetic Refrigeration at Room Temperature,” Technical University of Denmark, 2010.
[175] J. Tušek, A. Kitanovski, and A. Poredoš, “Geometrical optimization of packed-bed and parallel-plate active magnetic regenerators,” *Int. J. Refrig.*, vol. 36, no. 5, pp. 1456–1464, 2013.

PAPER I

R. Bulatova, K. B. Andersen, A. Kaiser, M. Della Negra, C. R. H. Bahl, “Thickness Control And Interface Quality As Functions Of Slurry Formulation And Casting Speed In Side-By-Side Tape Casting”, *J. Eur. Ceram. Soc.*, DOI: 10.1016/j.jeurceramsoc.2014.07.013.

Available online at www.sciencedirect.com
ScienceDirect
Journal of the European Ceramic Society xxx (2014) xxx–xxx
www.elsevier.com/locate/jeurceramsoc

Thickness control and interface quality as functions of slurry formulation and casting speed in side-by-side tape casting

R. Bulatova [a,*], M. Jabbari [b], A. Kaiser [a], M. Della Negra [a], K.B. Andersen [a], J. Gurauskis [a], C.R.H. Bahl [a]

[a] *Department of Energy Conversion and Storage, Technical University of Denmark – DTU, Frederiksborgvej 399, DK-4000 Roskilde, Denmark*
[b] *Department of Mechanical Engineering, Technical University of Denmark – DTU, Produktionstorvet, DK-2800 Kgs. Lyngby, Denmark*

Received 1 June 2014; received in revised form 5 July 2014; accepted 8 July 2014

Abstract

A novel method of co-casting called side-by-side tape casting was developed aiming to form thin functionally graded films with varying properties within a single plane. The standard organic-based recipe was optimized to co-cast slurries into thick graded tapes. Performed numerical simulations identified the stable flow beneath the blade with a shear rate profile independent of slurry viscosity as long as the slurry load in the casting tank was low. Thickness and interface shape could be well predicted if the rheological behaviour of slurries is known and the processing parameters are well-controlled. A well-defined steep interface was obtained by co-casting slurries with similar viscosities above 4000 mPas at a speed of 40 cm/min. The elastic properties of green tapes were proven to be defined by the binder concentration in the recipe formulation. The interfaces in graded tapes were shown to withstand high stresses identifying a good adhesion between side-by-side cast materials.

Keywords: Tape casting; Functional graded material; Tape thickness; Rheological properties; Flow behaviour.

1. Introduction

Tape casting is a large scale fabrication technique for flat thin tapes in ceramics, metals and glass processing. The ability to produce uniform tapes tens of metres long which can be subsequently green machined (punched), laminated and stacked to form a specimen with uniform composition and properties, makes tape casting a very versatile manufacturing technique for many products in many industries. Especially, the last decades' technological development requires production of functionally graded materials (*FGM*), meaning materials with a gradual variation in structure and/or composition over its volume and, as consequence, with a gradual change in properties within the sample.[1] Among all ceramic FGMs, recently fabricated by tape casting, multilayer design is the most common to be used in such applications as solid oxide fuel cells (*SOFC*),[2,3] membranes[4,5] and flue gas purification systems.[2] However, in some technologies, planar not layered segmented variation of properties is required. For instance, a planar gradual increase in magnetic phase transition temperature (Curie temperature), greatly improves performance of the active magnetic regenerator (*AMR*) used in the emerging magnetic refrigeration technology.[6,7] This design allows replacement of the expensive rare earth element gadolinium with ceramics as AMR. The requirements are adjacently adhered materials (stripes) varying by a stepwise increase in ceramic doping, forming homogeneous flat dense tapes. To produce such a planar gradual structure (Fig. 1a),[7] the novel shaping technique, so-called side-by-side tape casting (*SBS TC*) also referred to as adjacent tape casting, was proposed.[8]

SBS TC includes simultaneously drawing-out ceramic loaded slurries from the conventional doctor blade tank (tape caster reservoir), which is divided by Teflon partitions into compartments. The number and width of compartments can vary depending on application needs. Under the dragging force of the moving carrier, slurries are co-sheared adjacently forming a

* Corresponding author at: Frederiksborgvej 399, P.O. Box 49, Building 779, 4000 Roskilde, Denmark. Tel.: +45 4677 5871; fax: +45 4677 5858.
E-mail addresses: regb@dtu.dk, rrbulatova@gmail.com (R. Bulatova).

http://dx.doi.org/10.1016/j.jeurceramsoc.2014.07.013
0955-2219/

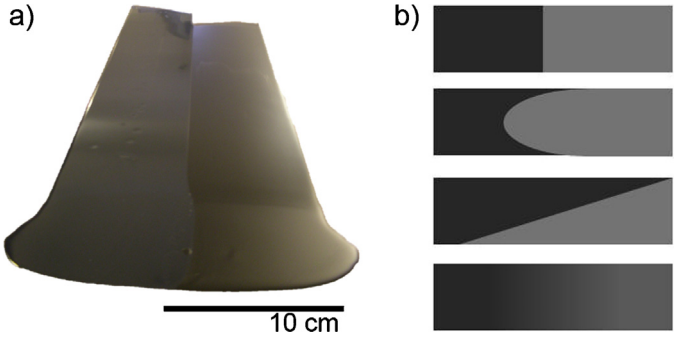

Fig. 1. (a) Photo of a side-by-side (SBS) graded tape with a length of about 40 cm and (b) schematic of possible shapes of interfaces formed between adjacently co-cast materials in SBS TC.

continuous thin tape with one-dimensional interfaces at the confluence areas. In that case, from the tape profile view, interface between SBS co-cast materials (adjacently co-cast materials, stripes) may form one of the following shapes (Fig. 1b): steep vertical, arc shape, angled to the surface of the substrate, or the boundary can be blurred due to mixing and interdiffusion between adjacently co-flowed slurries. The third case is so-called overlapping, which is covering or extending one of the SBS co-cast material beyond another due to the slurries overflow in the interface area.

The challenge of the new adjacent co-casting technique is to produce and maintain the same thickness of adjacent materials having different composition at comparable flow behaviour (similar rheology). Another challenge is the precise control of the interface shape and a sufficient adhesion between the adjacent stripes. In a first optimization of the novel technique, initial parameter settings, such as fluid (i.e., ceramic loaded slurry in current work) properties and processing features are to be determined. This would suggest SBS co-casting of slurries with similar well-studied dispersed phase and use of a well-developed recipe. However, in order to facilitate easier identification and study of the interface area, the adjacent materials are desired to possess solid loads of different compositional, morphological and/or magnetic parameters. Taking these demands into account, the first slurry was formulated based on strontium doped lanthanum manganite oxide $La_{0.85}Sr_{0.15}MnO_3$ (*LSM*), while for the second slurry a mixture of LSM and gadolinium doped cerium oxide $Ce_{0.9}Gd_{0.1}O_2$ (*CGO*) was chosen. LSM and CGO are widely used as cathode and inter-diffusion barrier layer in SOFC, as a solid constitute of the porous layer in gas purification applications and gas separation membranes, LSM perovskite is characterized by high magnetotransport properties and is applied in memory and sensor applications.[9,10] Due to the coarse structure and white colour of the CGO powder, as opposed to the fine rounded shape and black colour of LSM, the interface line between co-cast LSM and mixture of LSM and CGO (*LSM/LSM_CGO*) materials was easily distinguished both visually by colour and due to morphological and compositional differences. Concerning the choice of dispersive media, it was decided to use a well-developed organic-based recipe[2,10] with an azeotropic mixture of methylethylketone and ethanol (*MEKET*) as the solvent. It was important to use MEKET because organic solvents benefit, firstly, in sufficiently fast drying so to avoid inter-diffusion between stripes, and, secondly, minimizing the surface skinning and trapping of evaporating solvent what facilitate better control of the surface finishes. The same MEKET based recipes were applied for both SBS co-cast materials to guarantee similar drying kinetics and shrinkage.

The work addresses the processing approach of adjacently casting LSM and LSM_CGO slurry by the SBS TC technique. For this purpose (i) the influence of the slurry properties (slurry density, rheology, solvent content and loadings of organic additives) and (ii) the casting parameters (speed) on the adjacently graded tape quality were investigated. Specific focus was set on the thickness variation of green tapes and the quality of the interface between the two adjacent stripes.

2. Experimental procedures

2.1. Raw materials and slurry preparation

The SBS cast tapes were prepared by adjacent co-shearing of two slurries. The first slurry initially contained 62.05 wt.% of $La_{0.85}Sr_{0.15}MnO_3$ (LSM, Haldor Topsoe A/S, Denmark; calcined at 1200 °C for 2 h, 18.0 m^2/g, 6.55 g/cm^3). The second slurry had 52.05 wt.% LSM with 5.74 wt.% of $Ce_{0.9}Gd_{0.1}O_2$ (CGO, Rhodia, France; uncalcined, 12 m^2/g, 7.71 g/cm^3) as a solid loading. Slurries were prepared according to standard MEKET (azeotropic mixture of methylethylketone and ethanol) based recipe[2,10] using PVP (polyvinylpyrolidone) as a dispersant.

The preparation of both LSM and LSM_CGO slurries was performed taking into account the necessity to cast highly viscous slurries. In order to achieve homogeneous component distribution and avoid competitive adsorption of polymers in the slurry with a low solvent content, powder and PVP dispersant were dispersed in solvent in two steps. First, 52.05 wt.% of the powder and 0.85 wt.% of the PVP dispersant were milled in the MEKET solvent for about 20 h. The second portion of powder and the remaining 0.21 wt.% of PVP were added whenever the first portion of powder was fully dispersed. The obtained suspension was milled for another 20 h. After adding the binder system (binder polyvinyl butyral PVB, plasticizers dibutyl phthalate DBP, polyethylene glycol PEG, and release and wetting additive with commercial name Additol) in MEKET to the powder and dispersant suspension, the slurry was milled for another 20 h. Finally, d_{50} for both slurries was within 2.3–2.5 μm. Before tape casting, LSM and LSM_CGO slurries were filtered through a 100 μm meshed tulle and the slurries were degassed using a vacuum pump (100 mBar) in order to remove air bubbles.

Particles size distribution was measured during the whole period of the slurry preparation using Scattering Particle Size measurements (Beckman Coulter LS 13320, Beckman Coulter Inc., Miami, FL). The apparent viscosity (η) measurements were conducted on pre-sheared and recovered slurries with reversing increase of shear rate γ' up to 50 s^{-1} using a plate–plate system (Haake RheoStress 600, Thermo Electron GmbH, Karlsruhe, Germany). A solvent trap was used to minimize the evaporation of organic solvent during rheological measurements. Slurry

Please cite this article in press as: Bulatova R, et al. Thickness control and interface quality as functions of slurry formulation and casting speed in side-by-side tape casting. *J Eur Ceram Soc* (2014), http://dx.doi.org/10.1016/j.jeurceramsoc.2014.07.013

Table 1
Dependence of slurry's viscosity on the content of MEKET solvent and binder system. Because of experimental uncertainty the viscosity values were rounded to the nearest 100.

	Solvent (vol.%)	Binder syst. (vol.%)	S/C ($Vol_{solv.}/Vol_{ceram}$)	BS/C ($Vol_{bind.syst.}/Vol_{ceram}$)	Viscosity η (mPas) ($\gamma\acute{\imath} = 3.3\ s^{-1}$)	Density ρ (g/cm^3)
LSM	42.99	41.24	2.98	2.86	4200	3.52
LSM_CGO_1	43.98	42.47	3.61	3.48	2700	3.64
LSM_CGO_2	43.44	42.45	3.57	3.45	3200	3.68
LSM_CGO_3	42.84	43.73	3.54	3.62	3800	3.86
LSM_CGO_4	41.78	44.53	3.39	3.62	4300	3.82
LSM_CGO_5	40.69	45.37	3.24	3.62	4500	3.78
LSM_CGO_6	43.65	39.83	2.93	2.68	6000	3.35
LSM_CGO_7	41.02	41.69	2.63	2.68	6700	3.39
LSM_CGO_8	44.50	35.74	2.50	2.01	9400	3.34

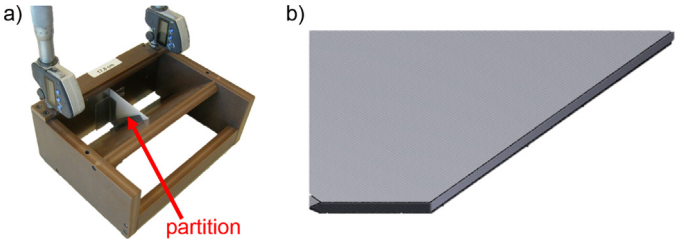

Fig. 2. (a) Tape caster used for SBS TC of two materials and (b) design of the partition dividing a doctor blade reservoir into compartments.

density was measured using pycnometer: a fixed volume container was filled with slurry and weighted; a capillary tube was used to accurately determine the volume of suspension. The density of each slurry was measured 3 times and the average value (uncertainty interval was maximum 0.02 g/cm^3) is given in Table 1.

In order to elucidate the effect of slurry characteristics on the tape interface formation, binder solution and solvent concentrations were varied with subsequent casting and drying processing steps to observe the effect of rheological behaviour on green tapes quality.

2.2. Tape casting

For adjacent tape casting the conventional casting tank has to be modified. Fig. 2a shows the doctor blade setup for SBS TC of two adjacent stripes. A special wing-shaped partition (Fig. 2b) was made to separate the entire tank space into two reservoirs, each the same width. The partition was fixed to the walls of the tank by two-side adhesive tape. Duct tape was stuck on the junction between partition and tank walls, partition and casting knife, aiming to precisely fix the partition to the tape caster and prevent slurries leaking between neighbouring reservoirs. The front side of Teflon partition was sharpened by about 1.5 mm in order to induce smooth merger of adjacently co-cast slurries. In experiments, when partition front edge was not acuminated, a concave trace of the partition on the dried tape was observed (not shown here). To make tests reproducible, the same amount of SBS co-cast slurries were synchronously added into each compartment of the doctor blade tank. No refilling of the slurries in the reservoirs was done during casting.

In order to clearly identify parameters which influence the interface quality in SBS TC the most, it was decided to simplify the tape caster design and use a well-studied single-blade tape caster setting. Although the use of a double-blade in tape caster design was invented to keep the slurry level in pre-sheared zone constant and thus produce a smooth tape, the inhomogeneous flow inside the spare pool of tape caster[11] and complicated design of the partition needed for double blade system did not guarantee a high reproducibility of casting experiments. This favours the use of single-blade over the double-blade system for SBS TC.

The blade gap was fixed at a height of 1000 μm due to the following reasons. First, it was dictated from the application needs to have the final post-sintered tape thickness of 250–300 μm. Second, the thicker the tape, the more obvious the changes in tape structure as a function of casting parameters[2,12] which makes experimental data change easier to detect.

Before starting the experiments, the gap was tightly occluded with the Duct tape, stuck on to the Mylar carrier. When the process starts this Duct tape moves together with the Mylar carrier. One reason to occlude the gap was to keep the slurries in the reservoir for about 30 s before the start of the casting process in order to let the rheological stresses, accumulated while slurry pouring, to relax. Another benefit of having the casting gap closed is the guarantee that adjacent slurries will start to co-flow simultaneously, providing a condition for good agreement between experiments and modelling simulation data.[13]

Two sets of experiments were conducted. The first test was oriented at understanding how fluid nature, i.e. density and viscosity (Table 1), affects the green tape thickness and the interface quality between SBS co-cast materials. Slurries were cast with a carrier speed of 20 cm/min, and viscosity varied by changing solvent/ceramics (*S/C*) and binder system/ceramics (*BS/C*) (binder system excluded solvent MEKET) volumetric ratios. The second series of experiments aimed to study the effect of casting speed on tape thickness gradient and interface behaviour. For that test, the recipe of co-cast slurries was fixed using LSM and LSM_CGO_4 slurries (Table 1), and casting speed varied from 10 cm/min up to 40 cm/min.

Please cite this article in press as: Bulatova R, et al. Thickness control and interface quality as functions of slurry formulation and casting speed in side-by-side tape casting. *J Eur Ceram Soc* (2014), http://dx.doi.org/10.1016/j.jeurceramsoc.2014.07.013

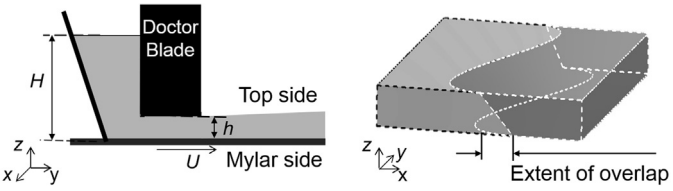

Fig. 3. Schematic illustration of tape caster and extent of overlap between SBS co-cast tapes. The scale of the tape doesn't match to the real size of green tape, and proportions between tape width and length are exaggerated. The sketch aims to show how the interface position may change along the tape and definition of the extent of overlap.

2.3. Characterization

The thickness values of green tapes were collected about 2 cm from the tapes' edges on both sides of the tapes every 10 cm along the length using a 15 mm diameter circle flat dual point digital micrometre.

The interface behaviour was characterized by the *extent of overlap* in tape profile plane *x*–*z* (Fig. 3). By overlapping is meant either the overflow of one slurry on top of the neighbouring one, or its displacement which results in interface shifting and/or its inclination (Fig. 1b, third schematic model). Therefore, to measure the extent of overlap between adjacently co-cast materials, position of the interface, viewed from the top side of the tape, was compared with the interface position, viewed from the Mylar bottom side of the tape (Fig. 3). From the tape profile view (plane *z*–*x*), the interface looked like either a steep line, giving an extent of overlap equal to zero, or like an angled line. In the last case the extent of overlap was measured in mm as the distance between interfaces seen from the top and Mylar sides of the tape.

For measurement of fracture tensile stress (strain–stress resistivity) of the green tapes and evaluation of the interface quality, green samples of 100 mm × 10 mm were cut with the interface in the middle of the long side. These pieces were fixed in an Instron tensile machine (the cell load was 5 N, 5900 Testing System, Instron, Norwood, MA). To secure getting relevant data, at least four tests for each specimen were collected. The data obtained from the specimens which failed nearby the fitting clips were excluded from evaluation. The tensile test was also performed on individual samples of LSM and LSM_CGO, which were punched from the graded sample but far from edge side and interface so to ensure the homogeneity and purity of analyzed specimens.

Cross sections of green tapes containing interfaces were examined with a scanning electron microscope (SEM) (Inspect, 50 nm at 30 kV, FEI Company, Kyoto, Japan) with possibility for energy dispersive X-ray spectroscopy (EDX, Oxford Instruments, Abingdon, United Kingdom). For reproductive comparison of interface shapes, samples for SEM and EDX were punched 10 cm from the end of each tape. Since polishing of green samples is impossible, the tapes were frozen in liquid nitrogen and then broken apart in order to have a smooth surface. The samples were retained between two plastic plates.

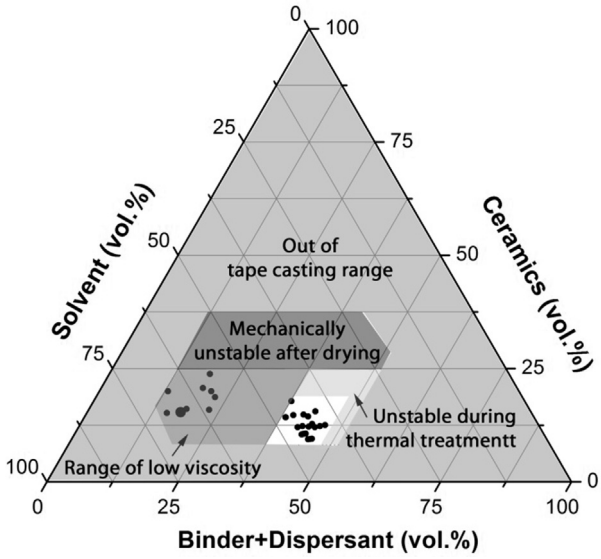

Fig. 4. Tape casting formulations used in the present work (dots in white area in the plot) compared to literature (dots in grey area in the plot).

3. Results and discussion

3.1. Slurry formulation

In most tape casting applications thin films with a thickness below 100 μm[12,14–16] are required, which dictates using low viscosity slurries as highly viscous slurries create inhibitive forces under shear in small casting gaps. For magnetic refrigeration thicker tapes of about 300 μm thickness are required, therefore, more viscous slurries compared to standard tape casting slurries have to be applied. Thus, a modification of conventionally used organic tape casting recipes[2,10] was needed. Fig. 4 shows the compositions of typical MEKET-based tape casting recipes found in literature[2,16–18] (each experiment from literature is presented as a dot in the grey range of low viscosities area in Fig. 4) and recipes that were designed in this work for adjacently co-cast tapes of a thickness about 300 μm (each experiment is given as a dot in the white area in Fig. 4). A higher viscosity for the slurries used in this work for SBS TC was achieved by increasing the binder system content and decreasing the solvent concentration, wherein the ceramics mass load was kept constant. Systematic change in the binder system's and the solvent's mass loading lead to a consistent volumetric change of the total slurry volume, making the components volume percentage look inconsistent. Thus, the components of the slurries (Table 1) are given both in volumetric percentage for easier comparison with standard slurry formulations (Fig. 4) and in volumetric ratios of binder system and solvent to constant ceramics load, BS/C and S/C, consequently.

The literature based slurry compositions (Fig. 4) contain about 55–75 vol.% of solvent and 15–25 vol.% of polymeric part including binder system (binder PVB, plasticizers DBP and PEG and wetting additive Additol) and dispersant PVP. The binder system content varies from 13 to 24 vol.%. Apparent viscosity

Please cite this article in press as: Bulatova R, et al. Thickness control and interface quality as functions of slurry formulation and casting speed in side-by-side tape casting. *J Eur Ceram Soc* (2014), http://dx.doi.org/10.1016/j.jeurceramsoc.2014.07.013

of these slurries with comparable molecular weight polymers was below 1000 mPas at 10 s^{-1} shear rate.

The optimal slurries formulations for SBS TC were determined based on the flexibility and surface quality of the obtained green tapes and the absence of cracks and deformations after the sintering process. The increase in binder content together with an increase in viscosity was aimed to improve adhesion between adjacently co-cast materials, but exceeding the binder system content over 47 vol.% was shown to form tapes with a very fragile post-sintered structure. Based on these results, feasible binder solution content was established as 35.5–43.5 vol.%, or 2.01–3.62 with respect to the ceramics volume (BS/C ratio). Another approach to increase slurry viscosity included reduction of the solvent content. Experiments showed, that using MEKET in concentrations below 40 vol.% leads to formation of cracks during the drying stage, which were provoked by accumulated stress due to constrained volume shrinkage. Hence, the optimum solvent content was found to vary as 40–48 vol.%, which corresponds to relative amounts, S/C of 2.50–3.61. Significant decrease in the amount of solvent as the only homogenizer in slurry formulation identified the need for dividing the milling process into 3 steps, as it is described in Section 2.

Among all working recipe formulations for further investigations we chose ones with high shear thinning (pseudoplastic) capabilities and composing a number of viscous slurries with gradually increasing viscosity values for the LSM_CGO slurries. Table 1 shows the formulations of these organic-based slurries.

3.2. Effect of slurries properties on quality of adjacently graded tape

Among slurry properties, the impact of slurry density and slurry viscosity affecting the tape consistency and quality of the generated interface was considered.

First, the importance of the density of the slurries on the quality of green tapes was evaluated. However, varying solvent and binder system concentrations in afore-established working range, density of slurries did not change significantly (3.60 ± 0.26 g/cm^3) (Table 1). That is because the density of slurries is mainly determined by the heaviest fraction load, i.e. by the load of ceramics in the studied system. However, in the current work the mass of ceramics was maintained constant, explaining minor variations of slurry density and complicating further study of the impact of slurry density on the interface formation in SBS TC. Additionally, the effect of slurry density was addressed by numerical modeling[19] using the rheological characteristics of the slurries in Table 1 as input. The range of density studied in the simulations was between 2 and 4 g/cm^3 which is essentially broader than in the current experimental work. The simulations of co-flow did not show major influence of the slurry density on the interface shape.[19] Hence, the role of slurries density on quality of SBS graded tape was neglected in the current study.

Unlike the density values, the rheological behaviour of slurries varied significantly with minor changes in solvent and binder system concentrations (Table 1). As expected, the viscosity of highly viscous slurries was more sensitive to changes in the binder system or solvent content compared to the viscosity of low viscosity slurries. Thus a slight increase in solvent concentration decreased the slurry viscosity drastically. The fact that the increase of binder system content increased slurry viscosity, indicated that the binder interacted as an adhesive agent without replacing dispersant from the powder surface.[2,20] Thus the dispersant is acting as intended and not accumulated between binder polymeric chains, deteriorating mechanical properties. Pseudoplasticity, required for tape casting, was typical for all prepared slurries (Fig. 5a).

Table 2
Rheological behaviour of cast slurries.

	k	n	Yield point τ_y (Pa)	R^2
LSM	4.7(7)	0.85(6)	1.0(8)	0.999
LSM_CGO_1	2.0(2)	1.00(3)	0.8(2)	1.00
LSM_CGO_2	3.0(8)	0.93(2)	0.7(6)	0.999
LSM_CGO_4	5.8(2)	0.81(2)	1.0(4)	0.999
LSM_CGO_6	6.2(9)	0.71(2)	4.8(3)	0.999

For a clear understanding the impact of flow behaviour on the quality of the formed tape, all slurries were described numerically by a constitutive model of fluid. Compared to other pseudoplastic models the Herschel–Bulkley[21] constitutive equation was chosen because it describes both yield point and shear-thinning factors, and nicely matches the fluid flows measured on the rheometer with the coefficient of determination R^2 close to one for all slurries:

$$\tau = \tau_\gamma + k \cdot \gamma'^n \quad (1)$$

where τ_γ is the yield point, k the Herschel–Bulkley viscosity, and n the Herschel–Bulkley index. For pseudoplastic slurries n is always below unity and deviation from unity implies the deviation from a Newtonian behaviour. The model parameters (Table 2) for five slurries considered were obtained from flow curves plotted in Fig. 5b.

The very low yield points, typical for all the studied slurries (Table 2), are negligible for tape casting processing. Since the yield point (yield stress) manifests itself as the stress needed for the slurry to flow, the use of slurries with low values of yield points widens the range of casting speeds, casting gaps and slurry loads that can be applied. Low yield stress or its absence for slurry is preferable if low shear stress (slow casting speed, low viscosity slurries, a big gap and/or a small amount of slurry load in tank) is the driving force of the casting process. Besides, all slurries but the least viscous LSM_CGO_1 have n value less than 1 (Table 2), which characterizes them as pseudoplastic fluids. Pseudoplasticity is required for tape casting process because of the viscosity dependence on shear stress behaviour: the viscosity of pseudoplastic slurries significantly decreases while the slurry passes under the casting blade simplifying uniform flow and levelling, and viscosity increases when the slurry is dragged out of the casting unit preventing the slurry from flowing aside and keeping the shape of the formed tape.

Since the viscosity of pseudoplastic slurry is shear stress dependent and changes during the tape casting process, study of a real flow profile, subject to a complex system of driving

Please cite this article in press as: Bulatova R, et al. Thickness control and interface quality as functions of slurry formulation and casting speed in side-by-side tape casting. *J Eur Ceram Soc* (2014), http://dx.doi.org/10.1016/j.jeurceramsoc.2014.07.013

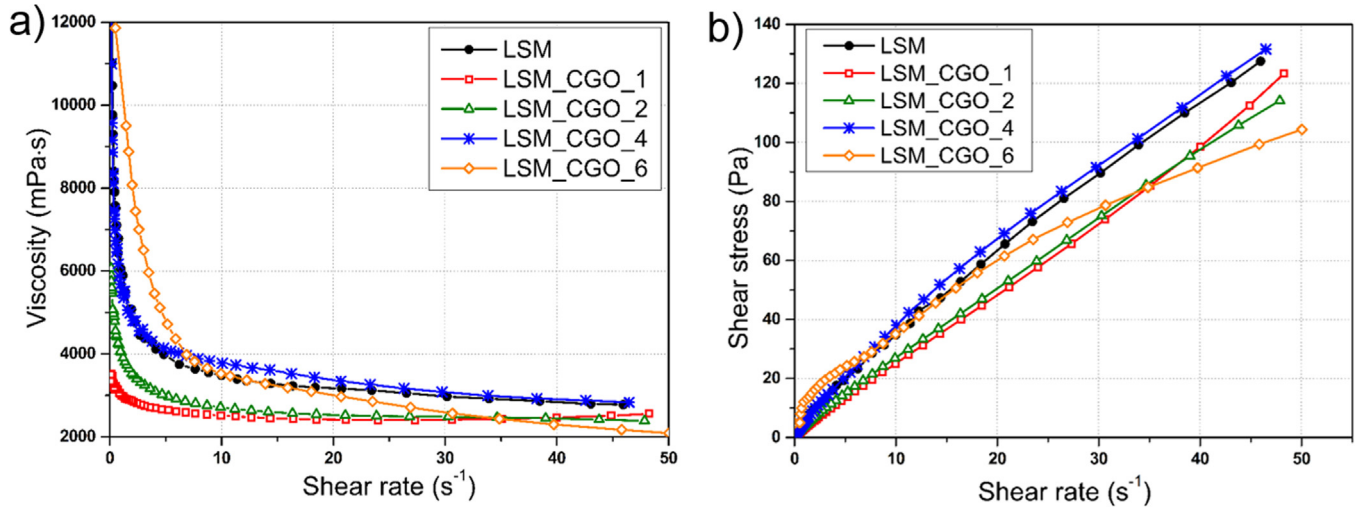

Fig. 5. (a) Viscosity curves and (b) flow curves of the studied slurries.

forces inside the whole casting unit, is required. Besides, the tape casting process with use of a single-blade system is hampered by continuous reduction of slurry load in the reservoir. In that case, the flow volume beneath the doctor blade, directly affecting the wet thickness of the formed tape, is governed not just by a steady state carrier speed (*shear rate*, *Couette flow*, *shear-driven flow*, *drag-driven flow*) but also by a continuously decreasing pressure-driven flow (*Poiseuille flow*).

A recently developed quasi-steady state model[11,13] of the shear rate and the pressure-driven flow in the tape caster unit included the dropping of the slurry height during casting. Using rheological parameters for all 5 slurries in Fig. 5b, the gap of 1 mm and casting speed 20 cm/min as input parameters, the shear rate profiles under the doctor blade were numerically calculated as shown in Fig. 6a. At an initial slurry loading of 22 mm it is observed that there is a very minor dependence of shear rate profile beneath the casting blade as a function of slurry viscosity values, i.e., the rate of the velocity change across the casting gap is closefor high and low viscosity slurries. The same tendency was observed for shear rate profiles re-calculated at different slurry load in reservoir.

The initial slurry column of about 22 mm was chosen because the shearing character is very sensitive to the slurry level in reservoir. At higher slurry loading, for example, 50 mm the velocity gradient under the doctor blade was calculated to change in a relatively wide range from 0.8 s^{-1} to 12 s^{-1}, giving a detrimentally high effect of the pressure-driven flow.[13] This would lead to inhomogeneous flow inside each slurry across the casting gap. With casting time the slurry level in the reservoir continuously declines, and shear rate profile becomes steeper until the reservoir is empty. Aiming for a smooth stable flow during the whole casting process, adjacent reservoirs were filled with slurries until reaching 22 ± 2 mm height as maximum. If it is required to produce a longer tape with the same 1 mm gap, either double-blade or pump system is advisable.

From the numerical simulations, described above, the relevant working range of shear rates can also be estimated. The highest deviation of shear rates across the gap, as it was already

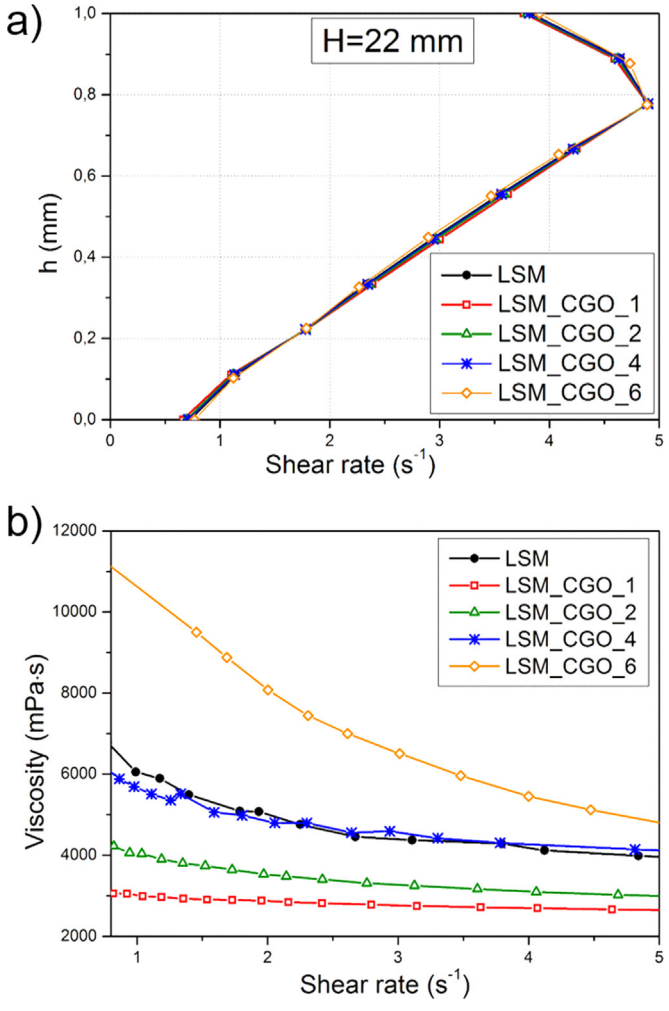

Fig. 6. (a) Shear rate profiles across the doctor blade gap calculated for the considered slurries at a slurry load in the reservoir of $H = 22$ mm; (b) Interval of slurries viscosity curves at re-calculated working shear rates acting underneath the doctor blade during the casting process.

Please cite this article in press as: Bulatova R, et al. Thickness control and interface quality as functions of slurry formulation and casting speed in side-by-side tape casting. *J Eur Ceram Soc* (2014), http://dx.doi.org/10.1016/j.jeurceramsoc.2014.07.013

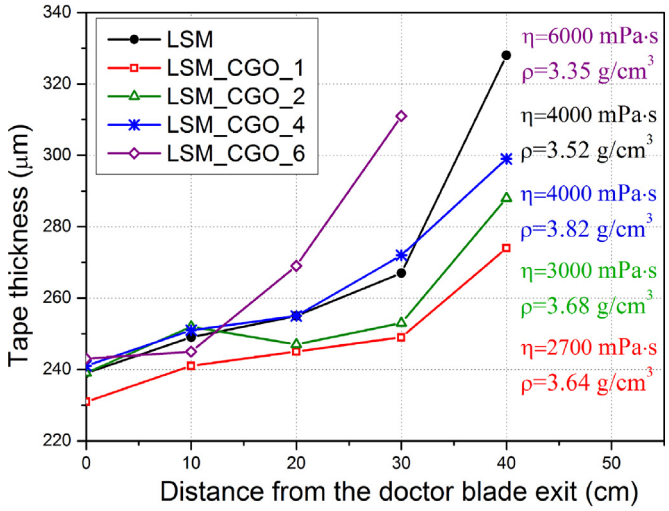

Fig. 7. Tape thickness gradient along the green tape length. Viscosity values are given at a shear rate $\dot{\gamma} = 3.3\ s^{-1}$ (corresponds to the casting speed of 20 cm/min); density values are referred to the slurry density values given in Table 2. The estimated error is 15 μm.

mentioned, is at the beginning of the process. In our case, at a slurry load of 22 mm the shear rate values varies from 0.7 s^{-1} to 5 s^{-1} (Fig. 6a). Transferring this shear rate working range into viscosity curves (Fig. 5a), measured on the rheometer, the rough evaluation of how slurry viscosity changes under the gap became possible (Fig. 6b). In the determined region of shear rates, the viscosity curves for all but the most viscous slurry LSM_CGO_6 are relatively flat and do not cross over each other. Taking into account the assumptions applied in the numerical simulations,[13] such as no flow movement next to the blade surface, fixed casting speed at the substrate surface, and also disregard of the wall slip effect, tension between surfaces and the compositional content of slurries; it is likely that in practice the actual working range of shear rate values is shifted to a higher values.

Thus, this study showed that slurries, obtained based on optimized recipes (Fig. 4) (Table 1), are characterized by the pseudoplastic behaviour, required for tape casting, and negligible small yield point (Table 2), these slurries are stable during the whole tape casting process and the rheological behaviour of the slurries can be described with a consistent viscosity for a whole SBS TC process carried with 1 mm gap and 20 cm/min speed (Fig. 6b).

3.2.1. *Effect of slurry viscosity on uniformity of tape thickness*

All four LSM_CGO slurries described above were adjacently co-cast with LSM slurry, and the four produced SBS graded tapes were dried in the same conditions. Fig. 7 depicts the change of the green tape thicknesses along the casting direction. From the density and viscosity values, given in the plot, it is again seen that the impact of the slurries' rheological behaviour on the tape thickness consistency is very strong, whereas, as it was shown before, there is not any dependence between slurry density and tape thickness uniformity.

For further analytical description of the thickness gradient and its dependence on casting parameters, the simple empirical formula derived by Chou et al.,[22] will be used. Although this expression assumes a Newtonian fluid, it is widely used in practice for estimation of dried tape thickness:

$$\delta = \frac{\alpha\beta}{2}\frac{\rho}{\rho'}h\left[1 + \frac{h^2\Delta P}{6\eta UL}\right] \quad (2)$$

where δ is the dried tape thickness, α the correction factor for side flow, β the correction factor for weight loss during drying, ρ the fluid density, ρ' the density of the formed tape, h the casting gap, ΔP the hydraulic pressure exerted by slurry head, η the slurry viscosity, U the casting speed, L the length of the doctor blade. In this formula viscosity η has a time and stress independent character. The first term describes the shear-driven flow and the second term describes the pressure-driven flow.

Regardless of the slurry viscosity, the first 10 cm of each tape is much thicker compared to the thickness of the rest of the tape (Fig. 7). This can be explained by (i) the cumulative force of externally applied shear-driven and hydraulic pressure-driven forces and (ii) a harsh start of the SBS TC process and instantaneous release of large amount of slurry onto the carrier film. This fast start also leads to a side bulb at the beginning of the tape seen in Fig. 1a. In order to avoid a large bulb at the beginning of the tape, the gap was tightly occluded before the casting process starts (see Section 2).

Besides, at the beginning of each curve, corresponding to the beginning of the SBS co-casting process, tape thickness is sensitive to the viscosity of the slurry. The hydraulic pressure ΔP, entering in the second term of Eq. (2), stems from the slurry weight and affects the volume flow below the casting blade. Viscosity η, also present in the second term of Eq. (2), describes the resistance of slurry to flow and, therefore, determines the extent of slurry to flow under an applied hydraulic pressure. Highly viscous slurry deforms to a lesser extent and is, consequently, more susceptible to a change from cumulative pressure- and shear-driven forces to a pure shear-driven forces.

The general tendency of less viscous slurries forming thinner tapes (Fig. 7) is also ascribed to the use of higher amounts of solvent in the slurry recipes, which evaporates during the drying stage. The weight loss during drying is corrected by a coefficient β in Eq. (2). Another comparably small feasible reason of tape thinning with slurry viscosity decrease, which is reasonable for consideration just for thick tapes, is the side flow effect[23] under tape gravity forces.

At the end of the drying process all green tapes are about 240 μm thick and their thicknesses are no longer affected by slurries viscosity values. This matches with the behaviour described in Eq. (2). Whenever the slurry column behind the casting blade is low, there is no pressure-driven flow. At $\Delta P = 0$, the influence of viscosity has a constant character and is only described by a side flow α and a drying coefficient β to some extent, therefore, the thickness is determined just by the first term. At the end of the process tape thickness is supposed to be half of the gap, and, taking into account that final dried thickness is 240 μm we assume the drying factor amounts to approximately 50% and

Please cite this article in press as: Bulatova R, et al. Thickness control and interface quality as functions of slurry formulation and casting speed in side-by-side tape casting. *J Eur Ceram Soc* (2014), http://dx.doi.org/10.1016/j.jeurceramsoc.2014.07.013

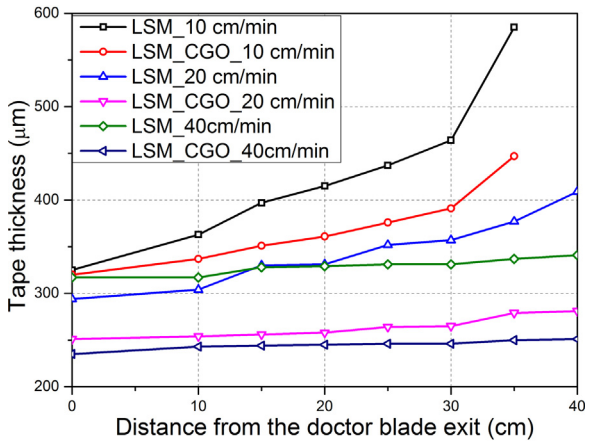

Fig. 8. The effect of casting speed on green tape thickness measured along both edges on LSM and LSM_CGO_4 sides. The estimated error is 15 μm.

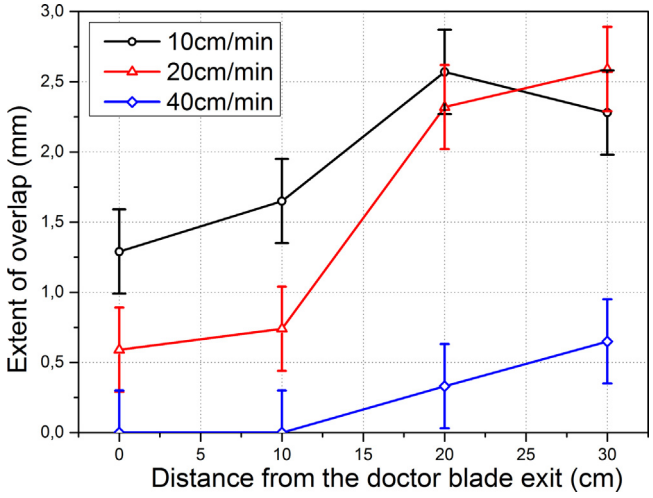

Fig. 9. The effect of casting speed change on overlapping between adjacent materials LSM and LSM_CGO_4. The errors are due to the width of the pen line marking the interface line.

α is close to one. Tape, fabricated from LSM_CGO_1 slurry, is thinner than other green tapes, as it contained more solvent and the correction factor β for weight loss during drying is higher in that particular case.

For future analysis LSM and LSM_CGO_4 slurries were chosen as they are characterized with similar rheological behaviour (Fig. 5a) (Table 2) and could be cast into a graded tape with comparable post-dried thickness of the two adjacent stripes.

3.3. Effect of tape casting parameters

Another factor of concern in tape casting control is the effect of processing parameters, such as casting gap, casting speed and slurry filling in the tank. In the present work it was decided to concentrate the study on correlations between casting velocity, tape thickness consistency and interface quality using LSM and LSM_CGO_4 slurries.

3.3.1. Effect of casting velocity on uniformity of the tape thickness

The relation between casting speed and tape thickness has been the subject of several studies.[24,25] Here, the same correlation between casting speed and tape thickness was considered in order to explain the main reasons of tape thinning of our particular slurry formulations and further elucidate the influence of casting speed on changes in interface character.

Fig. 8 shows the variation of green tape thicknesses, measured along the length on both LSM and LSM_CGO_4 sides of the graded tape. The differences in thicknesses of the LSM and LSM_CGO_4 sides at the same speeds was presumably due to different solvent content, which evaporated at the drying process. The drying ratio, estimated from Eq. (2), approximated to 30–40% for the LSM side and 35–50% for the LSM_CGO_4 side. As having a different binder system load in adjacent materials, a minor systematic additive error is possible during thickness measurement due to different softness of materials. This uncertainty disappears after the de-bindering step, forming a dense solid material with equal thicknesses both sides of the graded tape.

Thinning of the green tape does not originate from change in slurry viscosity (Fig. 8), because, as was shown above, at the applied casting shear rates viscosities for LSM and LSM_CGO_4 slurries are at a linear and quite flat part of the viscosity curves (Fig. 5a). Flattering and thinning of tapes with increasing casting speed is comprehensively explained by the domination of steady shear-driven flow, i.e. first term in Eq. (2), over a decaying pressure-driven flow. Here, the shearing or casting time plays a significant role on the flow characteristics of the slurry and quality of the tape. Due to pseudoplasticity, slurry viscosity is lower at all casting speeds under applied shear, and the viscosity increases when stress is released after the slurry leaves the doctor blade zone. Fast tape casting reduces the time when a slurry is viscous, hence, limiting the time when it is capable of undergoing pressure and viscosity effects typical for the pressure-driven flow. Oppositely, slow cast slurries experience pressure and viscosity effects for longer times. As a consequence, at low casting speeds the actual slurry volume flow below the blade is higher than the volume flow at the given carrier speed. Due to capillary forces, thick slurries experience welling after crossing the blade gap zone, causing thickening of dried tape cast with a slow speed. Casting duration, welling and slurry recovery impacts will be the subjects of our future work.

Other authors, along with tape thinning, detected alignment of particles and change in drying kinetics with increase in casting velocity.[21,22] These changes in tape structure also go along with the continuous shear rate profile change due to pseudoplasticity discussed above.

3.3.2. Effect of casting velocity on the extent of the overlap between SBS co-cast materials

The extent of the overlap was studied with an optical microscope comparing the position of the interface line seen from the Mylar side with the interface line seen from the top side of the tape (Fig. 9). The extent of overlap decreases with an increase of casting speed. A general tendency of irregularities at the beginning of tapes, cast with different velocities, is observed. These

Please cite this article in press as: Bulatova R, et al. Thickness control and interface quality as functions of slurry formulation and casting speed in side-by-side tape casting. *J Eur Ceram Soc* (2014), http://dx.doi.org/10.1016/j.jeurceramsoc.2014.07.013

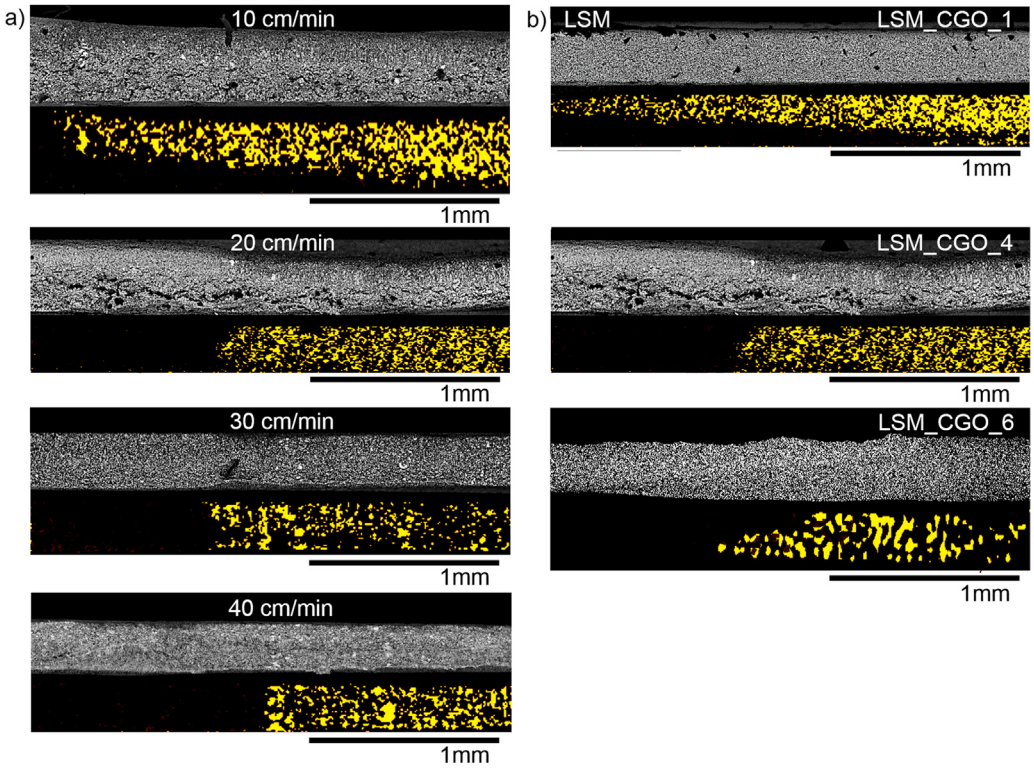

Fig. 10. SEM pictures and corresponding EDX image below visualizing the interface area of SBS co-cast (a) LSM and LSM_CGO_4 materials at various casting speeds, given on SEM pictures; (b) LSM and LSM_CGO slurries of different formulations at casting speed 20 cm/min. CGO phase is marked with a yellow colour here.

irregularities are assumed to result from either sharply applied casting speed at the beginning of the process (discussed above) or higher shear rate deviation beneath the blade owing to the complex correlation between pressure-and shear-driven flows.

To investigate the dependence between casting speed and the extent of overlap more precisely, the interfaces of each sample were studied with the energy dispersive X-ray (EDX) mapping as adjacent materials are often barely distinguished on SEM pictures. Samples were punched from the graded tapes 10 cm away from the end of the tape, corresponding to the end of the process, thus guaranteeing the same pressure in the reservoir during the casting process. No diffusion or intermix between adjacently co-cast materials was found (Fig. 10a).

The inclination of the interface line at low casting speeds and its steepening at higher speeds was detected (Fig. 10a). The increase in casting speed from 10 to 40 cm/min for our particular slurry formulations resulted in a decrease of overlap from 1.2 mm to its complete disappearance. As it was shown in Section 3.3.1, this behaviour can be explained by the duration of the slurry co-shearing process and side flow. Thus, slurries co-cast fast have a very short time beneath the blade to flow aside and barely merge to form the interface: in the drying zone dried slurries are not capable of moving anymore. In turn, slurries, cast at lower speeds, have more time in a low viscous state, leading to formation of wider contact area between adjacent materials. For casting speeds of 20 cm/min and 30 cm/min the increased role of surface tension between adjacent slurries is evident by a sudden change of the straight line interface shape to the arced shape (Fig. 1b). The correlation between slurry surface tension and interface shape formation is a subject planned to be studied in our future work.

Although the latter conclusion denies an influence of minor shear rate change on the interface shape, a change in slurry viscosity significantly affects the junction of adjacent slurries (Fig. 10b). As viscosity implies the fluid resistance to flow under applied shear stresses due to inner forces, then the change in inner forces, namely in the amount of interacting polymers and solving media, also change the resistance of slurries to flow aside. Therefore, more viscous slurries are eager to either keep the initially formed shape of the doctor blade slit they have been discharged from, forming steep contact angle to the substrate surface, or form more acute contact angle due to side-flow under gravity forces. For low viscous slurry it is easier to spread over any surface, causing its overflow on top of the adjacent more viscous slurry. As a result, the obvious tendency of a low viscous slurry overflowing on top of the adjacent more viscous slurry was observed (Fig. 10b). The absence of intermixing between slurries in the interface region can be explained by apparently high enough capillary hydraulic forces of co-sheared slurries.

Fig. 10b shows concisely that viscosity values of co-shearing slurries determine the extent of the overlap in the interface region. Adjacent co-casting of slurries of certain viscosity with various speeds (Fig. 10a) is shown to change the shape of the interface in a narrower range. The line of contact can be either settled into a long line tilted to the substrate surface when tape casting slowly (in case of SBS co-cast LSM and LSM_CGO_4

Please cite this article in press as: Bulatova R, et al. Thickness control and interface quality as functions of slurry formulation and casting speed in side-by-side tape casting. *J Eur Ceram Soc* (2014), http://dx.doi.org/10.1016/j.jeurceramsoc.2014.07.013

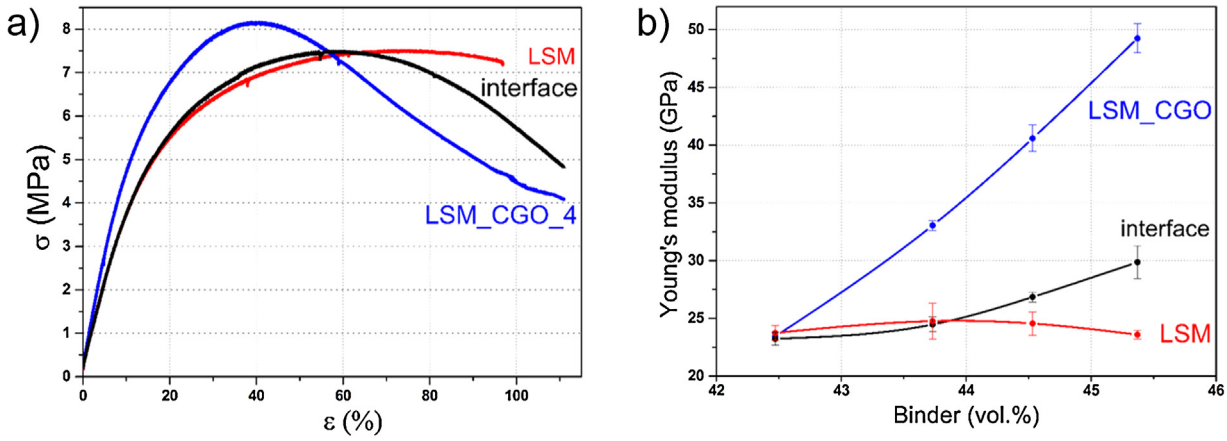

Fig. 11. (a) The stress–strain relations of green tapes of pure LSM, pure LSM_CGO_4 strips, and interface area; (b) Young's modulus change with binder content in the LSM_CGO material side and interface, the content of LSM side is constant.

at 10 cm/min), or be rounded towards the drying surface of the green tape and towards the carrier film (20 cm/min), or be steep, almost perpendicular to the substrate (40 cm/min). In the experiment with varying LSM_CGO viscosity, the dominant factor of forming the shape of green tape is the side flow, so it affects the extent of overlap but not the interface shape.

3.4. Adhesion between SBS co-cast materials

The final analysis was on understanding if tapes, which were optimized based on dimensional characteristic and interface quality, behave as a single piece of graded material or as a number of more or less weakly joined plates. The adhesion between adjacent materials was studied by tensile tests. The green strengths of pure LSM and LSM_CGO materials, as well as a graded tape, are high because of the high content of polymers, and particularly binder system content (Fig. 11a). Using the same polymer loading in adjacent materials the plasticity of both tapes is very similar despite the content of particles with different surface area, which according to Yoon and Lee[26] is supposed to have a dominant influence on the green tapes tensile strength.

On the example of LSM_CGO slurry, it is seen that slightly higher binder content generated higher green tape elasticity (Fig. 11b). The LSM slurry composition through all experiments was kept constant so the cause must be attributed to the high adhesion strength and uniform distribution of binder, as it is the only continuous phase in the green tape. The same tendency of increasing green tape elasticity was observed for the adjacently graded tape, as the pure LSM stripe composition remains constant from sample to sample (Fig. 11b). All the specimens of the graded tapes always broke on the pure LSM material side, characterized by a lower green strength. Therefore, adherence between the adjacently co-cast materials was strong enough to keep the interface area intact while applying the tensile stress.

In addition to proving a high adhesion between stripes, high strength performance of SBS tapes guarantees an easy removal of green samples from the Mylar substrate without deforming the green sample.

4. Conclusion

The flow field in a novel side-by-side tape casting technique was studied. With a goal to form dense self-supporting thick graded tapes a standard methylethylketone and ethanol-based recipe has been modified. Minor changes in binder and solvent content strongly influenced viscosity values but did not have a strong effect on slurry density as the ceramics mass load in our work was kept constant. Slurries with 35.5–43.5 vol.% binder content and 40–48 vol.% solvent load were proven to form adjacently segmented tapes with a well distinguished interface and high mechanical performance. The slurry densities varied in a very small range.

With rheological characteristics of the used slurries as the basis, the detailed velocity and the pressure field in the doctor blade region was numerically described. Developed model[13] showed that the investigated ceramic slurries with different viscosities emerge with similar shear rates during the casting process. The maximum feasible slurry load in the casting reservoir in our particular case was set to 22 ± 2 mm. Despite that numerically determined relevant working shear rate region was quite wide, and only slurries with viscosities below 5000 mPas at 3.3 s^{-1} shear rate were stable in the defined working region.

A qualitative analysis using the formula, derived by Chou et al.[22] for dried thickness calculation aimed to assess the main sources of flow instabilities and their further verification on the interface shape formation. Both when the viscosity of cast slurries and the casting speed were changed, the main reasons of tape thickness deviation were the correlation between shear-driven and pressure-driven forces and the difference in the duration of co-casting. As the slurry viscosities were corrected by solvent and binder content, a decrease in slurry viscosity resulted in a decrease in tape thickness due to a higher amount of solvent evaporating during drying. Describing the influence of casting speed on tape thickness consistency, the correlation between pressure- and shear-driven forces played the major role. Side flow, typical for low viscous slurries, gave a minor impact on tape thinning but a high impact on the interface formulation. Low viscous slurries were noticed to overflow slurries with a higher viscosity forming a tilted interface. When slurries of similar

Please cite this article in press as: Bulatova R, et al. Thickness control and interface quality as functions of slurry formulation and casting speed in side-by-side tape casting. *J Eur Ceram Soc* (2014), http://dx.doi.org/10.1016/j.jeurceramsoc.2014.07.013

viscosities were co-cast, the interface was steep perpendicular to the casting surface.

Considering the formation of steeper interfaces with increasing casting velocity, the duration of co-shearing, drying time and surface tension between adjacent materials played a dominant role. The faster the slurries were co-cast, the less time adjacent materials had to merge and form the interface and undergo instabilities, caused by pressure-driven flow. Future work will be devoted to studying the effect of co-shearing time and surface tension impact on the quality of graded tapes.

By carrying out the tensile test on green samples, it was proven that it is possible to shape a side-by-side graded material with a good adhesion in a one-dimensional interface.

Acknowledgments

The authors would like to acknowledge the support of the Scientific Research Councils on Technology and Production Sciences (FTP) (Contract No. 09-072888, OPTIMAC), which is part of the Danish Council for Independent Research (DFF)

References

1. Kieback B, Neubrand A, Riedel H. Processing techniques for functionally graded materials. *Mater Sci Eng A* 2003;**362**(1):81–106.
2. Mistler RE, Twiname ER. *Tape casting: theory and practice*. Wiley-American Ceramic Society; 2000.
3. Thorel AS. Tape casting ceramics for high temperature fuel cell applications. In: Wunderlich W, editor. *Ceramic materials*. Intechopen; 2010. p. 49–69.
4. Das N, Maiti HS, Glass C. Tape-cast ceramic membranes for microfiltration application. *J Mater Sci* 1996;**31**:5221–5.
5. Lindqvist K, Lid E. Preparation of alumina membranes casting and dip coating by tape. *J Eur Ceram Soc* 1997;**17**:359–66.
6. Smith A, Bahl CRH, Bjørk R, Engelbrecht K, Nielsen KK, Pryds N. Materials challenges for high performance magnetocaloric refrigeration devices. *Adv Energy Mater* 2012;**2**(11):1288–318.
7. Bahl CRH, Velazquez D, Nielsen KK, Engelbrecht K, Andersen KB, Bulatova R, et al. High performance magnetocaloric perovskites for magnetic refrigeration. *Appl Phys Lett* 2012;**100**(12):121905.
8. Dinesen AR, Linderoth S, Pryds N, Smith A. Risø National Laboratory, applicat. A magnetic regenerator, a method of making a magnetic regenerator, a method of making an active magnetic refrigerator and an active magnetic refrigerator. International patent US2012079834 (A1). 2006.
9. Lorenz B, Wang Y-Q, Chu C-W. Ferroelectricity in perovskite $HoMnO_3$ and $YMnO_3$. *Phys Rev B* 2007;**76**(10):104405.
10. Raeder H, Simon C. Tape casting of zirconia for ion conducting membranes: a study of dispersants. *J Eur Ceram Soc* 1994;**13**(6):485–91.
11. Wonisch A, Polfer P, Kraft T, Dellert A, Heunisch A, Roosen A. A comprehensive simulation scheme for tape casting: from flow behavior to anisotropy development. *J Am Ceram Soc* 2011;**94**(7):2053–60.
12. Guillemet-Fritschc S. The thickness of $BaTiO_3$ tape castings as function of the slip system. *J Ceram Process Res* 2012;**13**(2):101–4.
13. Jabbari M, Bulatova R, Hattel J, Bahl CRH. Quasi-steady state power law model for flow of $(La_{0.85}Sr_{0.15})_{0.9}MnO_3$ ceramic slurry in tape casting. *Mater Sci Technol* 2013;**29**(9):1080–7.
14. Natividad SL, Marotto VR, Walker LS, Pham D, Pinc W, Corral EL. Tape casting thin, continuous homogenous, and flexible tapes of ZrB_2. *J Am Ceram Soc* 2011;**94**(9):2749–53.
15. Song J-K, Um W-S, Lee H-S, Kang M-S, Chung K-W, Park J-H. Effect of polymer molecular weight variations on PZT slip for tape casting. *J Eur Ceram Soc* 2000;**20**(6):685–8.
16. Tok AIY, Boey FYC, Lam YC. Non-newtonian fluid flow model for ceramic tape casting. *Mater Sci Eng A* 2000;**280**(2):282–8.
17. Sanson A, Pinasco P, Roncari E. Influence of pore formers on slurry composition and microstructure of tape cast supporting anodes for SOFCs. *J Eur Ceram Soc* 2008;**28**(6):1221–6.
18. Jian G, Hu Q, Lu S, Zhou D, Fu Q. Effect of solid content variations on PZT slip for tape casting. *Process Appl Ceram* 2012;**6**(4):215–21.
19. Jabbari M, Spangenberg J, Hattel JH. Interface behavior in functionally graded ceramics for the magnetic refrigeration: numerical modeling. *Appl Mech Mater* 2013;**325**:1362–7.
20. Li N, Wen Z, Liu Y, Xu X, Lin J, Gu Z. "Preparation of Na-beta"-alumina film by tape casting process. *J Eur Ceram Soc* 2009;**29**(14): 3031–7.
21. Huang XY, Liu CY, Gong HQ. A viscoplastic flow modeling of ceramic tape casting. *Mater Manuf Process* 1997;**12**(5):935–43.
22. Chou YT, Ko YT, Yan MF. Fluid flow model for ceramic tape casting. *J Am Ceram Soc* 1987;**70**(10):280–2.
23. Jabbari M, Hattel JH. Numerical modeling of the side flow in tape casting of a non-newtonian fluid. *J Am Ceram Soc* 2013;**96**(5):1414–20.
24. Pitchumani R, Karbhari VM. Generalized fluid flow model for ceramic tape casting. *J Am Ceram Soc* 1995;**78**(9):2497–503.
25. Gutierrez C, Moreno R. Tape casting of non-aqueous silicon nitride slips. *J Eur Ceram Soc* 2000;**20**(10):1527–37.
26. Yoon D-H, Lee BI. Processing of barium titanate tapes with different binders for MLCC applications—Part II: Comparison of the properties. *J Eur Ceram Soc* 2004;**24**(5):753–61.

Please cite this article in press as: Bulatova R, et al. Thickness control and interface quality as functions of slurry formulation and casting speed in side-by-side tape casting. *J Eur Ceram Soc* (2014), http://dx.doi.org/10.1016/j.jeurceramsoc.2014.07.013

PAPER II

R. Bulatova, K. B. Andersen, L. Theil Kuhn, C. R. H. Bahl, and N. Pryds, “Functionally Graded Ceramics Fabricated With Side-By-Side Tape Casting For Use In Magnetic Refrigeration”, *Int. J. Appl. Ceram. Technol.*, IJAC 12298.

Int. J. Appl. Ceram. Technol., 1–8 (2014)
DOI:10.1111/ijac.12298

Functionally Graded Ceramics Fabricated with Side-by-Side Tape Casting for Use in Magnetic Refrigeration

Regina Bulatova,* Christian Bahl, Kjeld Andersen, Luise Theil Kuhn, and Nini Pryds

Department of Energy Conversion and Storage, Technical University of Denmark, Risø Campus, Roskilde, DK 4000, Denmark

Functionally graded ceramic tapes have been fabricated by a side-by-side tape casting technique. This study shows the possibility and describes the main principles of adjacent coflow of slurries resulting in formation of thin plates of graded ceramic material. Results showed that the small variations of solvent and binder system concentrations have a substantial effect on slurry viscosity. Varying these parameters showed that side-by-side tape casting with a well-defined interface area is possible for slurries with viscosities above 3500 mPa s at a casting shear rate of 3.3 s^{-1}. As it was expected, the choice of de-bindering and sintering regimes significantly influences crack formation, and a three-step heating programme was found to result in tapes of the highest quality. The interface regions of green graded tapes were investigated structurally by scanning electron microscopy; for a distinct identification of the interface region and analysing the degree of cross-interface diffusion, the isothermal entropy change was measured by a vibrating sample magnetometer as the magnetic transition temperature (Curie temperature) is very sensitive to the dopant level in ceramics. Also the purpose of developing this graded ceramic tape casting was applications of these specific magnetocaloric properties within the magnetic refrigeration technology.

Introduction

Over the last decades, the technology of magnetic refrigeration (MR) has been developed toward the level of becoming a potential substitute for the conventional compressor-based refrigeration or air-cooling devices [1,2] due to the potential for higher efficiency and the emission-free technology used. The principle of MR relies on the magnetocaloric effect (MCE),[3] that is the reversible temperature change of magnetocaloric materials as a response to the application of a magnetic field. For ferromagnets, the MCE is strongest close to the magnetic transition temperature, the so-called Curie temperature (T_C). Thus for room temperature applications, magnetocaloric materials with T_C in this range are desired.

Recently, a large number of papers have been published reporting on the MCE in the mixed valence perovskite manganites with the general formula $A_{1-x}A'_xMnO_3$ (A — rare earth element, A′ — Sr, Ca, Ba, etc.).[4–7] Among other advantages of ceramics such as easy shaping and cost-effective production, one of the most important features of the perovskites is that the compounds are suitable for chemical doping. As the magnetic properties of these powders, for example T_C, are strongly doping-dependent, these materials are suitable for MR at various operating temperatures and especially near room temperature. A compound, which has been demonstrated in use as a magnetocaloric material, is $La_{0.67}Ca_{0.33-x}Sr_xMn_{1.05}O_3$ (LCSM) (perovskite), which can exhibit a range of T_C by varying the ratio between Ca and Sr (Ca/Sr).[8]

The design of magnetic refrigeration devices[7,9] defines some geometrical requirements of the magnetocaloric materials to be used. Among all possible geometries,[1] thin dense plates are desired due to the fact that these plates provide low pressure drop and can transfer heat effectively. Plates with a thickness of about 300 μm are chosen for practical reasons of preparation, handling and stacking. The flatness of the plates is very important as it is desired to stack the plates as close as possible. A thickness variation of <5–10% of the average tape thickness is desirable to avoid maldistribution of the flow.[10] To extend the temperature span of the MR device, a graded material with varying T_C along the length is also needed (for details, see [8,11,12]).

The new "side-by-side" adjacent tape casting method has been suggested to achieve the goal of having a gradually increasing T_C within one dense platelet structure. Tape casting (also known as doctor blading, knife coating) was chosen as it is the most common technique proven to be effective for manufacturing uniform thin plates on a large scale.[13] In general, tape casting is a forming process in which a slurry, with a high concentration of solid loading, is pulled out by a moving carrier from the tank reservoir, forming a thin film of predefined geometry; subsequent sintering leads to forming of dense

*regb@dtu.dk

self-supporting plates. The principal novelty of the side-by-side tape casting technique is based on simultaneous adjacent cocasting of a number of slurries adjacently from the doctor blade reservoir, predivided into compartments by partitions. The advantage of side-by-side tape casting is versatility of materials adjacently cocast into a single plate with well-defined interfaces.

In this study, microstructure and magnetic properties of the interface regions between adjacent stripes both in the green and sintered states were investigated. Mixing/diffusion in the interface region were proven to be strongly dependent on the flow properties.

Experimental Procedure

Spherical particles of a series of commercially available manganites with five different compositions $La_{0.66}Ca_{0.33-x}Sr_xMnO_3$, $x \in [0.0375–0.0600]$ (LCSM) (CerpoTech AS, Heimdal, Norway) were prepared by spray pyrolysis; subsequent calcination at 1000°C for 2 h was applied to remove the absorbed water from the powders, increase the phase purity and get a coarser structure. The five LCSM powders were named from LCSM1 to LCSM5 according to increasing Curie temperature (T_C) (Table I) as the T_C is very sensitive to the composition of doped perovskites.[8] The Curie temperature was measured as the point of maximum heat capacity in zero applied magnetic field. This was measured on a custom-built differential scanning calorimeter (DSC),[14] and the results are shown in Fig. 1. Due to the chemical similarity of the powders, the exact composition of each powder is not known exactly. However, the correlation between the Curie temperature and the intended composition is consistent with that given in the Ref. (15).

The particle size distribution was identified at every step of slurry preparation by light scattering (LS 13320; Beckman Coulter, Miami, FL). Specific surface area of the powder was measured using the Brunauer, Emmett, and Teller method (BET) (SA3100; Beckman Coulter). The measured values are given in Table I.

Table I. Properties of the Calcined LCSM Powders

	T_C (K)	PSD (d_{50}) (μm)	BET (m^2/g)
LCSM1	272	1.43	7.53
LCSM2	277	2.04	10.85
LCSM3	281	2.08	7.97
LCSM4	284	1.63	15.04
LCSM5	288	1.74	10.86

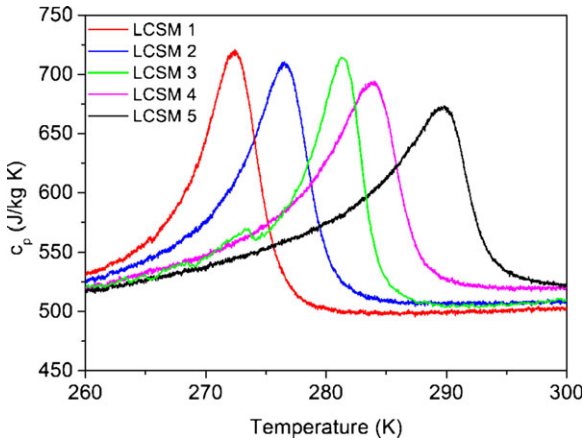

Fig. 1. Differential scanning calorimeter (DSC) data of the five LCSM powders at zero applied field after calcination at 1000°C.

The magnetic properties were analysed using vibrating sample magnetometer (VSM) (Model 7407; Lake Shore Cryotronics, Westerville, OH). Magnetization as a function of magnetic field and temperature was measured in fields up to 1.2 T. The magnetic entropy change ΔS_M (T,H) was calculated from magnetization curves employing the thermodynamic Maxwell relation (1):

$$\Delta S_M(T,H) = \int_0^H \left(\frac{\partial M}{\partial T}\right) dH \qquad (1)$$

The initial slurry composition with proportions of all ingredients as proposed by Raeder *et al.* [16] was used with polyvinylpyrrolidone (PVP, Mw = 10,000 g/mol) as a dispersant. An azeotropic mixture of methylethylketone and ethanol (MEKET) (2:1 wt%) was chosen due to the ability to dissolve most organic additives, uniform distribution of ingredients and drying fast enough to avoid formation of defects.[13] 0.2 wt% of the lubricant Additol was added to reduce friction between the materials. To find the optimal rheological behavior and improve the quality of green and sintered graded tape, the loading of MEKET as a solvent and the binder system [polyvinyl butyral (PVB), polyethylene glycol (PEG), dibutyl phthalate (DBP), and Additol] was varied in the range of 46.02–48.85 wt% and 38.54–41.80 wt %, respectively.

The desire to use high viscosity slurries for the tape casting requires the ball-milling process to be divided into steps to break apart the particle agglomerates to the smallest possible sizes and to ensure homogeneity of ingredient distributions. Initial suspensions were prepared

by, first, dissolving 85 wt% of dispersant in solvent and adding 80 wt% of the ceramic powder, followed by a low-energy ball-milling for 40 h; subsequently, the rest of the powder, dispersant, and solvent were added. Another 30 h of low-energy ball-milling was required to break down powder agglomerates. The duration of each milling step was identified experimentally by measuring the particle size at intervals during the milling. In the last step, the binder solution, containing the binder and plasticizer suspension, was added to the mixture to yield the final slurry composition. The slurries were kept slowly rotating for another 20 h to continue homogenization with minimum risk of bubble formation within the slurry. Before tape casting, slurries were poured over a 100-μm meshed filter to separate possible agglomerates. Any air bubbles in the slurries were removed by placing the slurries in a vacuum chamber at 200 mbar for 5 min. Rheological parameters of suspensions were measured at every step of the slurry preparation (Haake RheoStress 600; Thermo Electron GmbH, Karlsruhe, Germany). The shear rate programme was used with a plate–plate sensor system with plate diameters of 60 mm and a gap height of 0.1 mm. A preshear mode of 50 s^{-1} was applied for 1 min with a subsequent 1-min rest to approach measuring conditions close to those for tape casting and disregard the history of slurry pretreatment.

The slurries were cast using a single doctor blade vessel on a moving Mylar tape. The vessel was subdivided into five compartments as shown in Fig. 2a using pieces of Teflon. The quality of cast tapes was strongly dependent on a careful fixation of compartment partitions in the doctor blade chamber. Before attaching the plastic partitions in the vessel, the fronts of the plastic partitions were sharpened with sand paper, creating about 1.5 mm keen edge at 45 degrees to the Mylar substrate and to the doctor blade (Fig. 2b). This was done to avoid mixing and overlapping of adjacently moving suspensions. Partitions with a blunt front side were observed to result in furrows in the surface of the dried green tape, that is, because thick slurries dry fast, without having time to flow aside, and assume shape with a minimum surface area. After sharpening the front side, partitions were mounted inside the tank using double-side adhesive tape. On top of that, the partitions were fixed by a one-sided adhesive tape to avoid interleaking of slurries between adjacent compartments.

All the tapes were cast with a gap height of 1 mm and a casting speed of 20 cm/min on silicon-coated Mylar film. An example of a tape cast with five materials is shown in Fig. 3. After drying in room temperature for 2 days, tapes were punched out in 30-cm-long pieces.

To optimize de-bindering and sintering profiles, simultaneous measurements of thermogravimetric analysis (TG) and differential thermal analysis (DTA) of green tapes were performed in atmospheric air (Netzsch STA-449C; NETZSCH GmbH, Selb, Germany). The results from the TG and DTA analysis was used to optimize the sintering programme as discussed below.

X-ray analysis was carried out on each of the calcined LCSM powders using a Bruker D8 Advance powder diffractometer. All the powders were found to be highly phase-pure with an orthorhombic structure with the space group *pnma*.

To study the interface between the different materials after sintering, pieces of the tapes were embedded in epoxy, polished, and carbon coated. Pieces of the green tapes were held in clamps. The cross-sections of both green and sintered samples were observed with a scanning electron microscope (SEM) (Hitachi TM3000, Hitachi High-Technologies Europe GmbH, Krefeld, Germany) at 15 kV.

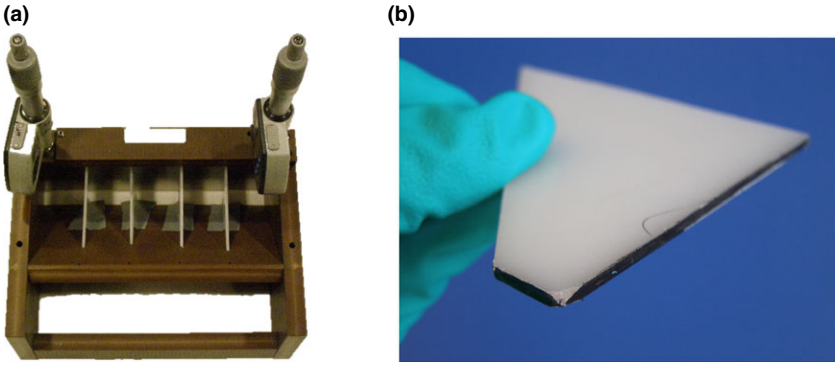

Fig. 2. (a) Tape caster vessel divided with partitions in a five-compartment setup; (b) sharpened front side of a Teflon partition, used for separation of doctor blade reservoir into compartments. The width of the tape caster vessel was 17.8 cm.

Fig. 3. Adjacently graded LCSM green tape. The width of the graded ceramic tape is 18.6 cm, and the length is 110 cm.

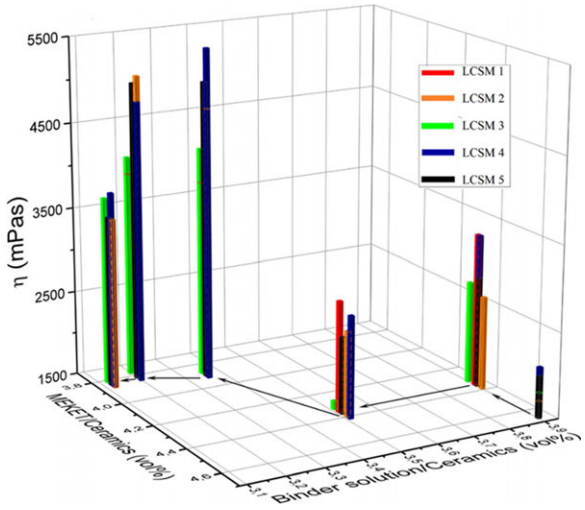

Fig. 4. Viscosity of LCSM slurries as a function of binder solution and solvent MEKET concentrations with respect to constant ceramics load. Five different formulations of five slurries are connected with arrows, which show the experimental sequence for each of slurry.

Results and Discussion

Based on the previous experience in ceramic-shaping techniques, the ability to tape cast slurries adjacently was assumed to rely on the following principles. Firstly, cocast slurries must be viscous enough to prevent intermixing in the interface area, minimize overlapping between cocasting slurries, and guarantee high physical adhesion between neighboring materials. Secondly, processed suspensions are to be characterized by a similar flow behavior (fluid properties), that is pseudoplasticity, density, surface tension, etc. This is required to ensure similar shrinkage rates and identical final thickness of neighboring materials, thus minimizing stress development during drying and sintering processes. To satisfy this, the same solvent system and organic additives for cocast slurries must be chosen. Thus, it was decided to use a recipe with a high solid loading as a starting formulation.[16] In addition to that, the desire to tape cast thick tapes demanded simplification and acceleration of the slurry drying process,[13] leading to the choice of the organic solvent MEKET. Initially, the same slurry formulation was used for preparation of all five suspensions (Fig. 4). However, viscosity values of precast slurries were different because of variations in the specific surface areas of the different powders (Table I). Slurries were cocast with these five identical slurry formulations, but the obtained graded tapes cracked during the sintering programme due to stresses accumulated at the interfaces between slurries with a different shrinkage behavior. Therefore, each slurry had to be individually tailored to account for the variation in shrinkage.

To optimize the slurries for cocasting, the viscous properties of each slurry were measured at different contents of binder and solid loading. As the amount of dispersant was optimized by a sedimentation test and was fixed at 11.24 vol% with respect to solid content for all five LCSM powders, it was decided to keep dispersant and solid loading constant. The recipe varied by adjusting the solvent and binder solution (binder and plasticizer) amounts referring to the volumetric content of the solid part (ceramics).

The general tendency of viscosity increase with a reduction in the amount of solvent (solid load was kept constant) was typical for all five formulations, as seen in Fig. 4. Increased slurry viscosities as a result of increased binder solution content are due to the effect of simultaneous decrease of solvent content in the total slurry volumes. It proves that the fraction of solvent affects the viscosity more compared to the binder solution content. However, the slurry viscosity is also sensitive to the binder system content, which was varied to adjust drying and sintering shrinkage of cocast materials. In tests, where the slurry formulation was corrected by raising the binder system concentration while keeping the solvent content constant, the viscosity for all five slurries also increased (Fig. 4). This indicates that polymeric chains of binder form a dense matrix, without replacing dispersant from the surface of the powder. A decrease of slurry viscosity with binder system would indicate insufficient stabilization of powder surface allowing the binder to act as a dispersant.[13]

In addition to optimizing the recipes with the aim of preparing slurries with similar high viscosity values,

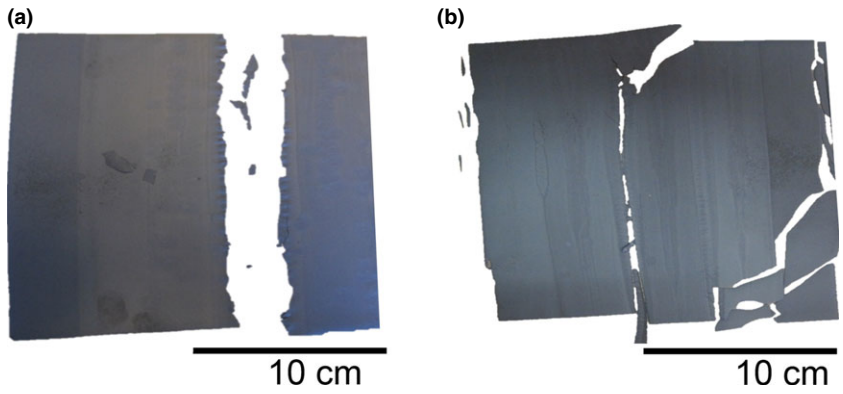

Fig. 5. Crack propagation due to (a) difference in drying and sintering between cocast materials (the second formulation of optimizing recipes) and (b) excess of the solvent load, happening during sintering of graded materials (the third formulation of optimizing recipes).

the main criterion for the final recipe formulation was obtaining flat uniform tapes of a certain thickness without any defects after the sintering process. It was decided to aim for slurries with viscosities in the range of 3500–4000 mPa s due to qualitative analysis of tapes cast with a given range of viscosities. The less viscous slurries resulted in more complicated control of tape thickness, and less uniform tapes were obtained. Thus, the difference in drying shrinkage rates induces stress accumulations at the interface area with subsequent crack nucleation (Fig. 5a). The second origin of fracture propagation was due to a weak microstructure being formed. In case of solvent excess, the polymer chains of the binder are more remote, making the polymeric matrix stretched over a long distance, and therefore the tape becomes more fragile (Fig. 5b).[13] Because of the low slurry viscosity, fractures may be caused even on the sintering stage.

The test indicated that reducing the amount of solvent by 10 wt% (2 g in slurry with 100 g of powder), the viscosity was increased from 2200 to 3000 mPa s. The results showed that the viscosity changed about 500 mPa s per 1 g of solvent with 100 g of powder in the range 2000 mPa s to 3500 mPa s. For higher viscosities, less reduction was needed. Up to approximately 5000 mPa s, a 1000 mPa s change for every gram of solvent with 100 g of powder was observed. So, by reducing the amount of solvent (Fig. 4) it was possible to achieve a viscosity in the range of 3500–5000 mPa s, which is what is desired for casting the tapes with a gap between doctor blade and casting carrier of 1 mm. This blade height resulted in thickness of the sintered plates in the range from 200 to 300 μm.

The measured viscosity curves for the binder solution for the five optimized slurries compositions show pseudoplastic (shear-thinning) behavior, reflecting their flocculating nature (Fig. 6). In the case of binder solution, in the region of small shear rates, polymer chains tend to curl up to globules to minimize surface energy.[13] Increasing the shear rate leads to elongation of polymers in the direction of tape casting, and apparent viscosity decreases as a consequence leading to shear-thinning behavior, required for tape casting slurries. No difference was observed in the viscosity curves from increasing the shear rate from 0.1 to 50 s^{-1} to the curves obtained when reducing the shear rate from 50 to 0.1 s^{-1}. This shows that the slurries for cocasting do not exhibit thixotropic behavior. The casting shear rate, purely driven by a moving carrier and neglecting the effect of the gradually decreasing pressure in the reservoir, was calculated by a simple formula, used for approximate estimation of the casting viscosities, $\gamma = v/h$, where γ is the shear rate, v is the casting speed, and h is a gap between doctor blade and carrier film. Thus with the parameters used here, the

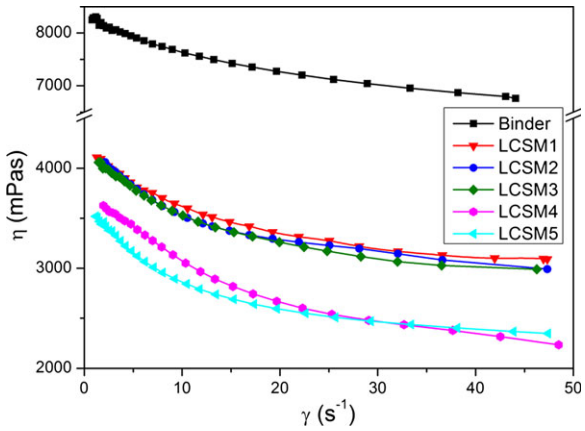

Fig. 6. Flow curves for the binder and five cocast slurries after recipe optimization.

shear rate will be 3.3 s^{-1}. At this shear rate, the viscosities of the final slurries prepared from the powders LCSM1–LCSM5 were 3950 mPa s, 3950 mPa s, 3920 mPa s, 3500 mPa s, 3320 mPa s, respectively, with a viscosity of 8000 mPa s for the pure binder solution.

The final formulation of slurries, containing 46.69–47.15 vol% of MEKET (MEKET/ceramics variation is 3.78–3.85) and 39.21–39.55 vol% of binder system (binder solution/ceramics is 3.20), was cast into a graded flexible tape with a crack-free surface.

Standard tape casting involves the use of two doctor blades. The first blade controls the shearing of the slurry, while the other blade, situated behind the first, is intended to control the slurry level and consequently keeps the pressure in the space between two doctor blades constant. That allows neglecting the factor of gradual hydrostatic pressure decrease during tape casting process. In the case of side-by-side tape casting, the double doctor blade adoption is hard to implement as the separation would have to extend below the second blade to prevent leaking across adjacent compartments. Oppositely, casting with just one doctor blade results in tapes with thickness variation along the tape length. Depending on casting velocity, gap height, viscosity and density of slurry, and loading level in the reservoir, this deviation could vary from tens to hundreds of micrometer.[17]

After tape casting, the green tapes were kept in a ventilated room for 40 h before being sintered. To create solid dense material, the dried graded tape is to be sintered with minimum stresses accumulated in polymeric matrix and minimum stresses generated during sintering programme.

The sintering profile was optimized by studying the mass loss during TG analysis of LCSM 2 green tape (Fig. 7) carried out up to 700°C. Two characteristic transition temperatures were observed at approximately 200, 350, and 400°C, and no other mass loss was found up to 700°C. The effect of minor mass loss at about 270°C was compensated with a slow heating speed in a sintering programme. To define dispersant, binder, and plasticizers burnout temperatures, TG was carried out for each individual polymer solution. Here the boiling points for plasticizers DBP and PEG are 200 and 250°C, respectively, and PVP burns off at 380–420°C. The mass loss curve of PVB showed two transition temperatures at 330 and 440°C. No significant difference in the TG was observed when comparing pyrolysis profile of single polymers solutions to the equivalent components in cast tapes. Thus, no reactions between polymers in cast tapes have taken place and the heating rate was slow enough to represent gradual removal of the polymer matrix without stress formation.

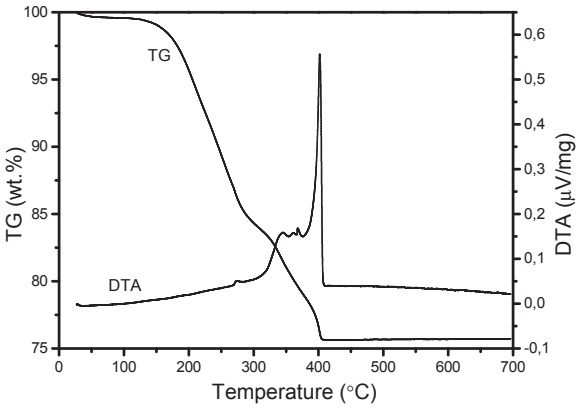

Fig. 7. TG-DTA results of green tape LCSM2, showing the temperature range of organic thermal decomposition.

Therefore, a three-step heating programme was chosen. First, green tapes were heated to 200°C and then to 400°C both with 15°C/h heating rate. At both temperatures, a dwell time of two hours was applied. Further sintering was performed with a heating rate of 60°C/h up to 1250°C keeping this sintering temperature for another four hours. The following cool down to room temperature was realized with a cooling rate of 100°C/h. Applying this sintering profile resulted in tapes free of defects by a visual inspection. The densities of the sintered tapes LCSM1–LCSM5 were 5.90(4), 5.28(7), 5.56 (5), 5.71(1), and 5.67(3) g/cm^3, respectively.

The SEM microstructure pictures in Fig. 8 show for both green and sintered tapes the cross-section of the interface regions between LCSM1 and LCSM2. The cracks observed in the microstructure of the green tape are the result of mechanically punching the sample from the green tape. Normally, polishing of cross-section of the bulk ceramic material is required to neglect any pretreatment influence of studied structure. However, polishing of green ceramic thin plates is not possible due to high flexibility of tapes. The sintered tape was polished in epoxy following the standard way described in the experimental part.

In the case of the green tape, the difference in particle and pore sizes of the adjacent materials can be used to visualize the interface, see Fig. 8a. The exact profile of the interface is hard to determine, but it is seen that any intermixing or overlapping takes place on a length scale of less than about 500 μm.

Unlike in the green tape, the interface in the sintered tape is hard to identify (Fig. 8b). The image confirms that the recipes of all slurries were adjusted well enough, so there is a perfect match of the shrinkage and strain development between neighboring materials.

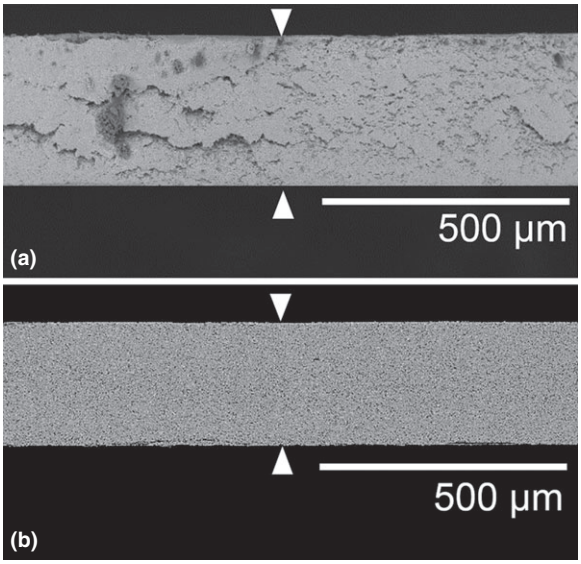

Fig. 8. SEM microstructure of interface between LCSM1 and LCSM2 stripes in (a) green and (b) sintered states. The arrows indicate the expected positions of the interfaces between cocast LCSM1 and LCSM2.

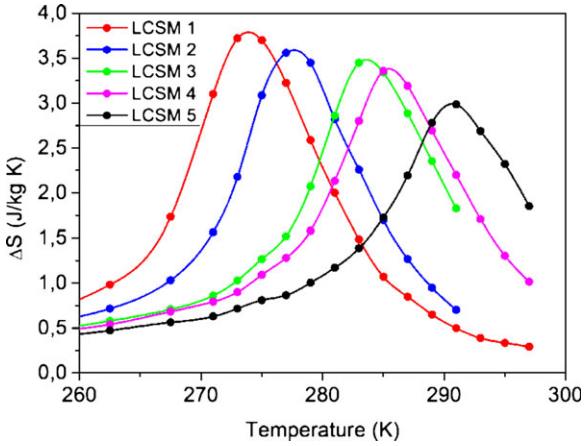

Fig. 9. Temperature dependence of magnetic entropy change for LCSM stripes of sintered graded tape in the field of 1.2 T.

Therefore, after sintering, a uniform grain size and pores distribution was achieved along the whole graded tape. Due to the very similar chemical compositions of the five LCSM materials used in this work, energy-dispersive X-ray spectroscopy (EDS), which would normally be used for the elemental analysis of chemical differences, was not able to resolve the interface. Thus, the profile of the interface in the sintered tape is unknown, but visual inception of the cross-sections indicates that the overlapping is on a scale of below 1 mm.

The magnetic properties of the different LCSM materials used here differ somewhat from each other due to the high sensitivity to the exact composition of the materials. Fig. 9 shows the isothermal entropy change ΔS_M of sintered tapes of the five materials LCSM1 to LCSM5 in an applied field of 1.2 T. The tapes were cast individually and sintered using the programme described above. Individual casting of the five tapes eliminated any risk of contamination between cocast materials at the region close to the interfaces. The entropy changes shown in Fig. 9 are seen to be relatively evenly spaced, with the peak height decreasing as the temperature increases. The peaks are found at values a few degrees higher than the specific heat peaks shown in Fig. 1. This is presumably due to a distribution of Curie temperatures in the samples, due to distributions of the dopants.[18]

The magnetic properties of a tape sample containing the two materials LCSM4 and LCSM5 and the interface between these were characterized in the VSM. However, as the ΔS_M curves from the individual materials were very broad and the peaks are only a few degrees apart, the resulting ΔS_M curve from the sample cut from the interface region showed just one broad peak. To better characterize an interface region between two materials, samples were taken from a tape cast using two other compositions of LCSM from a similar batch. The temperature spacing between the ΔS_M peaks of these two adjacently cast LCSM materials was approximately 20 K, so that the two peaks are easily distinguishable. Figure 10 shows the ΔS_M data recorded from the interface region in a field of 0.25 T. The low field was used to make the peaks narrower and thus easier to distinguish. The sample used for the measurements was broken from an area of the sintered tape containing the interface, with about 1 mm of material either side of the interface. However, a small overlapping of the two materials, on the order of 1 mm by visual inspection, made it hard to get equal amounts either side of the interface. So the difference in the height of the two peaks is due to a difference in the amounts of the two materials. Overlaid in Fig. 10 is a superposition of data recoded from individual samples of the two materials taken far from the interface region. It was found that using a ratio of 3.35 between the high and low transition temperature datasets reproduced the heights of the measured interface data best. It is observed that the peaks in the data recorded from the interface piece are spaced slightly closer together than the data from the individual pieces. This may be due to some interdiffusion of Ca and Sr between the two materials at the interface, causing the difference in the Ca/Sr ratio to even out. The profile of the peak in the ΔS_M data is determined by the local Ca/Sr ratios in the measured sample.

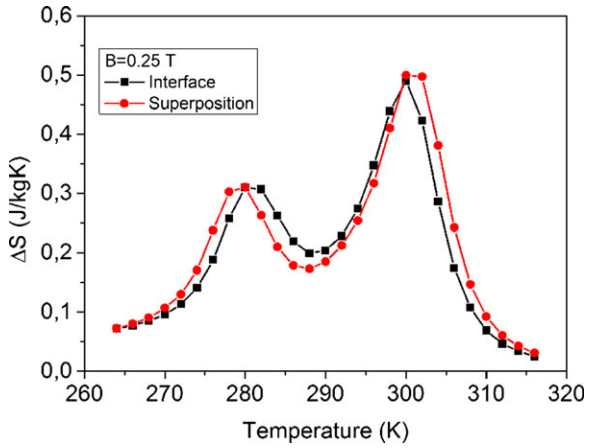

Fig. 10. Temperature dependence of magnetic entropy change for sintered sample, containing interface between two LCSM stripes, and for the superposition of the data from the individual materials in an applied magnetic field of 0.25 T.

The cation diffusion constant for similar materials at 1275 K is of the order of 10^{-17} m^2 s^{-1}.[15,17] Over a sintering time of four hours, this will only give rise to diffusion on the length scale of 10 μm. However, even a small overlapping of these thin tapes will result in a relatively large interface area. Thus diffusion and grain growth of mixed grains during the sintering process may well explain the small shifting of the peaks in Fig. 10.

Conclusion

This work showed that plates made by side-by-side tape casting with five different materials can be produced. Among the challenges of adjacent coflow are matching slurry viscosities by varying solvent and binder content, optimizing shrinkage magnitude and rate during drying and de-bindering, and control of stress development during sintering. Slurries with viscosities of 3500–5000 mPa s at a shear rate of 3.3 s^{-1} result in well-adhered samples. No signs of significant intermixing of the two stripes were observed in green state on the length scale of 0.1 mm (Fig. 7a).

The sintered graded tape of optimized composition was shown to be dense and highly uniform. To distinguish the interface region, the magnetic properties of a cocast plate were quantified. Curie temperature values, being very sensitive to dopant concentrations, showed a very good correlation of data measured empirically from the interface piece and recalculated as a superposition of entropy change of the individual materials. However, at increased sintering temperatures, only minor diffusion between cocast materials was found, which proves that quite well-defined interfaces between the materials can be maintained.

Tapes of adjacently side-by-side casted $La_{0.67}Ca_{0.33-x}Sr_xMn_{1.05}O_3$ materials have been produced in a quantity of 3 kg. These tapes are currently in use in a large-scale magnetic refrigeration prototype.

For future casting, the detailed study of the fluid flow impact and influence of the production parameters in cocasting technique is planned. The novel shaping technique of side-by-side tape casting opens a broad opportunity to form multistructural complex designs by a cost-effective and easy-scalable method.

Acknowledgment

The authors wish to thank Dr. Radha Krishnan Venkatesh for parts of the VSM and DSC measurements and Dr. Jonas Gurauskis for kind help in data treatment. The authors would like to acknowledge the support of the Scientific Research Councils on Technology and Production Sciences (FTP) (Contract No. 09-072888, OPTIMAC), which is part of the Danish Council for Independent Research (DFF).

References

1. A. Smith, C. R. H. Bahl, R. Bjørk, K. Engelbrecht, K. K. Nielsen, and N. Pryds, *Adv. Energy Mater.*, 2 [11] 1288–1318 (2012).
2. K. A. Gschneidner Jr and V. K. Pecharsky, *Int. J. Refrig.*, 31 [6] 945–961 (2008).
3. V. K. Pecharsky and K. A. Gschneidner Jr, 200 44–56 (1999).
4. M. H. Phan and S.-C. Yu, *J. Magn. Magn. Mater.*, 308 [2] 325–340 (2007).
5. Z. M. Wang, G. Ni, Q. Y. Xu, H. Sang, and Y. W. Du, *J. Appl. Phys.*, 90 [11] 5689–5691 (2001).
6. N. Pryds, *et al.*, *J. Am. Ceram. Soc.*, 94 [8] 2549–2555 (2011).
7. K. Engelbrecht, C. R. H. Bahl, and K. K. Nielsen, *Int. J. Refrig.*, 34 [4] 1132–1140 (2011).
8. C. R. H. Bahl, *et al.*, *Appl. Phys. Lett.*, 100 [12] 121905 (2012).
9. C. R. H. Bahl, T. F. Petersen, N. Pryds, and A. Smith, *Rev. Sci. Instrum.*, 79 [9] 093906 (2008).
10. K. K. Nielsen, C. R. H. Bahl, and K. Engelbrecht, *J. Phys. D Appl. Phys.*, 46 [10] 105002 (2013).
11. A. Rowe and A. Tura, *Int. J. Refrig.*, 29 [8] 1286–1293 (2006).
12. D. S. Arnold, A. Tura, and A. Rowe, *Int. J. Refrig.*, 34 [1] 178–191 (2011).
13. R. E. Mistler and E. R. Twiname, *3. Materials Processing: Slip Preparation, Tape Casting: Theory and Practice*. Wiley-American Ceramic Society, Westerville, OH, 2000, pp. 63–83.
14. S. Jeppesen, S. Linderoth, N. Pryds, L. T. Kuhn, and J. B. Jensen, *Rev. Sci. Instrum.*, 79 [8] 083901 (2008).
15. A. R. Dinesen, Magnetocaloric and Magnetoresistive Properties of $La_{0.67}Ca_{0.33-x}Sr_xMnO_3$, PhD thesis. Risø National Laboratory, Denmark, 2004.
16. H. Raeder, C. Simon, T. Chartier, and H. L. Toftegaard, *J. Eur. Ceram. Soc.*, 13 [6] 485–491 (1994).
17. M. Jabbari, R. Bulatova, J. H. Hattel, and C. R. H. Bahl, *Mater. Sci. Technol.*, 29 [9] 1080–1087 (2013).
18. C. R. H. Bahl, R. Bjørk, A. Smith, and K. K. Nielsen, *J. Magn. Magn. Mater.*, 324 [4] 564–568 (2012).

PAPER III

R. Bulatova, M. Gudik-Sørensen, A. Kaiser, M. D. Negra, K. B. Andersen, C. R. H. Bahl, ”The effect of tape caster operational parameters on the quality of adjacently graded materials” (to be submitted)

The effect of tape caster operational parameters on the quality of adjacently graded materials

R. Bulatova, M. Gudik-Sørensen, A. Kaiser, M. D. Negra, K. B. Andersen, C. R. H. Bahl

Department of Energy Conversion and Storage, Technical University of Denmark – DTU, Frederiksborgvej 399, DK-4000 Roskilde, Denmark

Abstract

The optimum condition among tape casting with single blade, double blade, using pump system and a proposed continuous speed change mode has been analysed for the purpose of forming green tapes of constant thickness. Advantages and limitations of every method are described here. The tape casting experiments were conducted using a solvent-based slurry and were built to be as generic as possible in order to allow the control of various processing conditions.

The single-blade tape casting technique from this study has been used for side-by-side tape casting of strontium doped lanthanum manganite oxide $La_{0.85}Sr_{0.15}MnO_3$ (LSM) slurry next to slurry, consisting of a mixture of LSM and gadolinium doped cerium oxide $Ce_{0.9}Gd_{0.1}O_2$ (*CGO*). In this work the influence of the geometric parameters of the partition, dividing the casting tank into chambers, on the quality of graded tape were studied. It was elucidated that at casting speeds above 30 cm/min and the shortest partition 'tongue' beneath the blade favours the formation of smooth graded tapes, while lower casting speeds and the presence of a partition tongue results in splitting and formation of a gap in the confluence area.

Introduction

Needs in manufacturing a functionally graded film grows together with development of such advanced technologies as solid-oxide fuel cells, piezoelectric devices, batteries, capacitors and actuators production. Tape casting (film casting, doctor blading, doctor blade casting), initially invented for manufacturing ceramic capacitors with the aim to improve dielectric properties and densify a microelectronics package [1], now is widely implemented into other advanced technologies. A wide range of shaping solid loads such as ceramic, polymeric, glass or metal particles of nano- and micro-sizes into thin, uniformly flat, hard or flexible films of tens meters, if required, is the one side of tape casting development. Nevertheless, in order to surpass more a machinery modern forming techniques and still tailor the requirements of smart technologies, the design of tape caster tank itself often has to be modernized. For instance, modernization of casting head included the inclination of the back wall of the tank, aiming to uniform the fluid flow inside the reservoir [2].

In the scope of enhancement the efficiency of advanced functional graded materials, the new side-by-side tape casting (SBS TC) (adjacent co-casting) forming technique has been invented. The fact that co-casting method itself was independently proposed by two scientific groups, working on magnetic refrigeration [3] and on improvement of a laser gain element [4], shows the high potential of SBS TC for gaining a broad commercial acceptance and development. Having the general idea of co-casting in common, these two works differed both by recipe composition and processing parameters. Kupp *et.al.* [5] tape cast xylenes- and ethanol-based slurry loaded with particles of micro- and nano-sizes; tapes were fabricated with a casting gap of 0.356 µm and a casting speed of about 70 cm/min. For magnetic cooling thicker films were required [6], so the graded tapes of micro-sized ceramic particles

were fabricated from the methylethylketone-based slurry using a gap of a 1000 μm and a casting speed of 20 cm/min. As it is seen, SBS cast tapes are possible to shape in a wide range of casting speeds and gaps with dissolving powders of both nano and micro sizes in organic solvents. Optical properties of Er:YAG graded tapes and magnetic properties of LCSM graded tapes were proven to be comparable with performances of typical commercially applied materials. Another critical difference in given works was the design of partition (divider). In Kupp's et.al. work [5], divider was made of steel and covered the whole tape caster reservoir and the gap under the shearing blade. Authors of magnetic cooling work used a Teflon partition, 1.95 mm wide and covering just the reservoir space, co-flowed slurries were sheared together underneath the blade.

Another aspect of dividing casting tank into segments is the target to improve alignment of elongated particles into the casting direction, since a torque, generated next to the tank walls, was proven to affect the particles rotation even more than a basic concept of increase in casting speed [5, 6]. In comparison of a set of tapered blades installed 5 mm apart from each other at the exit of the tank and array of sharpened pins 0.7 mm from each other, the latter ones shown to exhibit a higher degree of particles orientation in cast tape [8].

As one can see, the new idea of separating a standard casting tank into compartments came as an engineering solution for solving as different tasks as joining dissimilar materials into functional graded tape and forming of high-ordered thin films, however, optimization and study how partitions geometrical parameters affect the quality of cast tape is still missing. Current work is aimed to define and explore systematically which features of tapes is possible to control changing the design of the partition and changing the casting speed as one of the setting of machinery characteristics. For that, slurry with a solid load of ceramics strontium doped lanthanum manganite oxide $La_{0.85}Sr_{0.15}MnO_3$ (*LSM*) and another slurry, consisting a mixture of LSM and gadolinium doped cerium oxide $Ce_{0.9}Gd_{0.1}O_2$ (*CGO*) were co-cast.

In all three works [1, 2, 6], described above, tapes were cast using a single-blade system. However, nowadays lab-scale doctor blading technique use a double-blade system aiming to diminish the effect of the hydraulic pressure (pressure-driven flow, *Poiseuille flow*) on the tape thickness formation. The effect of hydraulic pressure stems from the differences in slurry level on opposite sides of the casting blade, affecting the actual slurry speed (shear-driven flow, during tape casting [9]. This pushing the slurry out of reservoir by a hydraulic force in addition to pulling force applied by a moving carrier (shear-driven flow, drag-driven flow, *Couette flow*) increase the total volume flow below the casting gap results in welling of the slurry right after it pass the blade. In some cases, due to welling the wet thickness of the tape exceeds the casting gap height.

Hence, the review of methods available in tape casting is proposed here in order to distinguish, first, which tape caster design guarantee a stable uniform slurry flow for the whole shaping process; and afterwards study the influence of the partition shape using selected tape caster design. Among tested, the double-blade system is the lab-scale solution for stabilizing the fluid flow and minimizing the effect of the hydraulic pressure drop behind the casting blade. Industrial finding differs mainly because of the higher volume of slurry used, which is supplied continuously on the long moving belt by a pump system. Another novel method of keeping tape thickness constant was invented as analysis of results of our previous work [10]. The concept relies on two simultaneous processes: at the beginning of the process the tape is usually thicker because of the cumulative effect of shear-driven viscous drag due to the peeling move of the substrate and pressure-driven hydraulic pressure

generated by a slurry column in reservoir; the second approach implies tape thinning with increase in casting speed [10], [11]. Therefore, the forth of proposed method is based on compensating the hydrostatic pressure decrease by a gradual decrease in casting speed.

Current study is comprehensively divided into two parts: establishing the tape caster design and a casting program with a focus to achieve a stable flow and uniform tape thickness, in another words, aiming to minimize or eliminate the hydrostatic pressure drop during the experiment. The second part of this study is devoted to clarification how partition design affects the graded tape formation at various casting speeds. As the output parameters for both adjacently cast slurries the tape thickness consistency and the interface shape between materials were controlled.

Experimental procedure

1. Raw materials and slurry preparation

The SBS cast tapes were prepared by adjacent co-shearing of two slurries. The first slurry contained 14.25 vol% of $La_{0.85}Sr_{0.15}MnO_3$ (LSM, Haldor Topsoe A/S, Denmark; calcined at 1200°C for 2 hours, arriving at a specific surface area of 18.0 m^2/g). The second slurry had 9.59 vol% LSM and 0.90 vol% of $Ce_{0.9}Gd_{0.1}O_2$ (CGO, Rhodia, France; uncalcined, specific surface area of 12 m^2/g) as solid loading. The choice of powders used is based on the wide usage of these ceramics in various applications [12], [13] with tape casting as the shaping technique. Another reason for using LSM and CGO is the difference in particle morphology and color, which facilitates detection of the interface between co-cast materials both visually by color and electronic microscopy due to the powders morphological and chemical differences.

Slurries were prepared according to the standard MEKET (azeotropic mixture of methylethylketone and ethanol) based recipe [9], [11], [14]. Uniform distribution of chemicals and fine grinding of particles in highly viscous slurry was achieved by the division of the milling process into steps. The detailed description of slurry content and workflow steps are given in our previous work [11].

In order to be able to compare and reproduce results from different tests, each step of slurry preparation has to be precisely controlled. To attain that, particles size distribution was measured during the whole period of the slurry preparation using Scattering Particle Size measurements (Beckman Coulter LS 13320, Miami, FL).

2. Rheological characterization

The apparent viscosity (η) measurements were conducted with pre-shearing and reversing increase of shear rate up to 50 s^{-1} using a cone-plate system (angle 1°) at 21 °C (MCR 301, Anton Paar GmbH, Graz, Austria), as shown in Figure 1. A solvent trap was used to minimize the evaporation of organic solvent during the rheological measurements. Both LSM and LSM_CGO slurries were characterize with a shear thinning behavior as required for tape casting.

Flow curve test (inset in Figure 1) showed that both LSM and LSM_CGO slurries possess an extremely low yield stresses, therefore the flow behavior of the slurries can be described by the Ostwald-de Waele power law fluid behavior:

$$\tau = k\dot{\gamma}^n \qquad (1)$$

where τ is the shear stress, $\dot{\gamma}$ the shear strain rate, k the constant describing the consistency of fluid, and n the constant describing deviation from the Newtonian flow. Due to thixotropy, viscosity curves for both LSM and LSM_CGO slurries yield individual hysteresis loops. The rheological behaviour and power law constitutive equation fit were chosen to be described by the reverse viscosity curves as they characterize the re-built viscosity. Fitting the experimental data of Figure 1 to Eq. 1, relatively high values of the correlation coefficient were obtained (Table 1), demonstrating a good compatibility of slurry fluid behavior with the Ostwald-de Waele power law model.

Table 1. Ostwald-de Waele power law model's fitting parameters and correlation coefficient.

	k	n	R^2
LSM	6.63(2)	0.73(3)	0.994
LSM_CGO	6.19(2)	0.77(3)	0.996

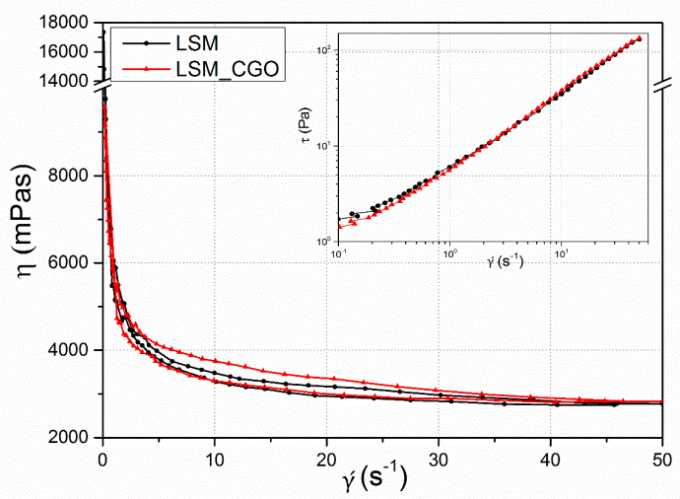

Figure 1. Viscosity and flow curves of LSM and LSM_CGO slurries.

In order to study how the rheological behavior of the slurries changes during the entire process of tape casting, the casting process was reproduced on the rheometer, using a specially built four step program (see Results and Discussion). To imitate the slurry drying process during the tape casting process, a spindle with 6 holes on its surface was implied. The test was performed using the spindle of 25 mm diameter with holes on top in order to improvise the drying process allowing the solvent to evaporate through these holes.

Before tape casting, LSM and LSM_CGO slurries were filtered through a 100 μm meshed tulle with a further de-airing step in a vacuum pump (100mBar) in order to remove air bubbles from the slurry volume. Slurries with viscosities (η) of about 4000 mPas at 3.3 s^{-1} shear rate ($\dot{\gamma}$) for both LSM and LSM_CGO were used for tape casting as discussed in Ref. [11].

3. Tape casting

3.1.Tape casting in the thickness control experiments.

LSM and LSM_CGO slurries were tape cast adjacently using a Teflon partition of 1.95 mm width, completely separating the two slurries into 4 cm wide sub-reservoirs [11]. The blade gap height was kept constant at 1 mm, and the casting speed for all experiments was 30 cm/min, except the fourth experiment, where the casting speed was changing. The

partition with no division (no partition ‘tongue’) underneath the casting blade was used for all tests. At the beginning of every test the casting gap was closed by Duct tape to ensure the simultaneous flow of adjacently cast slurries. Four different techniques for adjacently casting slurries were tested as described below.

Single-blade tape casting (SB) was taken as a reference test. The precise description of the casting head setup is described in details by the authors earlier [11], [15].

Double-blade tape casting (DB) is used in laboratories as a solution for avoiding a continuous slurry level decrease in the casting head. According to the work of Zhang’s et al. [16] on precise thickness control in tape casting, the rear gap was chosen to be at 1.2 mm height, and the front casting gap was fixed at 1 mm height. The partition had a more complicated shape, since it had to separate the tank both in the slurry loading reservoir, beneath the backside blade, and in a narrow supplemental reservoir between two blades. Besides, all joints between partition and caster walls, partition and blades had to be isolated with Duct tape in order to prevent leaking of slurries from adjacent sub-reservoirs. This introduced some non-controlled inaccuracies into the DB setup.

With the requirement to tape cast continuously for a long time with a steady slurry stream, industry normally employs a pump system in tape casting (PS). This method benefits in keeping the slurry under pressure and continuously agitated ensuring homogeneity of the slurry; besides, the slurry column in the reservoir in this case is constant during the whole process providing a uniform wet tape thickness. The single-blade system was used for this experiment.

The speed change (SC) mode for tape casting was developed based on our previous study [10]. The idea was to balance two of the following trends: continuous thickness decrease with processing time (as the hydraulic pressure behind the casting blade decreases), reduction of casting gap or increasing the carrier velocity, and the trend of thickness increase with enlargement of casting gap or slowing down the carrier movement. A change of casting gap during the casting process is not favourable as it demands the simultaneous screwing of two gap determining gauges on blade with micron-scale accuracy and, besides, needs the tape casting chamber to be open which can drastically affect the drying kinetics. Thus, it was chosen to compensate the decrease of tape thickness, associated with a pressure drop behind the casting blade, with tape thickening due to a decrease of carrier velocity. Taking into account mass conservation, the profile with which tape thickness reduces as the slurry filling in reservoir decreases was numerically calculated [10]. After testing the modelled program on LSM and LSM_CGO slurries in tape casting experiment, the program was corrected and exported to the process control machine (Figure 2).

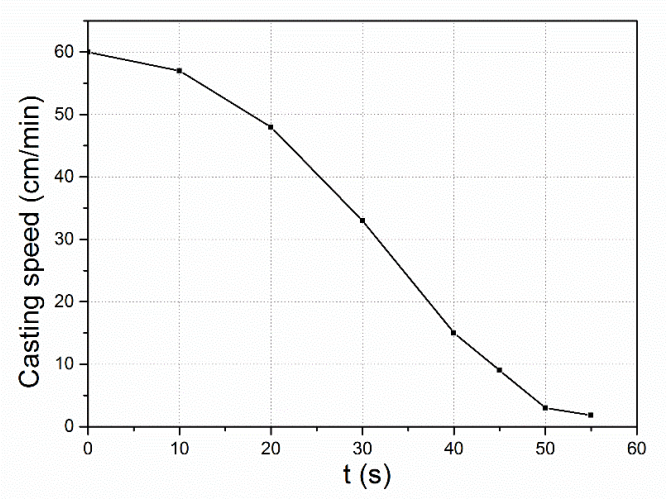

Figure 2. Casting program exported to the tape caster machine for steadying the dried tape thickness by continuous change of the casting speed.

3.2.Tape casting with varied length of the partition tongue.

All tests were carried out using the same LSM and LSM_CGO slurries with the same formulation and pre-casting rheological parameters as ones in the tape thickness control tests. The single blade tape casting unit has been applied. Experiments were conducted with different length of partition tongue at various casting speeds. Here, the partition tongue is the length of the Teflon partition beneath the casting blade, with a height identical to the casting gap of 1 mm, the width is equal to width of the whole partition, 1.95 mm; the maximum length of used partition matches the width of the casting blade of 6.5 mm and is referred to here as the whole (fraction of one) of the partition. The experiment sets were set as follows. First three experiments included co-casting of LSM and LSM_CGO slurries with the whole partition length and 10 cm/min, 15 cm/min and 30 cm/min casting speeds, consequently. Afterwards, the partition tongue was shortened by a quarter, the front edge was sharpened, and co-casting continued with a 0.75 fraction of partition with 20 cm/min and 30 cm/min alternately, *etc*. The shearing surface of blade was cleaned after each time and the sub-reservoirs were emptied in order to create reproducible conditions for each test.

4. Green tapes characterisation

The green tape thicknesses were measured both on LSM and LSM_CGO sides of the tape, about 2 cm from either edge of the tapes in order to neglect possible edge defects. Measurements were performed using a flat dual point digital micrometer of 15 mm in diameter at every 10 cm along the tape length. Precise collection of thickness data was necessary in order to track the general tendency of tape thickness regularities along the length.

Results and discussion

1. Tape casting in thickness control experiments

Figure 3 illustrates the thickness variation along the lengths of the LSM and LSM_CGO parts of the green tapes, produced by SB, DB and PS tape casting methods with 30 cm/min casting speed and by the SC casting mode. Similar tendencies in tape thickness consistency were detected for LSM and LSM_CGO slurries for all four tape casting modes.

Tapes are also shown to have a slightly different length because of a minor uncertainty in the initial slurry load in the reservoir. Since there was not an automatic control of slurry filling in the reservoir and slurry load was controlled manually, the difference in the resulting length of tapes was predictable and permissible. In order to ensure that thicknesses of tapes are compared when there was the same slurry level in tape caster, the curves correlated to tape thickness were aligned to the zero position, *i.e.* when the reservoir was empty in all casting modes.

Thickness irregularity at the start is pronounced when using the single blade for the tape casting (Figure 3) as the hydraulic pressure of the slurry column, accumulated behind the only casting blade, is ejected to the free space rapidly presumably resulting in a swelling effect. Swelling encounters when hydrostatic pressure pushes a large volume of slurry under the doctor blade so that the slurry exceeds the gap level. Swelling is normally determined by the height of the casting gap, polymer content in the slurry, slurry viscosity and casting speed. In other methods, the sharp release of a large amount of slurry onto the casting substrate was diminished due to either less slurry behind the casting blade like in the DB system or due to better control of hydrostatic pressure like in the cases of using SC and PS approaches.

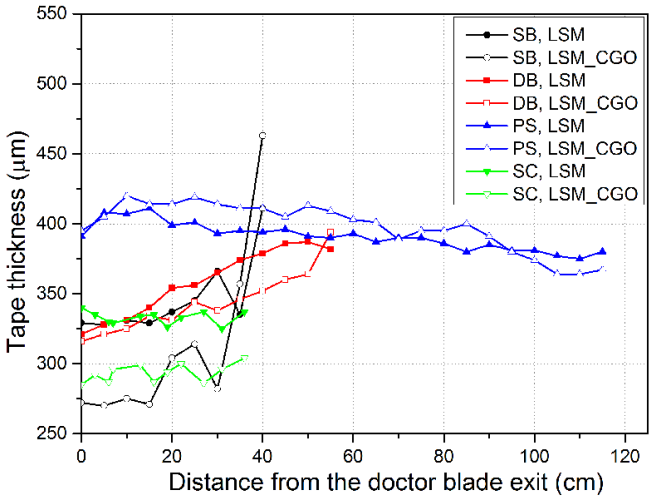

Figure 3. Thickness deviation of tapes, cast with usage of single-blade (SB), double-blade (DB), single blade and pump system (PS), single-blade and a program of casting speed change (SC). The estimated error in tape thickness measurement is 15 μm.

As for most other fluid forming techniques, the fluid flow for tape casting is determined by a complex combination of influencing factors, among which are the surface tension between slip and the moving carrier and, consequently, a side flow; air flow in the drying chamber affecting the drying kinetics; viscous friction of slurry and tape caster elements, shear thinning behaviour, etc. But the prevalent factor influencing the overall thickness variation in tape casting is the combination of the steady flow caused by the continuously moving carrier and irregular flow caused by the unfavourable decaying hydraulic pressure. A formula, which describes the influence of both shear- and pressure-driven forces on the thickness of a dried tape, was developed by Tok *et al.* [17] and considers the flow behaviour of non-Newtonian fluid using Ostwald-de Waele power law model (Eq. 1) (Table 1):

$$\delta_{tr} = \alpha\beta\frac{\rho_s}{\rho_{tr}}\left[\frac{1}{2}h_0 + \frac{2(h_0/2)^{\frac{1}{n}+2}(\Delta P)^{1/n}}{L(\frac{1}{n}+2)k^{1/n}U}\right] \qquad (2)$$

where δ_{tr} is a dried tape thickness, α the correction factor for side flow, β the correction factor for weight loss during drying, ρ_s the slurry density, ρ_{tr} the density of the formed tape, h_0 the casting gap, ΔP the hydraulic pressure exerted by the slurry column in a casting tank, L the length of the doctor blade in the casting direction, U the casting speed; k and n, as was described above, are slurry constants for the fluid consistency and the deviation from the Newtonian flow.

The simplest condition providing a uniform thickness across the entire tape length is when the actual slurry flow rate is equal to the carrier flow rate, *i.e.* the flow, determined just by the first term in Eq. 2, or when the actual slurry flow is constant for the whole duration of the casting process, *i.e.* when the flow rate, determined by the sum of both terms in Eq. 2 is constant during the whole casting process. The second concept is realized in the industrial tape casting by continuously pumping slurry into the tank maintaining a constant level of slurry in the tape caster reservoir, e.g. maintaining ΔP constant. The slight thickness changes of 7 and 9 % for LSM and LSM_CGO sides, respectively, were a result of adjusting casting and pumping speeds in the PS mode. Depending on the chosen slurry level which is analogue to the hydraulic pressure, the wet thickness might be even higher than the casting gap. In that case the slurry experiences the so-called swelling phenomena. An indirect method of measuring the swelling is comparing the thickness of tape obtained by a PS method and the stable part of a tape obtained by the SB method. For instance, for LSM slurry, cast with 30 cm/min speed and maintaining a slurry level in the reservoir of 22 mm, the swelling extent is found to be 70-80 µm (Figure 3). The direct method of measuring the swelling level is to measure the slurry trace on the side of the blade facing the drying area. The LSM slurry rise was 140-150 µm, which is higher than the values obtained from the analysis of the thickness curves in Figure 3.

An alternative method directed at minimizing the influence of the hydraulic pressure effect and maintaining the same level behind the casting blade is the DB approach. Tape thickness formed by DB tape casting was on average 10% smoother compared to the SB method. Nevertheless, the 20 % thickness gradient across the whole tape length was presumably because the gap under the rear blade was too high to keep the hydraulic pressure in the relief reservoir constant. As it is not the target of the current work, the choices of casting gaps were based on the study of Zhang *et al.* [16] and fixed at 1200 µm for the rear blade and 1000 µm for the front blade. Despite careful adjustment, the resulting tape thickness had a smoothly decaying character toward the end of the tape both in the LSM and LSM_CGO parts. At the end of the process, as expected, the tape thickness cast by DB mode was equal to the thicknesses of tapes, cast with the SB and SC methods. Further optimisation on the adjustment of the gaps in the double blade set-up was discontinued due to the presence of a vortex flow in the relief reservoir, proven both experimentally [18] and numerically [19]. The vortex flow affecting the rheological behaviour of the slurry makes a shearing flow during casting uncontrollable. Together with a complicated design of partition required to separate both reservoirs and both gaps under the blades, the DB approach was shown to be not applicable for the control of the multiple material flow applied in the current SBS TC work.

In the newly implemented technique SC, tape thickness was prescribed by a change in the casting speed U due to the decrease of the slurry pressure head ΔP. As a result, thickness irregularities stayed within 5%, identifying the SC approach as a well-controlled tool. The thickness values achieved on both the LSM and LSM_CGO sides of the graded tape are in good correspondence to the thickness values of the tape, produced by SB tape casting, exactly as the speed change program was settled and optimized. Despite the fact that the SC approach forms the smoothest dried tapes, this method should be applied with care, as the continuous

change of casting speed can lead to a change of microstructure and, consequently, porosity if the elongated particles and/or pore formers are in use. Moreover, the chosen pseudoplastic slurries have to have a plateau in the viscosity curves at the applied casting shear rates. Otherwise, slurry is not stable during the tape casting, which usually leads to morphological irregularities in green and sintered tapes.

Based on the conducted study, the novel casting speed change mode and tape casting using a pump system was shown to form smooth tape surfaces. The use of pump system in tape casting, however, is highly recommended if a large slurry volume is to be cast so that the high losses caused by the time, required to adjust casting and pumping speed during slurry supply, are reasonable. The use of the SC program was also eliminated for further SBS TC test, as the shear rate profile, determining the quality of the interface [11], was proven to be dependent on the casting speed [20]. For the same reasons of high possibility of unstable flow [19] during co-casting, the work with a DB set-up was discontinued. Considering the detailed study of the multiple materials co-flow in a lab-scale tape casting, the SB approach was decided to be applied for further SBS TC tests.

2. Tape casting with varied length of the partition tongue

The partition width of about 2 mm was chosen as it was complicated to set a thinner partition precisely in the middle of the tank. Besides, it is also challenging to fasten a thinner partition tight to the tank walls, causing leaking of slurries in between adjacent reservoirs at the seams. The use of thick partitions would hinder the merging of co-flowing slurries and would limit the use of highly viscous slurries with confined side flow.

During the primary experiments on SBS TC it was found that a tapered front edge of the partition was required since a blunt flat partition was shown to leave traces on the dried green tape and lead to undesired inhomogeneity at the interface area (Figure 4). These traces on the tape surface were a consequence of the significant distance, which was created by the blunt partition and which co-casting viscous slurries had to overflow just by flowing aside. Typical for highly viscous slurries limited side flow and rapid evaporation of organic solvent happening right after the doctor blade region hindered merging of two adjacent slurries and impeded a complete healing of the co-flowing gap. The two solutions were found to overcome this challenge. The first solution included the use of less viscous slurries, which was shown to affect the shape of the interface and final thickness [11]. Another solution was sharpening the partition at the front edge in order to create a smooth merging for co-casting slurries and thinning the confluence area (Figure 4). The use of the sharpened partition opened a chance to co-cast slurries with a wide variety of viscosity values including highly viscous ones.

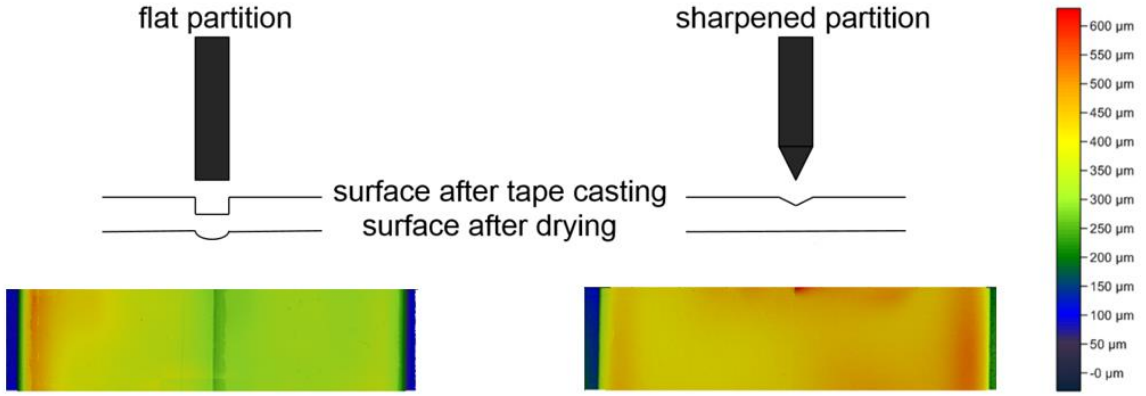

Figure 4. Schematic representation of surfaces of green graded tapes after co-casting using a non- sharpened and sharpened partition and below the pictures of surface topography of green tape samples, which were analysed by means of laser profilometry. The short slit on the sample, cast with the tapered partition, was made by knife in order to later identify the interface region on a completely smooth graded tape. The length of each piece of tape was 20 mm, and the width was 80 mm.

To examine the effects of partition design and casting speed on slurry flow behaviour, a number of experiments were carried out. Each dot in Figure 5a corresponds to a SBS TC experiment, carried out at casting speeds in a range from 10 cm/min to 50 cm/min, and various lengths of the partition tongue (Figure 5b). The dots marked in grey colour (Figure 5a) represent experiments, where the co-cast slurries did not merge and a gap in interface area was formed (inlet in Figure 5a). The ability of adjacently cast slurries to merge in the confluence area and form an interface was shown in general to grow as the casting speed was reduced and the partition tongue shortened.

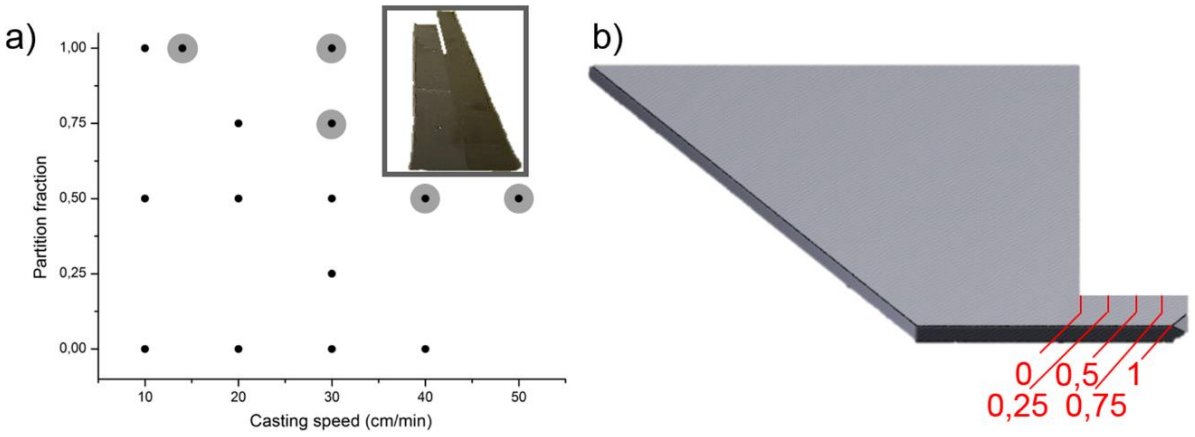

Figure 5. a) Experiments identifying the effect of the partition design and casting velocity; grey dots denote co-casting experiments where the splitting between co-cast materials was observed (an example is shown in the inset); b) Side view of a Teflon partition wall; red lines show the way of cutting the partition length.. The numbers indicate the fraction of partition tongue which was used in the experiment.

The ability of adjacently cast slurries to merge in the confluence area and form an interface was shown to grow as the casting speed was reduced and the partition tongue was shortened (Figure 5a). To indicate the influence of flow behaviour on the formation of the graded tape, the tape casting process was reproduced on a rheometer according to shear rates applied to slurries during each step of the real casting process. Basically, tape casting is a shearing processes (Figure 6): first, we pour slurries into a reservoir applying a certain shear rate about 5 s^{-1}, later we keep slurries in the reservoir for 10-15 s in order to remove any effects of the rheological history of the slurries. Afterwards, the casting process starts where shear rates can be approximately evaluated as the casting speed divided by the size of the gap under the blade; and the last step is drying, which we here assume as a step where no shear stresses are applied, ignoring the shrinkage stress and possible edge effects . However, in order to be able to measure the viscosity, a minor shear rate of 0.1 s^{-1} was applied on that last step of the rheological program. During this multistep program the, viscosity of LSM and LSM_CGO slurries were measured as a response to the applied shear rates. For SBS TC of an adjacently graded tape with a steep interface it is required [11] for the LSM and LSM_CGO viscosity curves to have a similar rheological response at each of described steps.

Figure 6a illustrates changes in LSM and LSM_CGO rheological behaviour during the test imitating tape casting at 10 cm/min casting speed. Tracking the flow field in the tape caster unit, three clear regions of characteristic viscosity changes are identified: (i) after pouring slurries into the tape caster reservoir and allowing the slurry to rest, the molecules of binder in the highly viscous slurries start to form a polymeric matrix increasing the viscosity of the slurries; (ii) under an applied shear rate polymeric chains elongate causing the uniform viscous flow of slurries under the casting blade; (iii) when slurries flow in a free space, reciprocal action of the polymeric matrix formation and the drying process increases the viscosities of the slurries. Hence, the changes in the system are caused by both shear thinning behaviour of casting slurries and the drying process.

The thixotropic behaviour, characteristic for both LSM and LSM_CGO_4 slurries, requires approximately 7 s to 10 s to completely recover the initial structure and retrieve initial viscosity. During that time the slurry is assumed to be a fluidly deformable. The fluidly deformable state is a state of cast tapes at the initial stage of the drying process when the dried film is still not formed at the tape surface and its edges are capable of shifting under the weight of the tape.

Low viscosity, typical for slurries passing the blade region, allows the slurry to flow aside under the influence of gravity, surface tension forces and levelling without revealing stresses in surfaces. Thus, complete absence or a short partition tongue below the blade favours the merging of the co-flowing slurries and formation of a uniform interface. When the partition tongue divides the co-flowing slurries all the way under the blade, the slurries are free to flow aside just after passing the blade region. Casting with a speed of 10 cm/min, the fluidly deformable state of slurries lasts for at least 7 s to 10 s. That time was proven (Figure 6a) to be enough for slurries to merge and form an interface.

However, when the slurries are cast faster, the duration when slurries are fluidly deformable drastically shortens (Figure 6b). Thus, the faster the casting speed, the lower is the possibility for co-casting slurries to merge when the whole partition tongue is used (horizontal tendency in Figure 5a). For instance, in the current work the small change in casting speed from 10 cm/min to 14 cm/min results in splitting between co-cast materials (Figure 5a).

Another noteworthy result is the shortening of the shearing time with an increase of the casting speed. For example, when the partition tongue divides the casting gap at a fraction of 0.75 of the blade width, the time, during which slurry has a low viscosity at the casting speed of 10 cm/min is 6 s (Figure 6a) and less than 3 s for a casting speed of 30 cm/min (Figure 6b). Thus, the time for adjacent flowing slurries to merge in the partition free area beneath the blade is 1.5 s and less than 0.75 s for 10 cm/min and 30 cm/min casting speeds, respectively. The results show (Figure 5a) that 1.5 s in a low viscosity state is enough for adjacent slurries to join in the confluence area of 1.95 mm (the width of the partition), while 0.75 s is too short time for slurries to flow aside and form the interface.

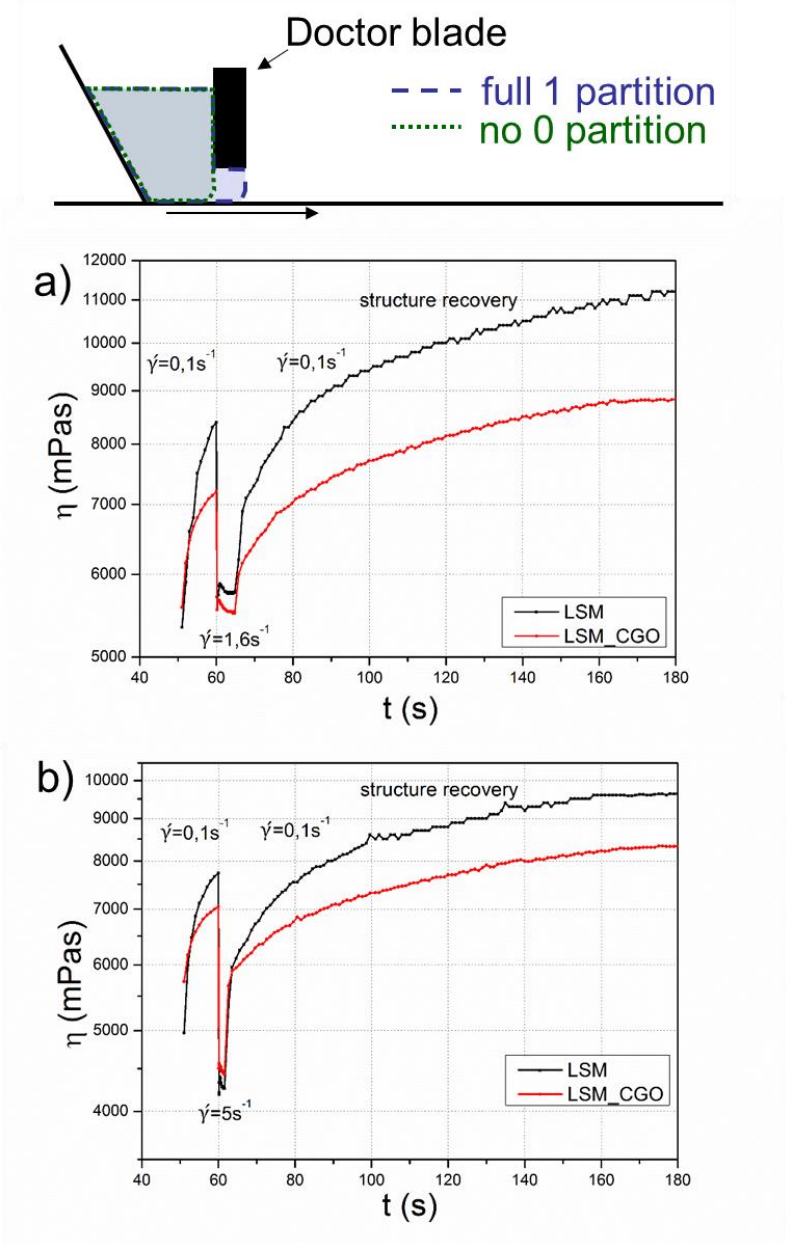

Figure 6. Structure recover test for LSM and LSM_CGO slurries co-cast at a) 10 cm/min and b) 30 cm/min casting speed.

Normally, gravity is ignored in tape thickness studies as it is assumed that its effect is negligible for tape dimensional consistency, but in SBS TC an accurate determination and tuning of all parameters, which influence the forming of the confluence interface area, is of

great importance. The study of the impact of gravity was built on the well-known fact that the tape thickness decreases when the casting speed is increased [11]. Thus, the tape thickness of the same slurry was shown to be halved when the casting velocity was increased from 10 cm/min to 40 cm/min [11]. In order to estimate the role of gravity forces on the side flow effect (the correction factor for side flow α in Eq.2), three 80 mm wide tapes were cast manually on a laser profilometer substrate covered with a Mylar film. The speed was about 80 cm/min and casting gaps of 1000 µm, 500 µm, and 90 µm were chosen. LSM slurry was used for all three experiments. The laser profilometer was used in order to measure the tape thickness gradient in-situ. Results showed (Figure 7) that the side flow of tapes cast with a 1000 µm gap, which was supposed to represent tape casting with slow casting speeds, exceeded 10 mm (α=0.89), while for the tape cast with 500 µm (α=0.96) and 90 µm (α=1) gaps, which were supposed to refer to faster casting, these numbers were 3.5 and 0 mm, consequently. In the experiment with a casting speed change, proportional change in tape thicknesses would lead to the proportional changes in side flow. When the partition creates a 1.95 mm wide confluence area to be filled by co-cast slurries from both sides, the side flow plays a crucial role. However the side flow is of practical value as long as slurries are able to flow, i.e. being at low viscous state.

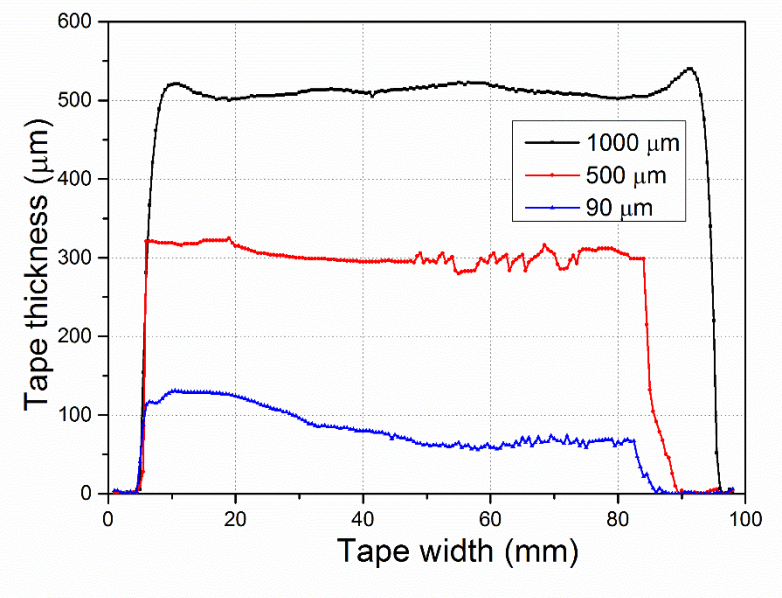

Figure 7. Cross-section profile of the LSM slurries made on a laser profilometer showing the side flow effect.

Conclusion

Tape casting with a single blade, double blade, with use of a pump system and tape casting with a continuous speed change have been compared in order to cast tapes with a uniform tape thickness. The proposed method of consistent casting speed change showed the minimum of tape thickness gradient of 5% along the casting length. However, this method requires the use of stable slurries with particles as close as possible to a spherical morphology (with no elongations). The use of a pump system in order to maintain the same slurry level in the casting reservoir exhibited about 10% of thickness gradient. A better representation of this test would presumably be possible if a larger amount of slurry was cast because of the required adjustment of casting and pumping speeds. The use of double blade to support the

same level behind the casting reservoir also showed an unexpected thickness fluctuation. Better results might be achieved if the casting gaps below both blades were adjusted. This work has been discontinued because of the presence of the vortex when high viscous slurries are applied [19]. Single blade was chosen for SBS TC process in the small lab-scale as it shows relatively small thickness gradient of below 10% after the cast first 10 mm. Moreover, the use of the single blade guarantees a stable flow with well-studied pressure and shear impacts on the tape formation.

The influence of partition geometry on the quality of the graded tape was also presented. It was shown that the chance to obtain a uniform adjacently graded tape decreases with an increase of the length of the partition tongue beneath the casting blade and with an increase in casting speed. Moreover, unlike the regular practice in shaping techniques, where rheological study of processing slurries and their numerical description are limited by providing viscosity and flow curves, a new approach of describing and measuring slurries fluid behaviour was proposed. The distinctive difference between the proposed approach and a routine rheological examination of pre-casting slurry is consideration of rheological test as the representation of dynamic sequence of tape casting process. Nevertheless, the application of a standard rheological program with pre-shear and increasing shear rate is required in order to analyse and be able to compare shear thinning behaviour of casting slurries.

References

[1] G. N. Howatt, "Method of producing high dielectric high insulation ceramic plates," US2582993 A, 22-Jan-1952.

[2] H. Loest, R. Lipp, and E. Mitsoulis, "Numerical flow simulation of viscoplastic slurries and design criteria for a tape casting unit," *J. Am. Ceram. Soc.*, vol. 77, no. 1, pp. 254 – 262, 1994.

[3] A. R. Dinesen, S. Linderoth, N. Pryds, and A. Smith, "A magnetic regenerator, a method of making a magnetic regenerator, a method of making an active magnetic refrigerator and an active magnetic refrigerator," PCT/EP2005/013654, 20-Jul-2006.

[4] "Method for manufacture of transparent ceramics." 21-Sep-2010.

[5] E. R. Kupp, G. L. Messing, J. M. Anderson, V. Gopalan, J. Q. Dumm, C. Kraisinger, N. Ter-Gabrielyan, L. D. Merkle, M. Dubinskii, V. K. Simonaitis-Castillo, and G. J. Quarles, "Co-casting and optical characteristics of transparent segmented composite Er:YAG laser ceramics," *J. Mater. Res.*, vol. 25, no. 03, pp. 476–483, Jan. 2011.

[6] H. Yang, P. Zhang, Q. Wu, H. Ge, and M. Pan, "Effect of monovalent metal substitution on the magnetocaloric effect of perovskite manganites $Pr_{0.5}Sr_{0.3}M_{0.2}MnO_3$ (M=Na, Li, K and Ag)," *J. Magn. Magn. Mater.*, vol. 324, no. 22, pp. 3727–3730, Nov. 2012.

[7] M. Wu and G. L. Messing, "Fabrication of Oriented SiC-Whisker-Reinforced Mullite Matrix Composites by Tape Casting," *J. Am. Ceram. Soc.*, vol. 77, no. 10, pp. 2586–2592, Oct. 1994.

[8] D.-S. Park and C.-W. Kim, “A modification of tape casting for aligning the whiskers,” *J. Mater. Sci.*, vol. 34, no. 23, pp. 5827–5832, Dec. 1999.

[9] R. E. Mistler and E. R. Twiname, *Tape Casting: Theory and Practice*. Wiley-American Ceramic Society, 2000, p. 298.

[10] M. Jabbari, R. Bulatova, J. H. Hattel, and C. R. H. Bahl, “Quasi-steady state power law model for flow of $(La_{0.85}Sr_{0.15})_{0.9}MnO_3$ ceramic slurry in tape casting,” *Mater. Sci. Technol.*, vol. 29, no. 9, pp. 1080–1087, Sep. 2013.

[11] R. Bulatova, M. Jabbari, A. Kaiser, M. Della Negra, K. B. Andersen, J. Gurauskis, and C. R. H. Bahl, “Thickness control and interface quality as functions of slurry formulation and casting speed in side-by-side tape casting,” *J. Eur. Ceram. Soc.*, Jul. 2014.

[12] *Solid Oxide Fuel Cells VIII: (SOFC VIII) : Proceedings of the International Symposium, Volume 8*. The Electrochemical Society, 2003, p. 1520.

[13] *Inorganic Membranes: Synthesis, Characterization and Applications: Synthesis, Characterization and Applications (Google eBook)*. Elsevier, 2008, p. 480.

[14] H. Raeder, C. Simon, T. Chartier, and H. L. Toftegaard, “Tape casting of zirconia for ion conducting membranes: A study of dispersants,” *J. Eur. Ceram. Soc.*, vol. 13, no. 6, pp. 485–491, Jan. 1994.

[15] R. Bulatova, C. Bahl, K. Andersen, L. T. Kuhn, and N. Pryds, “Functionally Graded Ceramics Fabricated with Side-by-Side Tape Casting for Use in Magnetic Refrigeration,” *Int. J. Appl. Ceram. Technol.*, p. n/a–n/a, Aug. 2014.

[16] G. Zhang, Y. Wang, and J. Ma, “Bingham plastic fluid flow model for ceramic tape casting,” *Mater. Sci. Eng. A*, vol. 337, no. 1–2, pp. 274–280, Nov. 2002.

[17] A. I. Y. Tok, F. Y. C. Boey, and Y. C. Lam, “Non-Newtonian fluid flow model for ceramic tape casting,” *Mater. Sci. Eng. A*, vol. 280, no. 2, pp. 282–288, Mar. 2000.

[18] M. Schmidt, H. Münstedt, M. Svec, A. Roosen, T. Betz, and F. Koppe, “Local Flow Behavior of Ceramic Slurries in Tape Casting, as Investigated by Laser-Doppler Velocimetry,” *J. Am. Ceram. Soc.*, vol. 85, no. 2, pp. 314–320, Dec. 2004.

[19] A. Wonisch, P. Polfer, T. Kraft, A. Dellert, A. Heunisch, and A. Roosen, “A Comprehensive Simulation Scheme for Tape Casting: From Flow Behavior to Anisotropy Development,” *J. Am. Ceram. Soc.*, vol. 94, no. 7, pp. 2053–2060, Jul. 2011.

[20] M. Svec, M. Schmidt, T. Betz, A. Roosen, F. Koppe, and H. Münstedt, “The influence of different blade geometries on the local flow behavior of ceramic slurries in the tape casting unit,” *Ceram. Forum Int.*, vol. 79, no. 5, pp. E39–E43, 2002.

PAPER IV

C. R. H. Bahl, D. Velázquez, K. K. Nielsen, K. Engelbrecht, K. B. Andersen, R. Bulatova, and N. Pryds, High performance magnetocaloric perovskites for magnetic refrigeration, *Appl. Phys. Lett*., vol. 100 (12), p. 121905, 2012.

High performance magnetocaloric perovskites for magnetic refrigeration

Christian R. H. Bahl,[1,a)] David Velázquez,[2] Kaspar K. Nielsen,[1] Kurt Engelbrecht,[1] Kjeld B. Andersen,[1] Regina Bulatova,[1] and Nini Pryds[1]
[1]*Department of Energy Conversion and Storage, Technical University of Denmark, DK-4000 Roskilde, Denmark*
[2]*Instituto de Ciencia de Materiales de Aragón (ICMA) CSIC, Universidad de Zaragoza, Plaza San Francisco, 50009 Zaragoza, Spain*

(Received 10 February 2012; accepted 21 February 2012; published online 20 March 2012)

We have applied mixed valance manganite perovskites as magnetocaloric materials in a magnetic refrigeration device. Relying on exact control of the composition and a technique to process the materials into single adjoined pieces, we have observed temperature spans above 9 K with two materials. Reasonable correspondence is found between experiments and a 2D numerical model, using the measured magnetocaloric properties of the two materials as input. © *2012 American Institute of Physics*. [http://dx.doi.org/10.1063/1.3695338]

Mixed valence manganites have recently found use in applications due to the rich physics present in these. The applications range from colossal magneto-resistance[1] to spintronics[2] and thus these ceramic perovskite materials have been extensively studied.[3] The magnetocaloric effect, which manifests itself as a temperature change of the material upon a change of the applied magnetic field, is maximised close to the magnetic phase transition. Numerous studies of the magnetocaloric properties of perovskite ceramics have been conducted, finding a strong dependence of both the magnetic transition temperature and the size of the magnetocaloric effect on stoichiometry and the level and type of various dopants.[4,5] Among the most promising of these ceramics, in view of application and device performance in the range of room temperature, are materials in the series $La_{2/3}(Ca,Sr)_{1/3}MnO_3$ (LCSM). While the adiabatic temperature change, ΔT_{ad}, is in general found to be relatively low compared to conventional metallic and intermetallic magnetocaloric materials, such as Gd, $La(Fe,Co,Si)_{13}$, or $Gd_5Si_2Ge_2$, the high specific heat gives these materials an isothermal entropy change, Δs, which is close to that of Gd.[6] We will show here how the ability of accurately tuning the Curie temperature by doping, coupled with the advantageous abilities of these materials to be shaped into fine structures, leads to high performance in magnetic refrigeration devices. This makes them promising materials for this technology, opening up yet another application for this class of materials. The high performance found in the experimental results is corroborated by numerical modelling results.

In the active magnetic regenerator (AMR) cycle, a porous magnetocaloric regenerator is alternatingly magnetised and demagnetised, e.g., by moving in and out of the magnet field source. After each movement, a heat transfer fluid is pushed through the void space in the regenerator in alternating directions. Upon performing this AMR cycle, a temperature gradient will build up across the regenerator, as heat is moved from the "cold end" to the "hot end". The use of layered regenerators consisting of materials with different magnetic transition temperatures has been proposed and experimentally tested in a few devices.[7–9] The regenerators are constructed so that each material along the temperature gradient is operating close to its optimal temperature, i.e., Curie temperature. Such a design relies heavily on the ability to tune the Curie temperature as well as the ability of constructing a multiple material regenerator in a practical way. We show how the materials series $La_{2/3}(Ca,Sr)_{1/3}MnO_3$ and the processing route of tape casting are well suited to achieve this.

Powders of the two materials $La_{0.67}Ca_{0.2925}Sr_{0.0375}Mn_{1.05}O_3$ and $La_{0.67}Ca_{0.2850}Sr_{0.0450}Mn_{1.05}O_3$, referred to in the following as LCSM-1 and LCSM-2, respectively, were prepared by spray pyrolysis. Each of these powders was calcined at 1273 K for 2 h and suspended in a slurry with an azeotropic mixture of methylethylketone and ethanol, polyvinyl pyrolidone and polyvinyl butyral. Using a so-called doctor blade to control the thickness, the slurries are applied from a vessel onto a moving substrate. This technique is known as tape casting and is a conventional processing route to produce thin and flat ceramic plates.[10] The recently developed technique of adjacently tape casting multiple slurries into a single tape[11] was employed to prepare tapes with adjacent stripes of LCSM-1 and LCSM-2. The resulting tapes were sintered at 1473 K for 4 h to densities of 96% and 95% of the atomic, for LCSM-1 and LSCM-2, respectively. Platelets containing equal amounts of the two materials were laser cut to the size 40 mm × 25 mm, with the boundary between the materials in the middle of the 40 mm side. A stack of 28 such platelets with a total mass of 51.1 g was assembled according to the method described in Ref. 12, using a laser profilometer to quantify the quality of the stacking. An average platelet thickness of 0.30 ± 0.04 mm and channel thicknesses of 0.39 ± 0.10 mm were measured attesting to the good quality of the stacking.

The magnetocaloric properties ΔT_{ad}, Δs, and specific heat, c_H, were measured as a function of temperature and applied magnetic field on pieces of the sintered platelets of each of the two materials using the equipment discussed in Ref. 13. The data for the peak values and temperatures, in good correspondence with literature values,[14] are given in Table I.

a)Author to whom correspondence should be addressed. Electronic mail: chrb@dtu.dk.

TABLE I. Measured magnetocaloric properties of the two materials. ΔT_{ad} and Δs are reported upon magnetisation in an applied field of $\mu_0 H = 1$ T while c_H is at zero applied field.

Properties	Peak temperature	Peak value
LCSM-1		
ΔT_{ad}	277 K	1.30 K
Δs	275 K	3.7 J kg^{-1} K^{-1}
c_H ($H = 0$)	273 K	780 J kg^{-1} K^{-1}
LCSM-2		
ΔT_{ad}	282 K	1.17 K
Δs	282 K	3.5 J kg^{-1} K^{-1}
c_H ($H = 0$)	278 K	750 J kg^{-1} K^{-1}

The 28 plate stack was mounted as an active magnetic regenerator in a magnetic refrigeration test device at the Technical University of Denmark with a 1.1 T Halbach type permanent magnet assembly and a heat transfer fluid of water containing 20% commercial ethylene glycol being moved through the channels between the plates by way of a piston. The LCSM-2 parts of the plates are oriented toward the hot end, while the LCSM-1 parts of the plates are oriented toward the cold end. A heat exchanger in the hot reservoir of the device allows the hot end temperature to be controlled. Further details of this device and the operation of it can be found in Refs. 15 and 16 and a sketch of the device is given in Figure 1.

The utilization, ϕ, of the AMR is conventionally defined as the ratio between the thermal mass of fluid pushed through the regenerator and the thermal mass of the regenerator

$$\phi = \frac{m_f c_f}{M_s c_{H,s}}, \tag{1}$$

where m_f is the mass of the fluid pushed through in one direction, c_f is the specific heat of the fluid, M_s is the mass of the solid regenerator, and $c_{H,s}$ is the specific heat of the regenerator. As the regenerator consists of equal amounts of two materials, each with a temperature dependent specific heat, the value chosen for $c_{H,s}$ is the average of the peak values of the two materials, i.e., 765 J kg^{-1} K^{-1}. Experiments were performed with the LCSM regenerator varying the mass flow rate, the utilization, and the hot end temperature. During operation, a steady state temperature span is reached between the set hot end temperature and the cold end temperature. Figure 2(a) shows the temperature spans achieved as a function of hot end temperature and utilization, keeping the fluid flow rate at a constant value of 1.32 gs^{-1}. The highest temperature span of 9.3 K was reached at a hot end temperature of 283.8 K and a utilization of 0.4, which results in a cycle time of 8.9 s. This is an exceptionally high span, more than 7.5 times the average maximum ΔT_{ad} of the two materials. For comparison, the highest temperature span obtained in this device with of the benchmark magnetocaloric material Gd was 10.2 K,[16] albeit with somewhat thicker flat plates of 0.9 mm. It is also seen that the temperature span decreases either side of the optimum utilization of 0.4, in good correspondence with previously obtained results.[16] Doubling the mass flow rate while maintaining ϕ results in a lowering of the maximum temperature span to a value of 8.1 K, again at an optimum utilization of 0.4 and a optimum hot end temperature of 283.9 K. This is due to a reduction in the number of transfer units (NTU) with an increase of the mass flow rate, leading to a reduced temperature span.[17]

A numerical 2D model of the AMR cycle has recently been developed.[18] Using only the measured properties of the LCSM plates and physical properties of the heat transfer fluid, the no-load temperature span has been modelled as shown in Fig. 2(b). Comparing the curves in Fig. 2, it is evident that the trend and peak temperatures are the same, albeit with the predicted temperature span being a little higher and

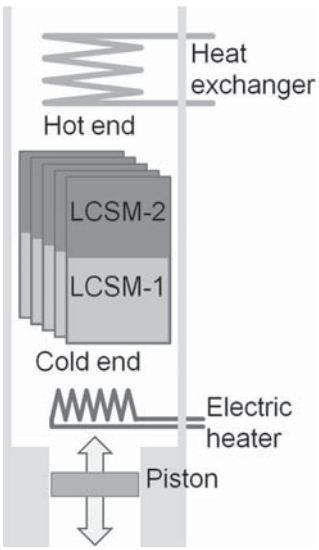

FIG. 1. Sketch of the experimental setup showing the different components.

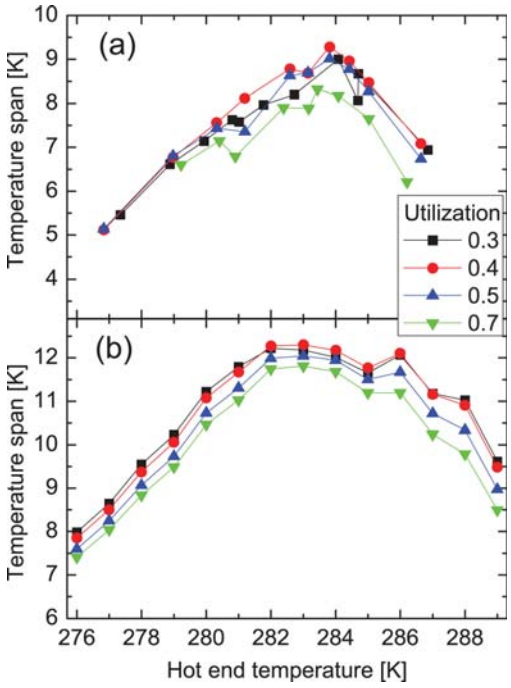

FIG. 2. (Color online) Temperature spans obtained at a mass flow rate of 1.32 gs^{-1}. (a) gives experimental results and (b) gives the predictions of the numerical model. The lines are guides to the eye.

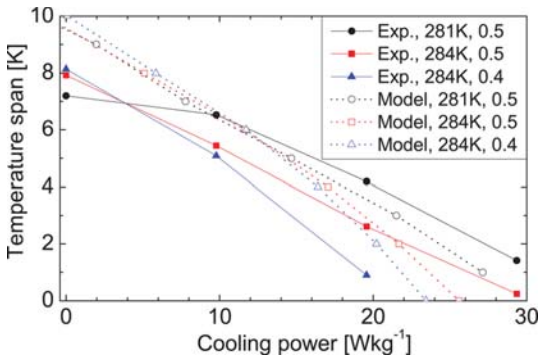

FIG. 3. (Color online) Cooling curves obtained at a mass flow rate of 2.63 gs^{-1} for both experiments and model predictions. Each curve is indexed by the hot end temperature and the utilization. The lines are guides to the eye.

the peak broader than the measured. Such a reduction in the experiment may be caused by a number of factors not accounted for in the model including thermal losses to the ambient, the effect of magnetostatic demagnetisation, and the variation of the plate spacing in the stack. Each of these factors has previously been shown to reduce the regenerator performance. Taking this into account, the correspondence seems reasonable.

Directly below the cold end of the regenerator, there is a small electrical heater. Applying power to this simulates the presence of a cooling load in the refrigeration device allowing the cooling curve to be mapped out. The cooling curves have been recorded for different utilizations and hot end temperatures keeping the mass flow rate at a constant value. Depending on the device performance, there will be a variation in the heat transfer between the heat exchanger and the hot end of the device. This results in a slight variation ($\sim$0.2 K) in the actual hot end temperature at a fixed set-point temperature, so for comparison rounded values of the hot end temperature are reported.

The best performance is observed at a mass flow rate of 2.63 gs^{-1} and Figure 3 shows the results, with the cooling power normalised to the mass of the regenerator for convenience. At zero load, the highest span is, as discussed above, at a utilization of 0.4 and a hot end of 284 K. As expected, the span is reduced as the load increases. This decrease is close to linear for single material regenerators[8,17] and for two material regenerators with a close spacing of Curie temperatures.[9] An increase in the maximum cooling power is observed when the utilization is increased to 0.5, due to the increased thermal capacity of the fluid being pushed through the regenerator. Also, the lower span at high cooling power favours the lower hot end temperature of 281 K as this brings the temperature span closer to the range where both LCSM materials operate best. Figure 3 also gives the results from the numerical model. Again, the trends are observed to be the same with regards to the order and crossing of the lines. As expected, the model over predicts the temperature span, but surprisingly the experimental zero span cooling powers are slightly above the predicted values. This may be caused by dissipation of some of the heater power through the walls of the device rather than into the regenerator. The extrapolated maximum zero-span cooling power of about 35 W kg^{-1} in the experiment is significantly larger than the highest measured value of 16 W kg^{-1} for Gd plates in the same device in similar conditions.[19] Due to the lower parasitic loss of larger devices and the faster operation possible when using packed bed regenerators, significantly higher values are reported for such devices[8,9] but at the cost of a significantly higher pumping pressure.

In conclusion, the results clearly show the potential value of the mixed valence manganese ceramics as magnetocaloric materials for application in devices. The strength of the materials lies in the ability to accurately tune the Curie temperature and process the materials into thin plates with adjacent regions of different Curie temperatures. Future regenerators will be constructed of numerous adjacent materials, leading to further improvements of the performance. The relatively low cost of materials and especially the processing route, compared to conventional materials and processing routes, reduces the price which is otherwise a major obstacle in the way of magnetocaloric applications.

The authors would like to acknowledge the support of the Programme Commission on Energy and Environment (EnMi) (Contract No. 2104-06-0032) which is part of the Danish Council for Strategic Research.

[1]S. Jin, T. H. Tiefel, M. McCormack, R. A. Fastnacht, R. Ramesh, and L. H. Chen, Science **264**, 413 (1994).
[2]J.-H. Park, E. Vescovo, H.-J. Kim, C. Kwon, R. Ramesh, and T. Venkatesan, Nature **392**, 794 (1998).
[3]J. M. D. Coey, M. Viret, and S. von Molnár, Adv. Phys. **58**, 571 (2009).
[4]M.-H.-H. Phan and S.-C.-C. Yu, J. Magn. Magn. Mater. **308**, 325 (2007).
[5]K. A. Gschneidner, Jr., V. K. Pecharsky, and A. O. Tsokol, Rep. Prog. Phys. **68**, 1479 (2005).
[6]K. A. Gschneidner, Jr. and V. K. Pecharsky, Annu. Rev. Mater. Sci. **30**, 387 (2000).
[7]A. Rowe and A. Tura, Int. J. Refrig. **29**, 1286 (2006).
[8]S. Russek, J. Auringer, A. Boeder, J. Chell, S. Jacobs, and C. Zimm, in *Proceedings of the 4th International Conference on Magnetic Refrigeration at Room Temperature, Baotou, Inner Mongolia, China* (International Institute of Refrigeration, Paris, France, 2010), p. 339.
[9]D. Arnold, A. Tura, and A. Rowe, Int. J. Refrig. **34**, 178 (2011).
[10]A. Larbot, *Fundamentals of Inorganic Membrane Science and Technology, Membrane Science and Technology*, Vol. 4, edited by A. Burggraaf and L. Cot (Elsevier Science B.V., Amsterdam, The Netherlands, 1996) pp. 119–139.
[11]R. Bulatova, K. B. Andersen, L. Theil Kuhn, C. R. H. Bahl, and N. Pryds, Adjacent tape casting of multiple ceramic slurries, (unpublished).
[12]K. Engelbrecht, K. K. Nielsen, and N. Pryds, Int. J. Refrig. **34**, 1817 (2011).
[13]R. Bjørk, C. R. H. Bahl, and M. Katter, J. Magn. Magn. Mater. **322**, 3882 (2010).
[14]A. R. Dinesen, S. Linderoth, and S. Mørup, J. Phys.: Condens. Matter **17**, 6257 (2005).
[15]C. R. H. Bahl, T. F. Petersen, N. Pryds, and A. Smith, Rev. Sci. Instrum. **79**, 093906 (2008).
[16]K. Engelbrecht, C. R. H. Bahl, and K. K. Nielsen, Int. J. Refrig. **34**, 1132 (2011).
[17]K. K. Nielsen, C. R. H. Bahl, A. Smith, N. Pryds, and J. H. Hattel, Int. J. Refrig. **33**, 753 (2010).
[18]K. K. Nielsen, C. R. H. Bahl, A. Smith, R. Bjørk, N. Pryds, and J. H. Hattel, Int. J. Refrig. **32**, 1478 (2009).
[19]K. K. Nielsen, R. Bjørk, J. B. Jensen, C. R. H. Bahl, N. Pryds, A. Smith, A. Nordentoft, and J. Hattel, in Proceedings of the 8th IIF/IIR Gustav Lorentzen Conference on Natural Working Fluids, Copenhagen, Denmark, September 7-10, 2008.

PAPER V

M. Jabbari, R. Bulatova, J. H. Hattel, and C. R. H. Bahl, “Quasi-steady state power law model for flow of $(La_{0.85}Sr_{0.15})_{0.9}MnO_3$ ceramic slurry in tape casting”, *Mater. Sci. Technol*., vol. 29 (9), pp. 1080–1087, 2013.

.

Quasi-steady state power law model for flow of $(La_{0.85}Sr_{0.15})_{0.9}MnO_3$ ceramic slurry in tape casting

M. Jabbari*[1], R. Bulatova[2], J. H. Hattel[1] and C. R. H. Bahl[2]

One of the most common ways used to produce multilayer ceramics is tape casting. In this process, the wet tape thickness is one of the single most determining parameters affecting the final properties of the product, and it is therefore of great interest to be able to control it. In the present work, the flow in the doctor blade region of a slurry containing $(La_{0.85}Sr_{0.15})_{0.9}MnO_3$ (LSM) material is described with a simple quasi-steady momentum equation in combination with an Ostwald–de Waele power law constitutive equation. Based on rheometer experiments, the constants in the Ostwald–de Waele power law are identified for the considered LSM material and applied in the analytical solution for the tape thickness. This solution is then used for different values of substrate velocity and doctor blade height and compared with experimental findings of the wet tape thickness, and good agreement is found.

Keywords: Tape casting, Doctor blade, Fluid flow, Non-Newtonian, Power law

Introduction

Tape casting is an important process for producing large area, thin, flat ceramics, which can be patterned, stacked and laminated to form three-dimensional structures.[1] The method was originally developed for producing electronic ceramics (insulating substrates and packages and multilayer capacitors) and is still mainly used for this. Structural laminates, knives, membranes and solid oxide fuel cells are examples of other applications for thin ceramics formed by tape casting. The tape thickness that can be achieved is generally in the range of 25 up to 1 mm, but it is possible to produce tapes with thicknesses of <5 μm.

The parallel (doctor) blade process was first used in preparing ceramic tapes in the 1940s, and it has a key role in producing thin and flat ceramic tapes.[2,3] Thickness control is of critical importance in tape casting, since it affects the final properties of the tape. Different parameters such as powder distribution, slurry composition, flow field and sintering affect the thickness of the final tape.[4–6] In addition to this, the geometry of the process set-up itself has different effects on the related final properties of the manufactured product.[7]

In the tape casting process, a slurry is pumped into a reservoir and this slurry is then moved by the peeling belt. Since this technique is used to produce tapes with relatively small thicknesses, accurate control of the tape thickness which exits the doctor blade is a key factor determining the final properties.

One of the most challenging parts of modelling the flow of the ceramic slurry in the tape casting process is to conduct the modelling with the proper constitutive equation which governs the material's rheological behaviour. In general, this rheological behaviour can be classified by five different material types as shown in Fig. 1. For Newtonian fluids, the shear stress τ has a linear correlation with the shear rate $\dot{\gamma}$ in which the slope of the line is the constant Newtonian viscosity μ. The second type is represented by pseudoplastic fluids that are often represented by the Ostwald–de Waele power law equation. The third one is named dilatant fluids, and they are characterised by an increasing slope of the shear stress–shear rate behaviour. The fourth is the Bingham plastic material which has a yield point τ_y below which no flow takes place, whereas above it, the behaviour is linear and characterised by the plastic viscosity. Finally, for viscoplastic materials, there is also a yield point like for the Bingham material, but above that, a polynomial behaviour can be seen.

The first model for predicting the tape thickness in tape casting was developed by Chou *et al.*[4] In their work, the Newtonian behaviour was used and they assumed that the flow in the parallel doctor blade region is a linear combination of pressure and drag flow. However, in the tape casting process of ceramics, the slurry seldom behaves like a Newtonian fluid. Pitchumdni and Karbhari[9] evaluated the effects of an imposed pressure gradient due to the height of the slurry in the casting head, as well as those of the drag due to the moving substrate on the slurry flow by modelling the slurry discharge as a generalised power law flow, i.e.

[1]Department of Mechanical Engineering, Technical University of Denmark, Nils Koppels Allé, Kgs. Lyngby 2800, Denmark
[2]Department of Energy Conversion and Storage, Technical University of Denmark, Frederiksborgvej 399, Building 779, Roskilde, Denmark

*Corresponding author, email mjab@mek.dtu.dk

Published by Maney on behalf of the Institute
Received 1 March 2013; accepted 20 March 2013
DOI 10.1179/1743284713Y.0000000255

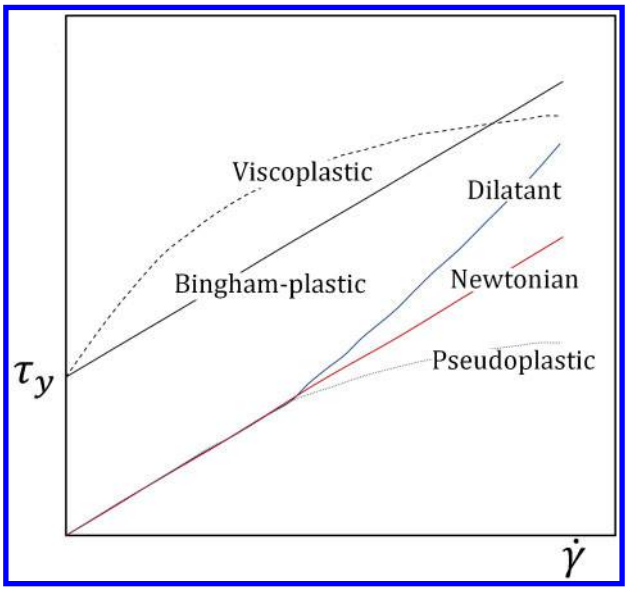

1 Rheological classification of flow[8]

$$\tau = k\dot{\gamma}^{n} \tag{1}$$

where k and n are the consistency of the fluid and deviation from a Newtonian fluid respectively, and both are constants for a specific slurry. However, in their work, the height of the ceramic slurry is assumed to be constant as opposed to the present work where it is allowed to vary.

Ring[10] modelled the tape casting slurry by applying the Bingham plastic constitutive law

$$\tau = \tau_0 + \mu\gamma \tag{2}$$

where τ_0 is the Bingham yield stress, which is the finite stress required for flow initiation, and μ is the plastic viscosity. In this model, the material acts as a rigid body below the yield point, and above it, the ceramic slurry flows with the constant plastic viscosity. However, the $(La_{0.85}Sr_{0.15})_{0.9}MnO_3$ (LSM) ceramic used in the present work did not show any yield point, which means that the slurry flows all the time. Recently, the Herschel–Bulkley model was used in the tape casting process for modelling the flow field by Huang *et al.*[11] This model is a combination of the Bingham plastic and power law models; however, again, they did not consider the transient behaviour of the ceramic slurry height.

Ceramics might be attractive materials for high temperature applications provided that both their reliability and toughness could be improved. The key factor improving the toughness of these materials is the presence of weak interfaces between fibres and the composite matrix or between the ceramic layers in multilayered structures. These interfaces allow for energy dissipation before fracture through mechanisms of crack deflection, crack bridging, fibre pullout and interface delamination. Multilayered ceramics are generally processed by tape casting and firing or hot pressing.[12] The presence of the different layers in multilayer materials controls the crack path, frequently avoiding completely brittle behaviour. When the layers are strongly bonded together, a crack in one layer can propagate readily into the adjacent layer, and then the material behaves as a conventional ceramic.[13] Most often, the graded structures are produced from laminating two or more single layers. In this respect, controlling the tape thickness and its uniformity along the casting direction becomes more important.

Moreover, the shape changes that happen during the sintering process due to the shrinkages in different directions will result in shape instability.[14] This shape instability is more important in the multilayer materials, since during the sintering process every layer has different thermal behaviour. However, even in the case of monolayer tape casting, it is of great importance to control the aforementioned shape instabilities. Raj and Cannon[14] proposed a formula to measure the percentage of anisotropic shrinkage in the tape casting process. They showed that the tape thickness and its variation have a great impact on the anisotropic shrinkage and the resultant mechanical properties, where an increase in the tape thickness causes a decrease in the anisotropic shrinkage. This emphasises the importance of the thickness control in the tape casting process.

Hence, in the present paper, an analytical model capable of predicting the final tape thickness is presented. It is based on a quasi-steady state description of the velocity and the pressure field in the doctor blade region, allowing the slurry height to drop during casting, and this is combined with a power law model for the fluid flow. Many of the affecting parameters in the process are embedded and they can easily be varied to evaluate their influence. The proposed models describe the flow characteristics of tape casting well. Results of the model are compared with experiments, and good agreement is obtained.

In the present paper, a quasi-steady state description of the velocity and the pressure field in the doctor blade region, allowing the slurry height to drop during casting, is combined with a power law model for the fluid flow. Many of the affecting parameters in the process are embedded, and they can easily be varied to evaluate their influence. The proposed models describe the flow characteristics of tape casting well. Results of the model are compared with experiments, and good agreement is obtained.

Analysis

In order to express the volume flow and thus the tape thickness, the velocity field equation in the doctor blade region must be developed. Based on the number of doctor blades, there are two kinds of tape casters: a simple tape caster that has only one doctor blade (illustrated schematically in Fig. 2), and a double blade tape caster in which a front doctor blade is used to ensure a hydrostatic pressure in front of the rear one.[15]

As shown in Fig. 2, δ is the green tape thickness, h is the doctor blade height, W is the width of the doctor blade, H_0 is the height of the slurry in front of the doctor blade, d is the depth of the reservoir, l is the inclined length of the reservoir and θ is the angle of the reservoir.

The pressure gradient inside the channel below the doctor blade is constant, since there is a hydrostatic pressure in front of the doctor blade and it can be determined by the height of the slurry as shown below[15]

$$\frac{dp}{dx} = -A_0 = -\frac{\rho g H_0}{W} \tag{3}$$

where ρ is the density of the slurry, and g is the acceleration due to gravity.

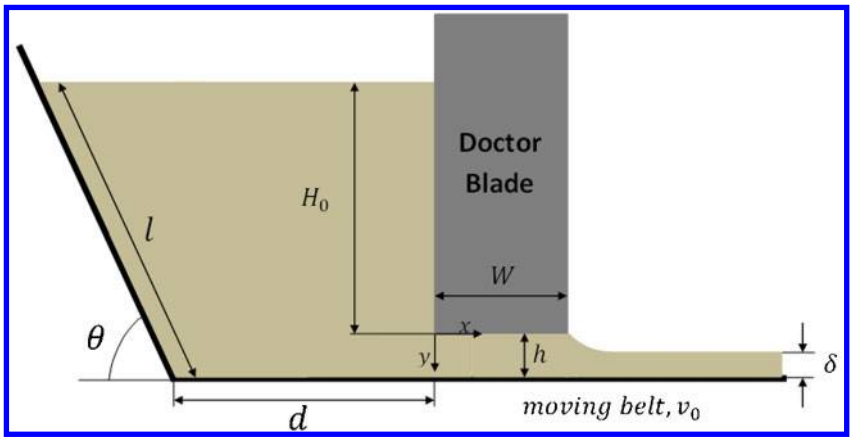

2 Schematic geometry of tape casting machine

By assuming an infinitely long and wide plate as compared to the thickness and combining with momentum conservation in the x direction under steady state conditions, we obtain the following[15,16]

$$\frac{d\tau}{dy}=\frac{dp}{dx} \tag{4}$$

where τ is the shear stress. From equations (3) and (4), τ is found to be

$$\tau=-A_0y+A_1 \tag{5}$$

where A_1 is an integration constant.

For power law fluids, the shear stress τ is given by the constitutive equation[16]

$$\tau=k\left(\frac{\partial u}{\partial y}\right)^n \tag{6}$$

where it has been assumed that the only velocity component contributing to the shear rate is the velocity in the x direction u.

Rewriting equations (5) and (6) and integrating along the channel height h

$$\int_0^h(-A_0y+A_1)dy=\int_0^h k\left(\frac{\partial u}{\partial y}\right)^n dy \tag{7}$$

and assuming that k and n are constants, we obtain

$$u=\left(-\frac{1}{A_0k\frac{1}{n}}\right)\left(\frac{1}{\frac{1}{n}+1}\right)(-A_0y+A_1)^{\frac{1}{n}+1}+A_2\ (0<y<h) \tag{8}$$

where A_2 is another integration constant.

The boundary conditions for equation (8) in the doctor blade region of tape casting are

$$\begin{cases}u(0)=0\\ u(h)=v_0\end{cases} \tag{9}$$

where v_0 is the velocity of the moving belt.

Applying these boundary conditions in equation (8), and introducing the expressions that $(1/n)+1=\chi$ and $-[1/A_0k(1/n)]=\psi$, we get

$$\begin{cases}0=\dfrac{\psi}{\chi}A_1^{\chi}+A_2\\ v_0=\dfrac{\psi}{\chi}(-A_0h+A_1)^{\chi}+A_2\end{cases} \tag{10}$$

which is rewriting into

$$\begin{cases}v_0=\dfrac{\psi}{\chi}\left[(-A_0h+A_1)^{\chi}+A_1^{\chi}\right]\\ A_2=-\dfrac{\psi}{\chi}A_1^{\chi}\end{cases} \tag{11}$$

In order to find the integration constant A_1, the Newton–Raphson method is used. To do so, the following equation originating from the upper expression in equation (11) is solved numerically to find the parameter A_1

$$F(A_1)=\frac{\psi}{\chi}\left[(-A_0h+A_1)^{\chi}+A_1^{\chi}\right]-v_0=0 \tag{12}$$

and consequently after finding A_1, the parameter A_2 is calculated from the lower expression in equation (11).

As a consequence of mass conservation, the thickness of the green tape δ, can then be determined by integrating u over the channel height and dividing by the tape velocity, i.e.

$$\delta=\frac{1}{v_0}\int_0^h u dy=\frac{-\left[(-A_0h+A_1)^{\chi+1}-A_1^{\chi+1}\right]}{v_0A_0\psi\chi(\chi+1)}+A_2h \tag{13}$$

Reaching to a constant tape thickness is not an impossible goal, since most of the manufacturing processes for tape casting are at the continuous form in which the reservoir at all times is fed by slurry. Moreover, using two doctor blades in the design of the machine will result in having almost constant hydrostatic pressure during the casting process. However, it is of great importance to control the tape thickness in the small tape casters especially in small scale production and laboratories, in which the slurry height is not constant in the reservoir but gradually decreasing with time. This phenomenon leads to the present modification of the standard steady state model,[2,4,9,15,16] making it dependent on the height variation.

Now, the proposed quasi-steady state formulation is developed based on the continuity equation. Assuming that the slurry is incompressible, the volume of the slurry which drops down in the reservoir is equal to the volume of the slurry which is conveyed out of the doctor blade region by the peeling belt. Assuming that during the time period equal to Δt, the height of the slurry will decrease from the initial value of H_0 to H_1, the aforementioned volume (equals area in the present

two-dimensional model) in the reservoir which is decreased will be given as

$$\Delta S_1 = \left[d + \frac{1}{2} l \cos\theta \left(1 + \frac{H_1 + h}{H_0 + h} \right) \right] (H_0 - H_1) \qquad (14)$$

This area is moved out of the doctor blade region with the constant velocity of υ_0 and the distance of $\upsilon_0 \times \Delta t$; hence, it is equal to $\upsilon_0 \times \Delta t \times \delta_1$. The new initial height in the next time step is now H_1 and the new ΔS_2 is found from using H_1 as initial height in equation (14) and so forth.

In the tape casting process, when the flow exits the doctor blade region, the fluid starts to flow in a transverse direction also (here in the z direction) and this is mostly named side flow. As the final tape is in general very wide in the z direction compared to its thickness, this side flow will be relatively small. Moreover, after the drying stage, the tape thickness is decreased due to weight loss. Considering both these effects, the final thickness of the dried tape is

$$\delta_{tp} = \frac{\alpha \beta \rho}{\rho_{tp}} \delta \qquad (15)$$

where δ_{tp} is the thickness of the dried tape, α is the fraction loss for side flow, β is the fraction loss for weight reduction due to drying, ρ is the density of green tape and ρ_{tp} is the density of dried tape, and δ is the thickness of the green tape.

Experimental

The different constituents and their function for the LSM slurry used in the experiments are given in Table 1. A commercial LSM was calcined at 1000°C and used in the amount of 62·05 wt-% in the final slurry. The average particle size and specific surface area were 12·42 μm and 23·24 $m^2\ g^{-1}$ respectively. Moreover, the weight ratios between LSM and MEKET (solution of methylethylketone and ethanol with the weight ratios of 1 : 3) and PVB/LSM were 1 : 2·44 and 1 : 11·53 respectively. To remove air bubbles from the slurries, mechanical vacuum was enforced for 15 min. The mean particle size and density of the final slurries were accordingly equal to 2·20–2·73 μm and 1·91 g mL^{-1}. The particle size distributions were measured with a laser diffraction particle size analyser LS 13 320 from Beckman Coulter (USA). The rheological profiles were measured using a narrow gap parallel plate sensor system in Rheometer HAAKE Rheo Stress 600 (Haake, Germany).

Experiments were carried out using a one-doctor blade continuous type of tape casting bench, and the plastic carrier tape (Mylar in the present case) was driven by stainless steel rollers. The doctor blade gap distance was set by using etalon sticks and a micrometre screw with an accuracy of 0·01 mm. After the propulsion of the torque drum, whose speed was programmed in advance, the slurry was peeled out according to the carrier movement, forming a thin layer of tape. The cast tapes were dried in air for 5 days, and their thicknesses were measured using the micrometer screw. The thicknesses of the cast tapes were measured in every 10 cm from doctor blade exit.

Experiments were conducted in three different cases, which are summarised in Table 2. For the first set of experiments, the same amount of ceramic slurry (constant H_0) was cast with three different substrate velocities. Then, in case 2, with constant velocity and slurry height, the amount of the doctor blade height was varied. In the last set of experiments during constant substrate velocity, the material load in the reservoir H_0 was varied. These experiments were carried out to investigate the effect of the three important parameters, i.e. drag forces related to substrate velocity, hydrostatic pressure and doctor blade height on the side flow amount.

Table 1 Material content and their function for LSM slurry used in experiments

Material	Function
$(La_{0.85}Sr_{0.15})_{0.9}MnO_3$ (LSM)	Ceramic substrate
Methylethylketone	Solvent
Ethanol	Solvent
Polyvinyl pyrrolidone (PVP)	Dispersant
Polyvinyl butyral (PVB)	Binder
Polyethylene glycol (PEG)	Plasticiser
Dibutyl phthalate (DBP)	Plasticiser
Additol	Deflocculant

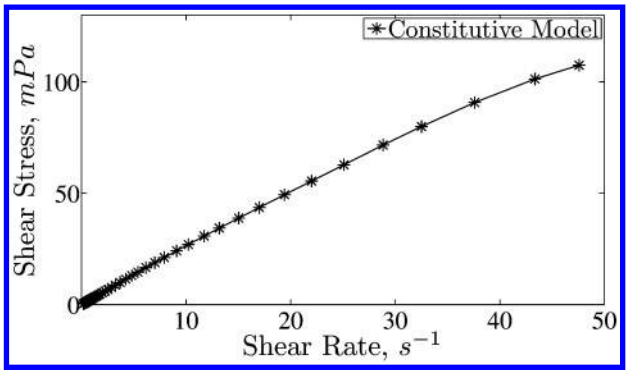

3 Rheology behaviour of LSM slurry

Results and discussion

Results from the rheology experiment showed that the LSM slurry follows the Ostwald–de Waele power law fluid behaviour. This is illustrated in Fig. 3, and the relationship for the shear rate and shear stress was found to be

$$\tau = 3{\cdot}31 (\partial u / \partial y)^{0{\cdot}90} \qquad (16)$$

where the constant k, which is the consistency of fluid, is equal to 3·31 mPa s^n (where n=0·90), and the constant n, which is the proximity to a Newtonian fluid, is equal to 0·90, quite close to the Newtonian fluid value of 1. The constant for the side flow α was obtained by a volumetric comparison of the tape which flowed outside

Table 2 Summary of experimental studies

Parameter	Case 1	Case 2	Case 3
W/mm	6·4	6·4	6·4
h/mm	1	0·25, 0·4, 1	0·4
v_0/mm s^{-1}	3·67, 10, 14·67	3·67	3·67
H_0/mm	1·2	10·6	3·1, 6·6, 20·8
d/cm	8·8	8·8	8·8
α/°	45	45	45

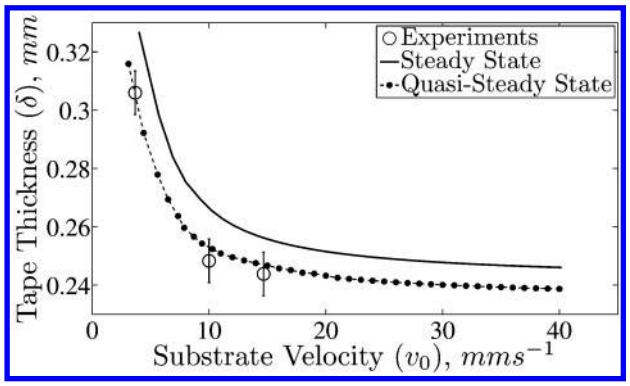

4 Effect of substrate velocity on tape thickness with doctor blade height of 1 mm

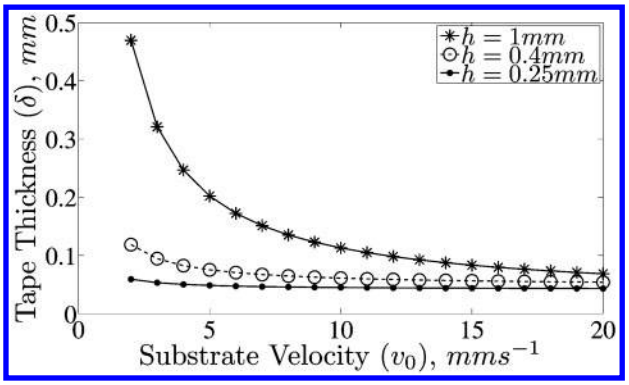

6 Results of modelling for effect of doctor blade height on tape thickness

the casting width to the tape within the casting width ($0{\cdot}8<\alpha<0{\cdot}9$). The drying weight loss factor β was obtained from drying experiments, which measured the dried tape mass and compared it to the wet slurry mass ($0{\cdot}58<\beta<0{\cdot}64$).

Effect of substrate velocity

Figure 4 shows the effect of the substrate velocity on the dried tape thickness for the experimental data, steady state and quasi-steady state model. As seen from the figure for all types of data, an increased substrate velocity results in decreasing of the tape thickness. By further increase in the substrate velocity, it is found that the tape thickness decreases hyperbolically,[4,9] which is also seen from equation (13). From previous works,[4,8,9] it was found that when the drag force is increased by increasing the substrate velocity, it becomes more dominant compared to the pressure force that results in more stretching of the slurry over the peeling belt. Figure 4 shows that the proposed quasi-steady state model is in better agreement with corresponding experiments as compared to the steady state model, since in the quasi-steady state model the effect of decreasing level of the slurry height was taken into account. It should be noted that the variation of the height in the slurry will change the parameter A_0 and the resultant values of A_1 and A_2 (which are calculated numerically); this of course is neglected in the steady state model.

Figure 5 depicts the velocity profiles below the doctor blade for three different tape velocities. It is seen that for the higher substrate velocity (of 14·67 mm s^{-1}), the distribution approaches a linear correlation, which corresponds to Couette flow conditions. For lower velocities, the hydrostatic pressure plays a more dominant role, resulting in a velocity peak ~0·25 mm above the peeling belt, which originates from the combination of Couette and Poiseuille flow conditions. These tendencies are also found in the analytical model for flow in tape casting originally proposed by Kim *et al.*[2] and further developed on dimensionless form by Jabbari and Hattel.[8]

Effect of doctor blade height

The effect of the doctor blade height on the tape thickness is illustrated in Fig. 6. It is seen that increasing the doctor blade height leads to a higher tape thickness, which is expected. However, the difference between the curves in Fig. 6 is decreased by increasing the velocity. For a constant pressure height, increasing the doctor blade height results in more material being carried out of the doctor blade region. This means that the thickness of the tape will be increased. As mentioned before, for high casting velocities (substrate velocity), the drag force becomes more dominant. The increase in the tape thickness coming from a higher doctor blade gap is reduced as the velocity is increased.

The comparison between the proposed model, steady state model and experimental results is shown in Fig. 7. It can be seen that the new proposed model is in better agreement with experiments in comparison to the steady state model. The highest deviation between data was observed for the higher values of the doctor blade height. This could arise from some of the assumptions used in the equations for the proposed model. The main assumption in this regards is the use of constant side

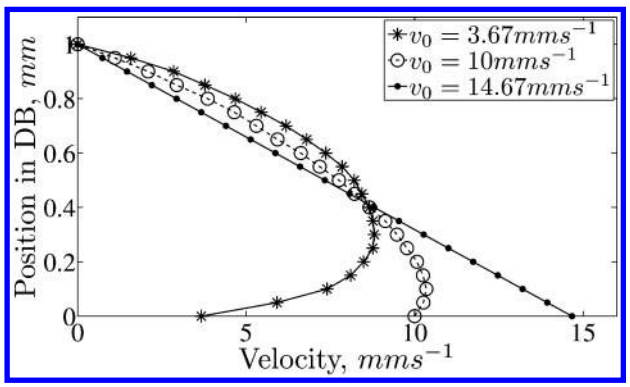

5 Average velocity profile below doctor blade region with different substrate velocities

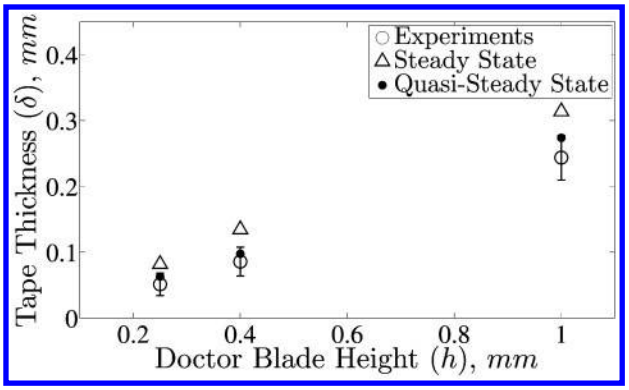

7 Comparison of proposed quasi-steady state model with steady state model and experiments for v_0=3·67 mm s^{-1}

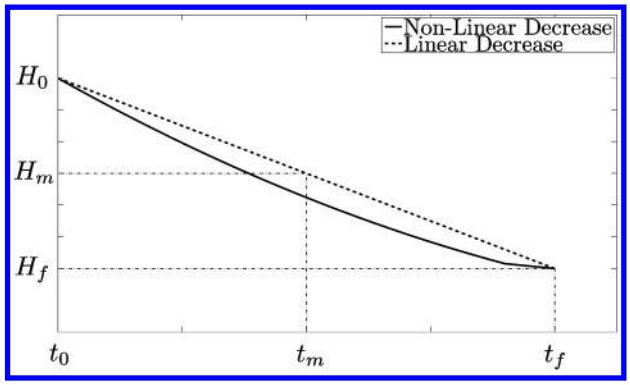

8 Schematic illustration of slurry height change by time

flow factor α for calculating the tape thickness based on equation (15). However, this factor is not constant based on the numerical investigation done by the authors,[17] and highly dependent on the geometry of the tape caster and the process parameter. On the other hand, in most cases, the desired thickness for the final tapes is in the range of $\leq$100 μm, in which the proposed model agrees well with the experimental data. The smaller deviation found in the experiment might be due to the effect of side flow, which obviously reduces the tape thickness as compared to the analytical solution.

Effect of slurry load

It should be emphasised that for the comparisons shown in Figs. 4 and 7, the height of the slurry that was inserted in the steady state solution[15,16] was the initial height H_0. This of course overestimates the hydrostatic pressure and hence the tape thickness in cases where the slurry height is actually decreasing over time.

Thus, in order to make a more fair comparison between the analytical steady state model and the proposed quasi-steady state model, it was chosen to represent the slurry height (which is constant) in the steady state model by some reasonable average.

Now, consider Fig. 8 in which the decrease in the height of the slurry in the reservoir over time is represented schematically. Here, H_0 is the initial ceramic height and H_f is the last point where the fluid experiences the hydrostatic pressure (equal to the doctor blade height h). Of course, the real trend for the decrease of the height is a non-linear behaviour, starting with high hydrostatic pressure and decreasing by time, but as a reasonable average, one could assume that there is a linear behaviour in the reduction of the slurry height by time, i.e.

$$H_m = \frac{H_0 + H_f}{2} \tag{17}$$

This mean value is used in the steady state model when comparing with the quasi-steady state model in Figs. 9 and 10.

By choosing fairly small time increments for the modelling, the results for different values of heights in the reservoir are shown in Fig. 9. As it seen from Fig. 9, the thickness of the tape in the end of a strip is higher than that in the beginning of a strip. This is due to the higher level of material in the reservoir in the beginning of the process. As time passes, the height of the slurry in the reservoir decreases, and consequently, the resultant height of the tape will decrease. This means that the hydrostatic pressure decreases by time and the drag forces start to show their dominance by making the tape thinner. However, this phenomenon cannot be detected by the steady state model, no matter which value of the slurry height (initial or average) is applied. Moreover, it can be seen that the higher level of slurry in the reservoir leads to a higher tape thickness in the strip. On the other

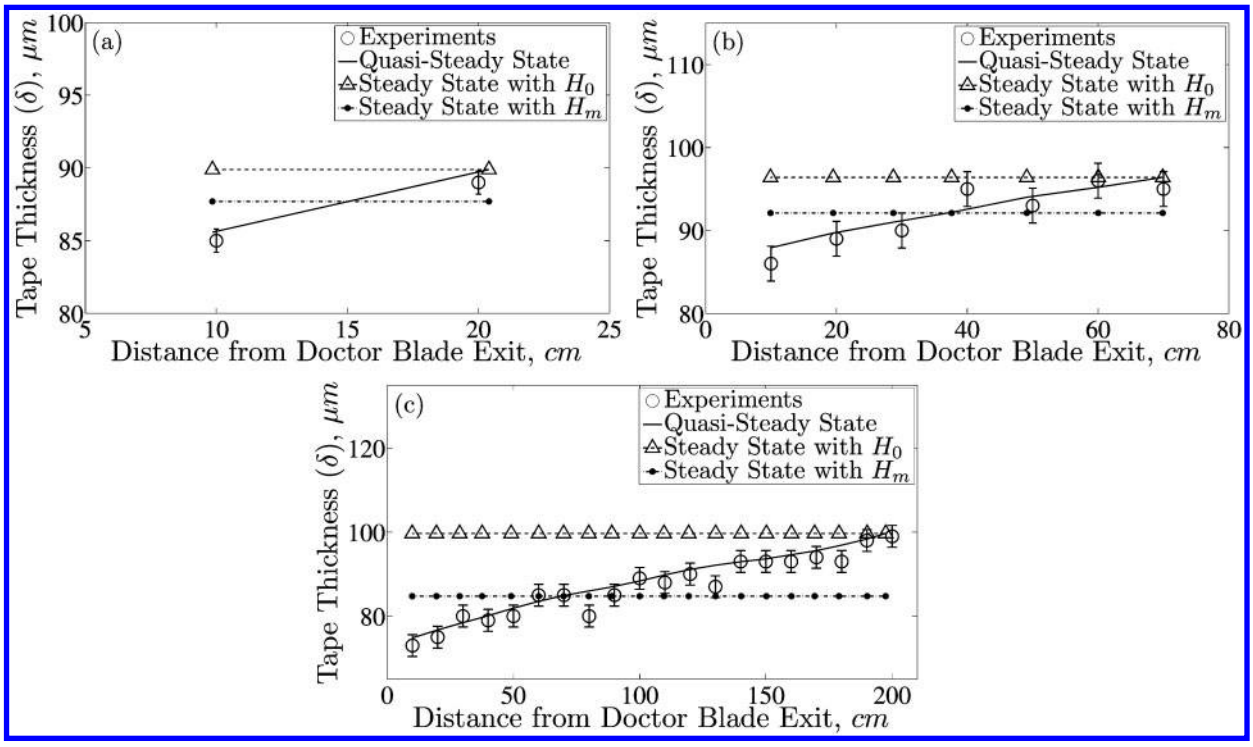

a H_0=3·1 mm; *b* H_0=6·6 mm; *c* H_0=20·8 mm

9 Results of modelling and their comparison with experimental data for case 3

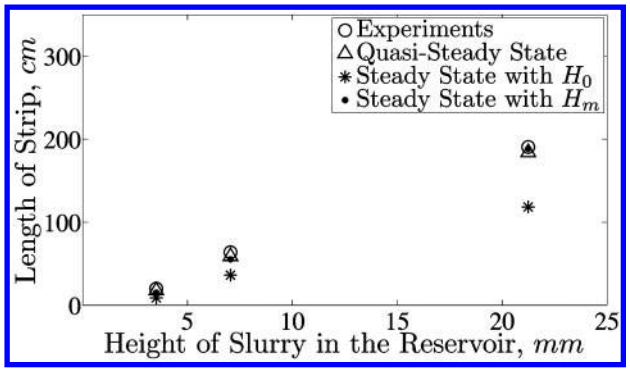

10 Correlation between height of slurry and length of strip from model and experiments with substrate velocity of 3·67 mm s^{-1}

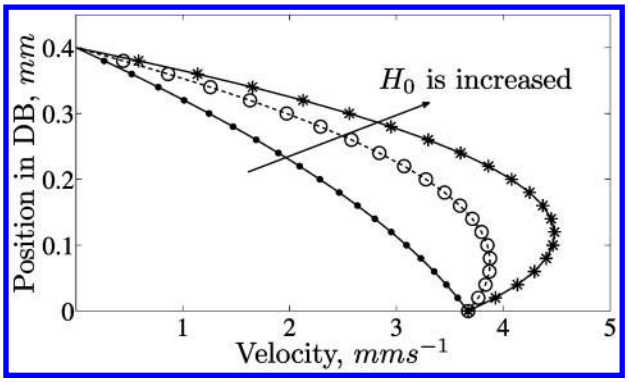

11 Effect of variation in slurry height on velocity profile below doctor blade region with doctor blade size of h=0·4 mm

hand, it is also seen that the mean assumption for the initial slurry height (steady state with H_m) in some points catches the experimental data better than the one with the initial height (steady state with H_0). However, it does not predict the transient behaviour of the slurry height, which is embedded in the quasi-steady state model.

Furthermore, the higher level of slurry will result in a longer final strip because of more material content in the process. The predicted values from the quasi-steady state, steady state model with initial height and steady state with the mean height assumption and the estimated data from experiments for the length of strip with the different heights of the slurry are shown in Fig. 10. The results of the quasi-steady state model are in very good agreement with the experimental data. The small differences between the experiments and the proposed model might be due to the influence of the side flow. However, it can also be seen that there is much more difference between the steady state model and the experimental data, which was expected. It is obvious that the steady state model with the initial height gives a constant value of the tape thickness, which only fits to the experimental and the quasi-steady state model in the beginning where the slurry height is actually H_0. Moreover, the results of the steady state model with the mean assumption for the initial slurry height are in good agreement with both the quasi-steady state and the experimental data; however, they are still constant and a more representative level is expected.

To get a better understanding of the effect of the variable slurry height on the tape thickness, the velocity profile was analysed below the doctor blade region for one of the tests in case 3 (H_0=20·8 mm, h=0·4 mm and v_0=3·67 mm) which is shown in Fig. 11. Here, the line with the asterisk marker represents the velocity profile for the initial slurry height (H_0=20·8 mm), the line with the 'o' marker is the representative of the velocity profile after some period of time and the line with the dot marker represents results even later in time. As seen, since the hydrostatic pressure decreases by time due to the reduction in level in the slurry height, the velocity profile is changed and the area under the velocity profile is decreased, which can be seen in Fig. 12, and consequently, the 'area' out of the blade is decreased. On the contrary, decreasing the pressure head for a constant velocity, the thickness of the tape is decreased in the exit and vice versa. This behaviour very much emphasises the importance of the proposed quasi-steady state model, in which the transient effect of the slurry height in the reservoir (which resembles the pressure head) is implemented. As already discussed, the variation in the velocity profile will cause a change in the tape thickness (Fig. 12). This phenomenon can easily be seen in Fig. 9, where the tape thickness decreases in the casting direction due to the transient decrease of the slurry height in the reservoir.

Conclusions

A quasi-steady state power law model for the constitutive behaviour of the non-Newtonian slurry of LSM was proposed and used to analyse the effect of substrate velocity, doctor blade height and slurry height in the reservoir on the final tape thickness in tape casting. This proposed model was based on the continuity equation assuming incompressibility such that the decrease of the volume of the slurry in the reservoir is equal to the one that leaves the doctor blade region. The results show that increasing the substrate velocity (casting speed) causes a decrease in the tape thickness due to the dominance of drag force over hydrostatic pressure. On the other hand, increasing the doctor blade height with constant velocity, the thickness of the final tape will be increased, since the gap size for the slurry is high enough for it to be conveyed more out of the doctor blade region. In both cases, the developed quasi-steady state model has better agreement with the experiments compared to the well known steady state model. For both quasi-steady state model and experiments, it is observed that the height of tape at the end point of the strip is higher in comparison to the beginning of the

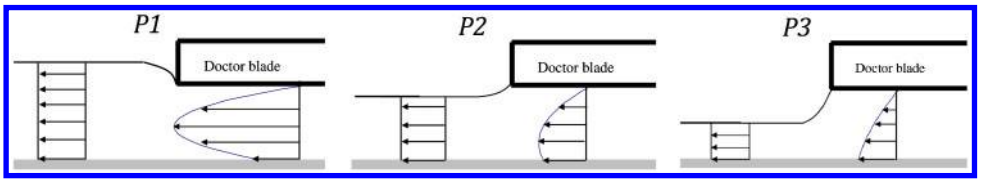

12 Schematic illustration of effect of increased pressure head on tape thickness (P_1>P_2>P_3)[2]

strip, which is not predictable by steady state solution. Moreover, by increasing the material load (the height of slurry in the reservoir), the aforementioned differences between the beginning and the end of strip and the length of strip will be increased. A new modified steady state model is also presented based on a linear correlation between the level in the slurry height and the time. Although the presented model does not have the full accuracy of the quasi-steady state model, it showed some good results compared to the conventional steady state calculations from the literature. Although the LSM ceramic used in the present study has a slightly non-Newtonian behaviour (n=0·90), the model contains all main parameters that influence the process, and it has the flexibility to be used for different slurries, which are more non-Newtonian, as well as different machine designs. Moreover, the results show that the classical steady state is not so well describing for the real process in which the ceramic height in the reservoir is not constant. However, the results of the proposed quasi-steady state model show that it has good agreement with the experimental data.

Acknowledgements

The authors would like to acknowledge the support of the Scientific Research Councils on Technology and Production Sciences (FTP) (contract no. 09-072888, OPTIMAC), which is part of the Danish Council for Independent Research (DFF).

References

1. G. S. Grader and L. Zuri: *J. Am. Ceram. Soc.*, 1993, **76**, 1809–1814.
2. H. J. Kim, M. J. M. Krane, K. P. Trumble and K. J. Bowman: *J. Am. Ceram. Soc.*, 2006, **89**, 2769–2775.
3. C. Pagnoux, T. Chartier, M. Granja, F. Doreau, J. M. Ferreira and J. F. Baumard: *J. Eur. Ceram. Soc.*, 1998, **18**, 241–247.
4. Y. T. Chou, Y. T. Ko and M. F. Yan: *J. Am. Ceram. Soc.*, 1987, **70**, 280–282.
5. Y. Tanimoto, T. Hayakawa and K. Nemoto: *Dent. Mater.*, 2007, **23**, 549–555.
6. M. P. Albano and L. B. Garrido: *Ceram. Int.*, 2005, **31**, 57–66.
7. P. H. Gaskell, B. Rand, J. L. Summers and H. M. Thompson: *J. Eur. Ceram. Soc.*, 1997, **17**, 1185–1192.
8. M. Jabbari and J. Hattel: AIP Proc. Int. Conf. on 'Numerical analysis and applied mathematics', Halkidiki, Greece, American Institute of Physics (AIP), September 2011, Vol. 1389, 143–146.
9. R. Pitchumdni and V. M. Karbhari: *J. Am. Ceram. Soc.*, 1995, **78**, 2497–2503.
10. T. A. Ring: *Adv. Ceram.*, 1989, **26**, 569–576.
11. X. Y. Huang, C. Y. Liu and H. Q. Gong: *Mater. Manuf. Processes*, 1997, **12**, 935–943.
12. C. Badinia, P. Fino, A. Ortona and C. Amelio: *J. Eur. Ceram. Soc.*, 2002, **22**, 2071–2079.
13. C. A. Folsom, F. W. Zok and F. F. Lang: *J. Am. Ceram. Soc.*, 1994, **77**, 689–696.
14. P. M. Raj and W. R. Cannon: *J. Am. Ceram. Soc.*, 1999, **82**, 2619–2625.
15. G. Zhang, Y. Wang and J. Ma: *Mater. Sci. Eng. A*, 2002, **A337**, 274–280.
16. A. I. Y. Tok, F. Y. C. Boey and Y. C. Lam: *Mater. Sci. Eng. A*, 2000, **A280**, 282–288.
17. M. Jabbari and J. H. Hattel: *J. Am. Ceram. Soc.*, 2013, **96**, 1414–1420.

PAPER VI

M. Jabbari, R. Bulatova, J. H. Hattel, and C. R. H. Bahl, “An evaluation of interface capturing methods in a VOF based model for multiphase flow of a non-Newtonian ceramic in tape casting”, *Appl. Math. Model.*, vol. 38 (13), pp. 3222-3232, 2014.

.

Applied Mathematical Modelling 38 (2014) 3222–3232

Contents lists available at ScienceDirect

Applied Mathematical Modelling

journal homepage: www.elsevier.com/locate/apm

An evaluation of interface capturing methods in a VOF based model for multiphase flow of a non-Newtonian ceramic in tape casting

M. Jabbari [a,*], R. Bulatova [b], J.H. Hattel [a], C.R.H. Bahl [b]

[a] Department of Mechanical Engineering, Technical University of Denmark, Nils Koppels Allé, 2800 Kgs, Lyngby, Denmark
[b] Department of Energy Conversion and Storage, Technical University of Denmark, Frederiksborgvej 399, Building 779, Roskilde, Denmark

ARTICLE INFO

Article history:
Received 21 August 2012
Received in revised form 11 November 2013
Accepted 26 November 2013
Available online 21 December 2013

Keywords:
VOF method
Tape casting
Non-Newtonian
Power law

ABSTRACT

The aim of the present study is to evaluate the different interface capturing methods as well as to find the best approach for flow modeling of the ceramic slurry in the tape casting process. The conventional volume of fluid (VOF) method with three different interpolation methods for interface capturing, i.e. the Geometric Reconstruction Scheme (GRS), High Resolution Interface Capturing (HRIC) and Compressive Interface Capturing Scheme for Arbitrary Meshes (CICSAM), are investigated for the advection of the VOF, both for Newtonian and non-Newtonian cases. The main purpose is to find the best method for the free surface capturing during the flow of a ceramic slurry described by a constitutive power law equation in the tape casting process. First the developed model is tested against well-documented and relevant solutions from literature involving free surface tracking and subsequently it is used to investigate the flow of a $La_{0.85}Sr_{0.15}MnO_3$ (LSM) ceramic slurry modeled with the Ostwald de Waele power law. Results of the modeling are compared with corresponding experimental data and good agreement is found.

1. Introduction

Tape casting is a forming method that has mainly been used in the electronics industry to produce multi-layer capacitors and electronic substrates [1,2]. This method basically starts with a specially designed slurry which can be cast by a blade to a flat sheet or layer, then dried into a flexible solid tape which can be sintered subsequently into a hard ceramic substrate layer [3]. This technique is a well-established process which is used to produce ceramic layers and multi-layered ceramics (MLC). The parallel (doctor) blade process was first used in preparing ceramic tapes in the 1940s and today it plays a key role in producing thin and flat ceramic tapes [4,5].

Generally, the fluid flow in the doctor blade region and the subsequent outflow can be analyzed using Navier–Stokes equations in two dimensions assuming that flow is generated by both viscous drag due to the peeling velocity of the substrate and the static hydraulic pressure in the slurry reservoir. There are a few research papers in which the flow field and the resulting tape thickness were modeled analytically. Chou et al. [6] modeled the flow in the parallel blade region and due to the low Reynolds number, they neglected the inertia forces by assuming Newtonian-Stokes flow.

* Corresponding author. Tel.: +45 45254734; fax: +45 45930190.
E-mail address: mjab@mek.dtu.dk (M. Jabbari).

0307-904X/$ - see front matter © 2013 Elsevier Inc. All rights reserved.
http://dx.doi.org/10.1016/j.apm.2013.11.046

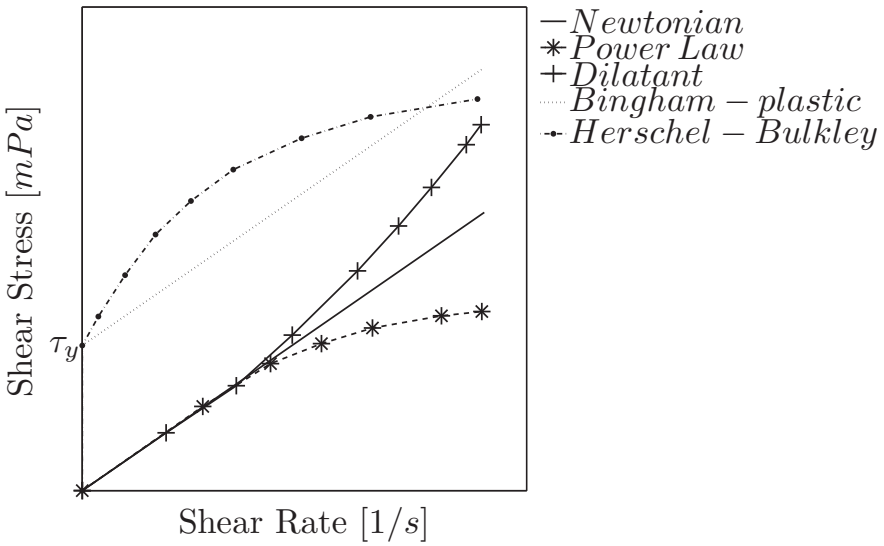

Fig. 1. Rheological classification of fluids.

In a general sense, fluids that exhibit characteristics not covered by the Newtonian constitutive equation are non-Newtonian. The exceptions to the Newtonian fluids are not of rare occurrence, and in fact many common fluids are non-Newtonian. Fig. 1 shows the rheological classification of the non-Newtonian fluids.

In the tape casting process, the ceramic slurry is mostly categorized as a non-Newtonian flow with relatively high viscosity. The viscoplastic description was used by Huang et al. [7] to model the flow field in the tape casting process. In their 2D analytical model the effects of pressure gradient, substrate velocity and resultant tape thickness were evaluated. The effect of different rheological behaviors of the tape slurry (Newtonian, power law and Bingham plasticity) for a generalized pressure flow in tape casting was investigated by Joshi and et al. [8]. They estimated the tape thickness analytically and controlled the size of the parallel channel in tape casting accordingly.

The flow of Bingham fluids are evaluated and investigated in different areas of the engineering sciences [9,10]. The ideal Bingham material model is characterized by a shear stress (τ) which is a linear function of shear rate ($\dot{\gamma}$). The yield stress (τ_y in Fig. 1) is the finite stress which is required for flow initiation (Fig. 1). The main mathematical difficulty when solving ideal Bingham flows is the non-differentiability of the constitutive law at the yield point. The most straightforward and convenient way to circumvent this difficulty is to approximate the material behavior by a bi-viscosity model, in which the material has no true yielding point but flows with a very high viscosity below the yield stress and with the plastic viscosity above it [11]. In most engineering applications, flow of non-Newtonian fluids are characterized by the Bingham, Herschel-Bulkley or Ostwald de Waele power law constitutive models which are shown in Fig. 1 [8,12–16]. A summary of work published regarding the rheological classification of non-Newtonian fluids and the existence of analytical/numerical models with focus on tape casting have been given previously by the authors [17].

Flow processes often involve the presence of free surfaces, the tracking of which has significant impact on the manufacturing and the final quality of the product. Examples abound, e.g., casting processes, mold filling, thin film processes, extrusion, coatings, spray deposition, fluid jetting devices in which material interfaces are inherently present. This phenomenon is also considered in multi-material flows with sharp immiscible interfaces [18]. Several CFD methods have been developed in the last decades with the aim of simulating such complex flows with free surfaces. Two very well-known example of this is the volume of fluid (VOF) and level set methods. In general, there are a lot of different research papers which are dedicated to free surface modeling, different interpolation schemes, liquid/gas phase flow, multi fluid flow, multiphase flow and different numerical methods to simulate the flow field with the presence of an interface [18–26].

A proper discretization of the convective term in the equation for transport of the VOF is crucial for simulation of a multiphase flow. It is well-known that numerical schemes, commonly used for discretization of the convection term, introduce numerical diffusion or numerical dispersion phenomena [27]. For this reason, some additional techniques are needed, i.e. high-resolution schemes. Examples of these can be found in [28–31] with special focus on capturing sharp interfaces.

The aim of this paper is to evaluate the different interface capturing methods and to find the best approach for flow modeling of the ceramic slurry in the tape casting process using the commercial software ANSYS FLUENT. The conventional VOF method will be used with three discretization schemes for the convection of the VOF: Geometric Reconstruction Scheme (GRS), High Resolution Interface Capturing (HRIC) and Compressive Interface Capturing Scheme for Arbitrary Meshes (CICSAM), which all will be discussed in detail. The main purpose is to find the best method for capturing the free surface in the flow of a non-Newtonian ceramic slurry described by the constitutive power law equation in the tape casting process. To do so, two different test cases will be investigated and compared with data in literature. One of the cases is the

flow of water (as a Newtonian fluid) in a box with a small obstacle in its path. In the other case, the flow of a power law ceramic fluid on an inclined plate will be tested. The aim of these cases is to serve as validation for the developed model and to investigate the influence of material behavior, i.e. a Newtonian fluid with $n = 1$ and a highly non-Newtonian fluid with $n = 0.5294$, on the different schemes for interface interpolation. Moreover, these cases are chosen because they are relatively simple modeling-wise in combination with being very well documented in literature [30,32]. After testing the developed model, it will be used to investigate the flow of a $La_{0.85}Sr_{0.15}MnO_3$ (LSM) ceramic slurry with the Ostwald de Waele power law constitutive behavior in tape casting. Results of the modeling will be compared with corresponding experimentally obtained data.

2. Governing equations

When dealing with flow problems, the coupled momentum and continuity equations should be solved:

$$\rho\left(\frac{\partial u}{\partial t} + u \cdot \nabla u\right) = -\nabla p + \nabla \cdot T + F \tag{2.1}$$

$$\frac{\partial \rho}{\partial t} + \nabla \cdot (\rho u) = 0 \tag{2.2}$$

where ρ is density, u is velocity, p is pressure, T is stress tensor and F is the contribution from external forces. Here, the momentum Eq. (2.1) expresses Newton's second law of motion, and the continuity Eq. (2.2) ensures conservation of mass. The momentum equation is dependent on the volume fraction of all phases through the properties ρ and μ (viscosity in the term T) via volume-fraction averaging as shown in Eq. (2.4)

The non-Newtonian Ostwald-de Waele constitutive law states that the shearing force (per unit area)) τ is proportional to the shear rates (the rate of shear strain $\dot{\gamma} = \partial u/\partial y$) as given below:

$$\tau = k\dot{\gamma}^n \tag{2.3}$$

in which k and n are the consistency of the fluid and amount of deviation from a Newtonian fluid, respectively.

The volume of fluid (VOF) model is a surface-tracking technique applied to a fixed Eulerian mesh. It is designed for two or more immiscible fluids where the position of the interface between the fluids is of interest. In the VOF model, a single set of momentum equations is shared by the fluids, and the volume fraction of each of the fluids in each computational cell is tracked throughout the domain [33].

The properties appearing in the transport equation are determined by the presence of the component phases in each control volume. In a two-phase system, for example, if the phases are represented by the subscripts 1 and 2, and if the volume fraction of the second of these is being tracked, the density in each cell is given by

$$\rho = f_2\rho_2 + (1 - f_2)\rho_1 \tag{2.4}$$

The evolution of scalar f (volume fraction) is governed by the simple advection equation:

$$\frac{\partial f}{\partial t} + \frac{\partial u_i f}{\partial x_i} = 0 \tag{2.5}$$

More information on the VOF method can be found in the original work by Hirts and Nichols [33].

When coupled with the Navier–Stokes equations, the volume fraction is treated as an active scalar (it has influence on the velocity field). The main numerical difficulties connected with discretization of the transport equation for the volume fraction are: keeping constant width of the interface, i.e. avoiding artificial diffusion of the step interface profile and assuring a monotonic change of the variables. This last condition is also known as the boundedness criterion [33]. In order to overcome the aforementioned problems different methods were proposed. For instance, in Hirt and Nicholls [33] a Donor–Acceptor Scheme (DAS), based on the availability criterion, was introduced. Problems that arose when using this scheme provoked other proposals that follow the idea of geometric interface reconstruction; examples are SLIC (Simple Line Interface Calculation) method, PLIC (Piecewise Linear Interface Construction) method or more recent methods that use the least-square procedure or splines [23]. Methods that employ these ideas give good approximation of the shape of the interface and they allow for proper calculation of the fluxes through faces of the control volumes. However, their application is often restricted to structured grids with simple shapes of the control volumes. Moreover, since estimation of a spatial orientation of the interface from the distribution of the volume fraction needs a substantial number of numerical operations, interface reconstruction methods increase the computational effort [34].

Unlike geometric interface reconstruction methods, the high-resolution schemes, i.e. Compressive Interface Capturing Scheme for Arbitrary Meshes (CICSAM) [27] and High Resolution Interface Capturing (HRIC) [28], do not introduce geometrical representation of the interface but try to satisfy the aforementioned conditions by properly chosen discretization scheme [34]. The different VOF differencing schemes of volume fraction equation, i.e. geometrical reconstruction, donor–acceptor, CICSAM and HRIC, and their definitions are well summarized by Lopez and Quinta-Ferreira [35].

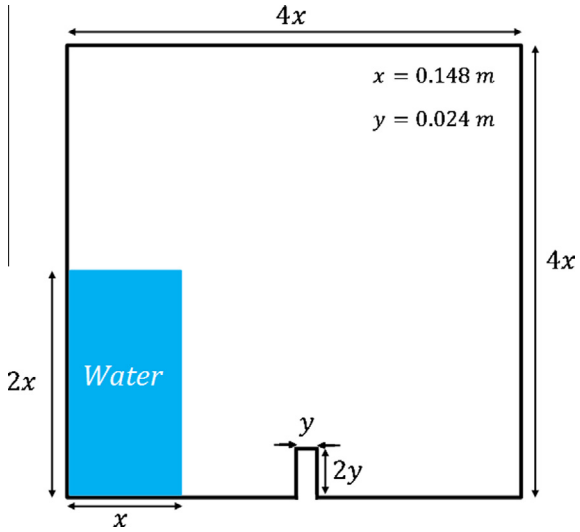

Fig. 2. Computational domain used for calculation of the flow for Newtonian (water) fluid.

3. Test case1: dam breaking with obstacle

In this case flow of water (Newtonian fluid) inside a box was investigated. The computational domain used for this calculation is illustrated in Fig. 2. The no-slip boundary condition was used for the wall and the thermal effect (energy equation) was neglected. The results of numerical modeling with different interface capturing methods are illustrated in Fig. 3a. It is seen that both the CICSAM and HRIC methods show the same profile, whereas the GRS is substantially different. Moreover, the numerical results of the present study were compared with the numerical and experimental data by Panahi et al. and shown in Fig. 3b and c [30]. It is obvious that the GRS scheme deviates from all other numerically obtained results, but it seems that it does not deviate a lot from the experimental data. Furthermore, the CPU times for the three methods are shown in Fig. 4. It is seen that the computational efforts are almost similar for the three schemes, however with a slightly higher value for the GRS scheme as compared to the others.

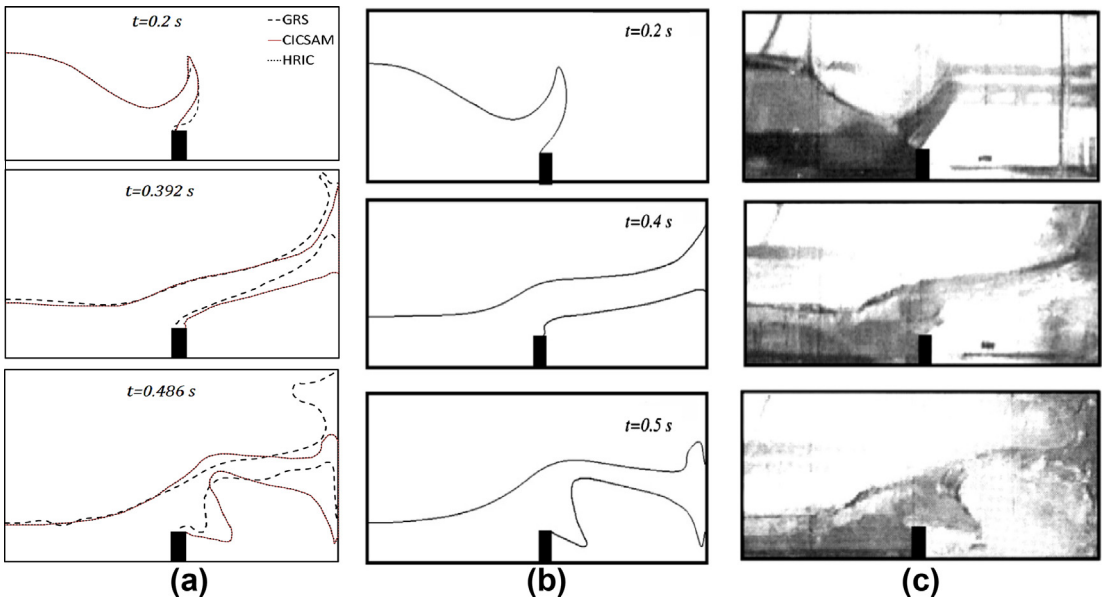

Fig. 3. Results and comparison of dam break for; (a) present study for different surface capturing methods, (b) numerical simulation by Panahi et al., and (c) experimental visualization by Koshizuka et al. [30].

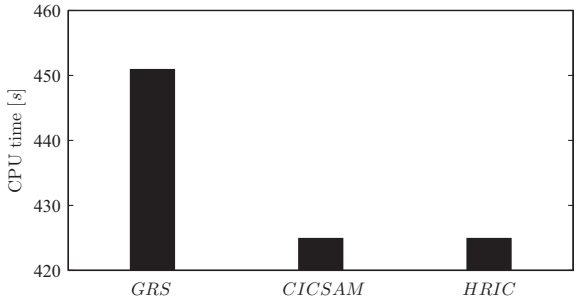

Fig. 4. CPU time comparison for different interface capturing method.

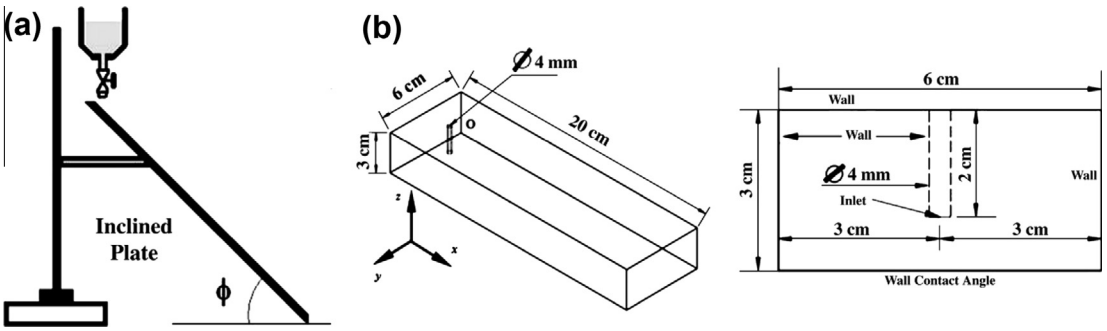

Fig. 5. Schematic of (a) experimental and (b) 3D computational domain used in the present case and taken from Haeri et al. [32].

4. Test case2: falling film on an inclined plate

The falling film of a non-Newtonian fluid on an inclined plate was investigated in this case. The geometry and the boundary conditions were used from the work by Haeri et al. [32] and are shown in Fig. 5. Full details of the modeling procedure can be found in Haeri et al. The constitutive model used for the material behavior is the power law equation with the constants shown below:

$$\tau = k\dot{\gamma}^n, (k = 11.007, n = 0.5294) \tag{4.1}$$

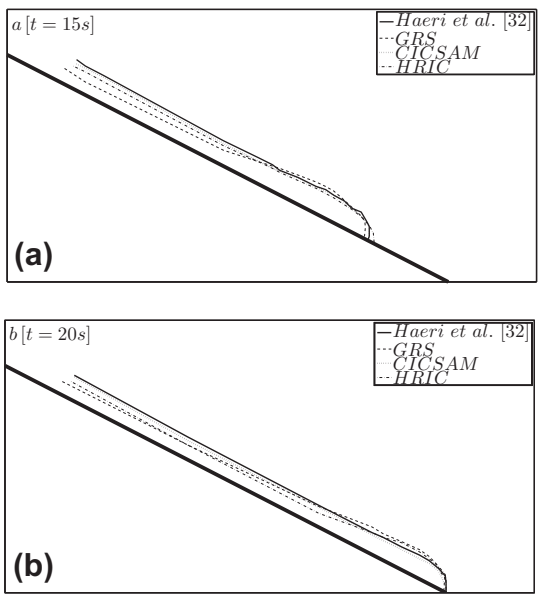

Fig. 6. Comparison of different interface capturing methods at different times of (a) t = 15 s and (b) t = 20 s.

The main purpose of this case is to test the model implemented in ANSYS FLUENT for the three different interface capturing methods and validate it for the case of a highly non-Newtonian fluid. The position of the resultant film thickness was extracted from the aforementioned work by Haeri et al. [32] and compared with the model developed in this study, see Fig. 6. The results reveal that the CICSAM method shows the best agreement. However it should be noted that the interpolation method that was used in Haeri et al. [32] was also the CICSAM method. Moreover, it is seen that the GRS again has the highest deviation from the other schemes. Moreover, in comparison to the Newtonian fluid (Test case1), the non-Newtonian fluid showed more instability in the interface. This was concluded from investigating the interface obtained by the HRIC method in more detail. Although the mentioned scheme has the highest accuracy as compared to the other methods, it still showed some oscillations in the interface.

The CPU times for the simulation of the falling film on a plate with different schemes are shown in Fig. 7. As seen, the computational time for the GRS method is again the highest. Moreover, for this special case there is a noticeable difference in the computational time between the CICSAM and the HRIC methods.

From the two test cases it can be concluded that for capturing the free surface, for both Newtonian and non-Newtonian fluids, the CICSAM scheme has less computational time as compared to the other interpolation schemes. More importantly, the CICSAM scheme showed less instability in the interface as well as a good prediction of the free surface for both the Newtonian and the non-Newtonian case.

5. Modeling of tape casting

5.1. Numerical procedure

A schematic illustration of the computational domain is shown in Fig. 8. The calculation domain is designed in 2D, and the side effect of flow outside the doctor blade region which to some extent affects the tape thickness is neglected. However, the mentioned effect is mimicked using extra parameters which were measured experimentally. The dimensions are chosen according to the machine design of the tape caster which was used in the experiments. The domain is discretized with a relatively fine mesh.

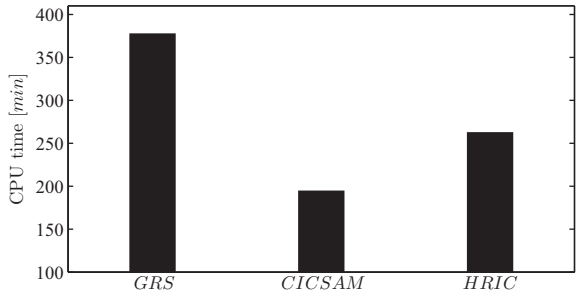

Fig. 7. CPU time comparison for different interface capturing methods.

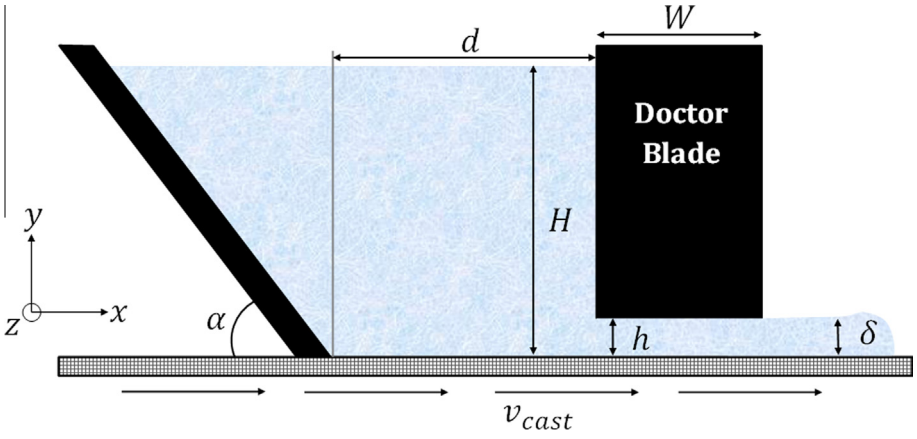

Fig. 8. Computational domain for modeling of tape casting.

For the inlet boundary condition the velocity is set to a very small value (10^{-8}m/s), just to avoid the initial zero boundary condition. A fixed velocity in the x -direction (v_0) is implemented on the substrate expressing the velocity of the peeling belt with no slip condition. A zero gradient is assumed for all flow properties in the outlet boundary condition. All other boundaries are implemented as wall boundaries with no slip condition.

For the transient calculations the non-iterative time-advancement (NITA) scheme is used to reduce the amount of computations. The idea underlying the NITA scheme is that, in order to preserve overall time accuracy, there is no need for reducing the splitting error to zero, but only having to make it the same order as the truncation error. The NITA does not need outer iterations and hence there is only one single "outer iteration" per time-step, which significantly speeds up transient simulations. The NITA is used with the fractional-step method, which offers the possibility of a considerable increase in efficiency [36].

The illustrated domain in Fig. 8 is discretized with a structured mesh. The general cell size is chosen to be 10 μm. However, in order to check the dependency of the solution on the mesh size, two other different mesh sizes were also tested. As shown in Fig. 9, the convergence history of the wall shear stress in the substrate (where the casting velocity is implemented) is evaluated by three different mesh sizes of 10, 5 and 1 μm. The results show that the simulation is reasonably independent of the mesh size where elements smaller than 10 μm are used. For the mesh and the velocity of the substrate used in this paper, the time step size is set in the range of 0.0005–0.002 s.

5.2. Experiments

The different materials used as well as their function for the $La_{0.85}Sr_{0.15}MnO_3$ (LSM) slurry are given in Table 1. A commercial LSM was calcined at 1000 °C, and used in the amount of 62.05 wt.% in the final slurry. The average particle size and specific surface area were 12.42 μm and 23.24 m^2/g, respectively. Moreover, the weight ratio between LSM:MEKET (solution of methylethylketone and ethanol) and PVB:LSM were 1:2.44 and 1:11.53, respectively. To remove air bubbles from slurries, the mechanical vacuum was enforced for 15 min. The mean particle size and density of the final slurries were accordingly equal to 2.20–2.73 μm and 1.91 g/ml. The particle size and particle size distribution were measured by the Laser Diffraction Particle Size Analyzer LS 13 320 from BECKMAN COULTER (USA). The rheological profiles were measured using a narrow-gap parallel plate sensor system in Rheometer HAAKE Rheo Stress 600 (Haake, Germany).

Experiments were carried out using a one-doctor blade continuous type of casting bench, and the plastic carrier (in the present case Mylar) was driven by a stainless steel roller. The doctor blade gap distance was set by using etalon sticks and a micrometer screw with an accuracy of 0.01 mm. After the propulsion of a torque drum, whose speed was programmed in

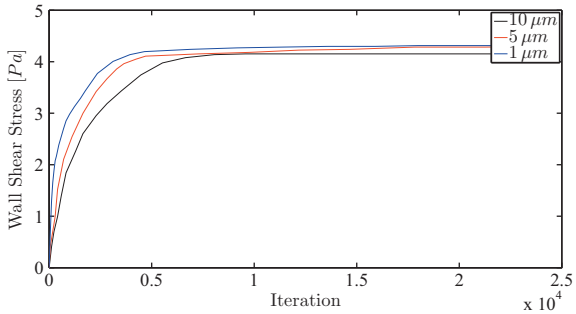

Fig. 9. Convergence history of the wall shear stress for numerical sanity of mesh dependency.

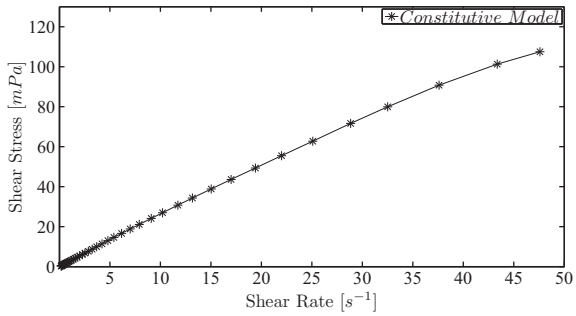

Fig. 10. Rheology behavior of LSM ceramic.

Table 1
The different materials used and their function for the non-Newtonian LSM slurry.

Material	Function
$La_{0.85}Sr_{0.15}MnO_3$ (LSM)	Ceramic substrate
Methyl ethyl ketone	Solvent
Ethanol	Solvent
Polyvinyl pyrrolidone (PVP)	Dispersant
Polyvinyl butyral (PVB)	Binder
Polyethylene glycol (PEG)	Plasticizer
Dibutyl phthalate (DBP)	Plasticizer
Additol	Deflocculant

Table 2
Summary of parameter settings during the two experimental studies.

Parameter	Case 1	Case 2
W (μm)	6000	6000
h (μm)	1000	400
v_0 (mm/s)	3.67, 10, 14.67	3.67
H_0 (μm)	1200	3536, 7074, 21222
d (cm)	8.8	8.8
α (deg)	45	45

advance, the slurry was peeling out along the carrier movement, forming a thin layer of tape. The cast tapes were dried in air for 5 days, and finally their thicknesses were measured using a micrometer screw.

Experiments were conducted in two different cases, which are summarized in Table 2. For the first set of experiments, the same amount of ceramic slurry (constant H_0) were cast with three different substrate velocities. Then in case 2, during constant substrate velocity the material load in the reservoir (H_0) was varied. These experiments were carried out to investigate the effect of the two important parameters, i.e. drag forces related to substrate velocity and hydrostatic pressure, on the tape thickness (δ).

6. Results and discussion

6.1. Material constants

The results of the rheology experiment showed that the LSM slurry follows the Ostwald power law fluid behavior. This is illustrated in Fig. 10 and the relationship between shear rate and shear stress is found to be:

$$\tau = 3.31 \cdot (\partial u/\partial y)^{0.90} \tag{6.1}$$

From Eq. (6.1) the constant k which is the consistency of the fluid is found to be equal to $k = 3.31\ mPa \cdot s^n$. Moreover, the constant n which is the amount of deviation from a Newtonian fluid is equal to 0.90 (indicating close to Newtonian behavior). These parameters are implemented in the numerical calculations for the behavior of the non-Newtonian LSM ceramic.

In the tape casting process, when the flow exits the doctor blade region, the fluid starts to flow in the transverse direction also (here the z direction which was neglected in the numerical model) and this is typically named side-flow. However, since the final tape in general is very wide in the z direction compared to its thickness, this side-flow will be relatively small. Moreover, after the drying stage, the tape thickness is decreased due to weight loss. Considering both these effects, the final thickness of the dried tape can be expressed as [37]:

$$\delta_{tp} = \alpha\beta(\rho/\rho_{tp}) \cdot \delta \tag{6.2}$$

where δ_{tp} is the thickness of the dried tape, α is the fraction loss for side-flow, β is the fraction loss for weight reduction due to drying, ρ is the density of green tape and ρ_{tp} is the density of dried tape. The constant for the side flow (α) was obtained by a volumetric comparison of the tape which flowed outside the casting width to the tape within the casting width leading to $0.8 < \alpha < 0.92$ [37]. The drying weight loss factor (β) was obtained from drying experiments which measured the dried tape mass and compared it to the wet slurry mass resulting in $0.58 < \beta < 0.65$.

6.2. Effect of velocity on thickness

The aim of this case study is to evaluate the effect of velocity changes in the peeling substrate on the tape thickness both experimentally and numerically. The results of the numerical modeling and the experiments are shown in Fig. 11. As seen, an increased substrate velocity results in decreasing of the tape thickness. By further increase of the substrate velocity it is

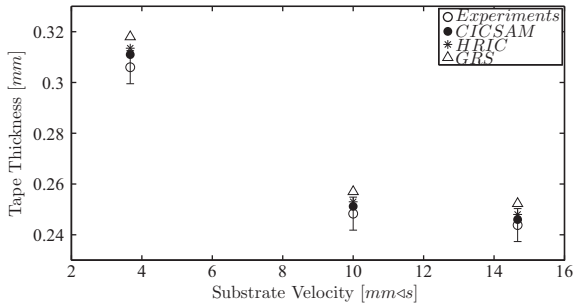

Fig. 11. Comparison of the numerical predictions and experiments for the effect of the substrate velocity on the tape thickness (doctor blade height is equal to 1000 μm).

found that the reduction in tape thickness decreases and it seems to become constant. The drag force is increased by increasing the substrate velocity and it becomes more dominant compared to the pressure force which results in more stretching of the slurry over the peeling belt. On the contrary, increasing the substrate velocity for a constant pressure force, the thickness of tape is decreased in the exit and vice versa. Moreover, it can be seen that the CICSAM method has the best prediction as compared to the other schemes. Moreover, a small difference can be detected between the two high resolution schemes, the CICSAM and the HRIC, which is due to the non-Newtonian behavior of the fluid. However, since the deviation from Newtonian behavior for the studied flow is small ($n = 0.90$), the difference between the aforementioned schemes is relatively limited, even when considering the GRS scheme. So, the only key factor that makes the CICSAM method more desirable for the tape casting process is the computational time, which is illustrated in Fig. 12.

6.3. Effect of slurry height

The effect of the material load (slurry height) in the reservoir (H_0) on the tape thickness is investigated with different interface capturing methods. Results of both numerical simulations and experiments are illustrated in Fig. 13. As the slurry height increases in the reservoir the hydrostatic pressure on the doctor blade region will be increased. Consequently, the tape thickness increases when it is conveyed out of the doctor blade region. The further increase in the numerical result

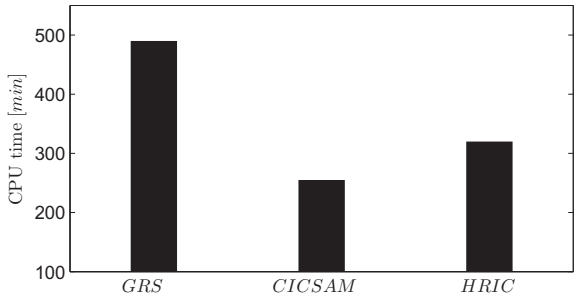

Fig. 12. CPU time comparison for different interface capturing method in the tape casting process.

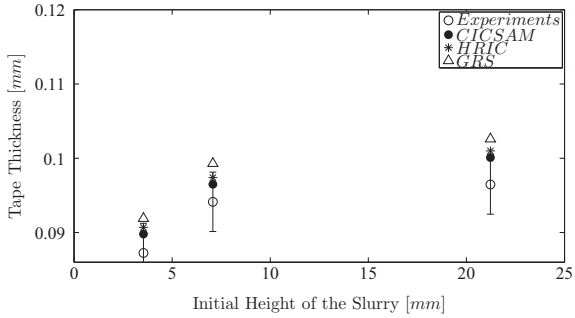

Fig. 13. Comparison of the numerical predictions and experiments for the effect of the slurry height on the tape thickness (the doctor blade height is equal to 400 μm).

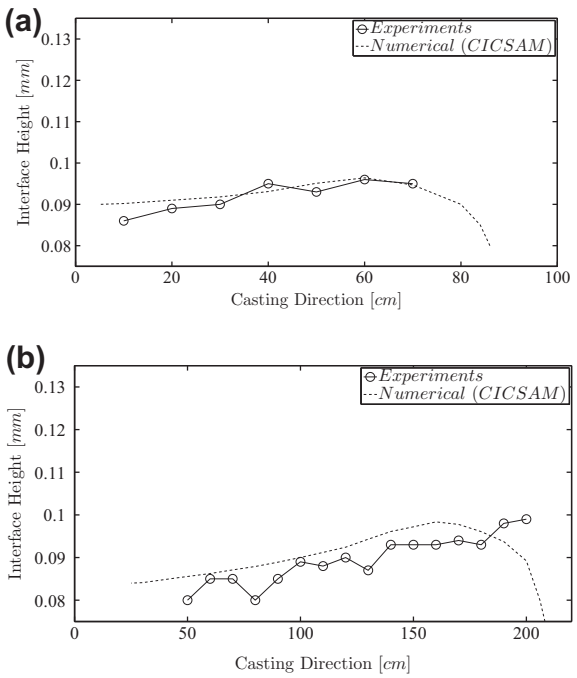

Fig. 14. Oscillations in the tape interface in the casting direction with the initial slurry height of (a) 7074 μm and (b) 21222 μm.

for H_0 = 21222 μm as compared to the experiment may be caused by the neglecting of the side effect flow which can decrease the final height of the tape especially for higher pressures. Again it is obvious that the CICSAM method has a somewhat better correlation with experimental data in comparison to the other methods. Based on the findings presented in Figs. 11–13, it was decided to use the CICSAM method for the final analysis in which a comparison with experiments was carried out. These experiments did show the non-constant tape height as well as the oscillation detected at the interface which arises from the decreasing slurry height in the reservoir over time. These variations in the tape thickness are recorded along the casting direction both experimentally and numerically (using the CICSAM scheme as mentioned before). Results of the measurements are shown in Fig. 14a and b for the slurry height of 7074 and 21222 μm, respectively.

Two types of information can be observed from Fig. 14. In the early stage of the process, the tape thickness is higher than that of the end due to the decrease in the slurry height in the reservoir over time. Moreover, this difference between the two ends of the strip gets higher as the initial slurry height is increased. On the other hand the more the height in the reservoir, the longer the strip which will be produced in the process.

As earlier mentioned, the increased level of material in the reservoir forces the ceramic to flow in the z-direction (and $-z$, side flow, see Fig. 8) which is neglected in the numerical modeling in both sides of the tape. Increasing the slurry height will therefore increase this side flow and decrease the tape thickness. However, increasing the slurry height will also increase the tape thickness due to the increased pressure. These two competing phenomena obviously work against each other, but the latter will be most predominant.

7. Conclusions

A multiphase flow model based on the volume of fluid (VOF) method was implemented in ANSYS FLUENT. Three different interpolation schemes, the Geometric Reconstruction Scheme (GRS), High Resolution Interface Capturing (HRIC) and Compressive Interface Capturing Scheme for Arbitrary Meshes (CICSAM), were investigated to find the optimum one for capturing of the free surface. The aforementioned methods were tested both for Newtonian and non-Newtonian fluids with two cases from literature regarding interface position as well as computational time. The results show that the CICSAM method has the best combination of accuracy of predicting the free surface and low cost of computation, especially for the non-Newtonian fluid. Moreover, the results of the validation show that in the fluids with Newtonian behavior, the high resolution interface capturing methods (both the CICSAM and the HRIC) give the same results. However, the higher deviation from a Newtonian fluid, the higher the difference between the two methods.

After testing the implemented model, numerical modeling of the non-Newtonian slurry of $La_{0.85}Sr_{0.15}MnO_3$ (LSM) was conducted by ANSYS FLUENT with the three different interpolation schemes, and the effects of substrate velocity and slurry height in the reservoir on the final tape thickness were evaluated. It was observed that the CICSAM method gave the closest

prediction to the experimental cases. Moreover, the results show that increasing the substrate velocity (casting speed) causes a decrease in the tape thickness due to the dominance of drag force over hydrostatic pressure. On the other hand, an increased value of the slurry height in the reservoir, results in increasing the final tape thickness. This is also the reason for the height of the tape in the end point of the strip being higher as compared to the beginning of the strip. Moreover, by increasing the material load (the initial height of the slurry in the reservoir) the aforementioned differences between the beginning and the end of strip and the length of the strip were increased.

Acknowledgment

The authors would like to acknowledge the support of the Scientific Research Councils on Technology and Production Sciences (FTP) (Contract No. 09-072888, OPTIMAC), which is part of the Danish Council for Independent Research (DFF).

References

[1] A. Kristoffersson, Elis Carlstrom, in: Tape casting of alumina in water with an acrylic latex binder, J. Eur. Ceram. Soc. 17 (1997) 289–297.
[2] A.J. Gurauskis, Sanchez-Herencia, C. Baudin, Al2o3/y-tzp and y-tzp materials fabricated by stacking layers obtained by aqueous tape casting, J. Eur. Ceram. Soc. 26 (2006) 1489–1496.
[3] Alfred I.Y. Tok, Freddy Y.C. Boey, K.A. Khor, Tape casting of high dielectric ceramic composite substrates for microelectronics application, J. Mater. Process. Technol. 89 (1999) 508–512. 90.
[4] Hyun Jun Kin, Matthe John M. Krane, Kevin P. Trumble, Keith J. Bowman, Analytical fluid flow models for tape casting, J. Am. Ceram. Soc. 89 (2006) 2769–2775.
[5] C. Pagnoux, T. Chartier, M. de F. Granja, F. Doreau, J.M. Ferreira, J.F. Baumard, Aqueous suspensions for tape-casting based on acrylic binders, J. Eur. Ceram. Soc. 18 (1998) 241–247.
[6] YE T. Chou, YA T. Ko, MAN F. Yan, Fluid flow model for ceramic tap casting, J. Am. Ceram. Soc. 70 (1987) 280–282.
[7] X.Y. Huang, C.Y. Liu, H.Q. Gong, A viscoplastic flow modeling of ceramic tape casting, Mater. Manufac. Proc. 12 (1997) 935–943.
[8] Sunil C. Joshi, Y.C. Lam, F.Y.C. Boey, A.I.Y. Tok, Power law fluids and bingham plastics flow models for ceramic tape casting, J. Mater. Process. Technol. 120 (2002) 215–225.
[9] G.G. Lipscomb, M.M. Denn, Flow of bingham fluids in complex geometries, J. Nonnewtonian Fluid Mech. 14 (1984) 337–346.
[10] Guillaume Vinay, Anthony Wachs, Jean-Francois Agassant, Numerical simulation of weakly compressible bingham flows: the restart of pipeline flows of waxy crude oils, J. Nonnewtonian Fluid Mech. 136 (2006) 93–105.
[11] P.G. Ciarlet, Handbook of Numerical Analysis, 16, Elsevier, 2011.
[12] C.R. Beverly, R.I. Tanner, Numerical analysis of three-dimensional bingham plastic flow, J. Nonnewtonian Fluid Mech. 42 (1992) 85–115.
[13] R.R. Huilgol, Z. You, Application of the augmented lagrangian method to steady pipe flows of bingham, casson and herschel-bulkley fluids, J. Nonnewtonian Fluid Mech. 128 (2005) 126–143.
[14] Alfred I.Y. Tok, Freddy Y.C. Boey, Y.C. Lam, Non-newtonian fluid flow model for ceramic tape casting, Mater. Sci. Eng. A 280 (2000) 282–288.
[15] T.G. Howell, D.R. Jeng, K.J. Dewitt, Momentum and heat transfer on a continuous moving surface in a power law fluid, Int. J. Heat. Mass. Transfer 40 (1996) 1853–1861.
[16] W. Kelly, B. Gigas, Using CFD to predict the behavior of power law fluids near axial-flow impellers operating in the transitional flow regime, Chem. Eng. Sci. 58 (2003) 2141–2152.
[17] M. Jabbari, R. Bulatova, J.H. Hattel, C.R.H. Bahl, Quasi-steady state power law model for flow of (La0.85Sr0.15)0.9MnO3 ceramic slurry in tape casting, Mater. Sci. Eng. 29 (2013) 1080–1087.
[18] Hao Tang, L.C. Wrobel, Z. Fan, Tracking of immiscible interfaces in multiple-material mixing processes, Comput. Mater. Sci. 29 (2004) 103–118.
[19] James M. Hyman, Numerical methods for tracking interfaces, Phys. 12D (1984) 396–407.
[20] A. Huerta, K.L.I.U. Wing, Viscous flow with large free surface motion, Comput. Methods Appl. Mech. Eng. 69 (1988) 277–324.
[21] Denis Gueyffier, Jie Li, Ali Nadim, Ruben Scardovelli, Stephane Zaleski, Volume-of-fluid interface tracking with smoothed surface stress methods for three-dimensional flows, J. Comput. Phys. 152 (1999) 423–456.
[22] J.P. Wang, A.G.L. Bortwick, R. Eatock Taylor, Finite-volume type vof method on dynamically adaptive quadtree grids, Int. J. Num. Methods Fluids 45 (2004) 485–508.
[23] James E. Pilliod Jr, Elbridge G. Puckett, Second-order accurate volume-of-fluid algorithms for tracking materials interfaces, J. Comput. Phys. 199 (2004) 465–502.
[24] E. Aulisa, S. Manservisi, R. Scardovelli, A surface marker algorithm coupled to an area-preserving marker redistribution method for three-dimensional interface tracking, J. Comput. Phys. 197 (2004) 555–584.
[25] R. Tavakoli, R. Babaei, N. Varahram, P. Davami, Numerical simulation of liquid/gas phase flow during mold filling, Comput. Methods Appl. Mech. Eng. 196 (2006) 697–713.
[26] S. Shin, I. Yoon, D. Juric, The local front reconstruction method for direct simulation of two- and three-dimensional multiphase flows, J. Comput. Phys. 230 (2011) 6605–6646.
[27] O. Ubbink, R.I. Issa, A method for capturing sharp fluid interfaces on arbitrary meshes, J. Comput. Phys. 153 (1999) 26–50.
[28] S. Muzaferija, M. Peric, Computation of free-surface flows using the finite-volume method and moving grids, Num. Heat Transfer B 32 (1997) 369–384.
[29] E.D. Dendy, N.T. Padial-Collins, W.B. VanderHeyden, A general purpose finite-volume advection scheme for continuous and discontinuous fields on unstructured grids, J. Comput. Phys. 180 (2002) 559–583.
[30] R. Panahi, E. Jahanbakhsh, M.S. Seif, Development of a vof-fractional step solver for floating body motion simulation, Appl. Ocean Res. 28 (2006) 171–181.
[31] P. Queutey, M. Visonneau, An interface capturing method for free-surface hydrodynamic flows, Comput. Fluid 36 (2007) 1481–1510.
[32] S. Haeri, S.H. Hashemabadi, Three dimensional CFD simulation and experimental study of power law fluid spreading on inclined plates, Int. J. Heat Mass Transfer 35 (2008) 1041–1047.
[33] C.W. Hirt, B.D. Nichols, Volume of fluid (VOF) method for the dynamics of free boundaries, J. Comput. Phys. 39 (1981) 201–225.
[34] T. Waclawczyk, T. Koronowicz, Comparison of CICSAM and HRIC high-resolution schemes for interface capturing, J. Theor. Appl. Mech. 46 (2008) 325–345.
[35] R.J.G. Lopez, R.M. Quinta-Ferreira, Volume-of-Fluid-based model for multiphase flow in high-pressure Trickle-Bed reactor: optimization of numerical parameters, AIChE J. 55 (2009) 2920–2933.
[36] S. Armfield, R. Street, The fractional-step method for the Navier-Stokes equations on staggered grids: the accuracy of three variations, J. Comput. Phys. 153 (1999) 660–665.
[37] M. Jabbari, J.H. Hattel, Numerical modeling of the side flow in tape casting of a non-newtonian fluid, J. Am. Ceram. Soc. 96 (2013) 1414–1420.

PAPER VII

Tesfaye Tadesse Molla, De Wei Ni, Regina Bulatova, Rasmus Bjørk, Christian Bahl, Nini Pryds, Henrik Lund Frandsen, “Finite Element Modeling of Camber Evolution during Sintering of Bi-layer structures”, *J. Am. Ceram. Soc.*, DOI: 10.1111/jace.13025.

.

J. Am. Ceram. Soc., 1–8 (2014)
DOI: 10.1111/jace.13025

journal

Finite Element Modeling of Camber Evolution During Sintering of Bilayer Structures

Tesfaye Tadesse Molla,† De Wei Ni, Regina Bulatova, Rasmus Bjørk, Christian Bahl, Nini Pryds, and Henrik Lund Frandsen

Department of Energy Conversion and Storage, Technical University of Denmark, Risø Campus, Frederiksborgvej 399, P.O. Box 49, Building 779, 4000 Roskilde, Denmark

The need for understanding the mechanisms and optimization of shape distortions during sintering of bilayers is necessary while producing structures with functionally graded architectures. A finite element model based on the continuum theory of sintering was developed to understand the camber developments during sintering of bilayers composed of $La_{0.85}Sr_{0.15}MnO_3$ and $Ce_{0.9}Gd_{0.1}O_{1.95}$ tapes. Free shrinkage kinetics of both tapes were used to estimate the parameters necessary for the finite element models. Systematic investigations of the factors affecting the kinetics of distortions such as gravity and friction as well as the initial geometric parameters of the bilayers were made using optical dilatometry experiments and the model. The developed models were able to capture the observed behaviors of the bilayers' distortions during sintering. Finally, we present the importance of understanding and hence making use of the effect of gravity and friction to minimize the shape distortions during sintering of bilayers.

I. Introduction

Ceramic structures with functionally graded multilayer architectures are generally considered as promising materials for various applications related to efficient energy technologies. Some of the application areas include solid oxide fuel cells, piezoelectric actuators, gas membranes etc.[1–4] Manufacturing of multilayered structures often includes co-sintering of laminated tapes prepared from different sets of powders. One of the problems often observed during sintering of bi-layer systems is distortion of the samples which often poses as a problem in the final assembly of the different components. For example, in the case of solid oxide fuel cells it is important to cofire the different layers with little or no shape distortion of the planar geometry to succeed with the intended assembly of the solid oxide fuel cell stacks.[4,5]

Distortion during sintering of bilayers occurs mainly due to mismatch in the shrinkage behaviors of the layers. The other factor affecting distortion in bilayers is the evolution of relative viscosity between the layers during the sintering cycle.[6,7] In an effort to reduce the distortions during sintering of bilayers, it is sometimes necessary to modify the intrinsic material behaviors of each tape. For example, though it requires cumbersome experimental works, tailoring the densification kinetics of each layer so as to minimize the mismatch in shrinkage strains could significantly reduce stress developments during cofiring. In addition to modifying the intrinsic material behaviors of the tapes, few authors have also suggested other techniques like applying external loads resisting the deformation[8] and optimization of the sintering temperature profile.[9]

However, camber evolution is also affected by geometrical parameters such as the ratio of layers' thickness and length of the sample.[6,10] Furthermore, additional factors like own weight of the sample (gravity) and friction (between the edges of the bilayer and the surface of the sample support while the bi-layer deforms) have often significant effect on the overall distortion of the sample.[3,5,11,12]

With regards to the effect of geometrical parameters, methodical studies describing the effect of the thickness ratio of layers on the camber evolution have been previously reported.[8,10] Olevsky *et al.* also discussed how the initial porosity of each layer making the bi-layer could also be used to optimize the camber evolution during cofiring.[10] On the other hand, Mücke *et al.* showed the effect of gravity on the evolution of camber by sintering bilayers in the horizontal and vertical orientations.[5]

For the basic understanding of the influence of materials intrinsic properties on the evolution of camber during sintering of bilayers, the continuum theory of sintering together with the use of beam theory have been applied and its use is widely reported.[2,13,14] In general, to model the sintering behavior of multilayers, the continuum theory of sintering with the assumption of linear response of the shrinkage rate to the applied load can be used.[2,3,13–16] Often free sintering of tapes is assumed to be isotropic but anisotropies due to nonuniform initial density distributions can also be introduced into the continuum model.[17]

Despite these works, there are still needs to create better understanding on how stress and distortions develop with respect to geometrical parameters and factors like gravity and also friction during cofiring in order to have better and refined process optimizations. This can be achieved by the use of numerical techniques, such as the finite element method.

The use of finite element method to describe stresses during the sintering process has so far focused mainly on the powder compaction process.[18–21] Numerical implementation of the continuum theory of sintering to describe shape distortions of cylindrical porous specimen under free sintering in the presence of gravitational forces is reported by Olevsky *et al.*[22] Schoenberg *et al.* modeled stresses during cofiring of bilayers consisting of layers with different initial densities.[23] In their study, Schoenberg *et al.* used temperature-dependent artificial coefficient of expansion (CTE) as an input to the finite element model to simulate the volumetric shrinkage strain in each layer. A good agreement between the stress predicted from the finite element model and analytical models is shown.[23] However, it is difficult to use the technique proposed by Schoenberg *et al.* to model stresses and distortions during isothermal sintering cycle as the artificial CTE is a function of the changing temperature in their iso-rate sintering experiment. Similarly, analysis of stresses during sintering of multilayered structures using the continuum the-

D. J. Green—contributing editor

Manuscript No. 34533. Received February 12, 2014; approved April 28, 2014.
†Author to whom correspondence should be addressed. e-mail: ttmo@dtu.dk

ory is reported by Brown *et al.*[24] Brown *et al.* was able to show the distortions during sintering of trilayered solar cells using experimental measurements of the free shrinkage of each layers to estimate the input parameters for the 3D finite element model.

In this study we have developed a finite element model in the commercial software, ABAQUS™, based on the continuum theory of sintering in order to be able to predict the curvature evolution during sintering of bilayered structures. To verify the model, different sintering experiments of bilayers composed of $La_{0.85}Sr_{0.15}MnO_3$ (LSM) and $Ce_{0.9}Gd_{0.1}O_{1.95}$ (CGO) tapes have been conducted. In addition, the influence of the geometric parameters of the bilayer, gravity, and friction on the evolutions of curvature have been studied both experimentally and numerically. For such purpose, systematic variation of the initial length of the samples and thickness ratio between the layers making the bilayer is made. Sintering experiments of similar bilayers with different orientations is also made to study the effect of gravity and friction on the evolution of curvature.

II. Experimental Procedures

$Ce_{0.9}Gd_{0.1}O_{1.95}$ (CGO, specific surface area: 5.2 m^2/g, Rhodia S.A., La Défense, France) and $La_{0.85}Sr_{0.15}MnO_3$ (LSM, d_{50}: 0.6 μm; specific surface area: 23.24 m^2/g, Haldor Topsoe A/S, Copenhagen, Denmark) were used as starting powders for the development of CGO and LSM tape cast layers by standard processing. Details of the tape casting processing can be found in Ni *et al.*[25,26] After drying, both the CGO and LSM green tapes had a uniform thickness of 220 and 110 μm respectively.

In this work, the conducted experiments involve measurements necessary for obtaining material input parameters for modeling (free shrinkage kinetics of the individual layers) as well as experiments necessary for validation of the model (sintering of bilayered laminates).

Individual CGO and LSM green tapes were rolled and pressed to obtain 'bulky' sample of the thin layers for dilatometry measurements. Final shapes of the samples were obtained by cutting the rolled tapes in cylindrical shapes of 3–5 mm in length and 2–3 mm in diameter.

The asymmetric CGO/LSM bilayered samples were assembled by colamination of the CGO and LSM green tapes both oriented along the tape-casting direction. Five different CGO/LSM bilayered samples with different thickness ratio and length were prepared by laminating different numbers of CGO and LSM green tapes. Final shapes of the laminated samples were obtained by stamping and punching rectangular shapes from the green material. Table I summarizes the initial size of five different CGO/LSM bilayered samples used in this work.

Measurements of shrinkage and curvature evolutions on all the samples were performed under the same heating profile in an optical dilatometer (TOMMI, Fraunhofer Institut Silicatforschung ISC, Neunerplatz 2, D-97082 Würzburg, Germany). This allows for the sample shape evolution during sintering to be followed *in situ* and noncontact, by simply collecting the sequential images (i.e., a video sequence) of the samples silhouettes projected by a source of visible light onto a high definition camera.

Table I. Initial Sizes of the Bilayered CGO/LSM Samples

Samples	Length l_0(mm)	Width b_0(mm)	Thickness ratio X(CGO:LSM)	Thickness of CGO h_{01}(μm)	Thickness of LSM h_{02}(μm)
1	25	5	2:1	220	110
2	25		6:1	660	
3	25		4:1	440	
4	15		4:1	440	
5	40		4:1	440	

The rolled tape samples were oriented in a way to allow measurement of the evolution of shrinkage of the samples in the length direction of the cylindrical samples. During the dilatometric measurements of bilayered samples, the CGO was placed on the bottom side of the asymmetric laminates. The bilayer samples were placed on a plane support (Alumina repton plates). The complete thermal cycle of the processing, including the de-binding step and sintering, was performed directly in the optical dilatometer to avoid moving the samples with possible mechanical failure after the de-binding step. The de-binding cycle includes a slow heating ramp at 0.33°C/min from room temperature to 400°C and an isothermal step at 400°C for 4 h aimed at removing the organic component from the samples. The sintering cycle was performed by an iso-rate heating ramp step up to 1250°C at a heating rate of 1°C/min, followed by an isothermal step at 1250°C for 4 h. The shrinkage (free sintering) and curvature evolution (bilayered CGO/LSM samples) were monitored *in situ* continuously during the heating and cooling cycles. Microstructures of cross-section were characterized using scanning electron microscopy (SEM, Supra, Carl Zeiss, Germany).

Figure 1 shows the dilatometric image from TOMMI depicting the sample geometry at the onset of the sintering cycle (i.e., after de-binding) for one of the bilayers built with an initial thickness ratio, X (CGO:LSM) = 4 and initial length of l_0 = 40 mm. Due to differential de-binding, significant deformations of the bilayer samples were observed after de-binding (600°C) or at the onset of the sintering cycle.

III. Model Development

The linear-viscous form of the continuum theory of sintering (SOVS) is used to define the inelastic (sintering related) strain rate in the porous body. According to SOVS, the total strain rate, $\dot{\boldsymbol{\varepsilon}}^{s}$, during sintering of a body is given by the sum of creep, $\dot{\boldsymbol{\varepsilon}}^{cr}$, and free sintering, $\dot{\boldsymbol{\varepsilon}}^{f}$,strain rates as:[14]

$$\dot{\boldsymbol{\varepsilon}}^{s} = \dot{\boldsymbol{\varepsilon}}^{cr} + \dot{\boldsymbol{\varepsilon}}^{f}$$

$$\dot{\boldsymbol{\varepsilon}}^{s} = \frac{\boldsymbol{\sigma}'}{2\eta_0\varphi} + \frac{\sigma_m - \sigma_s}{3(2\eta_0\psi)} I \tag{1}$$

where $\boldsymbol{\sigma}'$, σ_m, and σ_s are the deviatoric stress tensor, mean and sintering stresses, respectively. The mean stress is equivalent to the hydrostatic pressure, $\sigma_m = \frac{1}{3} tr(\boldsymbol{\sigma})$. During the implementation of SOVS, normalized parameters, φ and ψ, are used to relate the effective shear and bulk viscosities of the porous body to the viscosity of the fully dense body depending on the instantaneous amount of porosity, see Eq. (2).[14]

$$\varphi = (1-\theta)^2 \text{and } \psi = \frac{2}{3}\frac{(1-\theta)^3}{\theta} \tag{2}$$

In view of the continuum theory of sintering, the driving force for sintering or sintering stress is directly proportional

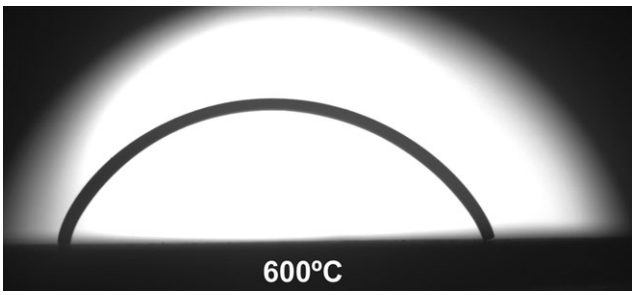

Fig. 1. Geometry of the sample at the onset of the sintering for bilayer with an initial length of 40 mm.

to the surface energy per unit area, α, of the porous surface and is given by:

$$\sigma_s = \frac{3}{2}\frac{\alpha}{G}(1-\theta)^2 \tag{3}$$

where θ and G are the instantaneous amount of porosity and grain size respectively. The viscosity of the fully dense body, η_0, varies with temperature,T, and is given by an Arrhenius form expression with an Arrhenius constant, A, and the effective or apparent activation energy for densification, E_a.[27] Here R is the universal gas constant.

$$\eta_0 = AT\exp(\frac{E_a}{RT}) \tag{4}$$

Sometimes the viscous parameters of the porous body are measured and reported in terms of the uniaxial viscosity, η_u, and viscous Poisson's ratio,ν_v, as:[10]

$$\eta_u = \frac{18\eta_0\psi\varphi}{6\psi+\varphi} \text{ and } \nu_v = \frac{3\psi-\varphi}{6\psi+\varphi} \tag{5}$$

The grain growth during the sintering process is a strong function of time, t, and the initial grain size, G_0, as given by:[28]

$$G^n = G_0^n + k_0\exp(\frac{-E_g}{RT})t \tag{6}$$

where k_0 and E_g are the grain growth pre-exponential factor and the activation energy for grain growth respectively. Here n is the grain growth exponent depending on the densification mechanism (e.g., $n = 3$ for volume diffusion).[28] In this work, the possible anisotropies in the pore-grain structure are not considered and hence the shrinkage rate in the free standing tape is assumed to be isotropic, which is formulated using Eqs. (2)–(4), see Eq. (7). For a detailed description of the continuum theory of sintering, please refer to Ref. [15].

$$\dot{\varepsilon}^f = -\frac{\sigma_s}{6\eta_0\psi} = -\frac{3}{8}\frac{\alpha}{AGT}\exp(\frac{-E_a}{RT})(\frac{\theta}{1-\theta}) \tag{7}$$

For the numerical implementation, the elastic part of the material response is assumed to be isotropic and characterized by Hooke's law as:

$$\dot{\boldsymbol{\sigma}} = \boldsymbol{C}\dot{\boldsymbol{\varepsilon}}^{el} \tag{8}$$

Here C is the elastic stiffness matrix and, $\dot{\varepsilon}^{el}$, is the elastic strain rate. The total strain rate, $\dot{\varepsilon}$, in the porous body can be given by:

$$\dot{\boldsymbol{\varepsilon}} = \dot{\boldsymbol{\varepsilon}}^{el} + \dot{\boldsymbol{\varepsilon}}^{s} \tag{9}$$

Combining Eqs. (1), (8), and (9), it is possible to get the constitutive relationship for the incremental stress during sintering as:

$$\dot{\boldsymbol{\sigma}} = \boldsymbol{C}\dot{\boldsymbol{\varepsilon}}^{el} = \boldsymbol{C}(\dot{\boldsymbol{\varepsilon}} - \dot{\boldsymbol{\varepsilon}}^{cr} - \dot{\varepsilon}^{f}\boldsymbol{I}) \tag{10}$$

The above model was used to simulate the sintering of bilayer systems made up of tapes with different initial density. This was made possible by implementing the linear-viscous form of the continuum theory of sintering (SOVS) in ABAQUS™ with the help of a user subroutine. The creep user subroutine provided by ABAQUS™ defines the total incremental inelastic strain, $d\boldsymbol{\varepsilon}$, as the sum of creep, $d\boldsymbol{\varepsilon}^{cr}$, and swelling, $d\boldsymbol{\varepsilon}^{sw}$, strains[40] which are obtained integrating Eq. (1) with time.

The evolving relative density or porosity in the structure can be updated using the principle of mass conservation. The inelastic volumetric strain is used to calculate the relative density as shown in Eq. (11) by using the initial relative density of the porous body, ρ_0.

$$\varepsilon^v = \varepsilon^{cr}\boldsymbol{I} + \varepsilon^{sw}$$

$$\rho_i = \rho_0\exp(-\varepsilon^v) \tag{11}$$

ABAQUS™ provides users with the ability to define solution-dependent state variables (SDVs) in the user subroutines. In this work, two SDVs have been employed to update the relative porosity and grain size in each layer. For example, the porosity in each tape is stored in one of the SDVs, such that it can be passed every time the subroutine is called, thereby updating the current value. At the end of the simulation, they can be used to analyze the model's behavior in time. The grain sizes and porosities in each layer are updated on every time step using the equations described above, see Eqs. (6) & (11).

Geometrically linear as well as nonlinear analysis can be performed using ABAQUS™ based on the strain measures defined as[41]:

$$\varepsilon = \begin{cases} \frac{L-L_0}{L_0}; & \text{Linear} \\ \ln\frac{L}{L_0}; & \text{Non-linear} \end{cases} \tag{12}$$

The effect of the evolving porosity on the mechanical properties of the tape i.e., on the elastic modulus, E, and Poisson's ratio,ν during densification is estimated by a composite sphere model suggested by Ramakrishnan and Arunachalam.[29] Here E_0 and ν_0 are the Young's modulus and Poison's ratio of the fully dense body.

$$E = E_0\frac{(1-\theta)^2}{(1+b_E\theta)} \text{ where } b_E = 2-3\nu_0$$

$$\nu = 0.25\frac{4\nu_0+3\theta-7\nu_0\theta}{1+2\theta-3\nu_0\theta} \tag{13}$$

Two dimensional plain strain formulations were used together with symmetry boundary conditions on half of the bilayer geometry. Quadratic elements with an average size of 50 μm have been chosen for meshing with visco analysis steps.

The distortion at the onset of the sintering, see Fig. 1, is taken into account as the initial geometric configuration of the bilayer model as shown in Fig. 2. The sintering temperature ramp is defined as a boundary condition on the entire geometry of the model. Figure 2 also shows examples of the directions of the gravity, F_g, and friction, F_f, forces acting on the bilayer bending towards the LSM layer. Note that the friction force is generated between edge and support of the sample in the furnace. The effect of gravity on the evolution of the distortions is considered by applying a body force obtained by using the theoretical density of each tape.

IV. Results and Discussions

(1) Obtaining Material Parameters

The parameters defining the viscosity of both CGO and LSM tapes, A and E_a, were estimated by fitting the free shrinkage strain model in Eq. (7) to experimental measure-

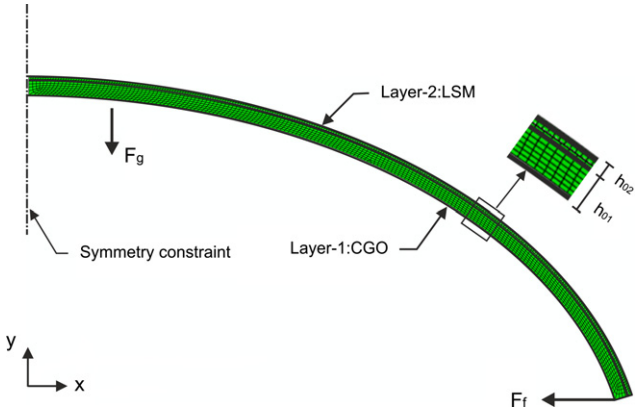

Fig. 2. The initial geometric configuration of the bilayer sample with an initial length of $l_0 = 40$ mm and initial thickness ratio of $X = \frac{h_{01}}{h_{02}} = 4$ with the finite element meshes.

ments of free sintering. The approach used here has been explained in detail in previous work by Molla *et al.*[12] and Reiterer *et al.*[27]

Based on the optimization procedure, Fig. 3(a) shows the comparison between the free shrinkage strains in each tape during the entire sintering cycle. About 11% and 26% of shrinkage was observed in CGO and LSM tapes respectively. The free shrinkage strain model is also shown to agree well with the experimental observations of shrinkage strains.

The evolution of the viscosity as a function of temperature is the other important parameter for modeling the distortions in the bilayer system. Figure 3(b) shows the fully dense viscosities of both CGO and LSM tapes during the iso-rate sintering cycle, which is calculated as per Eq. (4). The effect of porosity on the viscosity of the porous body is included based on the evolution of porosity during the sintering of the bilayer. The fully dense body viscosity results are consistent with previous observations of same materials reported in.[12]

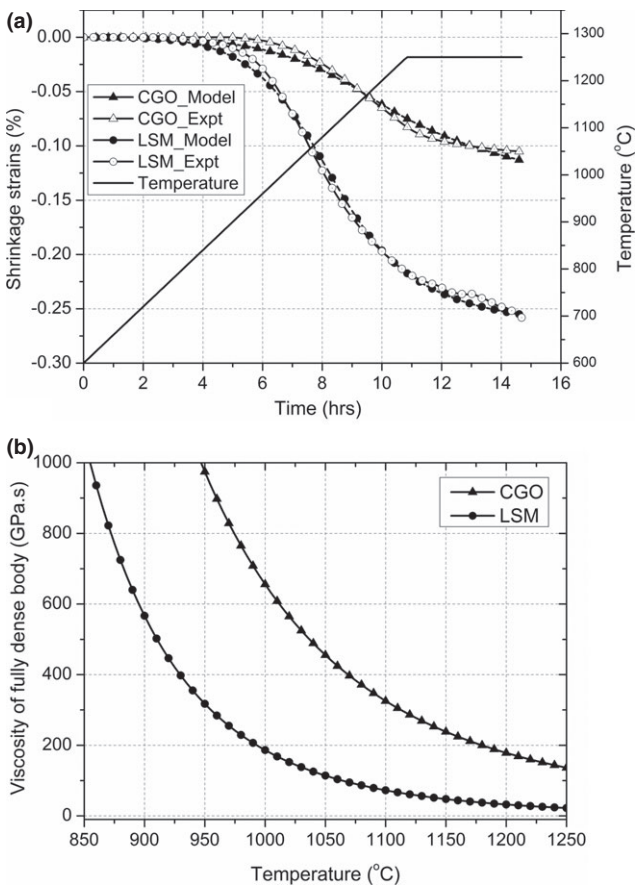

Fig. 3. (a) Comparison of model and experiments for free shrinkage strains and (b) The evolution of fully dense body viscosity as a function of temperature.

All the other parameters required to model densifications and distortions during the cofiring of CGO and LSM tapes are obtained from experimental measurements and are summarized in Table II. Note here that the impact of the grain growth on the viscosity of the fully dense tapes is not considered explicitly as shown by Eq. (4). But those effects can be included in the Arrhenius constant, A and the effective or apparent activation energy, E_a, as these, are made to be free parameters, while fitting the shrinkage strain model to the experimental measurements. This approach is explained in detail in previous works by Molla *et al.* [12] as well as Reiterer *et al.*[27]

The change in the elastic properties of both tapes as a function of the evolving porosity during the sintering process was considered using Eq. (13). Fan *et al.* and Atkinson *et al.* studied the elastic properties of CGO10 as a function of porosity where the fully dense CGO is reported to have a Young's modulus, $E_0 = 200$GPa at 800°C.[31,32] Similarly Giraud *et al.* studied the elastic properties of LSM tapes with different porosities in which he reported the Young's modulus of dense LSM at room temperature to be, $E_0 = 110$GPa and shown to change little with temperature between 350°C and 950°C.[33] In fact, the variation of the Young's modulus with temperature is not critically important as the elastic response from the porous bodies during sintering is very small. In this study, the Poisson's ratio for the dense bodies, ν_0, of both tapes is assumed to be 0.328.[32]

(2) Effect of Gravity and Geometric Nonlinearity

Figure 4 (left) shows the dilatometric images for the evolution of curvature at different temperatures for one of the bilayers built with an initial thickness ratio, X(CGO:LSM) = 4 and initial length $l_o = 40$ mm. The corresponding results from the finite element model are also shown in Fig. 4 (right). The model is shown to agree well with the experimental observations in terms of shape evolutions during the sintering cycle. Example of the 2D contour plot showing principal stresses in the xx direction (S11) at 1180°C is also shown where the CGO layer is under compressive stress due to the fast shrinking LSM layer.

Table II. The Parameters used in the Modeling for LSM and CGO Layers

Parameter	LSM	CGO	Source
Initial porosity, θ_0 (%)	0.58	0.38	Measurement
Initial grain size, G_0 (μm)	0.45	0.13	Measurement
Final grain size, G (μm)	1.34	0.2	Measurement
Surface energy, α (J/m^2)	2.5	1	[11,42]
Activation energy for grain growth, E_g (kJ/mol.K)	420	480	[25,30]
Grain growth coefficient, k_0	1.11 e^{-8}	4.39 e^{-9}	Fitting
Arrhenius constant, A (GPa.s/K)	121	1202	Fitting
Apparent activation energy, E_a (kJ/mol.K)	148	138	Fitting

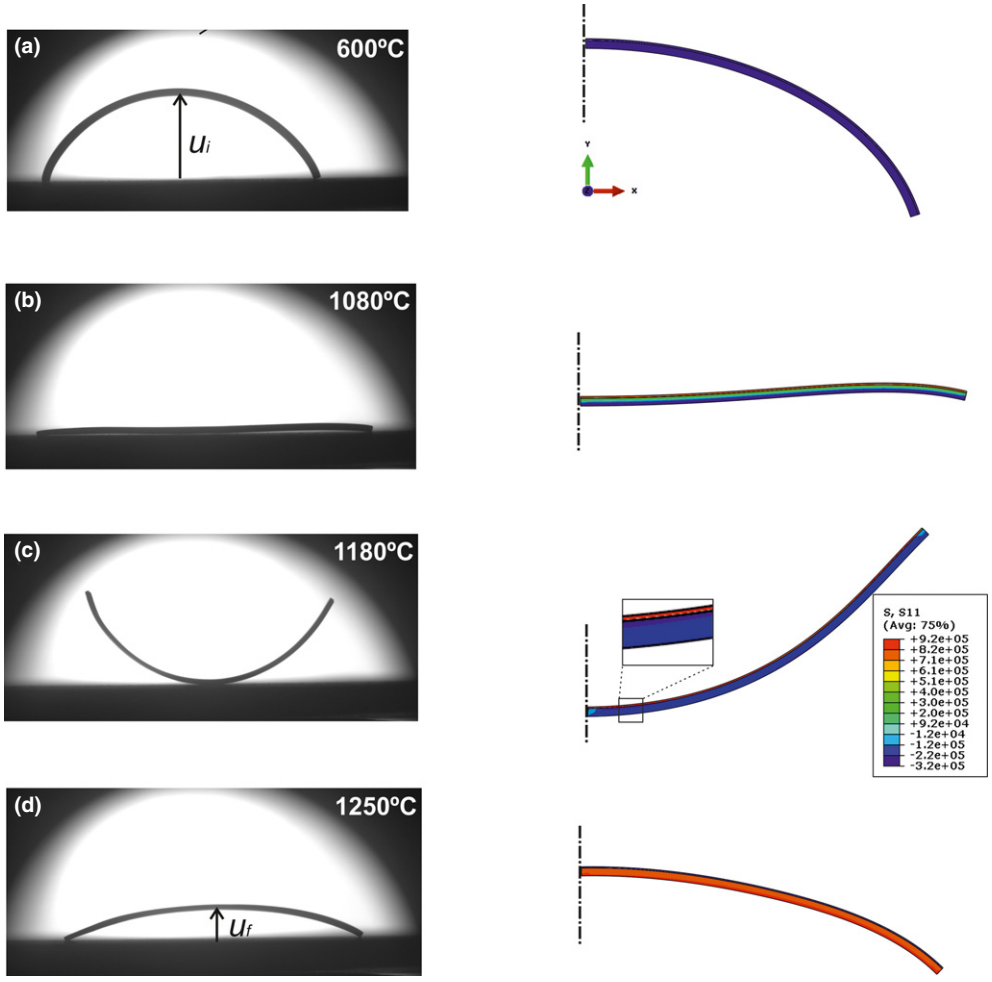

Fig. 4. Experimental (left) and finite element model results (right) showing the evolution of distortion during the sintering cycle.

To study the effect of gravity and geometric nonlinearity, the evolution of curvature during cofiring of CGO and LSM tapes is analyzed with different models. Two models based on linear-viscous theory as reported by Cai *et al.*,[6] which does not consider gravity, and Frandsen *et al.*,[11] which considers gravity, are compared with two finite element models based on geometrically linear and nonlinear analysis.

Comparison of model predictions for curvature including the experimental measurements in a bilayer with an initial length of $l_o = 40$ mm and thickness ratio $X = \frac{h_{01}}{h_{02}} = 4$ is shown in Fig. 5. Note that in this work, curvature development towards the bottom layer i.e., the CGO layer is taken as positive and vice versa.

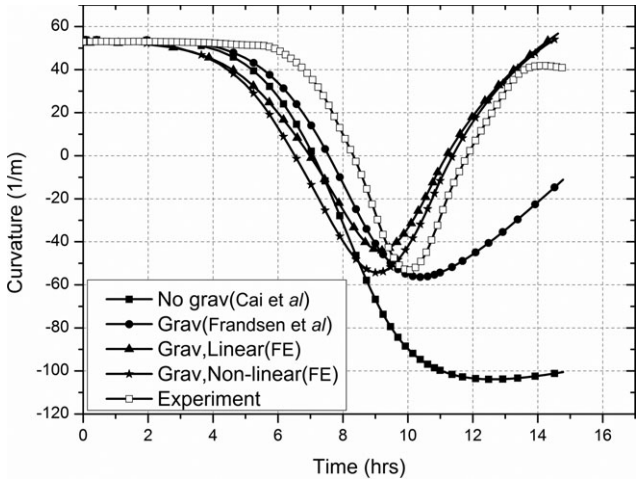

Fig. 5. Comparison of different model predictions for curvature evolution over time with the experimental measurements.

The experimental results show almost no curvature development for the first 5.5 h, which is due to the small shrinkage rate difference between the two layers. After this period of time the LSM (top) layer shrinks faster than the CGO layer. This is followed by development of stress in the bilayer sample and hence led to camber of the sample. After $t \approx 10$ h, the curvature changes in the bilayer sample starts to slowdown because of the combined effects of slower shrinkage activity in the LSM layer, gravity, and stress relaxation in the constraining CGO layer.

All the models considered predict a similar trend in camber growth for the first 9 h of the sintering. The model by Cai *et al.* predicts a further growth in curvature in the later stages of the sintering, while the other model by Frandsen *et al.* show reductions in the curvature after $t \approx 10$ h. The finite element models also show reductions in the curvature as observed in the experiment. Similarly almost all the models predict an early start in curvature evolution, when compared to the experiment, which may be caused by stress relaxations in the bilayer during the experiment. From the comparisons shown in Fig. 5, it is clear to see the significant effects of gravity on the evolution of curvature and it is obvious that including gravity capture the real physics of the camber development. It is also shown that the results from the linear-viscous model, which accounts for gravity (the model by Frandsen *et al.*) differs from the finite element models. This could be due to the absence of elasticity and/or the simplifications made by Frandsen *et al.* in the analytical

implementations of the effect of gravity in to the linear-viscous model.[11]

During the experiments, a significant amount of distortion after de-binding in the bilayer samples was observed. It is therefore important to model stresses and shape distortions because of differential de-binding of the layers during sintering of bilayer. In the finite element model, considering the initial deformed geometry of the sample at the onset of the sintering process is also important to properly include the effect of gravity. For example, in the beginning, the gravity force actually supports the evolution of curvature until the sample become flat (before bending to the LSM layer). The finite element model based on geometrically nonlinear analysis is also shown to predict the magnitude of the curvature better than the model based on geometrically linear analysis. Some discrepancy between the most advanced nonlinear model and the experiment are still present, though. Table III shows the convergence behavior of the FE model as a function of the total number of elements for bilayer sample with an initial length $l_0 = 15$ mm and thickness ratio $X = 4$.

(3) Effect of Initial Length and Thickness Ratio

Different finite element models based on geometrically nonlinear analysis have been developed to simulate the curvature evolutions for samples with different initial length and thickness ratio. As explained above, the respective initial deformations at the onset the sintering for all the samples are considered while building the bi-layer models.

Figure 6 shows the curvature measurements of three different bilayers of CGO/LSM tapes with the same initial thickness ratio of $X = \frac{h_{01}}{h_{02}} = 4$ but different initial length $l_o = 15$, 25, and 40 mm. For the sake of comparison, the initial curvature of all the samples is adjusted to zero. If there was no effect of gravity on the development of the distortions, all the three bilayer systems should have shown the same evolutions of curvatures. This is because the internal stresses balance over the thickness of the layers which makes the curvature to be affected only by the thicknesses in addition to the material properties.[9–11] However, it is observed that the curvature varies depending on the length of the samples where less curvature is shown as the length of the sample increases because of gravity.

Table III. Mesh Convergence Behavior of the Finite Element Model (for Bilayer Sample with an Initial Length of 15 mm and Thickness Ratio of 4)

Total number of elements	Maximum curvature (1 m^{-1})
200	93.62
250	100.21
390	112.43
940	136.84
1275	139.22
1850	140.01
2861	140.12

Figure 6 also shows the model predictions for curvatures of bilayers simulated for the three different samples described above. The variation of curvature with the length of the samples is also verified by the finite element models. The influence of gravity is pronounced when the length of the bilayer increases due to longer arm span of the distorted sample, which increases the effect of gravitational weight opposing the development of the distortion.

Similarly, three separate experiments and simulations have been made for bilayer geometries consisting of the same initial length $l_o = 25$ mm but different thickness ratios of $X = \frac{h_{01}}{h_{02}} = 2, 4,$ and 6. The simulations were used to study the effect of the initial thickness ratio of the layers on the curvature evolution, Fig. 7.

It is observed that for a bilayer having a thickness ratio of $X = 2$, the distortion is very large and it reduces with increasing thickness ratio. The trend shown in the experiments has also been verified by the finite element models built with different thickness ratios as shown also in Fig. 7. For the sake of comparison, the initial curvatures of all the samples have been adjusted to zero.

Although the model accounts for most of the known effects including geometric nonlinearity, some discrepancies between the model predictions and experimental measurements in all the bilayers are observed, see Figs. 6 and 7. These might be due to stress relaxation that results from some observed microcrack growth close to the interface of the bilayer after de-binding and/or during the sintering cycle. Microcracks close to the interface between the CGO and LSM layer and also around the surface of the CGO layer has been observed by SEM images taken from the bilayer samples at the end of the sintering cycle, see Fig. 8.

Development of microcracks especially in the constraining layer can reduce the stress development in the bilayer resulting in small curvature development. A similar observation is reported by Ollagnier *et al.*[3] The effect of micro-cracks is more pronounced when there is a very large stress as in the case of bilayer with initial thickness ratio $X = 2$, as seen on

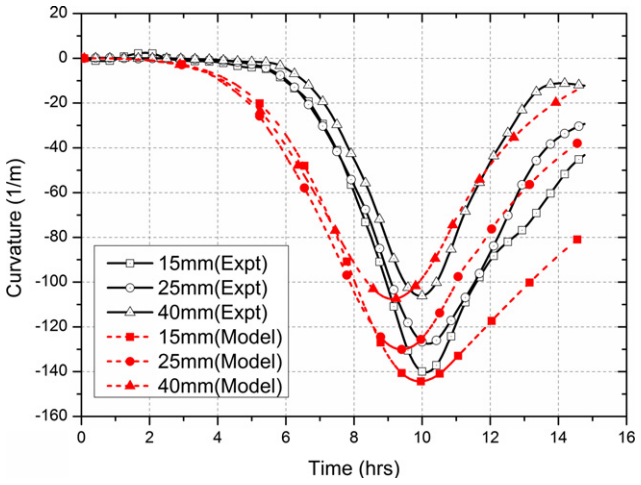

Fig. 6. Comparison of curvature evolutions for three bilayers with different initial lengths (solid lines) together with the corresponding model predictions (dashed lines).

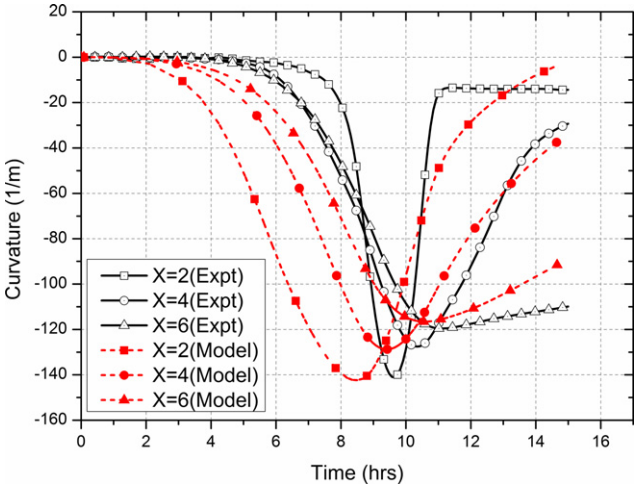

Fig. 7. Comparison of curvature evolutions for three bilayers with different initial thickness ratios (solid lines) together with the corresponding model predictions (dashed lines).

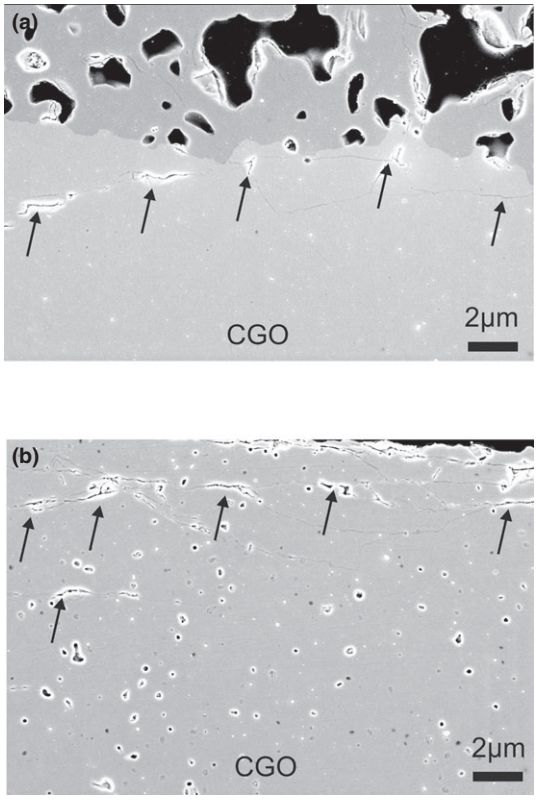

Fig. 8. Microcracks observed in the bilayers at the end of the sintering cycle (a) micro-cracks at the interface of the layers and (b) micro-cracks at the surface of the CGO layer.

Fig. 7 showing larger discrepancy between the model and experiments compared to the others. Other effects such as anisotropies in the pore-grain structure, which has not been considered in this work, could also explain the discrepancies between the models and experiments. Continuum theory of sintering, in its current state, is not able to account for these losses of continuity. The continuum theory of sintering could be combined with damage models [34] or meso-scale models[35–37] in order to describe the development of these micro-cracks and the consequent reduction of stresses. It is beyond the scope of this work to pursue such enrichments of the continuum theory of sintering.

In addition to the micro-cracks in the bilayer samples, the simplified constitutive models used in this study, for example, to describe sintering stress and creep properties could be the other factors for the discrepancy between the model and the experiments. For instance, the limitations of linear-viscous models, originally developed for bodies that sinter by viscous flow, are discussed by Garino *et al.*[38] Furthermore, the effective sintering viscosity could be described by more rigorous models which can account for additional parameters, e.g., grain size, as described by Argüello *et al.*[39] with more experimental works. Summary of the different models for sintering viscosity can also be found in Ref. [14].

As an example of how the change in the final curvature as a function of the initial thickness ratio of the layers after 8 h of sintering has also been shown in Fig. 9. The change in curvature is drastic for the range in the thickness ratio of $0 < X < 2$. By increasing the thickness of the slowly shrinking layer, in this case the CGO layer, it is possible to significantly reduce the curvature at the end of the sintering cycle.

(4) Effect of Friction

Finally the effect of friction between the edges of the sample and the surface of the sintering furnace has also been investigated. Two bilayers with the same initial length and thickness

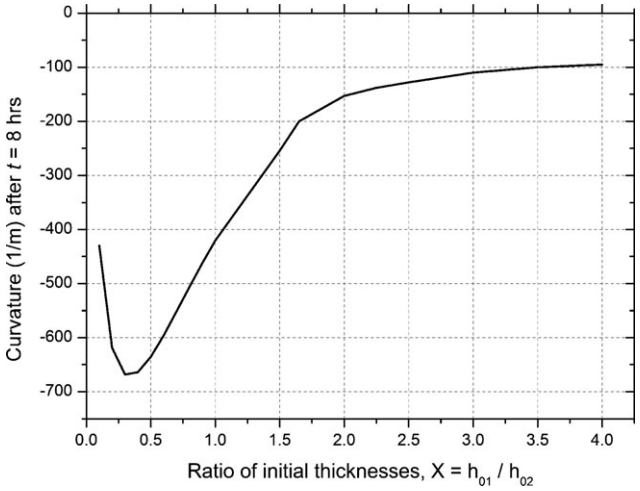

Fig. 9. Variation of final curvatures after sintering for 8 h as a function of initial thickness ratio.

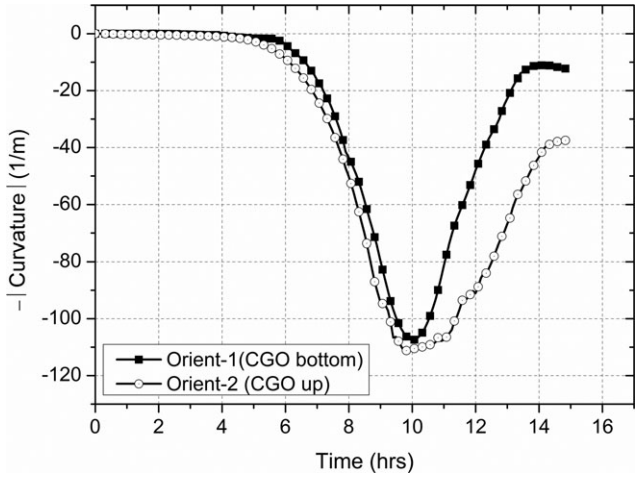

Fig. 10. Curvature evolution of the same bilayer samples in different orientations showing the effect of friction.

ratio of CGO and LSM tapes were cofired in different orientations. In the first orientation, the bilayer sample is cofired, where it is placed in such a way that the CGO layer is on the bottom side. The opposite is made in the second orientation i.e., the bilayer sample is placed in a way that the CGO layer is on the top side of the bilayer. Figure 10 shows the curvature evolutions measured during the sintering cycle. In the second orientation where the curvature is growing towards the LSM tape, in contact with the support surface, it is shown that the distortion is retarded compared to the first orientation. This is clearly due to the friction between the sample edges and the surface of the sample support hindering the kinetics of distortion. Furthermore the bumpy kinetics of distortion (curvature plot) in the second orientation clearly indicates the effect of friction. Note here that the curvature of the bilayer in the first orientation is opposite to the second one. The curvatures are plotted with opposite signs and normalized to zero at the start of the sintering for the sake of comparison.

V. Conclusions

A finite element model based on the continuum theory of sintering were developed to justify the distortions during sintering experiments of bilayers composed of LSM and CGO tapes. Free shrinkage kinetics of both tapes were used to estimate the input parameters necessary for finite element

models. Systematic studies on the effect of factors like gravity and friction together with the initial geometries on the kinetics of distortions of bilayers during sintering is presented. The finite element model simulations were able to capture the observed behaviors of distortions during different sets of experiments involving different bilayers. Some discrepancies are still observed, and it was speculated that these were due to stress relaxation near the interfaces of the bilayers due to micro-crack growth. Understanding the effect of factors like gravity and friction during sintering of bilayered porous structures could be helpful to reduce the shape distortion problems usually observed during cofiring.

Acknowledgment

The authors would like to acknowledge the support of the Danish Council for Independent Research Technology and Production Sciences (FTP) which is part of The Danish Agency for Science, Technology and Innovation (FI) (Project # 09-072888).

References

[1]J. Chang, O. Guillon, J. Rödel, and S. Kang, "Characterization of Warpage Behavior of Gd-Doped Ceria/Nio-Yttria Stabilized Zirconia bi-Layer Smaples for Solid Oxide Fuel Cell Applications," *J. Power Sources*, **185**, 759–67 (2008).

[2]J. Kanters, U. Eisele, and J. Rödel, "Cosintering Simulation and Experimentation: Case Study of Nanocrystalline Zirconia", *J. Am. Ceram. Soc.*, **84**, 2757–63 (2001).

[3]J. Ollagnier, O. Guillon, and J. Rödel, "Constrained Sintering of a Glass Ceramic Composite: I. Asymmetric Laminates", *J. Am. Ceram. Soc.*, **93**, 74–81 (2010).

[4]M. Cologna, V. Sglavo, and M. Bertoldi, "Sintering and Deformation of Solid Oxide Fuel Cells Produced by Sequential Tape Casting", *Int. J. Ceram. Technol.*, **7**[6] 803–13 (2010).

[5]R. Mücke, N. Menzler, H. Buchkremer, and D. Stöver, "Cofiring of Thin Zirconia Films During SOFC Manufacturing", *J. Am. Ceram. Soc.*, **92** [1] S95–102 (2009).

[6]P. Cai, D. Green, and G. Messing, "Constrained Densification of Alumina/Zirconia Hybrid Laminates, I: Experimental Observations of Processing Defects", *J. Am. Ceram. Soc.*, **80** [8] 1929–39 (1997).

[7]P. Cai, D. Green, and G. Messing, "Constrained Densification of Alumina/Zirconia Hybrid Laminates, II: Viscoelastic Stress Computation", *J. Am. Ceram. Soc.*, **80** [8] 1940–8 (1997).

[8]S. Lee, G. Messing, and D. Green, "Warpage Evolution of Screen Printed Multilayer Ceramics During co-Firing", *Key Eng. Mater.*, **264-268**, 321–8 (2004).

[9]A. Kaiser, A. Prasad, S. Foghmoes, S. Ramousse, N. Bonanos, and V. Esposito, "Sintering Process Optimization for Multi-Layer CGO Membranes by in Situ Techniques", *J. Eur. Ceram. Soc.*, **33**, 549–55 (2013).

[10]E. Olevsky, T. Molla, H. Frandsen, R. Bjørk, V. Esposito, D. Ni, A. Ilyina, and N. Pryds, "Sintering of Multilayered Porous Structures: Part I-Constitutive Models", *J. Am. Ceram. Soc.*, **96**[8], 2657–65 (2013).

[11]H. Frandsen, E. Olevsky, T. Molla, V. Esposito, R. Bjørk, and N. Pryds, "Modeling Sintering of Multilayers Under Influence of Gravity," *J. Am. Ceram. Soc.*, **96** [1] 80–9 (2013).

[12]T. Molla, H. Frandsen, R. Bjørk, D. Ni, E. Olevsky, and N. Pryds, "Modeling Kinetics of Distortion in Porous bi-Layered Structures," *J. Eur. Ceram. Soc.*, **33** [7] 1297–305 (2013).

[13]R. Bordia and G. Scherer, "On Constrained Sintering –I: Constitutive Model for Sintering Body," *Acta Mater.*, **36** [9] 2393-7 (1988).

[14]R. Bordia and G. Scherer, "On Constrained Sintering –II: Comparison of Constitutive Models," *Acta Mater.*, **36** [9] 2399–409 (1988).

[15]E. Olevsky, "Theory of Sintering: From Discrete to Continuum, "*Mater. Sci. Eng. R.: Reports*, **23**, 41–100 (1998).

[16]D. Green, O. Guillon, and J. Rödel, "Constrained Sintering: A Delicate Balance of Scales," *J. Eur. Ceram. Soc.*, **28**, 1451–66 (2008).

[17]S. Kiani, J. Pan, J. Yeomans, M. Barriere, and P. Blanchart, "Finite Element Analysis of Sintering Deformation Using Densification Data Instead of a Constitutive law," *J. Eur. Ceram. Soc.*, **27**, 2377–83 (2007).

[18]M. Gasik and B. Zhang, "A Constitutive Model and FE Simulation for Sintering Process of Powder Compacts," *Comp. Mater. Sci.*, **18**, 93–101 (2000).

[19]H. Zipse, "Finite Element Simulation of die Pressing and Sintering of Ceramic Components," *J. Eur. Ceram. Soc.*, **17**[14] 1707–13 (1997).

[20]M. Jeong, J. Yoo, S. Rhim, S. Lee, and S. Oh, "A Unified Model for Compaction and Sintering Behavior of Powder Processing," *Finite Elem. Anal. Des.*, 2012; **53**, 56–62.

[21]T. Kraft and H. Riedel, "Numerical Simulation of Solid State Sintering; Model and Application," *J. Eur. Ceram. Soc.*, **24**, 345–61 (2004).

[22]E. Olevsky, R. German, and A. Upadhyaya, "Effect of Gravity on Dimensional Change During Sintering-II: Shape Distortion," *Acta Mater.*, **48**, 1167–80 (2000).

[23]S. Schoenberg, D. Green, A. Segall, G. Messing, A. Grader, and P. Halleck, "Stress and Distortion due to Green Density Gradients During Densification," *J. Am. Ceram. Soc.*, **89** [10] 3027–33 (2006).

[24]G. Brown, R. Levine, A. Shaikh, and E. Olevsky, "Three Dimensional Solar Cell Finite Element Sintering Simulation," *J. Am. Ceram. Soc.*, **92** [7] 1450–5 (2009).

[25]D. Ni, C. Schmidt, F. Teocoli, A. Kaiser, K. Andersen, S. Ramousse, and V. Esposito, "Densification and Grain Growth During Sintering of Porous $Ce_{0.9}Gd_{0.1}O_{1.95}$ Tape Cast Layers: A Comprehensive Study on Heuristic Methods," *J. Eur. Ceram. Soc.*, **33**, 2529–37 (2013).

[26]D. Ni, V. Esposito, C. Schmidt, T. Molla, K. Andersen, A. Kaiser, S. Ramousse, and N. Pryds, "Camber Evolution and Stress Development of Porous Ceramic Bilayers During co-Firing," *J. Am. Ceram. Soc.*, **96**, 972–8 (2013).

[27]M. Reiterer, K. Ewsuk, and J. Arguello, "An Arrhenius-Type Viscosity Function to Model Sintering Using the Skorohod–Olevsky Viscous Sintering Model Within a Finite-Element Code," *J. Am. Ceram. Soc.*, **89**, 1930–5 (2006).

[28]F. Raether and P. Horn, "Investigation of Sintering Mechanisms of Alumina Using Kinetic Field and Master Sintering Diagrams," *J. Eur. Ceram. Soc.*, **29**, 2225–34 (2009).

[29]N. Ramakrishnan and V. Arunachalam, "Effective Elastic-Moduli of Porous Solids," *J. Mater. Sci.*, **25** [9] 3930–7 (1990).

[30]B. McCarthy, L. Pederson, R. Williford, and X. Zhou, "Low-Temperature Densification of Lanthanum Strontium Manganite ($La_{1-x}Sr_xMnO3$), x = 0.0-0.2," *J. Am. Ceram. Soc.*, **92** [8] 1672–8 (2009).

[31]X. Fan, E. Casen, Q. Yang, and J. Nicholas, "Room Temperature Elastic Properties of Gadolinia- Doped Ceria as a Function of Porosity," *Ceram. Int.*, **39**, 6877–86 (2013).

[32]A. Atkinson and A. Selcuk, "Mechnaical Behavior of Ceramc Oxygen ion-Conducting Membranes," *Solid State Ionics*, **134**, 59–66 (2000).

[33]S. Giraud and J. Canel, "Young's Modulus of Some SOFC Materials as a Function of Temperature," *J. Eur. Ceram. Soc.*, **28**, 77–83 (2008).

[34]G. Bruno, A. Efremov, A. Levandovskiy, I. Pozdnyakova, D. Hughes, and B. Clausen, "Thermal and Mechanical Response of Industrial Porous Ceramics," *Mater. Sci. Forum*, **652**, 191–6 (2010).

[35]T. Molla, R. Bjørk, E. Olevsky, N. Pryds, and H. Frandsen, "Multi-Scale Modeling of Shape Distortions During Sintering of bi-Laers," *J. Comp. Mat. Sci.*, **88**, 28–36 (2014).

[36]C. Martin and R. Bordia, "The Effect of a Substrate on the Sintering of Constrained Films," *Acta Mater.*, **57**, 549–58 (2009).

[37]T. Rasp, C. Jamin, A. Wonisch, T. Kraft, and O. Guillon, "Shape Distortion and Delamination During Constrained Sintering of Ceramic Stripes: Discrete Element Simulations and Experiments," *J. Am. Ceram. Soc.*, **95**[2] 586–92 (2012).

[38]T. Garino and H. Bowen, "Kinetics of Constrained-Film Sintering," *J. Am. Ceram. Soc.*, **73**[2] 251–7 (1990).

[39]J. Argüello, M. Reiterer, and K. Ewsuk, "Verification, Performance, Validation and Modifications to the SOVS Continuum Constitutive Model in a Nonlinear Large Deformation Finite Element Code," *J. Am. Ceram. Soc.*, **92** [7] 1442–9 (2009).

[40]Abaqus 6.11 User Subroutine Reference Manual, Providence RI, ©Dassault Systemes, 2011.

[41]Abaqus 6.11 Analysis User's Manual, Providence RI, ©Dassault Systemes, 2011.

[42]R. M. *Sintering of Ceramics*. 1st ed. CRC Press, Taylor & Francis Group, Boca Raton, Florida, 2008. □

PAPER VIII

M. Jabbari, R. Bulatova, J. H. Hattel, and C. R. H. Bahl, “On the Modelling of Tape Casting: A Review of Current Methods and New Trends” (to be submitted).

.

On the Modelling of Tape Casting: A Review of Current Methods and New Trends

Masoud Jabbari[1, a] , Jesper Hattel [a], Regina Bulatova [b], Christian Bahl [b]

a- Department of Mechanical Engineering, Technical University of Denmark, Nils Koppels Allé, 2800 Kgs. Lyngby, Denmark.

b- Department of Energy Conversion and Storage, Technical University of Denmark, Frederiksborgvej 399, building 779, Roskilde, Denmark.

Abstract

Since its onset, tape casting has been used to produce thin layers of ceramics that can be used as single layers or can be stacked and laminated into multilayered structures. Today, tape casting is the basic fabrication process that provides multilayered capacitors and multilayered ceramic packages. In addition, many startup products such as multilayered inductors, multilayered varistors, piezoelectrics, ceramic fuel cells and lithium ion battery components are dependent upon tape casting technology. One of the growing sciences in the processing of ceramics by tape casting is the use of fluid flow analysis to control and enhance the final tapes. The fluid dynamics analysis of the ceramic slurries during tape casting is an efficient mean to elucidate the physical parameters crucial to the process. A review of the development of the tape casting process with particular focus on modelling the material flow is presented and in this context the current status is examined and future potential discussed.

Keywords: tape casting, fluid flow, rheology, non-Newtonian, modelling

Contents

Nomenclature

English Letters

A	Area (m^2)	l	Reservoir tapered length (mm)
A_0	Integral constant	n	Power law constant
A_1	Integral constant	p	Pressure (Pa)
A_2	Integral constant	T	Stress tensor
d	Reservoir length (mm)	t	Time (s)
F	Force ($Pa \cdot m^2$)	u	Velocity (mm/s)
g	Gravity acceleration (m/s^2)	v_0	Substrate velocity (mm/s)
H_0	Initial slurry height (mm)	v_c	Critical velocity (mm/s)
h	Doctor blade height (mm)	W	Doctor blade width (mm)
k	Consistency of fluid ($Pa \cdot s^n$)		

Greek Letters

α	Side flow factor	ρ	Density (kg/m^3)
$\dot{\gamma}$	Shear rate (s^{-1})	τ	Shear stress (Pa)
δ	Tape thickness (μm)	τ_0	Yield stress (Pa)
θ	reservoir tapered angle (deg)	τ_0^B	Bingham yield (Pa)
λ	Time constant (s)	τ_0^H	Herschel-Bulkley yield (Pa)
μ	Dynamic viscosity ($Pa \cdot s$)	ψ	Constant
μ_0	Zero shear viscosity ($Pa \cdot s$)	χ	Constant
μ_∞	Infinite shear viscosity ($Pa \cdot s$)	ϖ	Pressure/viscous ratio
μ_B	Bingham viscosity ($Pa \cdot s$)		

Subscripts

0	Zero shear rate point	B	Bingham model
∞	Infinite shear rate point		

Superscripts

B	Bingham model	H	Herschel-Bulkley model

1. Introduction to tape casting

Tape Casting was first introduced in the 1940s during the second world war when there was a serious lack of the quartermaster materials to produce mica capacitors [1]. In tape casting, sometimes referred to as the doctor-blade process, the slurry is spread over a surface using a carefully controlled blade referred to as a doctor blade. The schematic of the tape casting process from beginning (powder preparation) to the end, is illustrated in Figure 1. The tape casting process was firstly reported publicly in 1947 by Howatt et al. [1] to produce thin ceramic sheets for usage of capacitor dielectrics, and was shortly after applied to industrial production of ceramic capacitors [2].

Years after in 1967, Stetson and Gyurk [3] prepared alumina (Al_2O_3) substrates by tape casting, which were used as substrates for thin film circuits, devices, and integrated circuits. Meanwhile, Schwartz and Kirkpatrick [4] together with the IBM corporation developed a layer packaging material for use in computers by means of the tape casting process. In the 1970s many new products

were successfully developed and a number of tape casting applications emerged [5–7]. Many works on materials development and process improvement were published in 1980s-1990s [8–16]. Basically this era was a period in which the technology matured and new applications were being explored, such as the production of thin membranes for fuel cells [17, 18]. Most of the work later on is dedicated to the different material investigations and development of different products by means of tape casting.

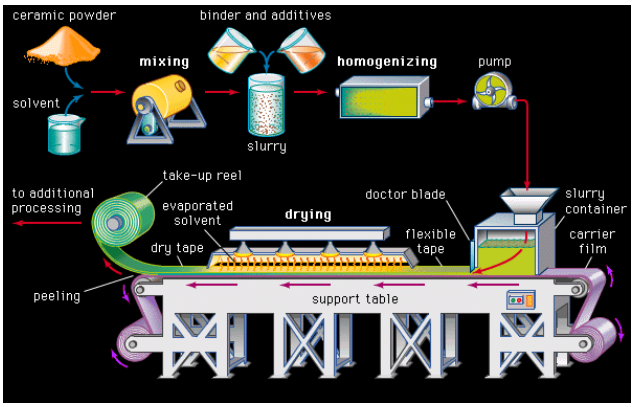

Figure 1: The tape casting process [19].

In general, the flow behavior of a fluid system can be analyzed using the principles of fluid dynamics. There have been extensive studies on fluid dynamics and transport phenomena in processing organic engineering materials, e.g., petroleum and polymers [20–24]. The same principles are applicable to the flow of ceramic slurries during the tape casting process. However, taking a closer look at the tape casting process, one will find that it is a multidisciplinary field combining different aspects to investigate. The most important aspects that have been investigated rely on the fluid behavior (rheology of fluid) and numerical/analytical models to simulate the process with the aforementioned rheology behavior taken to account.

1.1. Applications of tape casting

As mentioned earlier, the initial motivation for the tape casting process was to produce thin ceramic sheets for usage in the capacitors. However, after almost 60 years, the usage of the tape casting process has become more broad in the ceramic industry. A summary of the different applications of tape casting will be given below.

1.1.1. Substrates

For many years almost all of the (single-layered) substrate materials produced for the electronics industry were manufactured by tape casting. Substrates can be defined as the carrier or "backbone" of the electronic circuit. They are the ceramic insulator upon which the circuitry is deposited and patterned. These substrates range in size from as small as $6 \times 6mm$ $(0.25 \times 0.25in)$ to as large as $30 \times 30cm$ $(12 \times 12in)$, and in some cases larger sizes has been produced. What all of these substrates have in common is their very small thickness, usually $1.5mm$ $(0.060in)$ or less.

1.1.2. Multilayered ceramics

Multilayered ceramic packages (MLC) would not exist if tape casting had not been invented [9]. The basis for the multilayer industry is the ability to individualize layers with respect to metallization and via interconnections and then to laminate a set of these individual layers together into a package that can be sintered into a monolithic structure. Multilayered ceramic packages

with as few as two layers up to structures with as many as a hundred or more layers are common in the electronic ceramics industry today [25]. Moreover, multilayered ceramics produced by tape casting, have also been developed and used for flue gas purification [26], thus underlying the growing diversity of today's applications of the tape casting process.

1.1.3. Solid oxide fuel cell (SOFC)

Solid oxide fuel cells (SOFCs) are generally based on the same principle as the oxygen sensor, where the electrical energy is produced from a reaction of gases such as hydrogen and oxygen or natural gas and oxygen with water as a by-product [27]. The electrolyte in these fuel cells is the stabilized zirconia, which becomes a conductor of oxygen ions at elevated temperatures. In many cases the zirconia membrane, which is relatively large in the x and y directions and has a very thin cross section (z in Figure 2) is manufactured by tape casting.

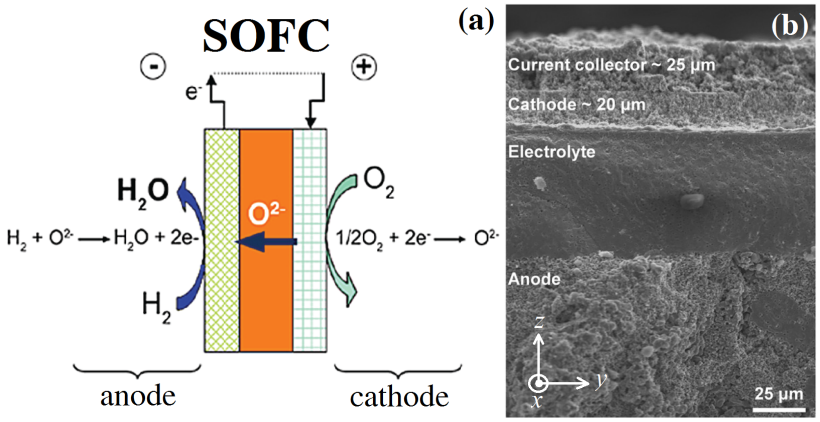

Figure 2: (a) Schematic illustration of a SOFC, (b) cross-sectional fracture surface of anode support, anode and electrolyte produced by tape casting after application of cathode and current collector and second firing step [28].

1.1.4. Functionally graded materials (FGMs)

A considerable amount of research has been conducted recently to produce functionally gradient materials (FGMs) for a wide variety of applications, e.g. [29, 30]. The ability to tape-cast and laminate several layers of materials with differing chemical compositions makes these FGMs possible [31, 32]. Although FGMs produced by tape casting are used for different applications, i.e. metal/ceramic composites and electronically graded composites, the newly developed FGMs for magnetic refrigeration applications [33] (see Figure 3) are of particular interest, and this will be discussed in detail in section 5.

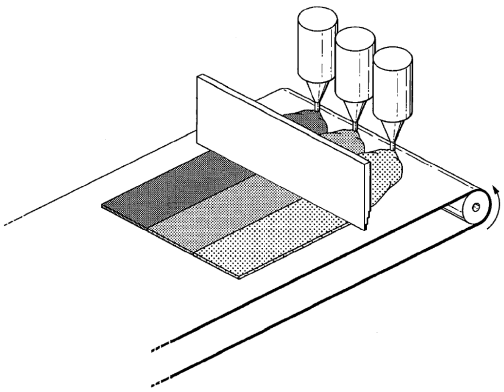

Figure 3: Schematic illustration of the newly developed method of tape casting to produce FGMs for magnetic refrigeration applications [33].

2. Rheology of fluids

Rheology is the study of the flow of matter, primarily in the liquid state, but also as soft solids or solids under conditions in which they respond with plastic flow rather than deforming elastically in response to an applied force. It almost applies to everything, but it is interesting to study for the listed materials which have a complex molecular structure, such as muds, sludges, suspensions, polymers and other glass formers (e.g., silicates), as well as many foods and additives, bodily fluids (e.g., blood) and other biological materials.

Most low molecular weight substances such as organic and inorganic liquids, solutions of low molecular weight inorganic salts, molten metals and salts, and gases exhibit Newtonian flow characteristics, i.e., at constant temperature and pressure, in simple shear, the shear stress (τ) is proportional to the rate of shear ($\dot{\gamma}$) and the constant of proportionality is the well-known dynamic viscosity (μ). Such fluids are classically known as Newtonian fluids, albeit the notion of flow and of viscosity predates Newton [34]. For most liquids, the viscosity decreases with temperature and increases with pressure. For gases, it increases with both temperature and pressure [35]. In general, the higher the viscosity of a substance in tape casting, the more resistance it presents to flow.

During the past 50-60 years, there has been a growing recognition of the fact that many substances of industrial significance, especially of multi-phase nature (foams, emulsions, dispersions and suspensions, slurries, for instance) and polymeric melts and solutions (both natural and man made) do not conform to the Newtonian postulate of the linear relationship between (τ) and ($\dot{\gamma}$) in simple shear, for instance. Accordingly, these fluids are variously known as non-Newtonian, nonlinear, complex, or rheologically complex fluids. Indeed, so widespread is the non-Newtonian fluid behavior in nature and in technology that it would be no exaggeration to say that the Newtonian fluid behavior is an exception rather than the rule.

2.1. Newtonian fluids

The first models that were developed for the flow analysis in tape casting were based on a simple Newtonian assumption, i.e.:

$$\tau = \mu \left(\frac{\partial u}{\partial y} \right) = \mu \dot{\gamma} \tag{1}$$

In paticular, the first model for predicting the tape thickness was developed by Chou et al. [36]. In their work Newtonian behavior was used and they assumed that the flow in the parallel doctor blade region was a linear combination of pressure and drag flow. The Newtonian fluid assumption

was also used by Gaskell et al. [37] to investigate the impact of the reservoir geometry on the flow behavior inside the tape caster. Kim et al. [38] developed an analytical model to investigate the impact of the relative magnitudes of the driving forces (wall shear and pressure gradient) on the resulting tape thickness. They also compared the beveled and parallel blades in terms of productivity, minimum thickness, and potential influence on particle alignment. The authors of the present work [39] also used the Newtonian fluid assumption in the numerical modelling of fluid flow in the doctor blade region by further developing existing models from literature [39] and introducing a non-dimensional tape thickness. However, in the tape casting process of ceramics the slurry seldom behaves like a Newtonian fluid, and consequently more general non-Newtonian fluid description should be applied if higher accuracy models are the goal. This will be addressed in more detail in the next section.

2.2. Non-Newtonian fluids

The simplest possible deviation from the Newtonian fluid behavior occurs when the simple shear data $\tau - \dot{\gamma}$ does not pass through the origin (equation (1)) and/ or does not result into a linear relationship between τ and $\dot{\gamma}$. Conversely, the apparent viscosity, defined as $\tau/\dot{\gamma}$, is not constant and is hence a function of τ or $\dot{\gamma}$. Indeed, under appropriate circumstances, the apparent viscosity of certain materials is not only a function of flow conditions (geometry, rate of shear, etc.), but it also depends on the kinematic history of the fluid element under consideration. It is convenient, though somewhat arbitrary, to group such materials into the following three categories:

1. Systems for which the value of $\dot{\gamma}$ at a point within the fluid is determined only by the current value of τ at that point; these substances are variously known as *purely viscous, inelastic, time-independent or generalized Newtonian fluids (GNF).*
2. Systems for which the relation between τ and $\dot{\gamma}$ shows further dependence on the duration of shearing and kinematic history; these are called *time-dependent fluids.*
3. Systems which exhibit a blend of viscous fluid behavior and of elastic solid-like behavior. For instance, this class of materials shows partial elastic recovery, recoil, creep, etc. Accordingly, these are called *visco-elastic* or *elastico-viscous fluids.*

As noted earlier, the aforementioned classification scheme is quite arbitrary, though convenient, because most real materials often display a combination of two or even all these types of features under appropriate circumstances. For instance, it is not uncommon for a polymer melt to show time-independent (shear-thinning) and visco-elastic behavior simultaneously and for a china clay suspension to exhibit a combination of time-independent (shear-thinning or shear-thickening) and time-dependent (thixotropic) features at certain concentrations and /or at appropriate shear rates. Generally, it is, however, possible to identify the most dominant non-Newtonian aspect and to use it as basis for the subsequent process calculations. In the following the time-independent fluids (first category) will be discussed in more detail, since they represent quite well the fluid behavior in the tape casting process [40–51].

As noted above, in simple unidirectional shear, this sub-set of fluids is characterized by the fact that the current value of the rate of shear at a point in the fluid is determined only by the corresponding current value of the shear stress and vice versa. Conversely, one can say that such fluids have no memory of their past history. Thus, their steady shear behavior may be described by a relation of the form,

$$\dot{\gamma}_{yx} = f(\tau_{yx}) \tag{2}$$

Depending upon the form of equation (2), three possibilities exist:

1. Shear-thinning or pseudoplastic behavior (power law)
2. Visco-plastic behavior with or without shear-thinning behavior (Bingham-plastic and Herschel-Bulkley)
3. Shear-thickening or dilatant behavior

Figure 4 shows qualitatively the flow curves (also called rheograms) for the above-noted three categories of fluid behavior [39]. The third type of the non-Newtonian fluids (dilatant) will not be discussed in the present review, since it is not relevant for tape casting.

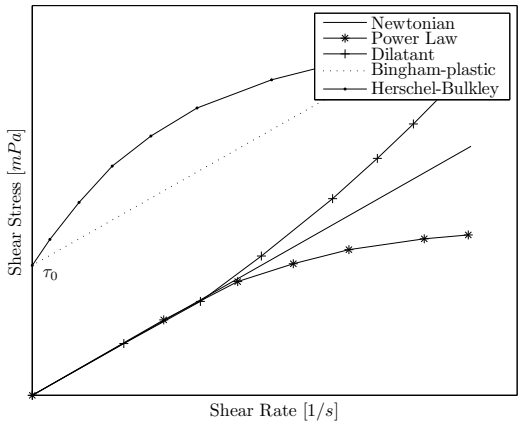

Figure 4: Rheological classification of different flows [39].

2.2.1. Shear-thinning

This is probably the most widely encountered type of time-independent non-Newtonian fluid behavior in engineering practice. It is characterized by an apparent viscosity μ (defined as $\tau_{yx}/\dot{\gamma}_{yx}$) which gradually decreases with increasing shear rate. In polymeric systems (melts and solutions), at low shear rates, the apparent viscosity approaches a Newtonian plateau where the viscosity is independent of shear rate (zero shear viscosity, μ_0).

$$\lim_{\dot{\gamma}_{yx}\to 0} \frac{\tau_{yx}}{\dot{\gamma}_{yx}} = \mu_0 \tag{3}$$

Furthermore, only polymer solutions also exhibit a similar plateau at very high shear rates (infinite shear viscosity, μ_∞), i.e.,

$$\lim_{\dot{\gamma}_{yx}\to \infty} \frac{\tau_{yx}}{\dot{\gamma}_{yx}} = \mu_\infty \tag{4}$$

In most cases, the value of μ_∞ for the solution is only slightly higher than the solvent viscosity μ_0. Figure 5 shows this behavior in a shear-thinning solution embracing the full spectrum of values going from μ_0 to μ_∞. Obviously, the infinite-shear limit is not seen for polymer melts and blends, or foams or emulsions or suspensions. Thus, the apparent viscosity of a pseudoplastic substance decreases with the increasing shear rate. The values of shear rate marking the onset of shear-thinning is influenced by several factors such as the nature and concentration of polymer, the nature of solvent, etc for polymer solutions and particle size shape, concentration of solids in suspensions, for instance. Therefore, it is impossible to suggest valid generalizations, but many polymeric systems exhibit the zero-shear viscosity region below $\dot{\gamma} < 10^{-2} s^{-1}$ [52]. Usually, the zero-shear viscosity region expands

as the molecular weight of polymer falls, or its molecular weight distribution becomes narrower, or as the concentration of polymer in the solution is reduced.

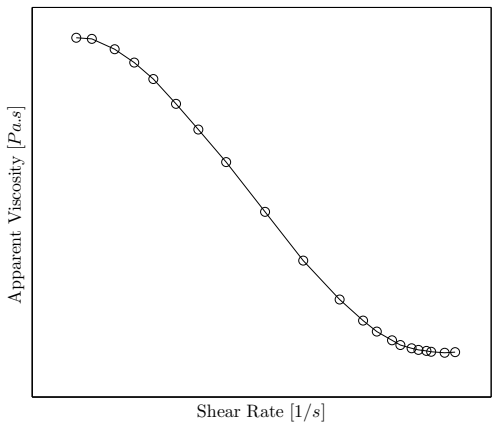

Figure 5: An example of shear-thinning behavior.

The next question which immediately comes to mind is how the fluid behavior can be approximated. Over the past 100 years or so, many mathematical equations of varying complexity and forms have been reported in the literature; some of these are straightforward attempts at curve fitting the experimental data ($\tau - \dot{\gamma}$) while others have some theoretical basis (blended with empiricism) in statistical mechanics as an extension of the application of kinetic theory to the liquid state, etc. [53]. While extensive listing of viscosity models is available in several books e.g., see, Ibarz and Barbosa-Canovas [54] and Govier and Aziz [55], a representative selection of widely used expressions is given here.

Power Law or Ostwald-de Waele law

Often the relationship between shear stress (τ)-shear rate ($\dot{\gamma}$) plotted on log-log co-ordinates for a shear-thinning fluid can be approximated by a straight line over an interval of shear rate, i.e.,

$$\tau = k \cdot \dot{\gamma}^n \tag{5}$$

or, in terms of the apparent viscosity,

$$\mu = k \cdot \dot{\gamma}^{n-1} \tag{6}$$

Obviously, $0 < n < 1$ will yield $d\mu/d\dot{\gamma} < 0$, i.e., shear-thinning behavior fluids are characterized by a value of n (power-law index) smaller than unity. Many polymer melts and solutions exhibit the value of n in the range $0.3 - 0.7$ depending upon the concentration and molecular weight of the polymer, etc. Even smaller values of power-law index ($n \sim 0.1 - 0.15$) are encountered with fine particle suspensions like kaolin-in-water, bentonite-in-water, etc [52]. Naturally, the smaller the value of n, the more shear-thinning the material is. The other constant, k, (consistency index) is a measure of the consistency of the substance.

Although, equations (5) or (6) offer the simplest approximation of shear-thinning behavior, it predicts neither the upper nor the lower Newtonian plateaus in the limits of $\dot{\gamma} \to 0$ or $\dot{\gamma} \to \infty$. Besides, the values of k and n are reasonably constant only over a narrow interval of shear rate range hence one needs to know a priory the likely range of shear rate to be encountered in an envisaged application.

The power law model is the most common used constitutive behavior for the rheology of the ceramic slurry in tape casting. Pitchumoni and Karbhari [56] evaluated the effects of an imposed pressure gradient due to the height of the slurry in the casting head, as well as those of the drag due to the moving substrate on the slurry flow by modelling the slurry discharge as a generalized power law flow. Tok et al. [57] also used the power law constitutive model in analytical modelling of flow below the doctor blade region and the resultant tape thickness. The power law constitutive behavior was also implemented in the quasi-steady state analytical model developed by the authors [58], capable of modelling a non-constant height of the ceramic slurry in the reservoir and its resultant variation in the tape thickness. A 2D simulation of a power law ceramic was conducted by the authors [59] in combination with a multiphase model (VOF) to track the free surface of the $La_{0.85}Sr_{0.15}MnO_3$ (LSM) ceramic slurry. More specifically, the power law behavior is given in equation (7) and shown in Figure 6.

$$\tau = 3.31 \left(\frac{\partial u}{\partial y} \right)^{0.90} \tag{7}$$

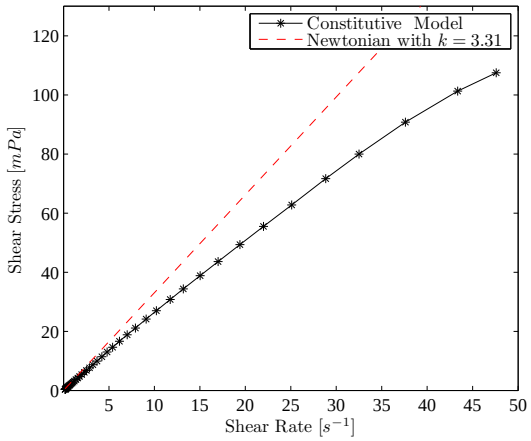

Figure 6: Rheology behavior of LSM ceramic [58].

The Cross/Carreau viscosity

In order to rectify some of the weaknesses of the power-law, Cross [60] presented the following empirical form which has gained wide acceptance in the literature. In simple shear, it is written as

$$\frac{\mu - \mu_\infty}{\mu_0 - \mu_\infty} = \frac{1}{1 + k \cdot \dot{\gamma}^n} \tag{8}$$

It is readily seen that for $n < 1$, this model also predicts shear-thinning behavior. Furthermore, the Newtonian limit is recovered here when $k \to 0$. Though initially Cross [60] proposed that $n = 2/3$ was satisfactory for numerous substances, it is now thought that treating it as an adjustable parameter offers significant improvement in terms of the degree of fit [52]. Evidently, equation (8) correctly predicts $\mu = \mu_0$ and $\mu = \mu_\infty$ in the limits of $\dot{\gamma} \to 0$ and $\dot{\gamma} \to \infty$ respectively. The Cross model was used by Wonisch et al. [40] in the tape casting for numerical modelling both the macroscopic flow behavior and the orientation of individual particles inside the ceramic slurry.

The inherent deficiencies in the power-law model are remedied by the Carreau model [41]:

$$\frac{\mu - \mu_\infty}{\mu_0 - \mu_\infty} = \frac{1}{\left[1 + (\lambda \cdot \dot{\gamma})^2\right]^{(1-n)/2}} \tag{9}$$

where λ is the time constant in seconds. The Carreau model was used by Terrones et al. [42] to predict the tape thickness of the aqueous suspensions numerically.

2.2.2. Visco-plastic fluids

This type of non-Newtonian fluid behavior is characterized by the existence of a threshold stress (called yield stress or apparent yield stress, τ_0) which must be exceeded for the fluid to deform (shear) or flow. Conversely, such a substance will behave like an elastic solid when the externally applied stress is less than the yield stress, τ_0. Of course, once the magnitude of the external yield stress exceeds the value of τ_0, the fluid may exhibit Newtonian behavior (constant value of μ) or shear-thinning characteristics, i.e., $\mu(\dot{\gamma})$. It therefore stands to reason that, in the absence of surface tension effects, such a material will not level out under gravity to form an absolutely flat free surface. Quantitatively this type of behavior can be hypothesized as follows: such a substance at rest consists of three-dimensional structures of sufficient rigidity to resist any external stress less than $|\tau_0|$ and therefore offers an enormous resistance to flow, albeit it still might deform elastically. For stress levels above $|\tau_0|$, however, the structure breaks down and the substance behaves like a viscous material. In some cases, the build-up and breakdown of structure has been found to be reversible, i.e., the substance may regain its (initial or somewhat lower) value of the yield stress.

A fluid with a linear flow curve for $|\tau| > |\tau_0|$ is called a Bingham plastic fluid, and is characterized by a constant value of viscosity μ_B. Thus, in one-dimensional shear, the Bingham model is written as:

$$\begin{aligned} \tau_{yx} &= \tau_0^B + \mu_B \dot{\gamma}_{yx} \qquad && |\tau_{yx}| > \left|\tau_0^B\right| \\ \dot{\gamma}_{yx} &= 0 && |\tau_{yx}| < \left|\tau_0^B\right| \end{aligned} \tag{10}$$

Application of the Bingham constitutive model for the tape casting process was attempted by Ring [43]. However, he wrongly used shear rate, rather than shear stress as a yield criterion. The Bingham model was used by Zhang et al. [44] to model the flow behavior below the doctor blade region and the resultant tape thickness. They proposed a critical velocity (v_c) and derived an analytical equation based on sufficient ($v_c \leq v_0$) or insufficient ($v_c > v_0$) belt velocity (v_0) to overcome the yielding point. Joshi et al. [45] also used the Bingham model in their analytical models to predict the tape thickness and compared with the corresponding data from Huang et al. [46]. The Bingham constitutive model was also used for analytical modelling of the fluid flow in a two doctor blade configuration by the authors [47], however this will be discussed later in section (3.1.3).

3. Modelling approaches

When dealing with the flow in tape casting, the coupled momentum and continuity equations should in general be solved:

$$\rho\left(\frac{\partial u}{\partial t} + u \cdot \nabla u\right) = -\nabla p + \nabla \cdot T + F \tag{11}$$

$$\frac{\partial \rho}{\partial t} + \nabla \cdot (\rho u) = 0 \tag{12}$$

where ρ is density, u is velocity, p is pressure, T is stress tensor and F is the contribution from external forces. Here, the momentum equation (11) expresses Newton's second law of motion, and the continuity equation (12) ensures conservation of mass. The aforementioned equations can be solved either analytically or numerically. In the following a review of the existing models for tape casting will be presented.

3.1. Analytical models

It is well-known that analytical solutions to the coupled flow equations given above are limited to relatively simple cases in terms of geometry, boundary conditions and material properties. This is certainly also the case for the relatively few analytical solutions for the flow in tape casting. More specifically only 1D flow is considered, constant material data is assumed as well as incompressible behavior of the slurry. Moreover, only steady state or quasi-steady state conditions are considered. Under these assumptions it is possible to develop some relatively simple, yet highly applicable analytical solutions for the flow in the doctor blade region in tape casting. The most important of these solutions will be presented next.

3.1.1. Steady state model

In order to express the volume flow and thus the tape thickness, the velocity field equation in the doctor blade region must be developed. Based on the number of doctor blades there are two kinds of tape casters, a simple tape caster which has only one doctor blade (illustrated schematically in Figure 7), and a double-blade tape caster in which a rear doctor blade is used to ensure a hydrostatic pressure in front of the rear one [44].

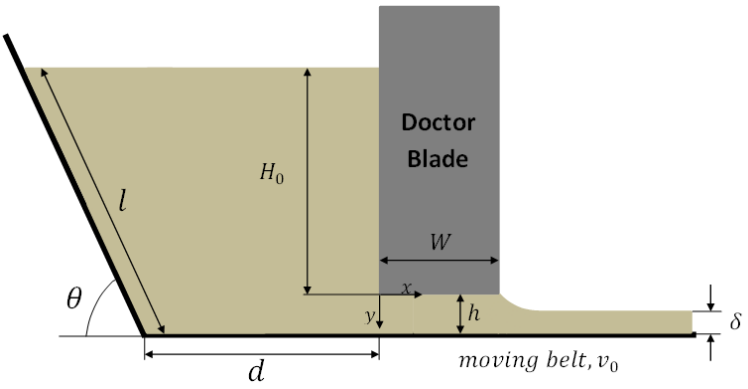

Figure 7: Schematic geometry of the tape casting machine in 2D.

The pressure gradient inside the channel below the doctor blade is constant, since there is a hydrostatic pressure in front of the doctor blade and it can be determined by the height of the slurry as shown below [44],

$$\frac{dp}{dx} = -A_0 = -\frac{\rho g H_0}{W} \tag{13}$$

where ρ is the density of the slurry, g is the acceleration due to gravity, H_0 is the height of the slurry in front of the doctor blade, and W is the width of doctor blade.

By assuming an infinitely long and wide plate as compared to the thickness and combining with momentum conservation in the x-direction under steady state conditions, we obtain the following [44, 57], highly simplified 1D version of equation (11)

$$\frac{d\tau}{dy} = \frac{dp}{dx} \tag{14}$$

where τ is the shear stress. From equations (13) and (14), τ is found to be

$$\tau = -A_0 y + A_1 \tag{15}$$

where A_1 is an integration constant.

For the power law or the Bingham fluid the shear stress, τ, is given by the constitutive equation [44, 57]:

$$\begin{aligned} \tau &= k\left(\tfrac{\partial u}{\partial y}\right)^n \\ \tau &= \tau_0^B + \mu_B\left(\tfrac{\partial u}{\partial y}\right) \end{aligned} \tag{16}$$

where it has been assumed that the only velocity component contributing to the shear rate is the velocity in the x-direction, u.

Rewriting equations (15) and (16) and integrating along the channel height (h) we get

$$\begin{aligned} \textstyle\int_0^h \left(-A_0 y + A_1\right) dy &= \textstyle\int_0^h k\left(\tfrac{\partial u}{\partial y}\right)^n dy \\ \textstyle\int_0^h \left(-A_0 y + A_1\right) dy &= \textstyle\int_0^h \left[\tau_0^B + \mu_B\left(\tfrac{\partial u}{\partial y}\right)\right] dy \end{aligned} \tag{17}$$

These equations compose the main structure of almost all research done to analytically model the fluid flow below the doctor blade region [36, 38, 44, 45, 56–58]. By solving the above equations the velocity profile below the doctor blade region ($u(y)$) will be found, and subsequently used to find the tape thickness as follows

$$\delta = \frac{1}{v_0}\int_0^h u(y)\cdot dy \tag{18}$$

which follows from mass conservation and incompressibility of the slurry. An example of such analytical model is illustrated in Figure 8. As seen, by decreasing the hydrostatic pressure (P) due to a reduction in the level of the slurry height, the velocity profile is changed and the area under the velocity profile is decreased. Moreover, an increased substrate velocity results in decreasing the tape thickness since the drag force is increased by increasing the substrate velocity, and it becomes more dominant compared to the pressure force which results in more stretching of the slurry over the peeling belt.

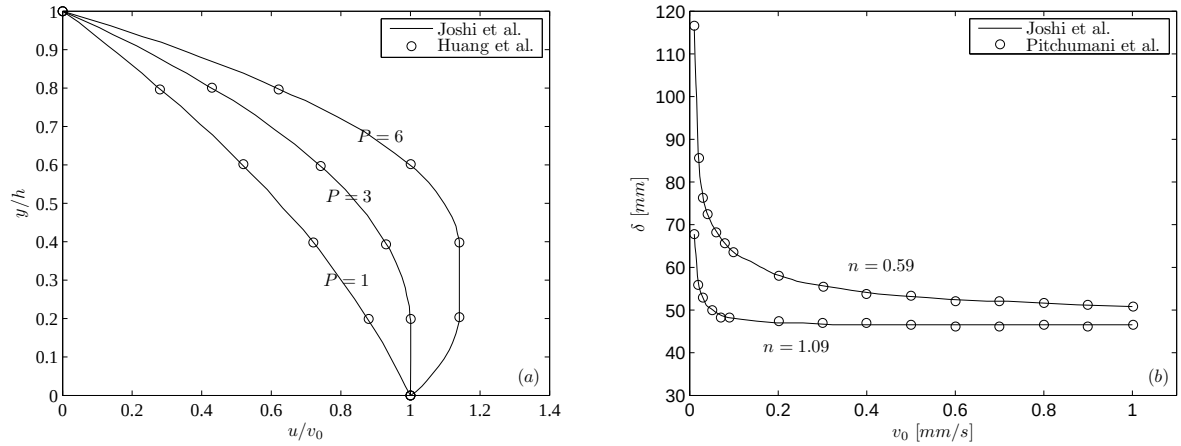

Figure 8: Results of analytical modelling for (a) velocity profile below the doctor blade region with different pressure head [45, 46], and (b) influence of the casting velocity on the tape thickness [45, 56].

3.1.2. Quasi-steady state model

By assuming that k and n are constants, equation (17) for the power law material can be solved for u [58]

$$u = \left(-\frac{1}{A_0 \cdot k^{\frac{1}{n}}}\right) \cdot \left(\frac{1}{\frac{1}{n}+1}\right) \cdot (-A_0 y + A_1)^{\frac{1}{n}+1} + A_2, (0 < y < h) \tag{19}$$

where A_2 is another integration constant.

The boundary conditions for equation (19) in the doctor blade region of tape casting are

$$\left\{ \begin{array}{c} u(0) = 0 \\ u(h) = v_0 \end{array} \right\} \tag{20}$$

where v_0 is the velocity of the moving belt.

Applying these boundary conditions in equation (19), and introducing the expressions that $\frac{1}{n} + 1 = \chi$ and $\frac{-1}{A_0 \cdot k^{\frac{1}{n}}} = \psi$, the thickness of the green tape, δ, can be determined by integrating u over the channel height and dividing by the tape velocity as indicated in equation (18) [58], i.e.:

$$\delta = \frac{1}{v_0} \int_0^h u \cdot dy = \frac{-\left[(-A_0 h + A_1)^{\chi+1} - (A_1)^{\chi+1}\right]}{v_0 \cdot A_0 \cdot \psi \cdot \chi \cdot (\chi + 1)} + A_2 h \tag{21}$$

Reaching at a constant tape thickness is not an impossible goal, since most of the manufacturing processes for tape casting are of the continuous form in which the reservoir at all times is fed by slurry. Moreover, using two doctor blades in the design of the machine will result in having almost constant hydrostatic pressure during the casting process (see section (3.1.3)). However, it is of great importance to control the tape thickness in small tape casters especially in small scale production and laboratories, in which the slurry height is not constant in the reservoir but gradually decreasing with time. This phenomenon leads to a modification of the standard steady state model [36, 38, 44, 56, 57] making it dependent on the slurry height variation.

The steady state formulation shown previously was developed by the authors [58] based on the continuity equation. For the quasi- steady state solution a similar approach was adopted. Thus, assuming that the slurry is incompressible the volume of the slurry which drops down in the reservoir is equal to the volume of the slurry which is conveyed out of the doctor blade region by the peeling

belt. Further assuming that during the time period equal to Δt, the height of the slurry will decrease from the initial value of H_0 to H_1, the aforementioned decrease in volume (which equals the area in the present 2D model) in the reservoir will be given as:

$$\Delta S_1 = \left[d + \frac{1}{2} \cdot l \cdot \cos\theta \left(1 + \frac{H_1 + h}{H_0 + h} \right) \right] \cdot (H_0 - H_1) \tag{22}$$

This area is moved out of the doctor blade region with the constant velocity of v_0 and the distance of $v_0 \times \triangle t$, hence it is equal to $v_0 \times \Delta t \times \delta_1$. The new initial height in the next time step is now H_1 and the new ΔS_2 is found from using H_1 as initial height in equation (22) and so forth.

As seen in Figure 8a, since the hydrostatic pressure (P) decreases by time due to the reduction in level of the slurry height, the velocity profile is changed and the area under the velocity profile is decreased, and consequently the "area" out of the blade is decreased. On the contrary, decreasing the pressure head for a constant velocity, the thickness of the tape is decreased in the exit and vice versa. This behavior very much emphasizes the importance and relevance of the proposed quasi-steady state model, in which the transient effect of the slurry height in the reservoir (which resembles the pressure head) is implemented. This phenomenon can easily be seen in Figure 9, where the tape thickness decreases in the casting direction due to the transient decrease of the slurry height (the pressure head) in the reservoir.

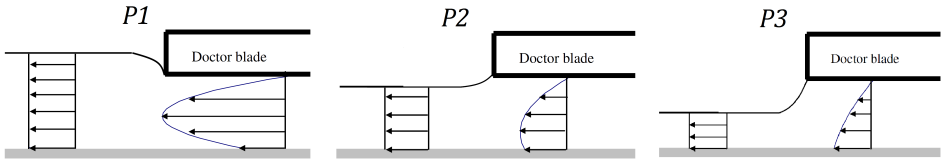

Figure 9: Schematic illustration of the effect of the increased pressure head on the tape thickness ($P_1 > P_2 > P_3$) [48].

3.1.3. Steady state two doctor blade model

As already mentioned, using the two doctor blade configuration is one of the ways to reach an almost constant tape thickness in the tape casting process. The interesting thing in this case is to control the height of the slurry in both doctor blade regions based on the desired tape thickness, substrate velocity, consitutive behavior of the ceramic slurry and the machine design parameters [47]. A general schematic of the two doctor blade configuration is illustrated in Figure 10. The authors [47] have modeled analytically the velocity and the pressure field in both doctor blade regions assuming the Bingham-plastic model for the fluid flow. The developed model then was used to predict the height of the slurry in both doctor blade regions based on the desired tape thickness and the belt velocity.

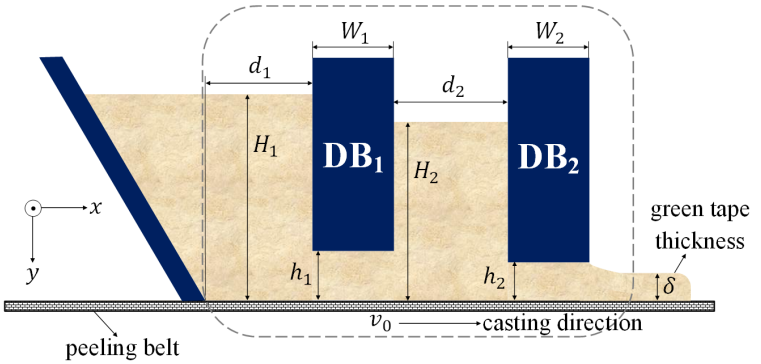

Figure 10: 2D illustration of the tape casting process with two doctor blades [47].

The authors [47] showed that based on the ability of the flow to overcome the yield stress (for the Bingham-plastic fluid), there are two different zones, i.e. a sufficient one and an insufficient one, in which the predicted values for the slurry height and velocity profiles are totally different. The region with the insufficient belt velocity shifts toward the higher velocities by increasing the value of the critical velocity, $v_{cr} = \frac{A_{0i}h_i^2}{2k}$, (see Figure 11), when increasing the doctor blade (h_i), increasing the slurry height behind the doctor blade (H_i), decreasing the doctor blade width (W_i), and the plastic viscosity (k), which all gives an increase in the critical velocity $v_{cr} = \frac{A_{0i}h_i^2}{2k}$. Moreover, the tape thickness is always larger than the half of the doctor blade height ($\delta > h_i/2$) no matter what belt velocity is used [47].

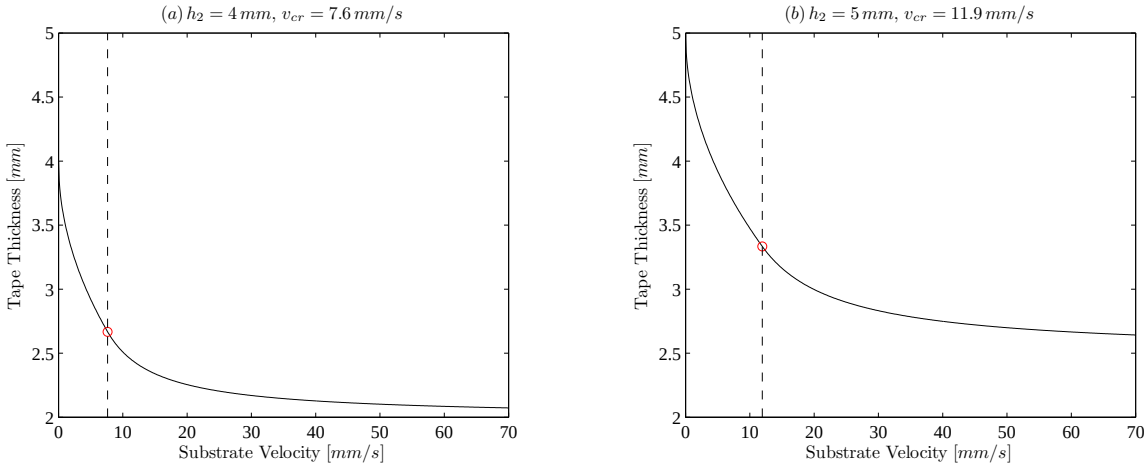

Figure 11: Variation of the tape thickness by the substrate velocity for (a) $h_2 = 4mm$, and (b) $h_2 = 5mm$ [47].

It was also found by the authors [47] that when the belt velocity is not high enough to overcome the Bingham yield point (insufficient belt velocity), there is always a region with zero shear rate below the doctor blade (see Figure 12), and this region decreases its width by increasing the plastic viscosity (k). The results of the required slurry height based on the desired tape thickness as well as the belt velocity showed that in the insufficient condition the slurry height behind both doctor blades will increase in comparison to the sufficient condition (see Figure 13). Moreover, the variation of the aforementioned heights are different in the sufficient and insufficient condition, showing a linear increase for the sufficient condition. On the other hand, increasing the doctor blade width, W_i, (or decreasing the reservoir size, d_i) with constant velocity and tape thickness, the required slurry

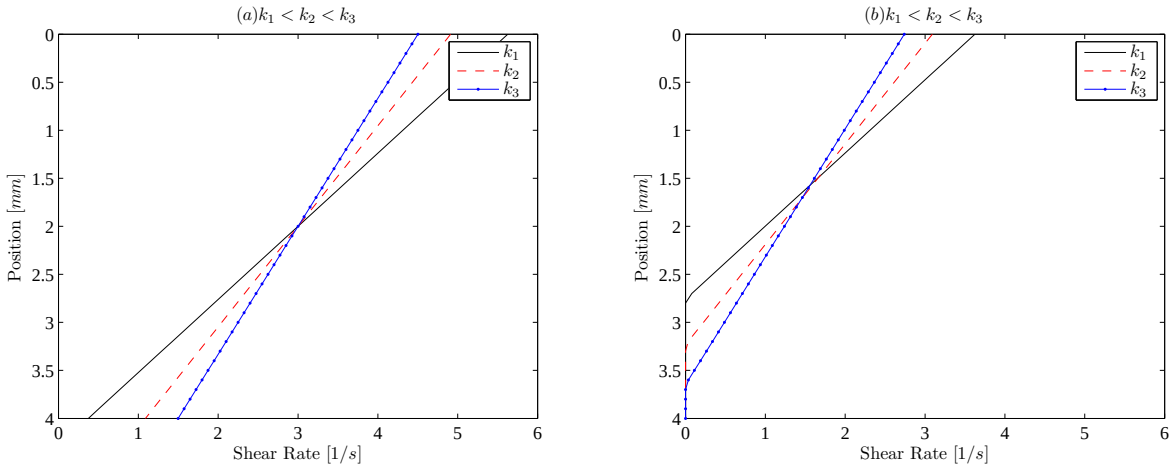

Figure 12: Shear rates below the doctor blade region for (a) $v_0 > v_{cr}$ and different k, and (b) $v_0 \leq v_{cr}$ and different k. The value of the critical velocity in these cases is equal to 10.5 [47].

height behind the both doctor blades will be increased. The proposed model by the authors [47] contains all main parameters which influence the process, and it has the flexibility to be used for different slurries with different constitutive behaviors as well as different machine design.

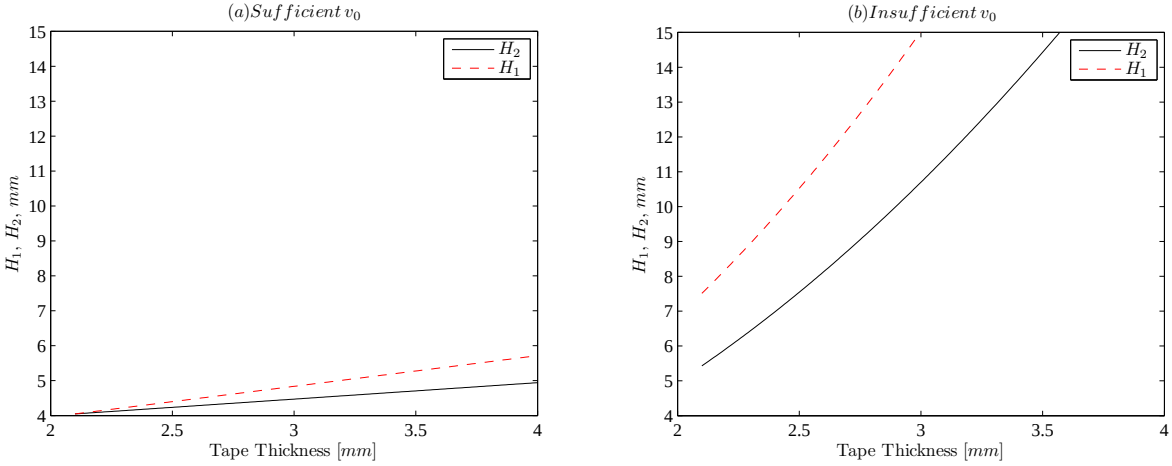

Figure 13: Impact of increasing the value of the tape thickness on the required height of the slurry behind both doctor blades with (a) sufficient and (b) insufficient belt velocity [47].

3.2. Numerical models

Numerical modeling is a powerful method of visualizing the dynamic behaviour of physical systems. Numerical solutions have several advantages over analytical solutions such as being much more intuitive and easy to handle. Thus more realistic models of greater complexity can be investigated using numerical techniques. This is certainly the case for computational fluid dynamics (CFD) methods, which numerically solve the differential equations governing the flow, and makes them a prime tool for analyzing manufacturing processes involving material flow. Nonetheless, only few CFD studies have considered tape casting so far and those which did have been restricted to two dimensions. One reason why CFD-based simulations are not widely used to simulate tape casting - despite their obvious benefits - might be due to their complex nature, requiring extensive know-how

and special software. In the following the numerical models used for modelling the tape casting process will be reviewed.

3.2.1. General fluid flow

The first numerical model to solve the fluid in tape casting was introduced by Loest et al. [49], where the finite element method (FEM) was used for the forming flow of ceramic tapes having viscoplastic Bingham behavior with a yield stress. In their work the flow domain encompassed both the slurry reservoir and the doctor-blade region with free surface (the free surface modelling will be discussed in detail in part 3.2.2) and was two-dimensional. They changed the design of the doctor blade from being a straight wall to a tapered one to avoid recirculation.

Gaskell et al. [37] modeled the fluid flow in the reservoir region of the tape casting process numerically using a linear finite element formulation. Their analysis showed that the flow is characterized by an ever-present primary recirculation, adjacent to the moving substrate, and that the size and number of secondary recirculations above the primary one depend upon both the aspect ratio of the reservoir (height over width) and the angle of inclination of the side walls (see Figure 14).

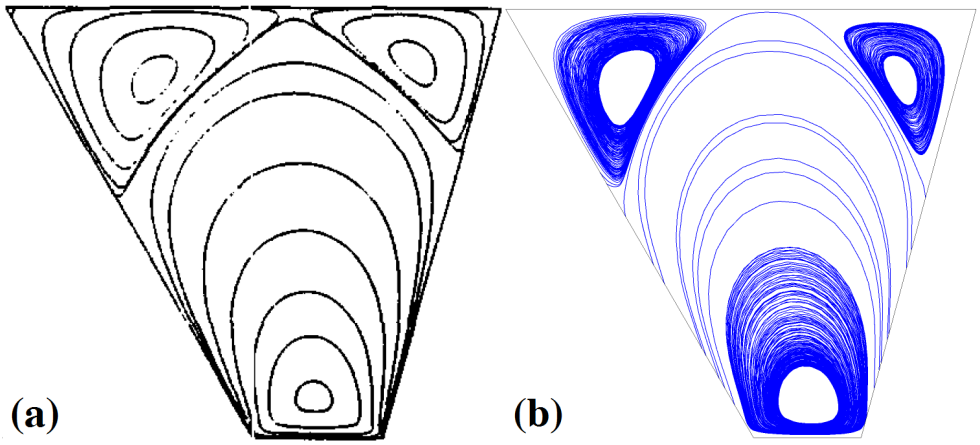

Figure 14: Flow pattern inside the reservoir solved by (a) finite element formulation [37], and (b) corresponding finite volume modelling conducted by authors.

The first numerical model based on the finite volume method was conducted by the authors [39]. The flow field was computed inside the reservoir and below the doctor blade region. Based on the velocity profiles obtained below the doctor blade region the tape thickness was predicted for a Newtonian fluid.

Wonisch et al. [40] also conducted a CFD calculation in the tape casting process. They used smoothed particle hydrodynamics (SPH) to simulate the flow of the non-Newtonian fluid, and consequently the orientation of the particles (and resultant anisotropic particle alignment) was predicted by Jeffery's equations of motion.

3.2.2. Free surface tracking

Flow processes often involve the presence of free surfaces, the tracking of which has significant impact on the manufacturing and the final quality of the product. Examples abound, e.g., casting processes, mold filling, thin film processes, extrusion, coatings, spray deposition, fluid jetting devices in which material interfaces are inherently present. Several CFD methods have been developed in the last decades with the aim of simulating such complex flows with free surfaces. Two very well-known examples of this are the volume of fluid (VOF) and level set methods. In general, there are a

lot of different research papers which are dedicated to free surface modelling, different interpolation schemes, liquid/gas phase flow, multi fluid flow, multiphase flow and different numerical methods to simulate the flow field with the presence of an interface [50].

As previously introduced, Loest et al. [49] conducted FEM simulations on tape casting combined with a free surface model. Though, their results showed that the free surface tracking was implemented in the close region to the doctor bled region. The authors [59] modeled the flow of a slightly non-Newtonian ceramics slurry with the power law constitutive behavior as well as tracking the free surface. They also investigated the different interface capturing methods in modelling of free surface tracking of tape casting, and reported that the Compressive Interface Capturing Scheme for Arbitrary Meshes (CICSAM) method is the most reliable scheme for capturing of the free surface in the modelling of the tape casting process [50]. Apart from this, the authors presented a coupled fluid flow-multiphase model to predict the influence of the process parameters on the side flow, as the flow leaves the doctor blade region [51]. Some 3D results for the flow of the $(La_{0.85}Sr_{0.15})_{0.9}\,MnO_3$ (LSM) slurry in the tape casting process are illustrated in Figure 15. The LSM slurry showed to follow the power law constitutive behavior for the viscosity as $\tau = 3.31 \cdot \dot{\gamma}^{0.90}$.

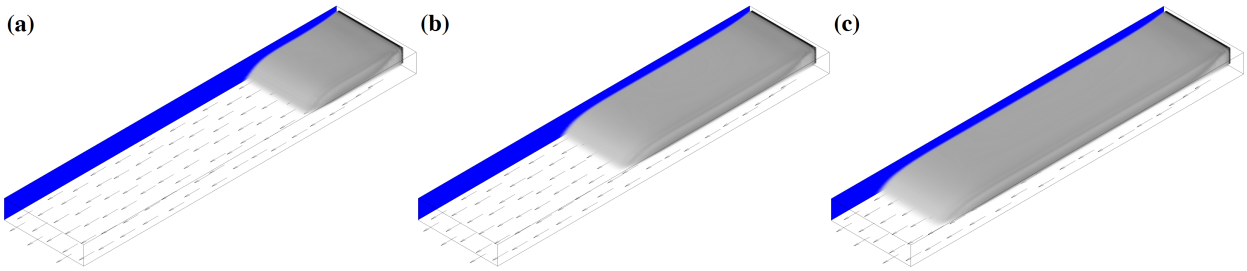

Figure 15: Flow of LSM ceramic slurry in tape casting in different simulation time (a) 2.5 sec, (b) 5 sec, and (c) 7.5 sec. The dark blue surface is the symmetry plane.

There is also ongoing research regarding the tape casting process, fluid flow modelling, and multiphase models, which has been conducted by the authors and this will be discussed in detail in part 5.

4. Process parameters

In general, for any manufacturing process, it is of great interest to identify the affecting parameters on the quality of the final product and evaluate their impact. Tape casting is no exception and in this process the parameters of interest are material composition in the slurry, physical properties (i.e. density), dimensions (design) of the machine, and the speed of the process (also known as the substrate velocity). Specifically, thickness control is of critical importance in tape casting, since this substantially affects the final properties of the tape. Having a uniform tape thickness along the casting direction is very often the final target, and in the following the influence of different parameters on this will be reviewed.

4.1. Material properties

The material properties considered here, are the ones describing the constitutive behavior of the flow used in tape casting. Considering the density as constant, the viscosity changes have an important influence on the tape thickness. The rheological classification of the flow was discussed shortly before in part 2 and an example of the changes in the materials function (n) was illustrated in Figure 8b for a power law material.

4.2. Tape caster machine

Almost in all of the works done on the modelling of tape casting [36, 38, 39, 44–46, 50, 51, 56–59], the influence of the tape casting machine design and geometry on the final tape thickness was investigated. All analytical models developed are somehow taking into account the tape caster dimensions and the constitutive behavior of the material. There are three important parameters (regardless of material properties) in the tape casting process that are of the great interest to investigate and easy to change in the real life experiments, i.e. the substrate velocity, doctor blade height, and the slurry load (slurry height in the reservoir).

4.2.1. Substrate velocity

Figure 16 shows the effect of the substrate velocity on the dried tape thickness based on experimental findings as well as steady state and quasi-steady state analytical models for the same set-up [58]. As seen from the figure for all types of data, an increased substrate velocity results in decreasing the tape thickness. More specifically, it is found that the tape thickness decreases hyperbolically with substrate velocity [36, 56], which is also seen from equation (21). From previous works [36, 39, 56], it was found that when the drag force is increased by increasing the substrate velocity it becomes more dominant as compared to the pressure force which results in more stretching of the slurry over the peeling belt. Figure 16 shows that the quasi-steady state model proposed by the authors [58] is in better agreement with corresponding experiments as compared to the steady state model, since in the quasi-steady state model the effect of decreasing the level of the slurry height is taken into account.

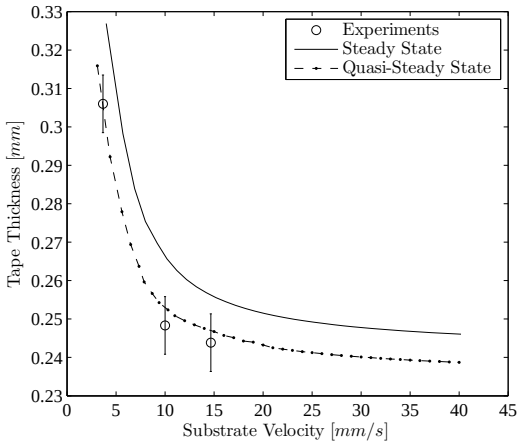

Figure 16: Effect of substrate velocity on tape thickness with a doctor blade height of 1 mm [58].

4.2.2. Doctor blade height

The effect of the doctor blade height on the tape thickness is illustrated in Figure 17. It is seen that increasing the doctor blade height leads to a higher tape thickness which is expected. However, the difference between the curves in Figure 17 is decreased by increasing the velocity. For a constant pressure height, increasing the doctor blade height results in more material being carried out of the doctor blade region. This means that the thickness of the tape will be increased. As mentioned before, for high casting velocities (substrate velocity) the drag force becomes more dominant. The increase of the tape thickness coming from a higher doctor blade gap is reduced as the velocity is increased.

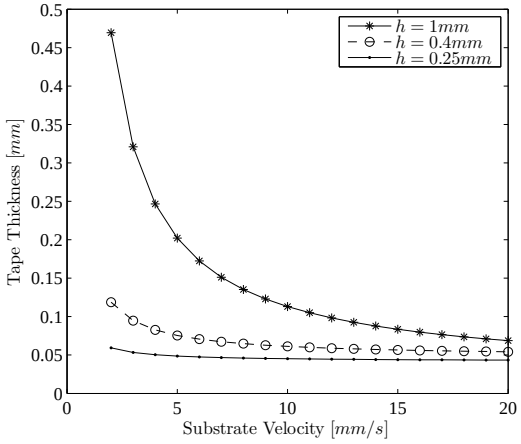

Figure 17: Results of modelling for effect of doctor blade height on the tape thickness [58].

Another comparison between the quasi-steady state model, steady state model and experimental results is shown in Figure 18 [58]. It can be seen that the proposed model by the authors [58] is in better agreement with experiments in comparison to the steady state model. The highest deviation between data was observed for the higher values of the doctor blade height.

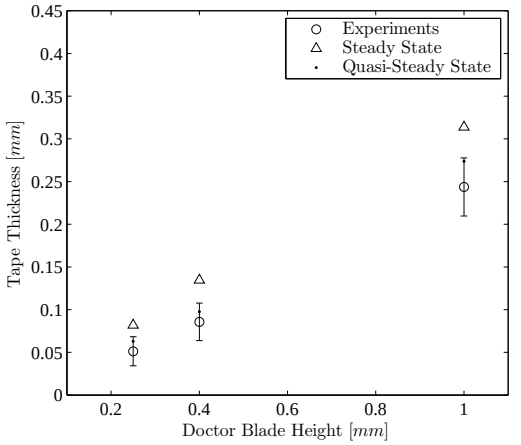

Figure 18: Comparison of the quasi-steady state model proposed by the authors with steady state model and experiments for $v_0 = 3.67mm/s$ [58].

4.2.3. Slurry load

The slurry load, known as the hydrostatic pressure, is the other main parameter which influences the final tape thickness. This parameter is a direct consequence of the height of the fluid behind the doctor blade region ($\triangle P = \rho g H$). Using this, it is possible to define one single parameter which determines the shape of the velocity profiles as well as the wet tape thickness and this is the ratio of pressure force to viscous force (ϖ) [38, 39]

$$\varpi = \frac{\triangle P \cdot h}{2\mu W v_0} \tag{23}$$

As illustrated in Figure 19 increasing the value of the aforementioned ratio (ϖ) results in increasing of the velocity shape (area) below the doctor blade region, and as shown before in Figure

9, this leads to an increase of the tape thickness.

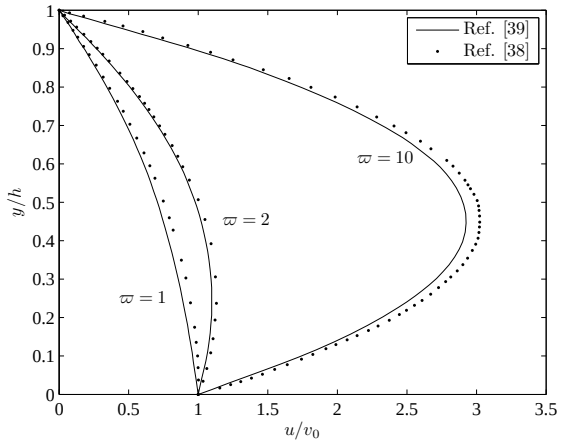

Figure 19: The non-dimensional velocity profile in the doctor blade region on the basis of different ϖ [39].

In most existing models [36, 38, 39, 44, 45, 56, 57] this ratio is assumed to be constant. However, as already discussed in part 3.1.2 the height of the slurry inside the reservoir is not constant, but decreasing by time [58]. As seen from Figure 20 the thickness of the tape in the beginning of a strip (which is the part leaving the doctor blade region first) is higher than the end of a strip. This is due to the higher level of material in the reservoir in the beginning of process. As time passes the height of the slurry in the reservoir decreases and consequently the resultant height of the tape will decrease. This means that the hydrostatic pressure decreases by time and the drag forces start to show their dominance by making the tape thinner. However, this phenomenon can of course not be detected by the steady state model.

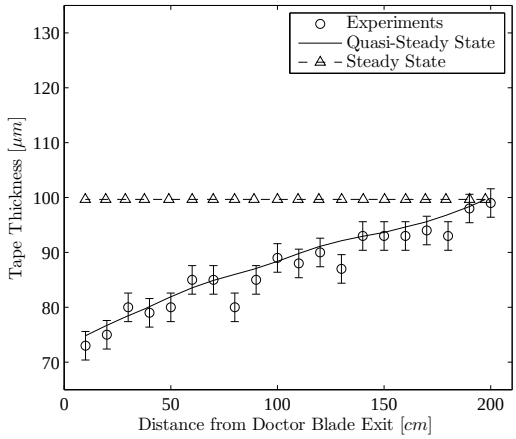

Figure 20: Results of modelling and their comparison with experimental data for tape casting of LSM slurry with a substrate velocity of $v_0 = 3.67mm/s$ and an initial slurry height of $H_0 = 20.8mm$ [58].

4.3. Side flow

As already discussed in the tape casting process the dried tape thickness is of great interest to control for the desired products and applications. One of the parameters that influences the final tape thickness is the side flow factor (α) which is mostly measured at the end of the process

by a volumetric comparison of the tape which flowed outside the casting width to the tape within the casting width. Although this side flow in tape casting is of relatively limited magnitude it is interestingly enough always mentioned as an influencing parameter in the calculations of the tape thickness and always measured experimentally [36, 39, 45, 57–59]. The authors have presented the first example in literature where the side flow factor (α) is predicted numerically [51]. Moreover, they investigated the influence of the process parameters, i.e. substrate velocity, doctor blade height and slurry height, on the side flow factor (see Figure 21).

The effect of substrate velocity on the side flow factor is illustrated in Figure 21a. The results showed that by increasing the velocity of the peeling belt, the value of the side flow factor will be increased, which means that the slurry flows less towards the sides. This is due to the increase of the drag forces in the casting direction compared to the side direction, which gives the slurry less possibility to flow towards the sides. Note that the side flow factor is defined in such a way, that when the side flow increases, the side flow factor decreases. As shown in Figure 21b, by increasing the doctor blade height, the size of the side flow factor (α) increases. For the lower value of the doctor blade height, since the slurry height in the reservoir and the velocity of the peeling belt are constant, the hydrostatic pressure behind the flow is higher compared to the one with the bigger doctor blade height. Increasing the hydrostatic pressure will increase the flow to the sides and hence lead to a decrease in the resultant side flow factor. On the other hand, due to the low velocity used in these series of experiments, the ceramic slurry has much time to flow towards the sides after leaving the doctor blade region. These two phenomena obviously interact, but with the bigger doctor blade height, the effect of hydrostatic pressure decreases and leads to a decrease in the flow to the sides and hence an increase of the side flow factor. And finally, increasing the initial slurry height in the reservoir will increase the tape thickness (see section 4.2.3), thereby promoting the flow towards the sides and hence decrease the resultant side flow factor (see Figure 21c).

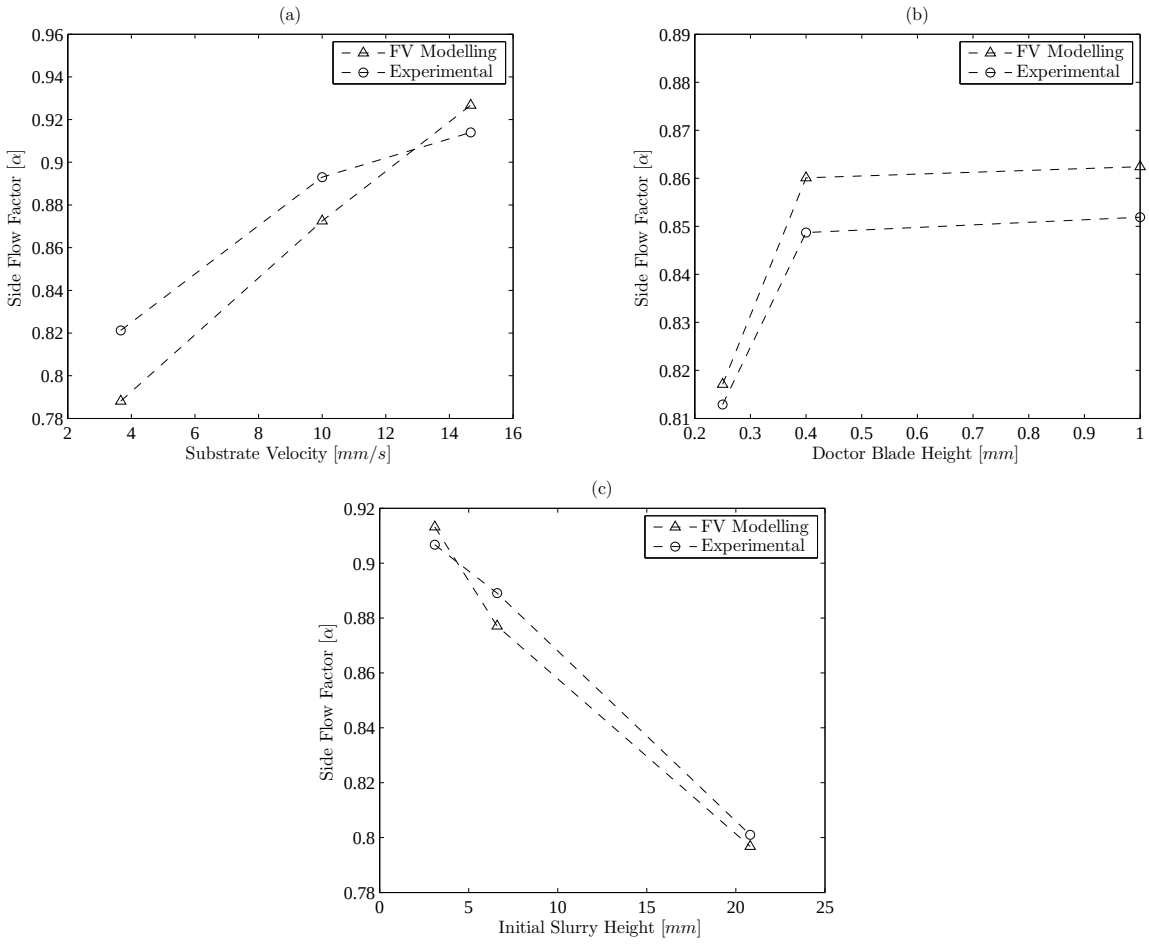

Figure 21: Numerical modelling and corresponding experiments values of side flow factor (α) influenced by (a) substrate velocity, (b) doctor blade height, and (c) slurry height [51]. The dash lines are guides to the eye.

5. Advaned application

Apart from the more common applications of tape casting mentioned in the introduction, the process is well suited for manufacturing of functionally graded materials (FGMs). The concept of graded materials was first established by Bever and Duwez[29] for composite materials, and then further developed for polymeric materials [30]. FGMs are materials that have a gradual variation of material properties from one end to another. The FGMs were originally developed as special materials which could sustain long-term exposure to high temperature and large differences of temperature. There are different techniques to produce FGMs which are well summarized by Kieback and et al. [61], and among them tape casting is reported extensively in literature [31, 32] due to producing large-area, thin, flat ceramics, which can be patterned, stacked, and laminated to form three-dimensional structures [62].

In an era of critical demand for the development of alternative energy sources, magnetic refrigeration attracts significant interest as an environmentally friendly and energy efficient alternative to conventional refrigeration [63]. The technology relies on the so-called magnetocaloric effect (MCE), for reversible heating and cooling of magnetocaloric material (MCM) in magnetization/demagnetization cycles [64]. It is known for ferromagnetic materials that the largest temperature changes, as a response to a variation in magnetic field, occurs near the phase transition, also

known as the Curie temperature. The Curie temperature is very sensitive to changes in electronic or crystal structure and can thus often be chemically tuned. In order for a magnetic refrigeration device to produce a temperature span a graded magnetocaloric material is desired, where the range of Curie temperatures is close to that of the device temperature span. In perovskite ceramic materials the Curie temperature can be tuned by a small amount of chemical doping. These materials can then be shaped into parts using the recently proposed method of side-by-side (SBS) tape casting [33]. Plates containing materials with two different ceramic materials have been prepared by this method and successfully tested in a magnetic refrigeration test device [65]. A large batch of plates containing five different Curie temperatures has recently been prepared and will soon be tested in a large-scale magnetic refrigeration device [66].

As explained by Dinesen et al. [33], in the recently developed technique of side-by-side (SBS) tape casting, multiple slurries are tape casted adjacently forming a single tape to produce functionally graded ceramics (FGCs). Then, these FGCs are used in the magnetic refrigeration process in which there is a temperature gradient along the part (see Figure 22(a)).

One of the most important parameters which has a significant effect on the final properties of the SBS ceramics, is the behavior of the interface (Φ) between the adjacent layers (see Figure 22(b)) [67]. The aforementioned interface in the FGCs used for magnetic refrigeration are supposed to be close in shape to its ideal form of a 2D in-plane surface (in the $y-z$ plane), which is perpendicular to the substrate plane ($x-y$ plane). However, based on the slurry properties (i.e. the density and the viscosity) and the process conditions (i.e. the initial slurry height in the reservoir and the velocity of the peeling belt), the interface between the two adjacent layers can vary from its ideal shape to have different shapes as follows:

1. $\alpha_1 = \alpha_2 \neq 90$: Φ is a planar interface.
2. $\alpha_1 \neq \alpha_2 \neq 90$: Φ is a twisted-planar interface.

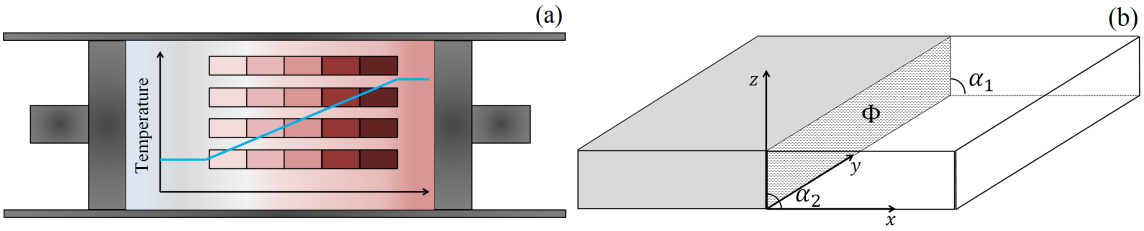

Figure 22: (a) Schematic example of FGCs used in magnetic refrigeration, and (b) schematic representation of the interface between the two adjacent layers [67].

Numerical modeling of the SBS tape casting process with two fluid entries was conducted by the authors [67–69]. The predicted interface was investigated to understand the influence of the material parameters of the two adjacent fluids, i.e. the density (ρ) and the viscosity (μ), on the position of the interface. It was observed that the densities of the fluids do not influence the interface between the adjacent fluids, whereas the viscosity of the fluids plays a key role in the interface behavior. Specifically, it is seen that the viscosity difference ($\triangle\mu$) causes the fluid with lower viscosity to move toward the one with the higher viscosity. Moreover, increasing the aforementioned difference leads to further movement of the interface toward the fluid with the higher viscosity.

The impact of the substrate velocity was also investigated. As expected, it was found that by increasing the substrate velocity the height of both fluids decreased. Moreover, in the presence of the viscosity difference for the adjacent fluids, by increasing the substrate velocity the interface moved more toward the fluid with the higher viscosity.

Finally, it was concluded that for the magnetic refrigeration applications with the objective of an ideal (totally perpendicular) interface between the adjacent fluids, the viscosities of the fluids should be kept as close as possible. Moreover, in the presence of a viscosity difference ($\triangle\mu$), to decrease the diffusive region, as low velocities as possible for the substrate should be used. This is illustrated in Figure 23. This is due to an increase of the drag force by increasing the substrate velocity (v_0), which makes it more dominant compared to the pressure force, and results in more stretching of the slurry over the peeling belt [38, 51, 56, 58, 59].

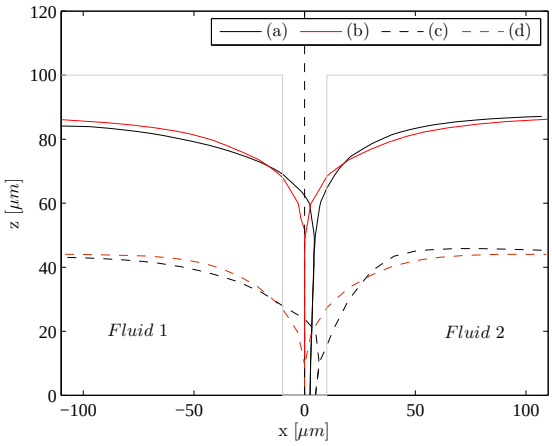

Figure 23: The change in the predicted interface between the adjacent layers for different cases, (a) $v_0 = 3.67mm/s$, $\rho_{F2} = 2\rho_{F1} = 4kg/m^3$ and $\mu_{F2} = 2\mu_{F1} = 6Pa.s$, (b) $v_0 = 3.67mm/s$, $\rho_{F2} = 2\rho_{F1} = 4kg/m^3$ and $\mu_{F2} = \mu_{F1} = 3Pa.s$, (c) $v_0 = 7.34mm/s$, $\rho_{F2} = 2\rho_{F1} = 4kg/m^3$ and $\mu_{F2} = 2\mu_{F1} = 6Pa.s$, (d) $v_0 = 7.34mm/s$, $\rho_{F2} = 2\rho_{F1} = 4kg/m^3$ and $\mu_{F2} = \mu_{F1} = 3Pa.s$. The gray lines indicate the geometry at the exit from the tape caster.

6. Concluding remarks

Tape casting technology has been developing rapidly and the commercial exploitation in manufacturing of different ceramic components is now growing even more rapidly. Most of the researches made in the field of tape casting are focused on the materials characterization and the slurry formulation for desired applications. However, the interest point of this review was the outlook for modelling of the process via fluid flow simulations. Fluid flow modelling as a tool, is an efficient mean to elucidate the physical parameters crucial to the process. Despite its benefit in simulating a real life process, fluid dynamic calculations have some complexity to overcome, which is the case lead to conduct analytical solution for a specific governing equation. This has been more common for the tape casting process, as the analytical models were developed to control the tape thickness. Most of the aforementioned models contain the rheological behavior of the ceramic slurry as well as the tape caster configuration, i.e. casting speed, doctor blade height and the height of the slurry in the reservoir. As reported by almost all researchers in the field, the Ostwald-de Waele power law model as well as the Bingham model are the common non-Newtonian models for the flow behavior of the ceramic slurry. The literature reviewed in this paper shows that most of the researchers have focused on the development of various analytical models to increase the precision of the predicted thickness of the produced tape, as one of the most affecting parameters in the final quality of the ceramic layers.

In addition to the development in the analytical models, some researchers have tried to model the flow of the ceramic slurry in tape casting numerically. Back into the 1990s (1994-1997), the initial numerical models were mostly dealing with the flow simulation inside the reservoir as well

as the doctor blade region. However, since then strong models have been developed to simulate the tape casting process as the computational size of the computers has increased. Except for one important contribution made by a group in Germany which has been published in 2011, most of the numerical models developed in the field were developed by the authors. The current numerical models can simulate the flow in tape casting capable of capturing the interface of the ceramic slurry. All parameters of the tape casters (i.e. casting speed, doctor blade height and the height of the slurry in the reservoir) together with different rheological behavior of the ceramic slurry can now be modeled with the present models developed by the authors. The developed models have been taken to the next levels to simulate the tape casting of functionally graded ceramics (FGCs) for the magnetic refrigeration applications.

The prospects for the development of the fluid flow modelling in tape casting can also be related to other processes such as extrusion, non-Newtonian flow mixer, biological flow and any other processes dealing with complex fluids. The influence of additional force fields should be taken into consideration. In conclusion, it may be said that, being a new fast developing interdisciplinary approach, the fluid flow modelling in tape casting offers considerable possibilities for progress in the area of mechanics and materials.

7. Future outlooks

The "model" and the "computer" are now integral components in studies for fluid mechanics and materials engineering. Indeed, numerical methods and computing techniques have become daily tools for formulating conceptual models and mathematical theories integrating diverse information about rheology, ceramic science, processing technique, energy systems and their interactions. This achievement has greatly enhanced the development of modern processing techniques from the traditional "try-and-error" art of producing ceramic components and support design to the rationalism of modern fluid mechanics, governed by and established on the three basic principles of physics: mass, momentum and energy conservation.

The use of numerical methods to describe the flow phenomenon in the ceramic industry has produced a large number of models. Some assumptions such as simplified geometrical shape, constant rheological properties during the process, homogeneous ceramic slurry, and most importantly neglecting the thermal influences during the processing were widely used in modelling of tape casting. However, more research should be conducted to justify the acceptability of those assumptions by sensitivity analysis and to improve the accuracy of models by finding more information on multiphase flow of the ceramic slurry which contains different ingredients (either liquid phase or particle phase) as well as the thermal impact on the flow behavior during processing.

Although much progress has been achieved, there remain several areas that warrant further investigation. Recalling from the aforementioned assumptions, the most pressing of these, in our opinion, is the impact of temperature changes on the flow behavior of the ceramic slurry during the process. Such modelling will pass important information for the follow up processes in tape casting such as the drying and the sintering processes. This means that, before fluid flow analysis and numerical methods can become a quantitative tool for correctly analyzing the tape casting process, determination of thermal-physical properties of a ceramic slurry remains an important area to be studied.

And finally, the demands for conducting accurate and complex numerical modelling of real life processes is an input for the information technology and computer science industry, which began to appear and, by the end of the 20th century, massively parallel supercomputers with tens of thousands of "off-the-shelf" processors were the norm. We believe that, existence of such computational power will give the engineering society this power to lead their research in an advanced way.

Acknowledgment

The authors would like to acknowledge the support of the Scientific Research Councils on Technology and Production Sciences (FTP) (Contract No. 09-072888, OPTIMAC), which is part of the Danish Council for Independent Research (DFF).

References

[1] G. N. Howatt, R. G. Breckenridge, and J. M. Brownlow, "Fabrication of Thin Ceramic Sheets for Capacitors," *Journal of American Ceramic Society*, vol. 30, pp. 237–242, 1947.

[2] G. N. Howatt, "Method of Producing High Dielectric High Insulation Ceramic Plates," January 1952. US Patents No. 2582993.

[3] H. W. Stetson and W. J. Gyurk, "Alumina Substrates," October 1967. US Patents No. 3698923.

[4] B. N. Schwartz and W. R. Kirkpatrick, "Switch for Selective Coupling a Sensor or Calibration Elemnt to aTerminal Block," April 1967. US Patents No. 6045260.

[5] R. Newnham, D. Skinner, and L. Cross, "Connectivity and piezoelectric-pyroelectric composites," *Materials Research Bulletin*, vol. 13, pp. 525–536, 1978.

[6] C. Fiori, G. Fusaroli, A. Krajewski, and P. Vincenzini, "On the fracture strength of tape-casted alumina substrates," *Ceramurgia International*, vol. 5, pp. 124–126, 1979.

[7] A. Bellosi and P. Vincenzini, "Microstructural observations on sintered alpha alumina," *Materials Chemistry*, vol. 4, pp. 721–729, 1979.

[8] H. Bowen, "Basic research needs on high temperature ceramics for energy applications," *Materials Science and Engineering*, vol. 44, pp. 1–56, 1980.

[9] B. Schwartz, "Review of multilayer ceramics for microelectronic packaging," *Journal of Physics and Chemistry of Solids*, vol. 45, pp. 1051–1068, 1984.

[10] K. Mikeska and W. Cannon, "Non-aqueous dispersion properties of pure barium titanate for tape casting," *Colloids and Surfaces*, vol. 29, pp. 305–321, 1988.

[11] J. K. Yamamoto, "Fabrication of controlled porosity in a tape cast glass ceramic substrate material," *Materials Letters*, vol. 8, pp. 278–282, 1989.

[12] T. Claaßen and N. Claussen, "Processing of ceramic-matrix/platelet composites by tape casting and lamination," *Journal of the European Ceramic Society*, vol. 10, pp. 263–271, 1992.

[13] T. Chartier and A. Bruneau, "Aqueous tape casting of alumina substrates," *Journal of the European Ceramic Society*, vol. 12, pp. 243–247, 1993.

[14] D. Hotza and P. Greil, "Review: aqueous tape casting of ceramic powders," *Materials Science and Engineering A*, vol. 202, pp. 206–217, 1995.

[15] K. Lindqvist and E. Lidén, "Preparation of alumina membranes by tape casting and dip coating," *Journal of the European Ceramic Society*, vol. 17, pp. 359–366, 1997.

[16] P. V. Vasconcelos, J. A. Labrincha, and J. M. F. Ferreira, "Porosity development of diatomite layers processed by tape casting," *Ceramics International*, vol. 24, pp. 447–454, 1998.

[17] B. Riley, "Solid oxide fuel cells - the next stage," *Journal of Power Sources*, vol. 29, pp. 223–237, 1990.

[18] A. J. Appleby, "Fuel cell technology: Status and future prospects," *Energy*, vol. 21, pp. 521–653, 1996.

[19] *http://www.britannica.com/EBchecked/media/262/Steps-in-doctor-blading-a-tape-casting-process-employed-in.*

[20] P. Cheneviere, M. Sardin, P. D. Farcy, and A. Putz, "Ch. R-20 Transient Transport of Bacterial Suspensions in Natural Porous Media: Modeling of the Adsorption Phenomenon," *Developments in Petroleum Science*, vol. 31, pp. 311–329, 1991.

[21] J. Sjoblom, T. Skodvin, Øystein Holt, and F. P. Nilsen, "Colloid chemistry and modern instrumentation in offshore petroleum production and transport," *Colloids and Surfaces A: Physicochemical and Engineering Aspects*, vol. 124, pp. 593–607, 1997.

[22] L. D. Nghiem, P. Mornane, I. D. Potter, J. M. Perera, R. W. Cattrall, and S. D. Kolev, "Extraction and transport of metal ions and small organic compounds using polymer inclusion membranes (PIMs)," *Journal of Membrane Science*, vol. 281, pp. 7–41, 2006.

[23] E. A. Molaei, S. H. Amrei, A. M. Dehkordi, and M. Haghi, "Transient and steady-state analysis of heat, mass, and momentum transfer in developing and fully-developed regions of homogeneous tubular reactors with non-Newtonian fluid flow," *Energy Conversion and Management*, vol. 65, pp. 308–321, 2013.

[24] C. Zhao, J. Xue, F. Ran, and S. Sun, "Modification of polyethersulfone membranes - A review of methods," *Progress in Materials Science*, vol. 58, pp. 76–150, 2013.

[25] Z. Yuping, J. Dongliang, and P. Greil, "Tape casting of aqueous Al_2O_3 slurries," *Journal of the European Ceramic Society*, vol. 20, pp. 1691–1697, 2000.

[26] Z. He, K. B. Andersen, F. B. Nygaard, and K. K. Hansen, "A combined SEM, CV and EIS study of multi-layered porous ceramic reactors for flue gas purification," *Ceramics International*, vol. 39, pp. 847–851, 2013.

[27] D. Stöver, H. P. Buchkremer, and S. Uhlenbruck, "Processing and properties of the ceramic conductive multilayer device solid oxide fuel cell (SOFC)," *Ceramics International*, vol. 30, pp. 1107–1113, 2004.

[28] N. O. Shanti, D. M. Bierschenk, S. A. Barnett, and K. T. Faber, "Direct lamination of solid oxide fuel cell anode support, anode, and electrolyte by sequential tape casting of thermoreversible gel slips," *Journal of Power Source*, vol. 212, pp. 43–46, 2012.

[29] M. B. Bever and P. E. Duwez, "Gradients in Composite Materials," *Materials Science and Engineering*, vol. 10, pp. 1–8, 1972.

[30] M. Shen and M. B. Bever, "Gradients in polymeric materials," *Journal of Materials Science*, vol. 7, pp. 741–746, 1972.

[31] J.-G. Yeo, Y.-G. Jung, and S.-C. Choi, "Design and microstructure of ZrO2/SUS316 functionally graded materials by tape casting," *Materials Letters*, vol. 37, pp. 304–311, 1998.

[32] N. C. Acikbas, E. Suvaci, and H. Mandal, "Fabrication of Functionally Graded SiAlON Ceramics by Tape Casting," *Journal of American Ceramic Society*, vol. 89, pp. 3255–3257, 2006.

[33] A. R. Dinesen, S. Linderoth, N. Pryds, and A. Smith, "Magnetic regenerator, a method of making a magnetic regenerator, a method of making an active magnetic refrigerator and an active magnetic refrigerator," 2012.

[34] R. Tanner and K. Walters, *Rheology: an historical perspective*. Elsevier, 1998.

[35] R. Reid, J. Prausnitz, and T. Sherwood, *The properties of gases and liquids*. McGraw-Hill, 3rd ed., 1977.

[36] Y. T. Chou, Y. T. Ko, and M. F. Yan, "Fluid Flow Model for Ceramic Tap Casting," *Journal of American Ceramic Society*, vol. 70, pp. 280–282, 1987.

[37] P. H. Gaskell, B. Rand, J. L. Summers, and H. M. Thompson, "The Effect of Reservoir Geometry on the Flow Within Ceramic Tape Casters," *Journal of European Ceramic Society*, vol. 17, pp. 1185–1192, 1997.

[38] H. J. Kim, M. J. M. Krane, K. P. Trumble, and K. J. Bowman, "Analytical Fluid Flow Models for Tape Casting," *Journal of American Ceramic Society*, vol. 89, pp. 2769–2775, 2006.

[39] M. Jabbari and J. Hattel, "Numerical Modeling of Fluid Flow in the Tape Casting Process," vol. 1389 of *AIP Conference Proceedings Series*, pp. 143–146, Numerical Analysis and Applied Mathematics : ICNAAM, 2011.

[40] A. Wonisch, P. Polfer, T. Kraft, A. Dellert, A. Heunisch, and A. Roosen, "A Comprehensive Simulation Scheme for Tape Casting: From Flow Behavior to Anisotropy Development," *Journal of American Ceramic Society*, vol. 94, pp. 2053–2060, 2011.

[41] R. B. Bird, "Useful Non-Newtonian Models," *Annual Reviews of Fluid Mechanic*, vol. 8, pp. 13–34, 1976.

[42] G. Terrones, P. A. Smith, T. R. Armstrong, and T. J. Soltesz, "Application of the Carreau Model to Tape-Casting Fluid Mechanics," *Journal of American Ceramic Society*, vol. 80, pp. 3151–3156, 1997.

[43] T. A. Ring, "A Model of Tape Casting Bingham Plastic and Newtonian Fluids," *Advanced Ceramics*, vol. 26, pp. 569–576, 1989.

[44] G. Zhang, Y. Wang, and J. Ma, "Bingham Plastic Fluid Flow Model for Ceramic Tape Casting," *Materials Science and Engineering A*, vol. 337, pp. 274–280, 2002.

[45] S. C. Joshi, Y. C. Lam, F. Y. C. Boey, and A. I. Y. Tok, "Power law fluids and Bingham plastics flow models for ceramic tape casting," *Journal of Materials Processing Technology*, vol. 120, pp. 215–225, 2002.

[46] X. Y. Huang, C. Y. Liu, and H. Q. Gong, "A Viscoplastic Flow Modeling of Ceramic Tape Casting," *Materials and Manufacturing Processes*, vol. 12, pp. 935–943, 1997.

[47] M. Jabbari and J. Hattel, "Bingham-Plastic Fluid Flow Model in Tape Casting of Ceramics Using Two Doctor Blades - An Analytical Approach," *Materials Science and Technology*, 2013.

[48] H. J. Kim, M. J. M. Krane, K. P. Trumble, and K. J. Bowman, "Analytical Fluid Flow Models for Tape Casting," *Journal of American Ceramic Society*, vol. 89, pp. 2769–2775, 2006.

[49] H. Loest, R. Lipp, and E. Mitsoulis, "Numerical Flow Simulation of Viscoplastic Slurries and Design Criteria for a Tape Casting Unit," *Journal of American Ceramic Society*, vol. 77, pp. 254–262, 1994.

[50] M. Jabbari and J. H. Hattel, "An Evaluation of Interface Capturing Methods in a VOF Based Model for Multiphase Flow of a Non-Newtonian Ceramic in Tape Casting." Submitted to an International Journal, 2012.

[51] M. Jabbari and J. Hattel, "Numerical Modeling of the Side Flow in Tape Casting of a Non-Newtonian Fluid," *Journal of American Ceramic Society*, vol. 96, pp. 1414–1420, 2013.

[52] H. Barnes, J. Hutton, and K. Walters, *An introduction to rheology*. Elsevier, 1989.

[53] D. G. Lessard, M. Ouslaem, X. X. Zhu, A. Eisenberg, and P. J. Carreau, "Study of the Phase Transition of Poly (N,N-diethylacrylamide) in Water by Rheology and Dynamic Light Scattering," *Journal of Polymer Science: Part B: Polymer Physics*, vol. 41, pp. 1627–1637, 2003.

[54] A. Ibarz and G. Barbosa-Canovas, *Unit operations in food engineering*. CRC Press, 2003.

[55] G. Govier and K. Aziz, *The flow of complex mixtures in pipes*. Van Nostrand, 1977.

[56] R. Pitchumani and V. M. Karbhari, "Generalized Fluid Flow Model for Ceramic Tape Casting," *Journal of American Ceramic Society*, vol. 78, pp. 2497–2503, 1995.

[57] A. I. Y. Tok, F. Y. C. Boey, and Y. C. Lam, "Non-Newtonian fluid flow model for ceramic tape casting," *Materials Science and Engineering A*, vol. 280, pp. 282–288, 2000.

[58] M. Jabbari, R. Bulatova, J. H. Hattel, and C. R. H. Bahl, "Quasi-Steady State Power Law Model for the Flow of $La_{0.85}Sr_{0.15}MnO_3$ Ceramic Slurry in Tape Casting," *Materials Science and Technology*, vol. 29, pp. 1080–1087, 2013.

[59] M. Jabbari and J. Hattel, "Numerical Modeling of the Flow of a Power Law Ceramic Slurry in the Tape Casting Process," Tenth International Conference on Advances and Trends in Engineering Materials and their Applications, pp. 151–157, AES-ATEMA INTERNATIONAL CONFERENCE, 2012.

[60] M. M. Cross, "Rheology of non-Newtonian fluids: A new flow equation for pseudoplastic systems," *Journal of Colloid Science*, vol. 20, pp. 417–437, 1965.

[61] B. Kieback, A. Neubrand, and H. Riedel, "Processing techniques for functionally graded materials," *Materials Science and Engineering A*, vol. 362, pp. 81–105, 2003.

[62] G. S. Grader and L. Zuri, "Tape Casting Slip Preparation by in Situ Polymerization," *Journal of American Ceramic Society*, vol. 76, pp. 1809–14, 1993.

[63] K. A. G. Jr. and V. K. Pecharsky, "Thirty years of near room temperature magnetic cooling: Where we are today and future prospects," *International Journal of Refrigeration*, vol. 31, pp. 945–961, 2008.

[64] A. Smith, C. R. H. Bahl, R. Bjørk, K. Engelbrecht, K. K. Nielsen, and N. Pryds, "Materials Challenges for High Performance Magnetocaloric Refrigeration Devices," *Advanced Energy Materials*, vol. 2, pp. 1288–1318, 2012.

[65] C. R. H. Bahl, D. Velázquez, K. K. Nielsen, K. Engelbrecht, K. B. Andersen, R. Bulatova, , and N. Pryds, "High performance magnetocaloric perovskites for magnetic refrigeration," *Applied Physics Letters*, vol. 100, p. 121905, 2012.

[66] R. B. et al.

[67] M. Jabbari, J. Spangenberg, and J. Hattel, "Modeling of the Interface Behavior in Functionally Graded Ceramics for Magnetic Refrigeration Parts," *International Journal of Refrigeration*, vol. XXX, pp. 1–7, 2013.

[68] M. Jabbari, R. Bulatova, J. Hattel, and C. Bahl, "Interface Oscillation in the Side-by-Side (SBS) Tape Casting of Functionally Graded Ceramics (FGCs)," *American Physical Society Bulletin*, vol. 57, p. H7.00002, 2012.

[69] M. Jabbari, J. Spangenberg, and J. Hattel, "Interface Behavior in Functionally Graded Ceramics for the Magnetic Refrigeration: Numerical Modeling," *Applied Mechanics and Materials*, vol. 325-326, pp. 1362–1367, 2013.

PAPER IX

R Bulatova, M. Jabbari, K. B. Andersen, C. R. H. Bahl, “The Variation of Interface Formation with Slurry Viscosity Change in Side-By-Side Tape Casting”, 5th International Conference on Shaping of Advanced Ceramics, 2013.

.

THE VARIATION OF INTERFACE FORMATION WITH THE SLURRY VISCOSITY CHANGE IN SIDE-BY-SIDE TAPE CASTING

Regina Bulatova [a,*], Masoud Jabbari [b], Kjeld B. Andersen [a], Christian R.H. Bahl [a]
a - Department of Energy Conversion and Storage, Technical University of Denmark, Frederiksborgvej 399, 4000 Roskilde, Denmark.
b - Department of Mechanical Engineering, Technical University of Denmark, Nils Koppels Allé, 2800 Kgs. Lyngby, Denmark.
regb@dtu.dk

Summary

Homogenous and flexible adjacently graded tapes were produced by casting the organic-based slurries simultaneously. To develop side-by-side tape casing (SBSTC), the material optimization, modernization of the doctor blade design, and parameters control of such processes as casting, drying, de-bindering and sintering were studied. Solvent and binder concentrations were varied in order to optimize co-casting flow, as well as the drying and sintering shrinkage. Tapes were evaluated in terms of rheological behavior of the slurries, the green and sintered tape microstructure, the quality of the interface area, and the mechanical properties of the green tapes.
↔

Introduction

Magnetic refrigeration (MR) at room temperature is a developing alternative for conventional vapor compression refrigeration due to lower energy consumption and environmentally friendly materials [1,2]. For this application, high efficiency magnetocaloric materials with a graded Curie temperature are desired. The functional ceramics with the continuously variable composition and the transition temperature has been recently produced by side-by-side tape casting (SBSTC) [3, 4], resulting in new advanced technique to form thin ceramic plates with adjacently graded materials. One of the main scientific challenges of the graded materials produced by tape casting is to control the interface between the adjacent fluids.
The goal of this work is a deep research of SBSTC with the main focus on the fundamental understanding of controlling of the well-defined and steep interface between the adjacent slurries. For this purpose, a graded tape (**LSM_CGO**) with the solid loadings of $La_{0.85}Sr_{0.15}MnO_3$ and $La_{0.85}Sr_{0.15}MnO_3/Ce_{0.9}Gd_{0.1}O_2$ (**LSM** and **LSM/CGO**) were used for the first and the second stripes, consequently. In this work, CGO was added into the second slurry in order to form well distinguished interface in between co-casted materials. With the overall aim of developing the SBSTC process, a number of experiments were carried out. The other objective of this work is to predict morphological and mechanical properties of the green tapes given the initial production conditions, i.e. slurry compositions and rheological characteristics.
As mentioned earlier, the main part of this work is to study the multiple material flows. The rheological behavior of the slurries influences not only the entry flow of the multiple materials, but also the homogeneity and stability of the suspensions. Moreover, it results in developing a stress in the contact area while drying, de-bindering, and sintering. Taking all these factors into account, slurries with different viscosity values (achieved by using different ratios between components) have been tape cast. As a result, formation of different interface shapes lead to variations in the shrinkage behavior.
Additionally to the standard procedure, SBSTC technique requires modernization of the doctor blade design. To form well adhered interconnected interface, each individual partition, dividing doctor blade reservoir into smaller vessels, have to be sharpened in the front side [3]. The main challenge of SBSTC is to acuminate partition by a way to let adjacent slurries join and co-flow smoothly, and, as a consequence, without intermixing or leaving partition trace in the interface area.

Experimental

Based on the well-known industrially used recipes [5], the slurries, initially containing of 14,02 vol% $La_{0.85}Sr_{0.15}MnO_3$ (LSM, calcined at 1000°C) and 11,15 vol% LSM with 1,05 vol% of uncalcined $Ce_{0.9}Gd_{0.1}O_2$ (LSM/CGO) were prepared.

To insure a stable slurry, the powder was added in two steps: The 80% of the LSM powder was suspended in MEKET with PVP dispersant and ball milled for 72 h. CGO, if any, and the last 20% of the LSM with PVP as dispersant, was then added to the suspension; and the slurry was milled for further 72 h. Powder, MEKET solvent and PVP dispersant were milled in two steps until the powder is fully dispersed, with the average particle size of 3 μm for both slurries and no further reduction of the particle size was observed. After adding binder solution (binder B60H, plasticizers DBP, PEG, and Additol), suspension was milled for another 24 h. To study kinetics of milling, particle size distribution was measured during the whole period of the slurry preparation using Scattering Particle Size measurements (Beckman Coulter LS 13320 with a measurement range of 0.04–2000 μm, Miami, FL). All slurries were characterized by a pseudoplastic behavior (viscosity curves are not shown here) as it is required for tape casting.
For the first screening, binder solution and solvent concentrations were varied with subsequent casting and sintering to observe the effect not just on rheological behavior, but also on microstructure formation. After milling and before casting, the slurries were filtered on a 100 μm mesh (thin tulle) to ensure a structure with a powder fine. Then suspensions were degassed in vacuum in order to avoid bubbles in the slurry volume, and to minimize the defects formation during drying process.
The doctor blade was prepared by splitting the loading reservoir into two compartments. The splitting was done with the camper partition [3]. Tapes with the sintered thickness of 300μm were required [4]. To achieve that, the high of doctor blade was adjusted to 1 mm, and tapes were formed with 20 cm/min casting speed. The slurry couples were simultaneously added to each compartment of the doctor blade. After drying, the tapes were punched out and sintered at 1250°C for 4h.
Post sintered tapes were embedded in epoxy, grinded and the cross sections with interfaces were investigated. To study the interface between the adjacent materials in the green state, a cross section of green tapes was prepared and studied with a scanning electron microscope (SEM) (Zeiss, EVO 60 at 15kV with Noran EDS).
For measurement of tensile stress (strain-stress resistivity), samples were fixed in Instron tensile machine keeper providing independent conditions.

Results and discussion

The special procedure of ball milling was used due to necessity to work with slurries of high viscosities (2000 mPa·s to 8000 mPa·s at casting shear rate 4 s^{-1}) while producing adjacently graded tape (Fig.1). Fig. 2 shows decreasing of particles size distribution with milling LSM_CGO slurry, with the casting viscosity of 3000 mPa·s at casting shear rate. The same tendency was observed for all used slips.
The main target of ball milling is to ensure in isotropic reproducible dimensional stability of final tape properties. The high viscosity was achieved by decreasing the amount of the solvent, therefore, milling and mixing was hindered. To achieve a fine microstructure of the cast tapes, solid phase was added in two steps. First, the solvent, dispersant and 80 wt% of the powder were mixed. Once this suspension became less viscous and the smallest particle size was achieved, next 20 wt% of powder was added. On that stage one can see a little jump on the curve, which is due to the addition of the bigger particles to the milled mixture with the finer ones. After this portion of powder was broke down, the third stage of chemicals, such as binder and plasticizers solution, were added. To prevent matrix formation, re-agglomeration of particles, and slurry thickening, 20 hours of milling after binder addition was required.
One of the key factors, influencing the interface shape and position of adjacent tapes, is the slurries viscosity which will be described here in details. To detect the influence of the solvent and binder content on the tape structure formation, two simultaneous experiments were conducted. The first experiment implied solvent content variation, which was proved to have stronger effect on the slurries viscosities, while small variations in binder concentrations had a high impact on tape densification and adherence between the adjacent strips. The majority of the matrix instabilities in the form of the pores and cracks appear throughout the drying process due to the binder lack, while binder excess leads to tape deformations during de-bindering. The biggest challenge of necessity of matching the properties for the co-casted components, especially during densification, was overcome by using the same organic systems for the adjacent materials as well as varying the solvent and binder concentrations in a narrow area of 5 wt% maximum for both ingredients. Four samples with different binder/powder ratio were tested and investigated on a sense of interface area quality (Fig. 3).
Adjacent tape casting, in addition to the possibility of creating sheets of desired thickness and density, aims overlapping and interface position control. Here overlapping is either overflow of one slurry on top of neighboring one, or it's displacement what result to the interface shifting and/or inclination. Fig. 4 shows that beginning of green tape is thicker comparing with end of the cast tapes, no matter which slurry viscosities were used. The changes in the tape thickness are predictable due to constant decrease in

hydrostatic pressure behind the doctor blade region [6]. However, after the first 10 cm the thickness of the graded tapes become more uniform. Moreover, the more viscous slurry is cast, the smoother the tape was produced. Due to the variation of the side flow based on the viscosity of the slurry, the thickness and the width of the tapes uncontrollably vary along the length. More viscous slurries keep the shape stronger, reducing the side flow, and hence the tape thickness becomes more uniform. However, impact of the viscosity on the green tape density is not that strong as on the tape thickness (Fig. 5). That advance one-doctor blade technique for industrial production.

With advantages of adjacently graded tapes properties, the process should comprise formation of steep and flat interface formation. Fig. 6 shows continuous decrease in the overlapping along the tape length. That effect attributes to sharp processing start, due to that overlapping on the beginning of the tape is higher. Co-casting of similarly high viscous slurries leads to formation of steep interface with comparably small overlapping.

To evaluate the SBSTC further in the interface area, the energy dispersive X-ray (EDS) mapping has been carried out. The EDS analysis was performed to compare the composition in the area of the pure material and in the interface region. Unified behavior for the whole range of slurries viscosities with the only difference in overlapping value was observed. No diffusion or intermix between co-casted materials was found. The overlap between the two materials at the interface was less than 600 μm (Fig.7).

Magnetic cooling application requires for the magnetocaloric materials to be able to withstand the heat exchange while the liquid is pumped through graded plates. And to insure in nonablative system, the tensile test was chosen to evaluate the green tapes. Polymers influence on the flexibility and the green strength for the cast tapes, as a result, mechanical properties of pure LSM_CGO green tapes were increasing with loading binder solution and increasing of viscosity, consequently (Fig. 8b). The same tendency was observed for the graded tape, as pure LSM stripe remain constant from sample to sample (Fig. 8a). Therefore, adherence between the co-casted materials improves with increasing of the polymer content.

After tape casting, sheets were subjected to thermo-treatment including burnout and sintering. The heating regime was optimized based on TGA and DTA data (not shown here). Samples were heated up to burn-out temperatures of 200 and 400 °C with 0,5 °C/min heating speed and 2 hours dwell time. Further tapes were heated up to sintering temperature of 1250 °C following by cooling with 1°C/min speed. No any damages or distortion were observed.

Conclusion

Modifying doctor blade reservoir and optimizing slips recipe generates the new design of the cast tapes generation, namely formation of adjacently graded materials different natures, what could be considered for a wide variety applications. The parametric study of SBSTC has been conducted to see how slurries viscosities influence on interface formation. The co-casted green tapes were characterized by uniform density, dimensional stability after 10 cm of cast tape, sufficient flexibility for tapes handling and machining, high strength in green state, absence of defects after de-bindering and sintering. It was shown that the adjacent co-casting of slurries with viscosities higher than 4000 mPa·s leads to the flat interface. Moreover, the more viscous slurries were used, the more uniform tapes with not significant overlapping were achieved.

For the future work, SBSTC with a constant slurry loading in reservoir is planned. That will decrease the tape thickness instabilities. Moreover, experiments with various casting speed will be carried out.

1. Jiyu Fan, LiPi, Lei Zhang, WeiTong, Langsheng Ling, Bo Hong, Yangguang Shi, Weichun Zhang, Di Lu, Yuheng Zhang, Magnetic and magnetocaloric properties of perovskite manganite $Pr_{0,55}Sr_{0,45}MnO_3$, Physica, B406 (2011), 2289–2292,
2. Y. Xu, M. Meier, P. Das, M.R. Koblischka, U. Hartmann, Perovskite manganites: potential materials for magnetic cooling at or near room temperature, Crystal Engineering, 5 (2002), 383–389,
3. R. Bulatova, K. B. Andersen, L. Theil Kuhn, C. R. H. Bahl, and N. Pryds, Adjacent tape casting of multiple ceramic slurries, (unpublished),
4. C. R. H. Bahl, D. Velazquez, K. K. Nielsen, K. Engelbrecht, K. B. Andersen, R. Bulatova, N. Pryds, High performance magnetocaloric perovskites for magnetic refrigeration, Applied Physics Letters, 100 (2012),
5. H. Raeder, C. Simon, T. Chartier, H. L. Toftegaard, Tape casting of zirconia for ion conducting membranes: a study of dispersants, Journal of the European Ceramic Society, 13 (1994), 485-491.

6. M. Jabbari, R. Bulatova, J. H. Hattel, C. R. H. Bahl, Quasi-steady state power law model for the flow of $La_{0.85}Sr_{0.15}MnO_3$ ceramic slurry in tape casting, (submitted).

Thanks to the Danish Council for Independent Research Technology and Production Sciences (FTP) which is part of The Danish Agency for Science, Technology and Innovation (FI) (Project # 09-072888) for sponsoring the OPTIMAC research work.

PAPER X

M. Jabbari, R. Bulatova, J. Hattel, C. Bahl, "Interface oscillation in the side-by-side (SBS) tape casting of functionally graded ceramics (FGCs)", *Am. Phys. Soc. Bull.* (ISSN: 0003-0503), vol. 57 (17), pp. H7.00002, 2012.

.

Abstract Submitted
for the DFD12 Meeting of
The American Physical Society

Interface Oscillation in the Side-by-Side (SBS) Tape Casting of Functionally Graded Ceramics (FGCs) MASOUD JABBARI, Department of Mechanical Engineering, Technical University of Denmark, REGINA BULATOVA, Department of Energy Conversion and Storage, Technical University of Denmark, JESPER HATTEL, Department of Mechanical Engineering, Technical University of Denmark, CHRISTIAN BAHL, Department of Energy Conversion and Storage, Technical University of Denmark — Room temperature magnetic refrigeration is a new highly efficient and environmentally protective technology. Although it has not been maturely developed, it shows great applicable prosperity and seems to be a potential substitute for the traditional vapor compression technology. Tape Casting is a common process in producing multilayer ceramics, which now is used for producing side-by-side (SBS) functionally graded ceramics (FGCs). These FGCs are mostly used in the magnetic refrigeration sectors due to the varying composition of the magnetocaloric materials so that the magnetic transition temperature of the magnetic regenerator varies along the paths. The main goal of this research is to study the multiple material flow in SBS tape casting and analyze its influence on the interface between the stripes. The materials used for the experimental part are $La_{0.85}Sr_{0.15}MnO_3$ and $Ce_{0.9}Gd_{0.1}O_2$ ceramic slurries. The rheological behavior of the slurries are extracted from experiments and used in the ANSYS FLUENT commercial code to develop a fluid flow model for the non-Newtonian ceramic slurries and evaluate the interface oscillation between the stripes in SBS tape casting. The Numerical results show reasonable agreement with corresponding experimental results.

Masoud Jabbari
Dept of Mechanical Engineering, Technical University of Denmark,
Nils Koppels Allé, 2800 Kgs. Lyngby, Denmark

Date submitted: 31 Jul 2012 Electronic form version 1.4